JAERI-M
86-112

JAERI TANDEM, LINAC & V.D.G.
ANNUAL REPORT
1985

April 1, 1985—March 31, 1986

August 1986

Department of Physics

日本原子力研究所
Japan Atomic Energy Research Institute

JAERI-Mレポートは，日本原子力研究所が不定期に公刊している研究報告書です。

入手の問合わせは，日本原子力研究所技術情報部情報資料課（〒319－11茨城県那珂郡東海村）あて，お申しこしください。なお，このほかに財団法人原子力弘済会資料センター（〒319-11茨城県那珂郡東海村日本原子力研究所内）で複写による実費頒布をおこなっております。

JAERI-M reports are issued irregularly.

Inquiries about availability of the reports should be addressed to Information Division, Department of Technical Information, Japan Atomic Energy Research Institute, Tokai-mura, Naka-gun, Ibaraki-ken 319-11, Japan.

© Japan Atomic Energy Research Institute, 1986

編集兼発行　日本原子力研究所
印　　刷　日立高速印刷株式会社

JAERI TANDEM, LINAC & V.D.G.
Annual Report
1985

April 1, 1985 - March 31, 1986

Department of Physics
Tokai Research Establishment
Japan Atomic Energy Research Institute
Tokai-mura, Naka-gun, Ibaraki-ken, Japan

(Received July 12, 1986)

This annual report describes research activities which have been performed with the JAERI tandem accelerator, the electron linear accelerator and the Van de Graaff accelerator from April 1, 1985 to March 31, 1986. Summary reports of 52 papers, and list of publications, personnel and cooperative researches with universities are contained.

Keywords: JAERI TANDEM, e-LINAC, V.D.G., Atomic & Solid State Physics, Material Science, Nuclear Chemistry, Nuclear Physics, Neutron Physics, Annual Report

Editors Naomoto Shikazono
Masashi Iizumi
Mitsuhiko Ishii
Yuuki Kawarasaki
Michio Maruyama
Yohta Nakai
Yukio Kazumata
Yoichi Suto

原研タンデム，リニアック，バンデグラフ加速器60年度年次報告

日本原子力研究所東海研究所物理部

（1986年7月12日受理）

本年次報告は，原研タンデム，リニアック及びバンデグラフ加速器で，1985年4月1日から1986年3月31日までの間に東海研で行われた研究活動をとりまとめたものである。1）加速器運転と開発研究，2）原子及び固体物理，3）材料の放射線損傷，4）核化学，5）核物理　及び6）中性子物理の6部門にまたがる52編の研究報告，公表された文献，関与した職員及び大学との協力研究のリストを収録している。

東海研究所：〒319-11　茨城県那珂郡東海村白方字白根2－4
（編集者）鹿園　直基・飯泉　　仁・石井　三彦・河原崎雄記・丸山　倫夫・中井　洋太・数又　幸生
須藤　洋一

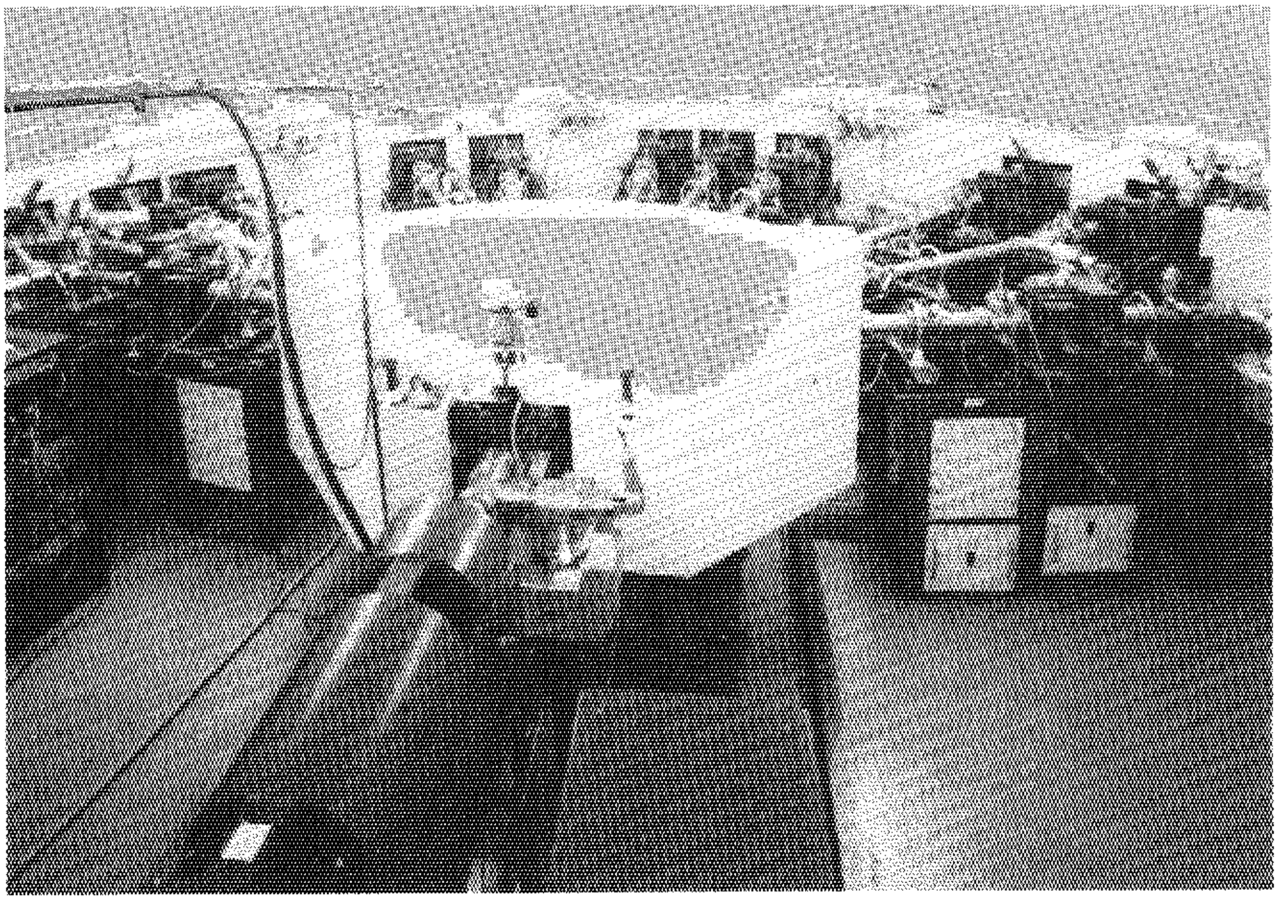

Switching magnet with 12 extended beam lines

PREFACE

This is the annual report on research activities which have been carried out with the accelerators of Department of Physics, JAERI during the period from April 1, 1985 to March 31, 1986.

All the accelerators, i.e. the tandem accelerator, the electron linear accelerator and the Van de Graaff accelerator, have been operated satisfactorily in this period. The tandem accelerator, with which a majority of the research works have been performed, opreated on a regular schedule in accordance with the cycle of three months operation for research studies and the one month for the maintenance. A development of superconducting quater wave resonator has been carried out for the tandem heavy ion booster. The final goal is to obtain the 30 MV of accelerating voltage with the 40 resonators. The electron linear accelerator and the Van de Graaff accelerator have been used for some of the researches of neutron physics and solid state physics, respectively.

Main subjects of our research activities are as follows:

1) Atomic and solid state physics
2) Radiation effects in materials
3) Nuclear chemistry
4) Nuclear physics
5) Neutron physics.

In the period, more than 70 staff members of JAERI have been working in the five fields of researches, and about 100 colleagues of universities and institutions outside JAERI have joined and collaborated in these studies.

A joint seminar on heavy ion nuclear physics and nuclear chemistry was held at Tokai Research Establishment of JAERI, January 9 - 11, 1986, and several experimental results described in this annual report were presented in the seminar. The report of the seminar is published in JAERI-M 86-067.

Naomoto Shikazono

Naomoto Shikazono
Director,
Department of Physics

CONTENTS

I ACCELERATOR OPERATION AND DEVELOPMENT …… 1
1.1 Tandem Accelerator Operation …… 3
1.2 Control System for the JAERI Tandem Accelerator …… 6
1.3 Development of Ion Optics Computer Code (II) …… 8
1.4 Service Lives of Carbon Stripper Foils in the JAERI Tandem …… 10
1.5 A Prototype Superconducting Quarter Wave Resonator for Heavy Ion Booster …… 14
1.6 New Data Acquisition System Using a VAX-11/780 and a MBD-11 …… 16
1.7 Electron Linac Operation and Improvements …… 18
1.8 Improvement of the JAERI Linac Control System …… 22
1.9 Preparation of a Fast TOF Data Acquisition System Based on an a Personal Computer with an Intelligent CAMAC …… 25

II ATOMIC AND SOLID STATE PHYSICS …… 29
2.1 Performance of the X-Ray Crystal Spectrometer …… 31
2.2 Radiative Electron Capture for $Cl^{16+,17+}$ Ions on He Target …… 34
2.3 Beam-Foil Spectra of Chlorine Ions in High Energy Region (III) …… 37
2.4 Absence of Stage I Recovery Peak in Nickel Irradiated with Heavy Ions in Energy Range 100-120 MeV …… 41
2.5 Radiation Effects of Negative Thermal Expansion in Semiconductors by Heavy Ion Irradiation …… 45
2.6 Damage Profiles in Metals Irradiated with High Energy Ions …… 49
2.7 Transmission Sputterings of Copper and Silver by 114 MeV F^{7+} Ions 53
2.8 Ion Beam Analysis on $Nb_{0.8}Mo_{0.2}$ Alloy
I. Lattice Location of Dissolved Deuterium …… 57
2.9 X-Ray Diffraction Topographic Observation of Si Single Crystals Irradiated with Energetic Heavy Ions (4) …… 61
2.10 Lattice Defects in Silicon Carbide …… 65
2.11 Further Measurements of Induced Radioactivities in Silicon and Germanium Irradiated with High-Energy Heavy Ions …… 69

III RADIATION EFFECTS IN MATERIALS …… 73
3.1 Cross-Sectional TEM Observation of 316 Stainless Steel Irradiated with 90 MeV Br-Ion …… 75
3.2 Effect of Injected Helium on Microstructure in Ti-Modified Type 316 Stainless Steels Irradiated with Helium Ions …… 79

3.3 Microstructure and Mechanical Properties of He Irradiated Stainless Steel 83
3.4 Effect of Implanted-Helium Depth Profile on Damage Structure in Electron-Irradiated Stainless Steel 86
3.5 Conductivity of A Li_2O Single Crystal Irradiated by Oxygen Ions 90
3.6 Microstructure of Ion-Irradiated Si_3N_4 94
3.7 Irradiation Effect on Some Ceramics 98
3.8 Chemical Reactions Induced by Energetic Particles 100

IV NUCLEAR CHEMISTRY 105
4.1 Production of Actinides in Reactions of ^{242}Pu with ^{12}C and ^{238}U with ^{16}O 107
4.2 Transfer Reactions in 105-MeV ^{16}O + ^{197}Au 109
4.3 Neutron Transfer Reaction in the System ^{37}Cl + ^{103}Rh 113
4.4 A Study of Nuclei Far from Stability by Using JAERI ISOL 115
4.5 Preparation of ^{211}Rn-^{211}At Generator from ^{209}Bi Irradiated with ^{14}N. 120

V NUCLEAR PHYSICS 123
5.1 B(E2) Anomaly in Ground-State Bands of ^{126}Ce and ^{124}Ce 125
5.2 Yrast States of Two Quasi-Protons Coupled with Bosons 127
5.3 Larmor Precession of Excited States in Sm-138 and Sm-136 128
5.4 Multiple Coulomb Excitation of ^{161}Dy 129
5.5 Signature Dependence Observed in Rotational Levels Based on a $f_{7/2}$ Single-Particle State in ^{163}Dy 133
5.6 Transfer Cross Sections for ^{28}Si + $^{58,62}Ni$ Reactions 138
5.7 Coincidence Measurements of Light Particles and Evaporation Residues in the System ^{16}O + ^{27}Al 142
5.8 Coincidence Measurement of Damped Reaction Fragments for the Systems of ^{35}Cl + ^{46}Ti and ^{37}Cl + ^{48}Ti 145
5.9 Shell-Model Evidence for the Exchange Term in the Interacting Boson-Fermion Hamiltonian 149
5.10 Exciton Model Approach to the Moving Source Model 151

VI NEUTRON PHYSICS 153
6.1 Scattering of 14.9 and 18.0 MeV Neutrons from ^{118}Sn 155
6.2 Preliminary Measurements for Elastic and Inelastic Neutron Scattering in the Energy Region of 30 MeV 159

6.3 Measurements of Gamma-Ray Production Cross Sections 162
6.4 Neutron Total Cross Section Measurements on Oxygen, Aluminum and Carbon Below 1.2 MeV 166
6.5 Neutron Resonance Parameters of ^{148}Sm 168
6.6 Measurements of Neutron Total Reflections on Metallic Surfaces 172
6.7 New Informations Contained in the Pulse Shape of an NE213 Liquid Organic Scintillator 176
6.8 Effects of the Timing Walk on the Time Resolution of the Large Volume Neutron Detector 181
6.9 Reduction of Delayed Gamma-Ray Backgrounds for a Pulsed Neutron Source 185

VII PUBLICATIONS 189

VIII PERSONNEL AND COMMITTEES 209

IX CO-OPERATIVE RESEARCHES 219

I ACCELERATOR OPERATION AND DEVELOPMENT

1.1 TANDEM ACCELERATOR OPERATION

Tandem Accelerator Group

Department of Physics, JAERI

Accelerator operation

The scheduled operation for experiments was performed through the past one year containing three short periods for the scheduled maintenance. The following are summary of the operation from April 1,1985 to March 31, 1986. In this period, available days for the research activity exceeded 50 percent of calendar days.

1) Time distribution by terminal voltage

16-17 MV	34 days	18.3 %	10-11 MV	10 days	5.4 %
15-16	58	31.2	8- 9	1	0.5
14-15	24	12.9	7- 8	2	1.1
13-14	20	10.7	6- 7	2	1.1
12-13	25	13.4	4- 5	3	1.6
11-12	7	3.8			

2) Time distribution by projectile

H	3 days	1.6 %	Si	10 days	5.4 %
D	19	10.2	S	7	3.8
B	1	0.5	Cl	81	43.6
C	13	7.0	Ni	1	0.5
N	2	1.1	Br	11	5.9
O	30	16.1	Au	3	1.6
F	5	2.7			

3) Time distribution by activity

Operation for research		196 days	53.7 %
Atomic and solid state physics	39		
Radiation effects in materials	26		
Nuclear chemistry	25		
Nuclear physics	72		
Fast neutron physics	22		
Accelerator development	12		
Voltage conditioning		39	10.7
Operation training		2	0.5
Scheduled maintenance (3 tank openings)		73	20.0
Unscheduled repair (1 tank opening)		5	1.4
Holidays and vacation		50	13.7

Tank openings

The accelerator was opened three times for the scheduled maintenance and once for the unexpected repair in the period.

1) June 4-7, 1985
   Annual maintenance and legal inspection of the annular and center service platforms.
2) July 3-5, 1985
   Unscheduled repair of the rotating shaft bearings and the freon circulation pump of the terminal ion source.
3) July 23-August 20, 1985
   Scheduled maintenance.
   Realignment of the horizontal and vertical low energy beam lines and the low energy acceleration tubes.
   Removal of all enclosed corona needles.
   Installation of a hoist for the terminal shell.
   Reload of the terminal stripper foils.
4) December 23, 1985-January 23, 1986
   Scheduled maintenance.
   Repair of the insulating transformer for the terminal ion source.
   Exchange of all open corona needles.
   Replacement of the belts in the transmission between the rotating shafts and the terminal generators by gear mechanisms.
   Installation of a 400 to 60Hz frequency converter to drive some terminal devices.

Improvement and development

The enclosed corona needles used with the open ones for voltage distribution were partly opened and inspected in July, 1985. Serious defects were found in several gaps in spite of a running period shorter than one year and they seemed to be one of the causes for the poor voltage holding experienced in the previous running. Also considering troublesome maintenance works, we decided to remove all enclosed corona needles and to use only open ones hereafter.

In order to improve transmission rate of the CAMAC highways and simplify electronic circuits along them, the highway cables from the control computer to the negative ion injector and the control console were replaced by optical fibers. The transmission rate became five times higher, and the optical isolators for the crates and the spatial light link to extend the highway to the injector terminal were eliminated. As a result, the CAMAC system has got much more reliable and stronger for electrical surges.

Two hundred of JAERI-type long-life carbon stripper foils were installed in the terminal in July, 1982. They were taken out and inspected in July, 1985 after three-years scheduled operation. Eighty-two foils had been used for heavy ion acceleration in this period. Seven of them were still in good condition for further use. Twenty-six foils had a hole at the beam spot but no cracks in the periphery. The beam spots were clearly observed to get thinner due to the heavy ion sputtering. Thirty-two foils had a hole at the beam spot and cracks from the hole to the periphery. Seventeen foils were damaged more or completely. As a whole the foil ruptures due to the shrinkage of the beam spot were not so serious, but the sputtering effect was rather dominant.

Several rubber timing belts had been used in the high voltage terminal to drive the generators by the rotating shafts. They had been dust sources and ruined sometimes high voltage holding of the terminal. Gear mechanisms were developed and installed in the terminal to eliminate the timing belts in January, 1986.

1.2 CONTROL SYSTEM FOR THE JAERI TANDEM ACCELERATOR

Susumu HANASHIMA, Isao OHUCHI, Katsuzo HORIE, Susumu KANDA,
Tadashi YOSHIDA and Yoshihiro TSUKIHASHI

Department of Physics, JAERI

1. Development of automated accelerator control

Renewal of the control program of the JAERI tandem accelerator was planed and proceeding for the development of the automated accelerator control. In the new control system, a concept, "easily programmable" was introduced. All programs run under control of an operating system and most of them are written in the high level language, Pascal. When an operator is using an automation program, it is executed concurrently with the control system's communication processes. The control system has interfaces which enable a program to access to the accelerator by the names of devices and their functions. The programmer need not know about the locations of the data and the addresses and formats of the I/O. He can concentrate on what he want to do with the accelerator and he need not worry about how it is done in the computer.

In this fiscal year, the test of CAMAC handler was completed(we use a CAMAC serial highway system to control the accelerator). A sub-system was constructed, which enabled application programs to access to the accelerator by the names of devices.

2. Improvement of CAMAC serial highway

The previously reported[1)] optical highway for the negative ion injector has worked without any trouble. The optical highway system showed strong noise immunity. Even when a negative ion source generated discharges in it, the optical highway worked without bit errors.

The serial highway for the control console was replaced by the optical one. The transfer rate was changed from 5 Mega-bits per second to 5 Mega-bytes per second. The speed-up of the highway was very effective, because the traffic on the highway was very heavy.

Three of five serial highway loops in the system were left with electric cables. In the electric serial highways, optical isolators have been used for ground isolation. They were changed to new isolators made for higher reliability. The termination of the signal transmission was also refined for better impedance matching.

We reported[1)] unsuccessful voltage tests of an optical fiber. We tested another type of optical fiber. The fiber wears Epoxi sheath(hardened with ultra violet rays). It withstood the high voltage gradient of 50KV/15mm, in 5Kg/cm^{2}SF$_6$ gas. It was also tested in the JAERI 2MV Van de Graaff and withstood the voltage gradient of 2MV/1.2m.

3. Improvement of devices along the beam line

The new current logarithmic amplifiers(log-amps as an abbreviation) developed last year[1),2)] were found to have good reliability and stability in the accelerator. The use of them was expanded. Seven sets were installed in the accelerator(two on the high voltage terminal, 5 out of the pressure vessel). They all worked well without any trouble. Especially, three sets along the low energy beam line were very useful, because of their exact current readings, for an operator to find out the section where the beam current decreased.

New power supplies for magnetic steerers and magnetic quadruple poles were made to improve reliability, accuracy and also maintenability. The power supplies for the qaudruple poles are switching-regulated ones. They were introduced to improve the energy efficiency and to reduce their cooling problems.

References

1) S. Hanashima et al. : JAERI Tandem, Linac & V.D.G. Annual Report 1984, JAERI-M 85-104(1985) pp.10-12.

2) T. Yoshida and S. Hanashima: JAERI-M 85-085(1985).

1.3 DEVELOPMENT OF ION OPTICS COMPUTER CODE (II)

Shiroh KIKUCHI, Suehiro TAKEUCHI and Eisuke MINEHARA

Department of Physics, JAERI

The computer code BEAM[1)] has been further developed so as to display on the CRT the dependence of the waist locations on the parameters k_1 and k_2 of the Q-lenses used in the tandem accelerator system.

Fig. 1 shows the waist vs k_1 curves in the X-s and Z-s planes for the Q-lens named as EQ-02-1 in the system, as an example. The k_2 value is fixed at $k_2 = 4.200$. The waist locations are measured from the exit of the Q-lens in meter, and the lines WAIST = 2.000 indicate the expected waist at 2.0 m. In this case, it is seen that the waist is formed at the expected location with $k_2 = 4.200$ when $k_1 = 3.773$ or 4.053 for the X-s plane and when $k_1 = 4.328$ or 4.533 for the Z-s plane.

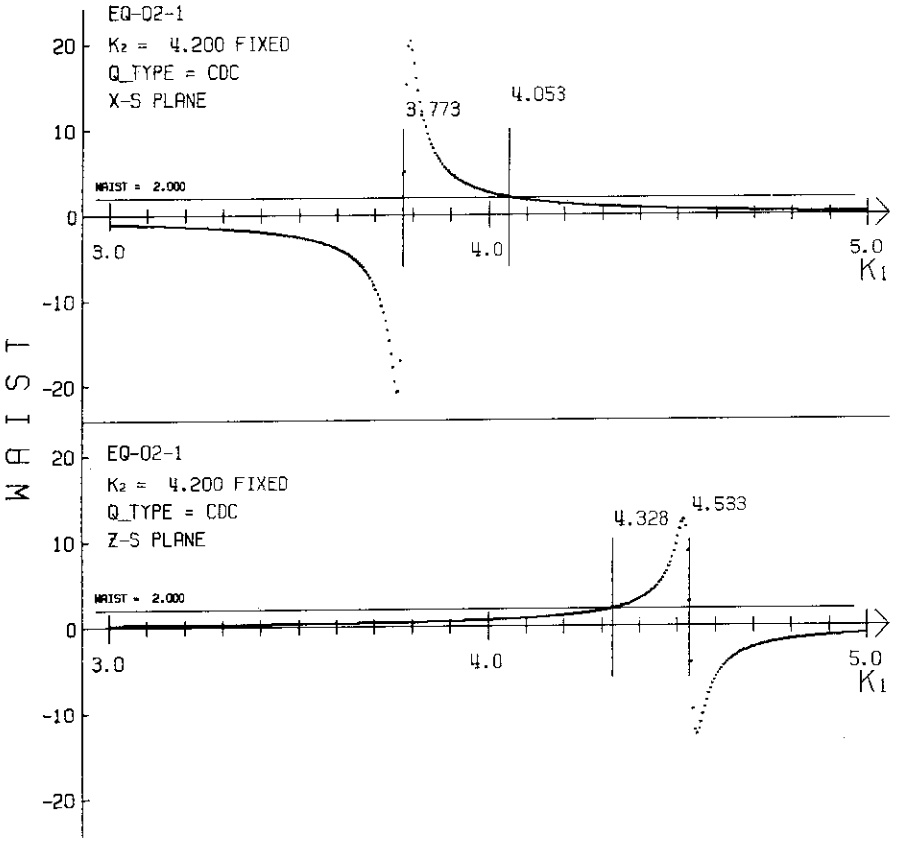

Fig. 1. The waist vs k_1 curves with fixed k_2 value.

In order to obtain the k_1 and k_2 pair which forms the waists in both planes at the same expected locations simultaneously, the parameter search process is performed in the code BEAM. The result is shown in Fig. 2, which displays that the expected waists are obtained in both planes when $k_1 = 3.872$ and $k_2 = 3.910$.

These figures illustrate the behaviors of the waist locations caused by the Q-lenses visibly, and give the useful information to the ion optics calculation.

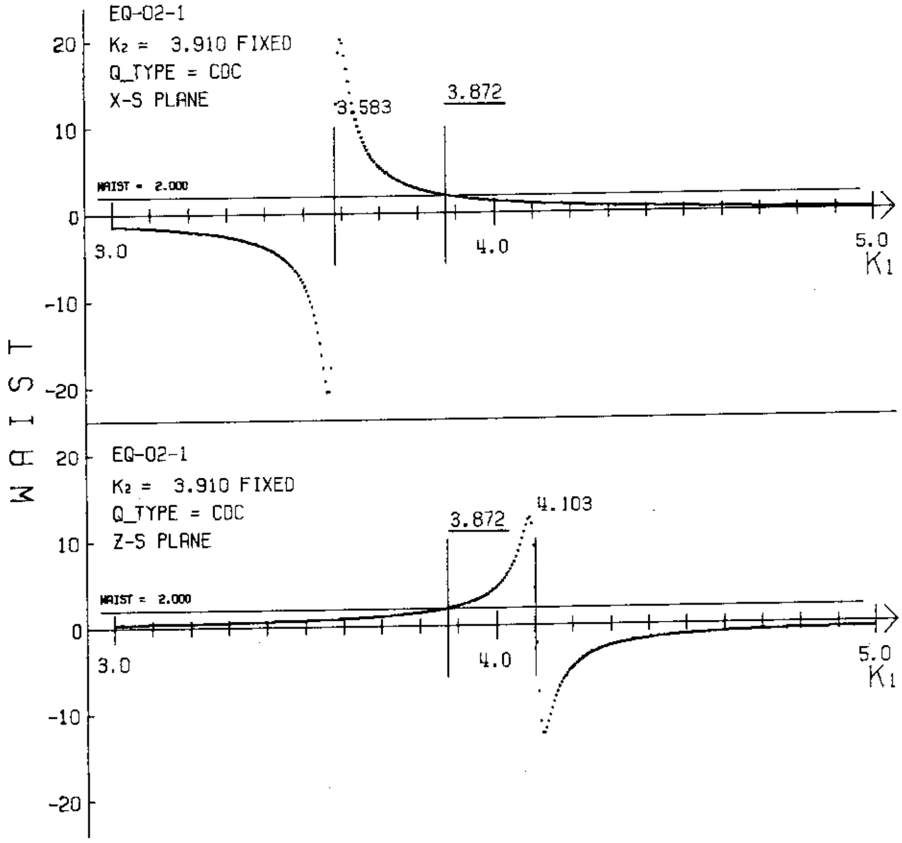

Fig. 2. The waist vs k_1 curves. The k_1 and k_2 pair, which gives the waists in both planes at the same location can be obtained.

Reference

1) S.Kikuchi, S.Takeuchi and E.Minehara: JAERI TANDEM, LINAC & V.D.G. Annual Report 1984, p.13.

1.4 SERVICE LIVES OF CARBON STRIPPER FOILS IN THE JAERI TANDEM

Suehiro TAKEUCHI and Shuhei KANAZAWA

Department of Physics, JAERI

Since long-lived carbon stripper foils, which we made by the arc-discharge technique developed till 1982[1,2], were installed in the in-terminal foil changer in July, 1982, three years past without resupplying new foils. In the period of three years from August, 1982 to July, 1985, eighty-two out of two hundred 10 $\mu g/cm^2$ thick foils were actually used for the operation of the tandem accelerator. We took them out from the foil changer and studied their service lives and their conditions after use in statistical ways.

Their service lives are shown in fig. 1. We took the data relating to the service lives from the operation records of the tandem accelerator, so that they might have some ambiguity due to unrecorded beam stops and beam handling work. Seven of the eighty-two foils were found to be still good for further use. The average service life except the seven good foils was 97 h. Table 1 shows the bombarding ion mass numbers and their respective average energies, average current intensities and total bombarding times, which were summarized for the three years operation.

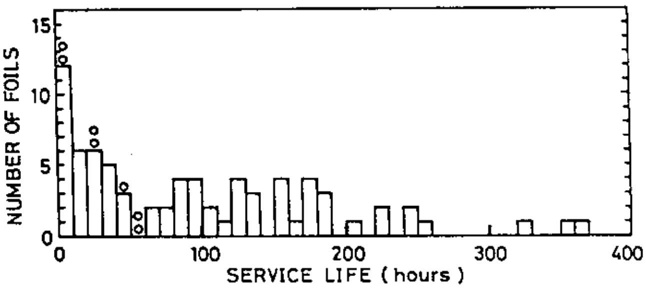

Fig.1. Service lives of 10 $\mu g/cm^2$ carbon stripper foils used in the JAERI tandem for three years. The o marks indicate good foils for further use.

The foils have been bombarded by different ion beams with different conditions during their lives. We tried to analyze the data in the following ways. 1) We divided their service lives into four groups by bombarding ion mass numbers averaged with integrated beam currents in order to see the mass number dependence. The result is shown in fig.2. 2) We reduced the service lives to the ones expressed in a unit of integrated beam current. The distribution of the reduced service lives

Table 1. Distributions of bombarding ion mass, average energy, average current intensity and total bombarding time in the period of August of 1982 to July of 1985 at JAERI tandem accelerator.

Mass	Average Energy (MeV)	Average Current (pμA)	Total bombarding Time (hours)
1	8.4	2.04	94
2	12.4	0.78	179
10	15.7	0.31	37
12	13.3	0.55	1257
16	14.5	0.57	1979
19	15.0	0.36	163
27	16.7	0.15	2
28	13.0	0.14	115
32	15.6	0.20	567
35	13.8	0.52	1762
37	15.1	0.42	682
56	16.7	0.22	2
58	14.9	0.13	466
63	15.2	0.01	23
79	13.9	0.30	35
81	13.0	0.23	46
84	14.1	0.01	4
115	13.8	0.05	18
127	15.1	0.10	22
163	14.1	0.07	3
194	14.4	0.15	2
197	12.9	0.39	40
209	13.1	0.002	10

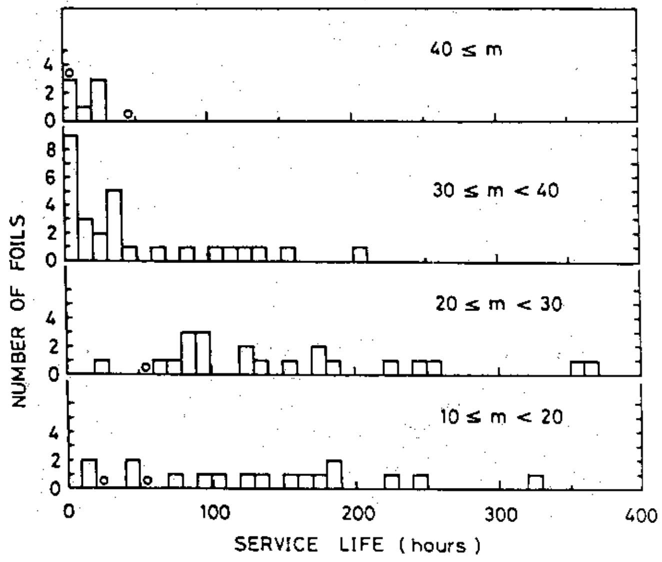

Fig. 2. Distributions of service lives divided into four groups by their average bombarding ion mass numbers m.

was not so different from the one shown in fig. 2. 3) Eventually, we evaluated the lives more generally by taking account of the theoretical dependences on mass numbers, beam intensities and beam energies. The result is shown in fig. 3, in which the integrated damage energy is the energy deposited in the foil material in the form of structual radiation damage during the whole lives. From the lifetime test done with 2 MeV Ar beams on a stable beam condition2), the integrated damage energy of our long-lived stripper foils is expected to be 78 eV(w_o). The integrated damage energies deposited in the present foils during their lives are mostly less than w_o or as large as a half of w_o in average.

This result is quite reasonable and satisfactory, because foil lives are shortened by frequent beam stops or changes of beam intensities.

On the other hand, we inspected the used foils and classified them into four groups by their appearences. Typical appearences from the group 1 to 4 are shown in fig. 4. The group 1 contained seven good foils. The group 2 contained 26 foils which had a hole at the beam spot but no cracks in the non-irradiated area. The group 3 contained 32 foils which had a hole and cracks from the hole to the non-irradiated area. The group 4 contained remaining 17 foils damaged more or completely. It is noticeable that a large fraction, 35 percent, of the damaged foils belonged to the group 2, because they did not have cracks caused by the shrinkage of the beam spots. The foils of the group 3 and 4 might get cracks due to the shrinkage. Thinning was obviously seen in the beam spot, as is seen in fig. 4.b. From these two evidences, we conclude that the heavy ion sputtering is as serious as the shrinkage for

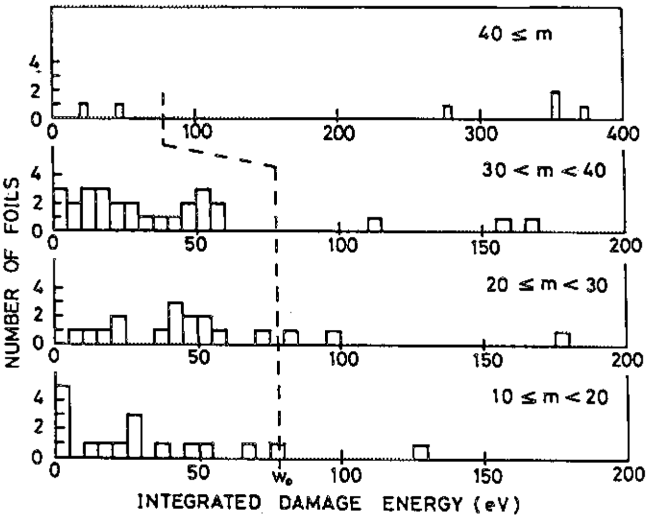

Fig. 3. Distributions of integrated damage energy. w_0 is the one obtained for 2MeV Ar beams.

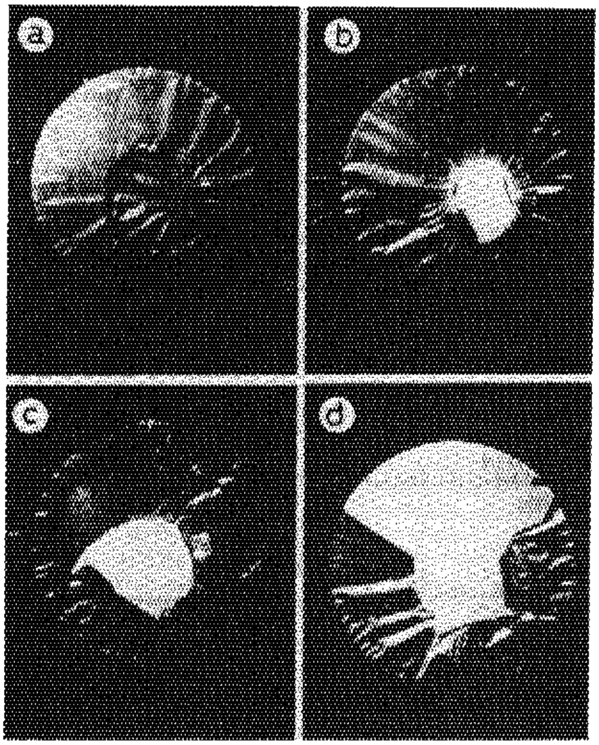

Fig. 4. Used carbon stripper foils. a) to d) show typical appearences of the foils in the groups 1 to 4 , respectively.

the beam conditions shown in table 1.

Our foils of 10 $\mu g/cm^2$ were sufficiently long-lived for the operation of the tandem. Thinner foils are, however, required for better beam transmission. We have been developing long-lived and thinner (3 to 6 $\mu g/cm^2$) foils. We are employing a slackening technique for foils with collodion supporting film in order to make foils relaxed for a long time against the shrinkage, because thinner foils shrink much faster under heavy ion bombardments than 10 $\mu g/cm^2$ foils do. Thinner foils preliminary prepared will be examined in the tandem. We are planning to improve the way of examination by installing a monitoring camera to the in-terminal foil changer.

References

1) S. Takeuchi and S. Kanazawa, Nucl. Instr. and Meth. 206(1983)331.
2) S. Takeuchi and S. Kanazawa, Proc. of "11th World Conf. of the Int. Nuclear Target Development Society" Seattle Wa, USA (1982)1.

1.5 A PROTOTYPE SUPERCONDUCTING QUARTER WAVE RESONATOR FOR HEAVY ION BOOSTER

Suehiro TAKEUCHI, Tetsuro ISHII, Hiroshi IKEZOE and Mitsuhiko ISHII

Department of Physics, JAERI

We have been fabricating a prototype superconducting quarter wave resonator designed in the previous year for the JAERI tandem heavy ion booster. Electron beam welding(EBW), annealing and electro-polishing as well as machining are important in the fabrication. Mitsubishi Electric Company(MEC) was in charge of machining, annealing and EBW. We did electro-polishing in JAERI.

The resonator is illustrated in fig. 1. The inner structure is composed of a drift tube, a center conductor and an upper end plate, all of which are made of niobium. The center conductor is tapered in order to lower the surface magnetic field near the upper end. The inner structure is hollow for liquid helium space. The wall thickness is between 2.5 and 3 mm. The outer conductor is a race-track-like-oval cylinder made of niobium-clad-copper plates; it has two flat sides with beam ports. Field distortion around the beam axis is reduced by this configuration. An rf input port, an rf pick-up port and a fine tuner are put in the bottom end plate made of a niobium-clad-copper plate. Thermal anchors made of copper strips are used to connect thermally the copper flange on the side of helium space and the copper-clad outer conductor.

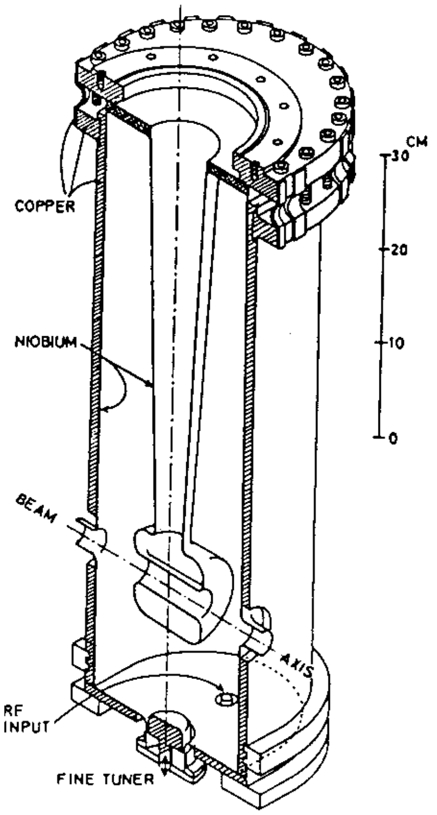

Fig. 1. Cut away view of a prototype superconducting quarter wave resonator

In the fabrication at MEC, all parts of the inner structure were made by cutting niobium rods and thick sheets. The drift tube was composed of three parts; an outer tube with round ends, an inner tube with flaring ends and a neck part to the center conductor. The center conductor was made of two tapered tubes which were coaxially cut out of a single rod. The drift tube, the center conductor and the upper end plate were assembled by EBW, polished and annealed at 1000 °C for 6 hours. The outer conductor was made of two halves. The niobium-clad-copper plates were annealed at 400 °C for a half hour and sheet-processed into the halves. They were welded together by EBW at the ends of niobium plates after the copper ends were removed by about 5 mm. The grooves formed along the welding lines were plugged up with copper strips by EBW. The fabrication proceeded successfully. The components came to JAERI at the end of March, 1986. They are shown in fig. 2.

Their niobium surfaces were electro-polished by an order of 150 μm. The polishing rate was about 1 μm per cycle. In each cycle, dc current with the density of an order of 50 mA/cm^2 was applied for a minute and cut off for about 3 minutes. The surfaces were well smoothed and shined. The resonator components were sent back to MEC. The inner structure will be annealed again at 1000 °C for 6 hours. The outer conductor needs to be mended at several points by EBW. The two components will be welded together in June, 1986. The fabrication will be completed by light electro-polishing as the final surface treatment. A test cryostat is ready for a performance test of this prototype resonator.

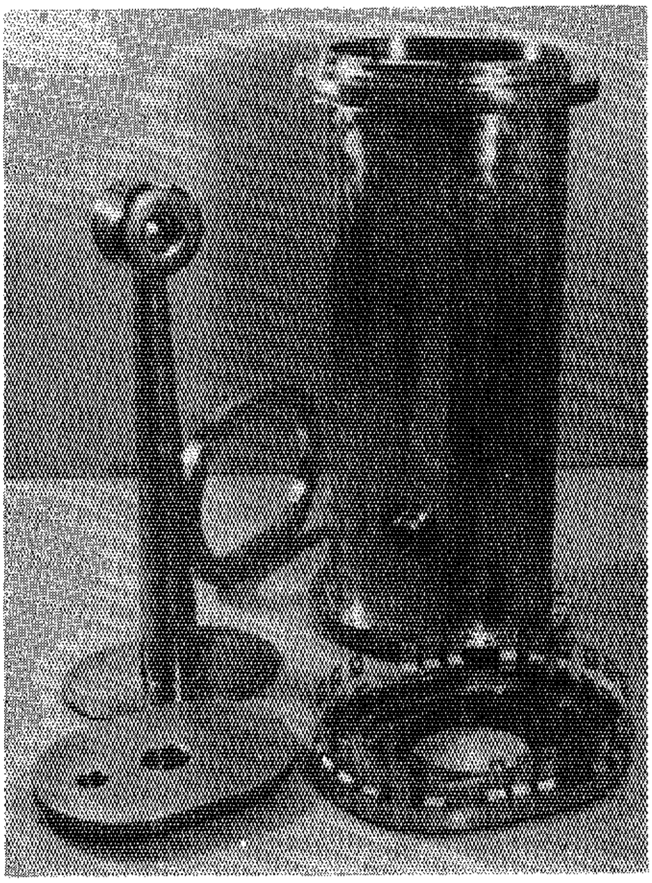

Fig. 2. Resonator components before electropolishing.

1.6 NEW DATA ACQUISITION SYSTEM USING A VAX-11/780 AND A MBD-11

Yoshiaki TOMITA, Isao OHUCHI and Shiro KIKUCHI

Department of Physics, JAERI

The data acquisition system at the tandem accelerator facility, composed of a PDP-11/55, a PDP-11/04 and a CAMAC system with a MBD-11, has been used in many experiments since the installation of the accelerator. Though this system has been flexible enough to fulfill most of the requirements in various experiments, some limitations have been felt in view of the rapid advance in computer technology:

1) The memory sizes of the computers are too small to accomodate enough data area.
2) The small memory sizes inhibit the use of higher level languages making it difficult to modify the programs.
3) The speed (50 KB/sec) to dump list-mode event data to magnetic tapes is not sufficient for some experiments.
4) More computational speed is desirable for on-line processing raw data.

In order to improve the above problems, it was decided to interface the MBD-11 to the VAX-11/780 used for off-line data analysis. The first step was to write a device driver for the MBD-11. The driver$^{1)}$ is somewhat nonstandard to reduce the system overhead and to fully utilize the speed and flexibility of the MBD-11. Writing the driver was not so difficult as was first anticipated from its nonstandard character. However several hardware problems had to be solved: invalid timing of control signals, cross talk between UNIBUS signals, etc. These problems have not been met in the old PDP system and were caused by the different handling of interrupts from UNIBUS devices in VAX-11/780. After fixing these malfunctions, writing the application programs was rather straightforward. All the programs have been written in FORTRAN 77 except for microprograms for the MBD-11 and a few special small subroutines. In reproducing all the functions of the old system, 7 man-month coding time has been used. This time is very short compared with 60 man-months needed to prepare the programs of the old system, all of which had to be written in assembler language.

Though the software development is still in progress, the new system has completely surpassed the old system and many new functions have been added. The system has successfuly used in an experiment already.

As to the data rate, 300 KB/sec of event data can be routed continuously from CAMAC to magnetic tapes.

One of the changes in hardware configuration is the use of two touch panels attached to DEC VT-100 terminals to control the system. Compared with the specially made control panels of the old system, the touch panels are not expensive and are very flexible. Though somewhat inconvenient in controlling the graphic display, they provide rather good environment for acquisition control.

After rearrangement of hardware components, the new system will replace the old system shortly.

Reference

1) Y.Tomita,I.Ohuchi,S.Kikuchi,H.Ikezoe,M.Sugimoto,S.Hanashima and M.Maruyama: JAERI-M 85-198 (1985)

1.7 ELECTRON LINAC OPERATION AND IMPROVEMENTS

Electron Linac Group

Department of Physics, JAERI

Operation

During the fiscal year of 1985, the 120 MeV JAERI electron linear accelerator (linac) was operated mainly to produce high intensity neutrons, of which energy spectrum ranged from thermal to several MeV region. The most of the machine time (more than 80 %) was used for neutron cross section measurements, which required the short pulse (25 ns) and high repetition rate (600 pps). A new research project related to the developments of low energy neutron mirror for the research reactor started this year. This project used thermal neutrons with about 10 % of the machine time, while neutron diffraction experiments also continued using 3 % of the machine time. A summary of the linac condition is listed in Table 1. The total linac operation time increased by 30 % compared to the previous year.

Table 1 Machine Time and Output Beam for Research Programs in 1985

Research Program	Time (h)	Ratio (%)	Energy (MeV)	Rate (pps)	Length (nsec)	Ave. Current (μA)
Neutron Cross Section (Time of Flight Method)	1579	83.4	120	300～600	25	48
Solid State Physics (Neutron Diffraction)	60	3.2	100	150	1000	35
Development of Research Reactor (Development of Neutron Mirror)	197	10.4	100	50	1000	18
Radioisotope Production	18	1.0	60	150	1000	20
Tuning and Test Operation	37	2.0	60～120	50～600	25～1000	53
Total	1891	100.0				

Because the total machine time has reached to 25,000 hours since first operation of 1972 and the high duty operation of 600 pps has been continued for two years, the frequency of troubles with main apparatuses seems gradually increasing. The causes of troubles happened last year are listed in Table 2. The vacuum leak of the RF window to the #1 accelerator structure necessitated one week shut down to change the window and reactivate the oxide cathode in the electron gun. Fortunately, nitrogen gas filled in the wave guide instead of SF6 only gave a small damage to the cathode.

Table 2 Causes of Troubles with Main Apparatuses of Linac in 1985

Apparatuses	Specification	Number	Cause	Manufactured
Induction Regulator	AC 3¢ 200V±200V 110kVA	1	Poor Isolation	1971
Slidac	AC 3¢ 0~200V 40kVA	1	Poor Isolation	1959
Transformer	AC 3¢ 200V:15kV 2.5A	1	Layer Short	1959
Heat Exchanger for Klystron cooling	7501/min 500,000kcal/h	1	Electrolytic Corrosion	1983
Klystron Focus Coil	DC 100V 20A 2kW	2	Poor isolation	1971,1976
Charging Choke Coil	50kV 6.8A peak, 600pps	3	Poor isolation	1971
Klystron	RF 21MW peak, 53dB	2	Life end, Vacuum leak	1981,1983
Thyratron	50kV, 5000A peak	1	Life end	1981
RF Window	RF 21MW peak, duty 1×10^{-3}	1	Vacuum leak(pin hole)	1976
Condenser (P.F.N.)	50kV, 3000A peak	4	Poor isolation	

Improvement

A number of modifications have been carried out during the 3 week scheduled maintenance period in December. Some of the improvements have been still continued since 1984 fiscal year1) ; The interlock system was renewed by adding a total of 80 sensing points, the 5 units of the trigger circuits to the main thyratrons were replaced from a small thyratron (5C22) to the SCR' (Silicon Controlled Rectifier)2) and the computer controlled data logging system is being prepared by replacing the electric power suppliers with I/O units for beam transport components. Several other modifications carried out last year are summarized as follows.

(1) Design and construction of a new buncher and prebuncher.

These new components were designed with high Q values of the cavities to increase the beam current with a short pulse operation. Table 3 shows the comparison of the specifications between old and new ones. Main changes consist of the decrease of 2a (bore radius of the buncher) by 6.3 % and of strengthening of magnetic fields around the accelerating cavities by as much as 50 %. The Q value of the prebuncher was increased from 500 to 1000. The outer sizes of the buncher and prebuncher are kept as the same as the previous ones so that other components had not to be rearranged. The low power RF test for the buncher was performed satisfactory with the measured VSWR of 1.05 as shown in Picture 1.

Table 3 Comparison specifications between the new buncher and old buncher

	Old Buncher	New Buncher
Type	3 step constant gradient	3 step constant gradient
Center of Frequency	2856.5±0.05MHz	2856.5±0.05MHz
Mode	$2/3\ \pi$	$2/3\ \pi$
Phase Deviation	± 4°	± 3°
Q Value	>12000	>12000
VSWR	fo 1:1.05 fo±1.5MHz 1:1.1	fo 1:1.05 fo±1MHz 1:1.1
Input Power	8MW max	12MW max
Magnetic Field (Center of wave guide axis)	1000 Gauss	1500 Gauss
Number of Cavities	21 (Including 2 coupler)	21 (Including 2 coupler)
Mechanical Size of Accelerator Wave Guide	(1)777mm long (2)t 5.84mm (3)D 26.25 ~30.79mm (4)2a 28.6~25.2mm φ	(1)777mm long (2)t 5.84mm (3)D 26.25 ~30.79mm (4)2a 26.8~24.2mm φ
Accelerator Beam	0.6A at pulse width 2 μsec 4A at pulse width 30nsec 6A at pulse width 10nsec	1A at pulse width 1 μsec * 5A at pulse width 30nsec * 15A at pulse width 10nsec *
No Load Energy	5MeV	7MeV

* These values are not experimentally confirmed.

(2) The stabilizer for the AC power supply to the filaments of klystrons and thyratrons.

A number of components which used the electronic vacuum tubes was decreased because of their replacements to the transistor circuits. Since the tubes such as high power klystrons and thyratrons are restrictively used as the linac components, it becomes easier to control only one AC power supply for the filaments. The stabilization is made using a motor drive 10 kVA slidac in combination with the micro-computer (SBZ80-2). Reliable operation with a stability of 100±0.2 V has been continued for more than 10 months.

(3) The temperature control circuits to the accelerator structures.

The old temperature control circuits with the SCR' were replaced with the simple and stable devices of relay switches (OMRON E5B). The Pt resistance thermometers to check the temperature are used with the setting value of 35 degrees.

(4) New moderator for the neutron target.

The boron loaded polyethylene moderator had been used for a long time to produce low energy neutrons. But the troubles frequently happened because of the damage of the polyethylene and its carbonization caused the gradual change of the neutron spectrum especially after the 600 pps operation started. The water moderator mixed 15 % BN (Boron Nitride) has been tested and used for about 6 months. So far this moderator seems working satisfactorily except the cooling water leaked due to the corrosion of the copper pipe, which was replaced, afterward, with the stainless steel.

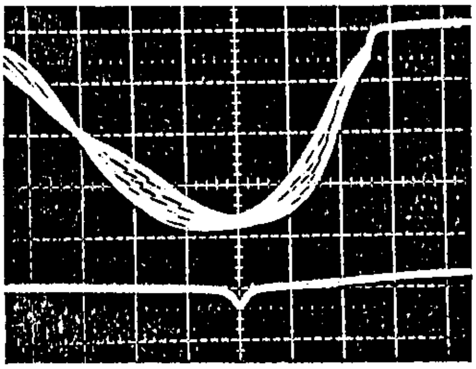

X-Axis 1.5 MHz/div
Y-Axis 1 mV/div

Picture 1 The upper curve shows the VSWR, where the frequency of the microwave was modulated by FM (50Hz). In the lower curve, the dip corresponds to the center frequency of 2856.74 MHz in the air.

References

1) Electron Linac Group: JAERI-M 85-104 (1985) 19.
2) T.Shoji: JAERI-M 86-049 (1986).
3) K.Mashiko et al.: Proceedings of the 10th Meeting on Linac in Sendai (1985) 16.

1.8 IMPROVEMENT OF THE JAERI LINAC CONTROL SYSTEM

Tokio SHOJI

Department of Physics, JAERI

At the JAERI Linac, a program of the improvement of the control system including the linac's components is continuing for the efficient and safe operation, because the system was constructed in 1972. At that time, main elements were vacuum tube circuits, hard wired logics and so on. Thus, the improvements include the replacement of the old circuits by semiconductorized ones and the addition of powerful functions of microcomputer technology to the system.

The improvements and preparations performed in the fiscal year 1985 are itemized as follows: 1) Beam status display unit. 2) The trigger pulsers using SCRs to drive a large thyratron. 3) Semiconductorized interlock circuits. 4) Replacement of the Q magnets and deflection magnet power supplies.

1. Beam status display unit

This unit displays[1] the linac operation condition on CRT monitors located at the control room, the data acquisition room (computer room), the experiment room 1 and room 2, and the meeting room. The items displayed are 1) beam energy, 2) average beam current, 3) pulse repetition rate, 4) beam width and 5) operator's name. An example of the CRT display is shown in Fig. 1 and the block diagram in Fig. 2. This unit uses a board microcomputer. For good seeing, large size charactors are written in video ROM (read-only-memory). Other than the display in Fig. 1, this can display other optional messages: "Trouble", "Interruption" and "Tune-up".

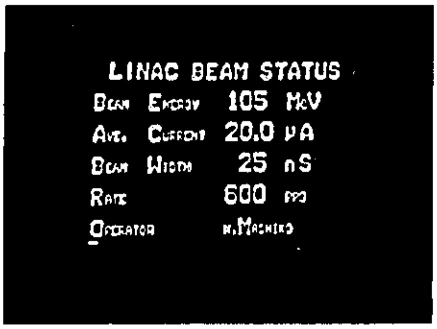

LINAC BEAM STATUS
Beam Energy 105 MeV
Ave. Current 20.0 μA
Beam Width 25 nS
Rate 600 pps
Operator N.Machiko

Fig. 1 An example of beam status display

2. Large thyratron trigger pulsers using SCRs

A small thyratron 5C22 in the old pulser was replaced by SCRs(sillicon controlled rectifier). The SCR pulsers[2] are of a resonantly charging line-type. The SCR pulsers amplify the input pulses from timing delay circuit.

The output pulses drive the large thyratron. The design features are as follows:

1) Two SCRs in series (Maximum peak voltage of SCR is 1600 volts).
2) 10Ω impedance of pulse forming network and output pulse transfomer (primary).
3) Stabilized DC high voltage power supply by a switching regulation.
4) Generation of the constant voltage pulses for SCR gate trigger.
5) Protection circuits against over heat and over voltage for the SCRs.
6) Interlock circuit and monitor signal for miss-fire of the SCR circuit.

Eight pulsers have been prepared and are in operation with satisfactory performance.

3. Semiconductorized interlock circuits

There are three hundred inputs in the interlock system for the personal safety and for the protection of the circuits against over load condition. About a half of them have been replaced by ten semiconductorized interlock modules. Each of which has sixteen inputs in double NIM widths. The status data from them can be read by a microcomputer through general purpose interface bus (GP-IB). The block diagram is shown in Fig. 3. The input signals for the personal safety are sent from the sensing points located at the entrance doors of measurement station, high voltage circuit rooms and danger places. The input signals for the circuit protection are interlock signals from cooling systems, vacuum systems in acceralator tube or beam transport lines and other protection circuits.

4. Replacement of Q magnets and deflection magnet power supplies

In the electron beam transport lines, four deflection magnets and approximately thirty Q magnets are used, whose power supplies are old and sometimes in trouble. The power supplies have been replaced by new ones with GP-IB interfaces.

The software preparation for the data logging, the control of the interlock circuits and the control of the magnet power supplies is now in progress.

References

1) T.SHOJI : JAERI-Internal report (1985)
2) T.SHOJI : JAERI-M 86-049 (1986)

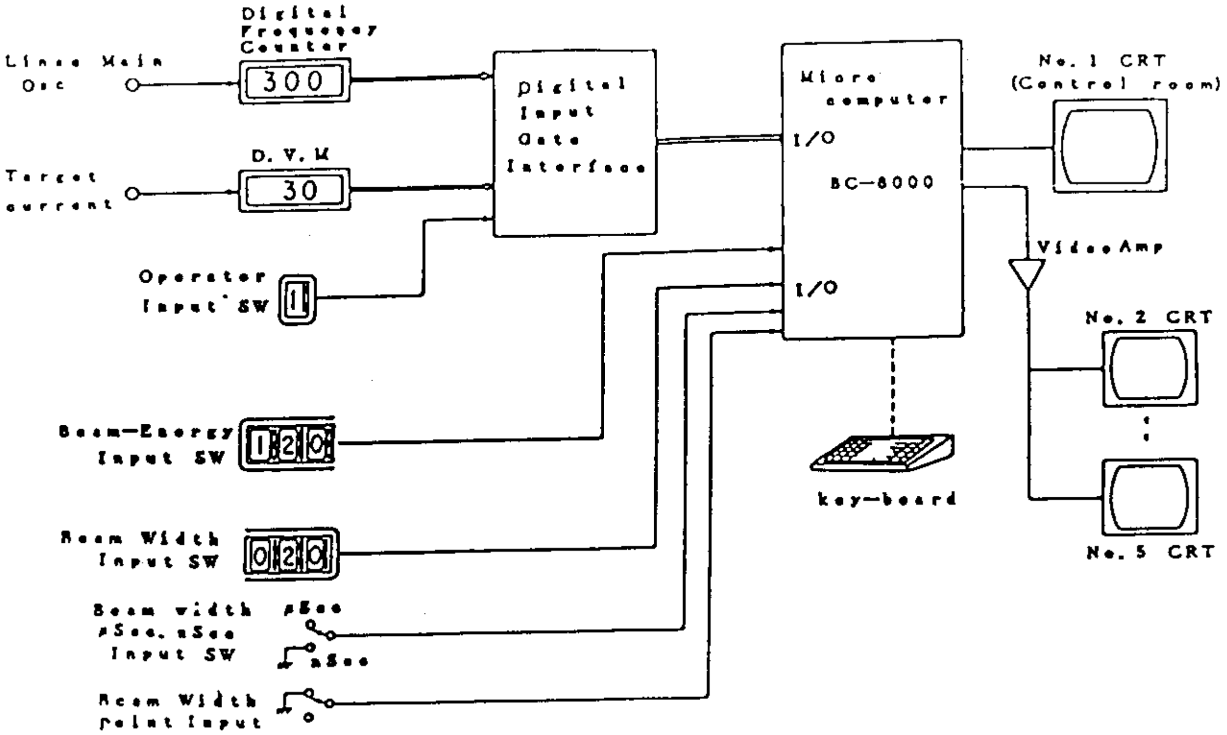
Linac Main Osc
Digital Frequency Counter
300
Target current
D.V.M
30
Operator Input SW
1
Digital Input Gate Interface
Micro computer
I/O
BC-6000
I/O
No. 1 CRT (Control room)
Video Amp
No. 2 CRT
No. 5 CRT
key-board
Beam-Energy Input SW
120
Beam Width Input SW
020
Beam width μSec, nSec Input SW
μSec
nSec
Beam Width point Input

Fig. 2 Block diagram of beam status display unit

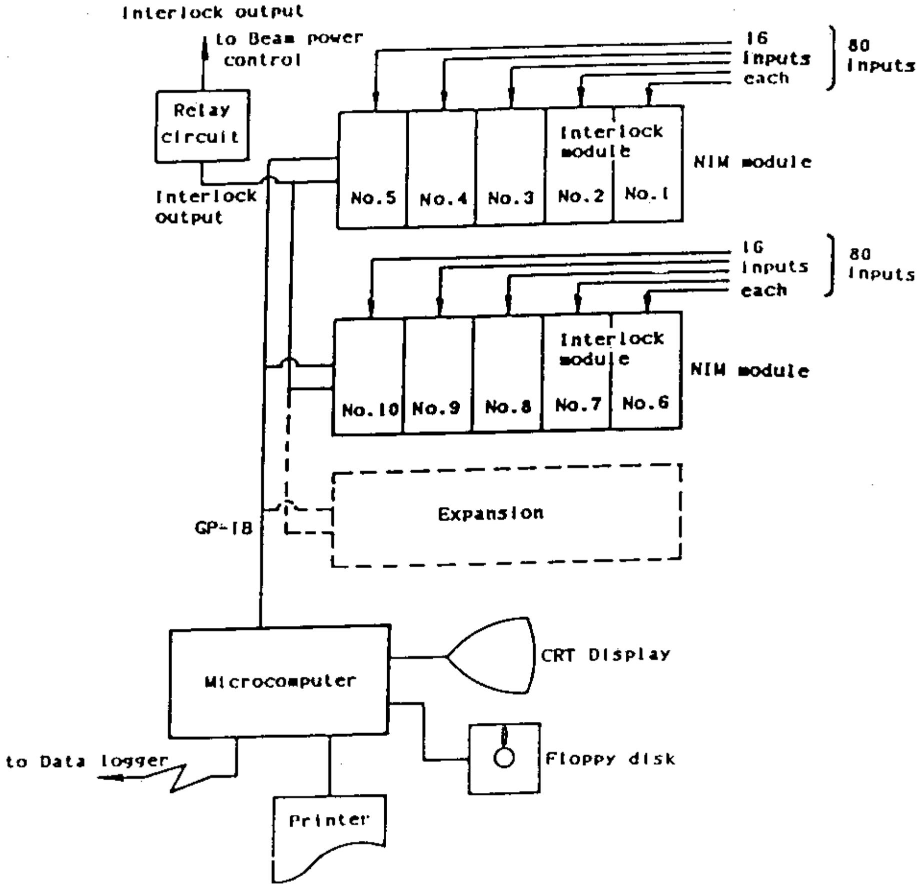
Interlock output
to Beam power control
Relay circuit
Interlock output
16 inputs each
80 inputs
Interlock module
No.5
No.4
No.3
No.2
No.1
NIM module
16 inputs each
80 inputs
Interlock module
No.10
No.9
No.8
No.7
No.6
NIM module
Expansion
GP-IB
Microcomputer
CRT Display
Floppy disk
to Data logger
Printer

Fig. 3 Block diagram of interlock circuit

1.9 PREPARATION OF A FAST TOF DATA ACQUISITION SYSTEM BASED ON A PERSONAL COMPUTER WITH AN INTELLIGENT CAMAC

Y.KAWARASAKI and T.SHOJI

Department of Physics, JAERI

A time-of-flight (TOF) data acquisition system of high resolution (min. channel width 1 ns), of multi hit (max. 8 events) capability and of large storage capacity (max.128 k channels) has been prepared, based on a personal computer with an intelligent CAMAC system. The interactive operation of the system can be achieved effectively through the implemented software written in FORTH. As the simple configuration of a linked microcomputer system, this will easily find other applications such as accelerator controls.

Introduction

According to a program of the renewal of the data acquisition and processing system, we have introduced three personal computer (PC) systems and a medium size minicomputer, FACOM S-3300, respectively. Among the acquisition systems, there are two personal computers with CAMAC systems. One is for TOF measurements and another for pulse height analysis (PHA). These will be linked finally with S-3300. In these systems, full implementation of the software for the purpose is remaining works.

The TOF system is dedicated to measure the neutron cross section data in the MeV region as well as the keV region, using the neutron TOF facility of JAERI linac. For the above measurements, the following specifications are desired.

1) Adequate channel width is helpful, i.e., approximately 5 times narrower than the neutron burst width (roughly equal to that of the linac's beam, 20 ns at present, and 5 ns achievable in the near future).
2) Multi-hit capability is required, instead of a conventional method by time-to-amplitude conversion(TAC), which can sort at most one event in the one neutron-burst-to-burst period.
3) Large storage capacity is desirable, e.g., 128 k channels with 1 ns width cover 128 μs, enough for the interested neutron energy region.

Another feature of the system is to be based on a PC with an intelligent CAMAC. The intelligent CAMAC module is called auxiliary controller(AC), which can control the other individual CAMAC modules.

Hardware

The CAMAC crate contains the following individual modules in this application.

1) Crate controller(CC, TOYO model CC/8800 linked with the PC through the interfacing board circuit TPC8800).
2) Auxiliary controller(AC, an intelligent CAMAC module, JAERI 1104, designed and made by Electronics Division,, JAERI).[1)]
   The AC is equipped with a 8-bit MPU Z80A with 16k byte memory, 9 parallel I/O ports, 1 serial I/O port, interrupt controller and miscellany.
3) Time digitizer (TOF) module(Le Croy CAMAC model 4208, fixed 1 ns time resolution, 8 input channels or 8 hits in one channel).
4) Adapter for the TOF module 4208 (made by Electronics Div.).
5) DATA ACQUISITION STORE (Sension Scientific Ltd., type 1631-4; 64 k channels of 16 bits/channel, two modules used here).
6) CRT driver (model JAERI 1082).
7) Optional modules for aid of the development.

As the host microcomputer, a PC-8801 (NEC) is used, because PC-8801 runs with the MPU μPD 780C-1, which is fully compatible to Z80A.

Software

There are several items to be discussed for the software system design in the linked microcomputer configuration.

1) Node relationship or hierarchical structure.
   Here it is suitable that the PC-8801 is the host (master) node and the AC is the station (slave) node.
2) AC's software and communication.
   The functional flexibility of the AC is achieved, because the most of programs can be transfered from the PC to the RAM area of the AC, instead of the fixed programs previously burnt in the ROM. This leads the following advantages.
   a) The ROM's program gets only a small size accepter for the down-

loaded programs and b) thus the debugging on the application programs becomes greatly timesaving. All communications pass through the CC as those in non-intelligent CAMAC system, however in this case many commands are issued locally from the AC to the individual modules.

3) Task partitioning.

The AC's task is the TOF data acquisition with an optional data display; a) read the data in the registers of the TOF module, b) store them in the data storage module and c) display them in a spectrum form on a CRT display as a background task.

The PC's task is the following; a) command to start the AC's operation with the AC's program down-load and to stop, b) transfer the storage module's data from the CAMAC to the PC's memory and c) process the data in suitable forms independently from the AC's operation.

4) Programming languages.

In the AC, the high execution speed is required, thus the language used is Assembler or equivalent. Since in the PC, the high software productivity, the adequate execution speed and the interactive operation are desired, FORTH in a larger part and Assembler (or equivalent) in a smaller part are used. Because FORTH belongs to an interpreter type language and does to a functional type, the above requirements can be satisfied.

5) Environment for the software preparation.

Another specific feature of FORTH is self-producing, i.e., any FORTH system can be constructed by FORTH itself. Thus the FORTH support system previously prepared serves as the effective environment.

Performance, discussion and conclusion

In such an application, the execution speed of the AC is a stringent point. The actual run of the data acquisition yielded a good result under the following condition: the channel width was selected at 8 ns and the linac's repetition was selected at 300 pps. The channel width of 8 ns was realized by the AC's program, which executed the bit shift by 3 bits for 8 24-bit data between the data-read and data-store cycles.

In the accordion mode, in which the TOF data were stored by sorting with varied channel width to saving the number of channels, this system made an appreciable countloss in the case of the heavy load to the AC's ability. However, the large memory capacity can save partly the difficulty.

The background task of the data display in a spectrum form on a CRT at the CAMAC side runs slower. The static representation of events in the CAMAC side seems to be enough for monitoring, because the more flexible spectrum display at the PC side is possible.

The interactive operation with the system through the PC was satisfactorily realized as the designer's intention. Further improvements of on-line processing jobs depend on the next software developments.

Applications for other purposes will be easily performed by changing individual modules and preparing software in both the AC and the PC.

The authors wish to thank the persons of the Electronics Division for their preparation of the AC's hardware.

Reference

1) Design Group, Electronics Division: Private communication (1982)

II ATOMIC AND SOLID STATE PHYSICS

2.1 PERFORMANCE OF THE X-RAY CRYSTAL SPECTROMETER

Kiyoshi KAWATSURA, Masao SATAKA, Hiroshi NARAMOTO
Kunio OZAWA, Yohta NAKAI, Akio OOTUKA*,
Ken-ichiro KOMAKI* and Fuminori FUJIMOTO*

Department of Physics, JAERI, *College of General Education,
University of Tokyo

Introduction

An x-ray crystal spectrometer has been constructed at the H-2 beam line of JAERI Tandem accelerator facility for the purpose of measuring the high resolution x-ray spectra of the target atom and the projectile ion following the beam-foil or beam-gas interaction. To satisfy these conditions, the curved crystal spectrometer (Johannson type) was designed and manufactured by Rigaku Co.

The study using a crystal Bragg spectrometer has shown that the characteristic x-ray spectra could be resolved into various components.[1,2] In order to examine the performance of the x-ray crystal spectrmeter, we have tried to measure both satellite and hypersatellite K x-ray spectra of Al produced by high energy Cl ion incident on Al target. The projectile Cl K x-ray spectra were also measured using different analyzing crystal.

Experimental methods

The high resolution x-ray spectra were measured using a 12.7 cm, Johannson-type, curved crystal spectrometer manufactured by Rigaku Co. This spectrometer is provided with a remotely controlled linear wavelength drive which covers the Bragg angle range of 25° - 60°. The fine adjustments for the crystal angle and focal circle radius are also operated by remote control system. The crystal amount allows for the selection of one of two crystals without having to disturb the vacuum system. A gas-flow proportional counter is used as detection of x rays, which is operated at +1300 V with P-10 gas (90 % Ar - 10 % CH_4) having an entrance slit of 0.1 mm width. The counter is operated at a flow rate of 50 ml/min and is isolated from vacuum by a 6 μm polypropylene window. The K x rays of Al target were analyzed in first order with an ADP (101) crystal, 2d spacing of 10.64 A. the Cl K x rays were analyzed with a Si (111) crystal, 2d spacing of 6.27 A. The experimental data for all spectra was taken in a multiscaler mode.

Results and discussion

The Al K x-ray spectra produced by bombardment of Al target by Cl^{9+} ion at 120 MeV are shown in Fig. 1. The Kα satellite lines are clearly observed. The peak is labelled by a symbol of KL^n which corresponds to the initial configuration having one K-shell vacancy and n L-shell vacancies. The Kβ satellite lines are not clearly identified because the Kα hypersatelite lines are excited strongly. The experimental energy resolution of full width at half maximum (FWHM) are about 3.0 eV for the Al Kα x-ray spectra. This value is comparable to that obtained by other works.[1,2]

The projectile Cl K x-ray spectra were also measured with high resolution, changing the analyzing crystal by the remote control system. The representative K x-ray spectra induced in the Cl projectile are shown in Fig. 2. The experimental resolution (FWHM) was about 9.0 eV for the Cl K x-ray spectra. The KL^5 line, and the doublet $KL^6(^2P, ^4P)$ and $KL^7(^1P, ^3P)$ lines are observed at the x-ray energy region from 2.70 to 2.80 keV. The Lyα transition line is found at 2.96 keV and the hypersatellite transitions ($2p^2$-1s2p, $2p^3$-$1s2p^2$) are also found at the lower energy side of the Lyα line. The x-ray spectra produced in the H-, He- and Li-like atoms are observed at the higher energy region. Now, we are measuring the high resolution x-ray spectra induced in highly ionized ion at high energy as functions of charge states of the projectiles and thickness of the C-foil targets.

References

1) A.R.Knudson, D.J.Nagel, P.G.Burkhalter and K.L.Dunning: Phys. Rev. Lett. 26 (1971) 1149.

2) D.Burch, P.Richard and R.L.Blake: Phys. Rev. Lett. 26 (1971) 1355.

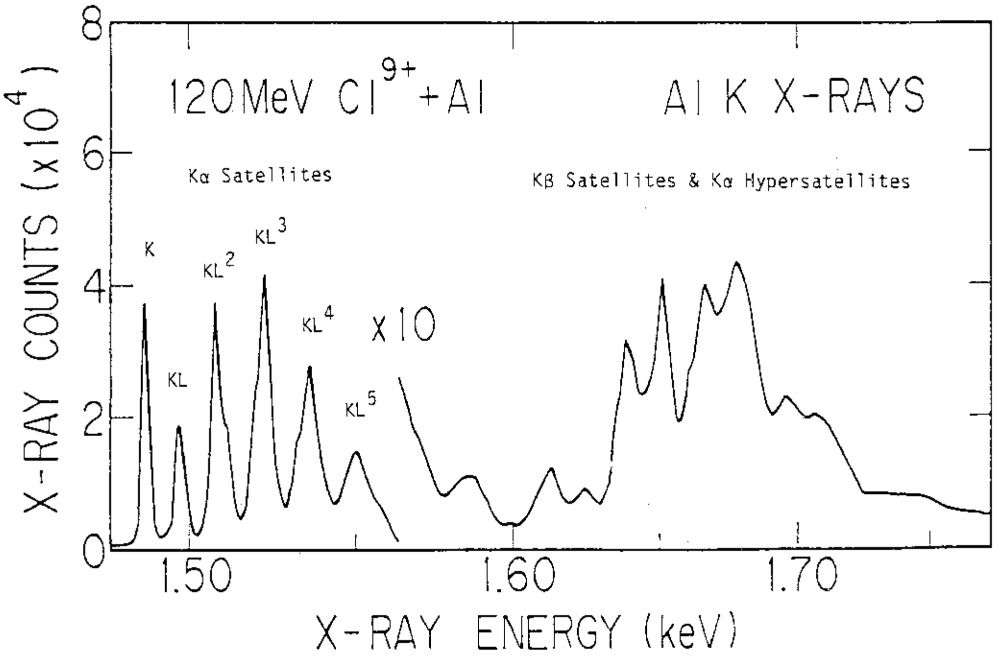

Fig.1 The Al K x-ray spectra produced by Cl ion bombardment at 120 MeV.

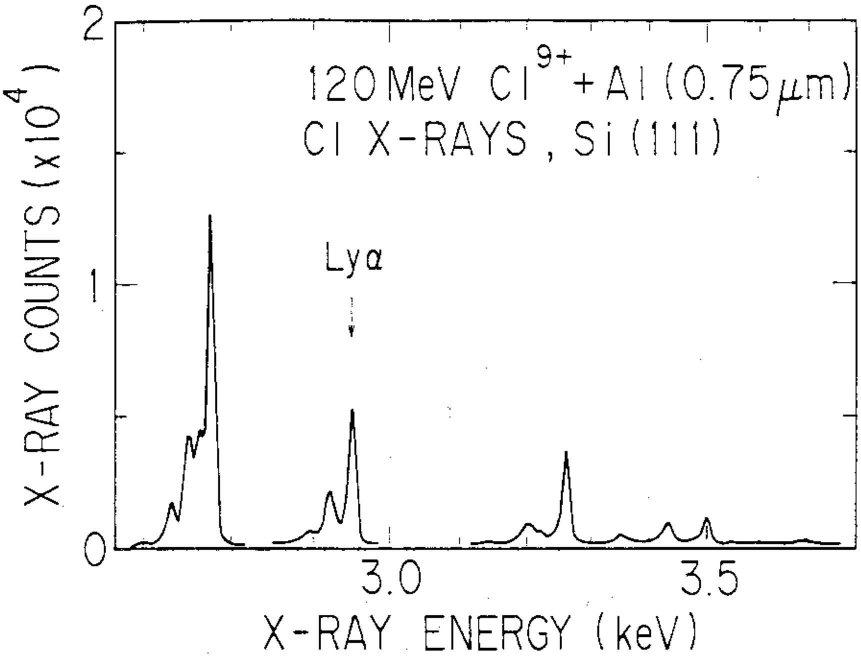

Fig.2 The K x-ray spectra emitted by beam of Cl ions passing through a thin Al foil target at 120 MeV.

2.2 RADIATIVE ELECTRON CAPTURE FOR CL$^{16+,17+}$ IONS ON HE TARGET

Kiyoshi KAWATSURA, Masao SATAKA, Hiroshi NARAMOTO
Kunio OZAWA, Yohta NAKAI, Akio OOTUKA*,
Ken-ichiro KOMAKI* and Fuminori FUJIMOTO*

Department of Physics, JAERI, *College of General Education,
University of Tokyo

Radiative electron capture (REC) in fast ion-atom collisions was first observed by Schnopper et al.$^{1)}$ Since then, many investigations of REC processes have been reported. Most of the experimental data were taken by using solid or thick gas target. The experiments should be carried out under single collision conditions to compare with theoretical calculations. This work was done in order to extend our data under single collision conditions$^{2)}$ to higher energies and different projectiles.

The JAERI Tandem accelerator provided Cl^{9+} ions at 140 MeV. Using the post stripper (C foil, 15 μg/cm^2), the Cl^{16+} and Cl^{17+} ions were incident on He gas target. Some data was also taken at 120 MeV. The REC and Cl K x-ray spectra were taken with a HORIBA Si(Li) x-ray detector at 90° to the beam direction. The energy resolution of the Si(Li) detector system was about 170 eV for Mn Kα x rays. Figure 1 shows the x-ray spectra for Cl^{17+} ion incident on He gas target. The centroid energies and widths of the REC x rays are given as$^{3)}$

$$h\omega = \varepsilon_f - \varepsilon_i + (m/M)E_0 \qquad (1)$$

$$\Delta h\omega = 2v_0 p_{iz} \ . \qquad (2)$$

Here hω is the x-ray energy, ε_i and ε_f are the binding energies of electron in the initial and final states, respectively. E_0 is the energy of the incident projectile ion, m and M are electron and projectile masses, respectively. The width of the REC x rays is given as Δhω, v_0 is the velocity of the projectile ion and p_{iz} is the momentum of the electron in the initial state. The observed centroid energies of the REC x-ray spectra are shown in Fig. 2 as a function of the projectile energy. The data points are few, but the experimental results are in good agreement with the expected ones. The observed widths for He target atom are also shown in Fig. 3 as a function of the projectile velocity with the results of Kawatsura et al,$^{2)}$ Sohval et al$^{4)}$ and Kambara et al.$^{5)}$ The present data seems to be in agreement with our previous results. The measurements for various energies and for different projectiles are in progress.

References

1) H.W.Schnopper, H.D.Betz, J.P.Delvaille, K.Kalata, A.R.Sohval, K.W.Jones and H.E.Wegner: Phys. Rev. Lett. 29 (1972) 898.
2) K.Kawatsura, H.Tawara and P.Richard: IEEE Trans. Nucl. Sci. NS-28 (1981) 1053; H.Tawara, P.Richard and K.Kawatsura: Phys. Rev. A 26 (1982) 154.
3) M.Kleber and D.H.Jakubassa: Nucl. Phys. A 252 (1975) 152
4) A.R.Sohval, J.P.Delvaille, K.Kalata, K.Kirby-Docken and H.W.Schnopper: J. Phys. B 9 (1976) L25.
5) T.Kambara, Y.Awaya, A.Hitachi, M.Kase, I.Kohno and T.Tonuma: J. Phys. B 15 (1982) 3759.

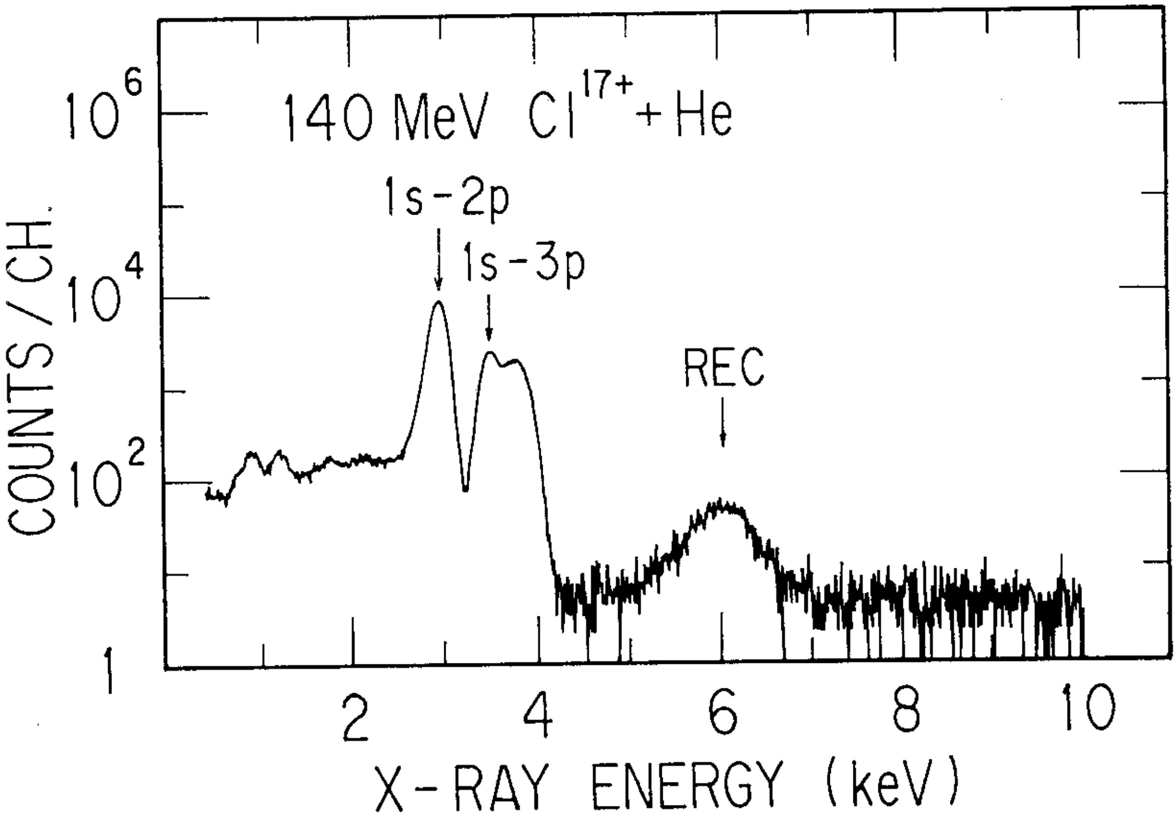

Fig.1 The Cl and REC x-ray spectra for 140 MeV Cl^{17+} ion incident on He gas target.

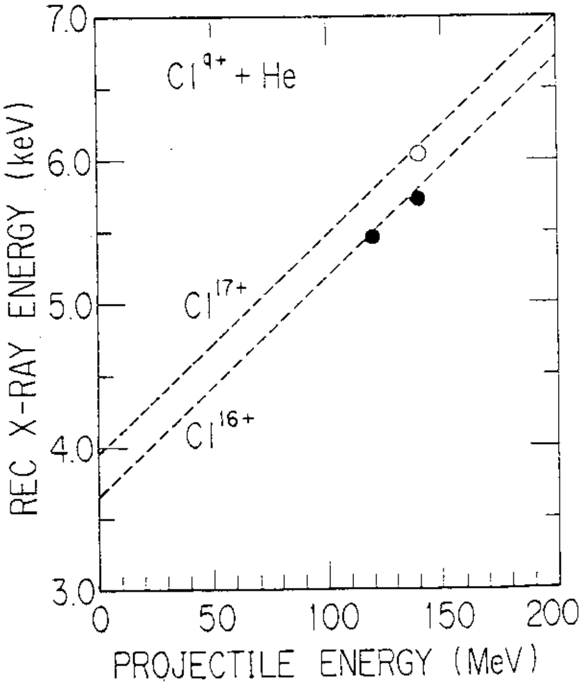

Fig.2 The centroid energy of the REC x rays.

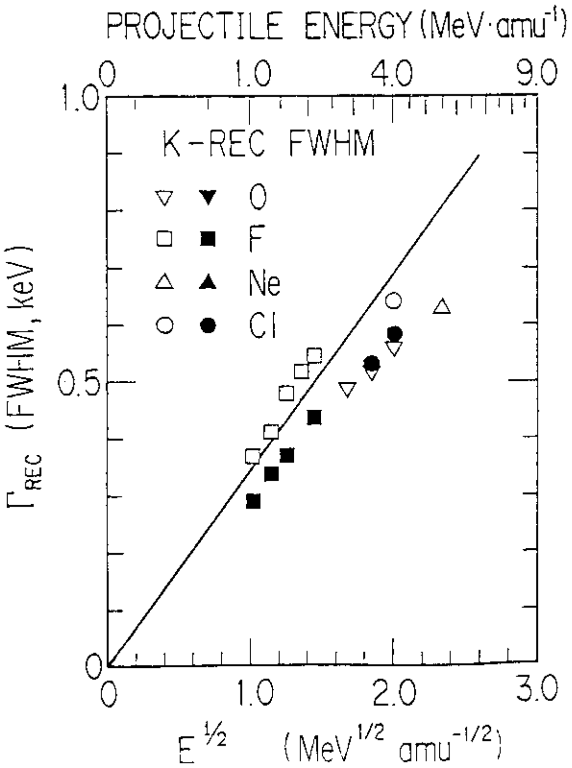

Fig.3 The width of the REC x rays with the results of other works.

2.3 BEAM-FOIL SPECTRA OF CHLORINE IONS IN HIGH ENERGY REGION (III)

Masao SATAKA, Kunio OZAWA,[+] Kiyoshi KAWATSURA, Hiroshi NARAMOTO, Yohta NAKAI, Keishi ISHII*, Akio OOTUKA**, Ken-ichiro KOMAKI**, Fuminori FUJIMOTO** and Akira KIKUCHI***

Department of Physics, JAERI, *Faculty of Engineering, Kyoto University, **College of Arts and Sciences, University of Tokyo, ***Faculty of Engineering, Ibaraki University

Beam-foil investigation of highly ionized chlorine has been performed in the wavelength region 30 - 470 Å at the JAERI tandem accelerator. The ion beam energy is varied from 80 to 150 MeV.

The beam-foil studies of Cl ions at an energy as high as a several ten MeV have been reported thus far by the two groups.[1-3] The ion beam energy in the present work is the highest among all. The spectrum contains less blended lines with line multiplet belonging to low charge states. Many lines attributed to high nl transitions are also measured.

Experimental apparatus has been described in reference 4). The radiation from foil excited chlorine beam is measured by a 2.2 m grazing incidence spectrometer mounted at 90° to the beam direction. The carbon foils whose thickness was 15 μg/cm^2 could be positioned with accuracy of 0.1 mm.

We have measured the spectra emitted from Cl ions with better spectral resolution than before. The measured lines of hydrogen-like transitions belong to Cl XIII - Cl XVII. Figure 1 shows a partial spectrum between 170 and 260 Å of foil-excited Cl at beam energy 80 MeV. Most of lines were attributed to the 2s-2p transitions in Cl XII - Cl XIV. The wavelength and the gf-value have been calculated by use of the "atomic structure calculation program", developed by Cowan.[5)]

Two lines at ~180 Å and ~206 Å are newly identified as nl transitions

---

[+] Present address: Energy Research Institute, Hitachi Ltd.

in Cl XV and Cl XIV respectively. The wavelength and the associated line strength for each transition have been calculated with use of the polarization formula.6) The further discussion has been described in reference 7).

We have also measured the radiative lifetimes of 2s-2p transitions belonging to Cl XII - Cl XV. A number of lifetimes are newly determined. We are analyzing those intensity decay curves. In Figure 2 shown is the intensity decay curve for 2s2p $^1P_1$ level in the Cl XIV (237.8 Å) measured at 120 MeV. The decay curve is decomposed into two exponentials by non-linear least squares method. In table 1. we list the some results of measured lifetimes with the lifetimes measured by Ishii et al2) and Forester et al.3) The measured lifetimes already reported by above authors are in good agreement with our results.

References

1) R. Hallin, J. Lindskog, A. Marelius, J. Pihl and R. Sjödin: Physica Scripta 8 (1973) 209.
2) K. Ishii, E. Alvarez, R. Hallin, J. Lindskog, A. Marelius, J. Pihl, R. Sjödin, B. Denne, L. Engström, S. Huldt and I. Martinson: Physica Scripta 18 (1978) 57.
3) J. P. Forester, D. J. Pegg, P. M. Griffin, G. D. Alton, S. B. Elston, H. C. Hayden, R. S. Thoe, C. R. Vane and J. J. Wright: Phys. Rev. A18 (1978) 1476.
4) M. Sataka, K. Ozawa, K. Kawatsura, K. Masai, K. Ishii, A. Ootuka, K. Komaki, F. Fujimoto, A. Kikuchi and T. Kitahara: JAERI-M 85-105 (1984) 25.
5) B. Edrén: in Handbuch der Phisik, edited by S. Flugge (Springer-Verlag, Berlin, 1964), Vol.27, p.80.
6) R. D. Cowan: The Theory of Atomic Structure and Spectra (Univ. California Press, Berkely, Calif., 1981).
7) M. Sataka, K. Ozawa, K. Kawatsura, H. Yamaguchi, K. Ishii,T. Kitahara A. Ootuka, K. Komaki, F. Fujimoto, A. Kikuchi and : JAERI-M 85-125 (1985) 58.

ION	WAVELENGTH (Å)	TRANSITION	LIFETIME (nsec) Present	Forester	Ishii
XIV	458.4	$2s2p\ ^1P_1 - 2p^2\ ^1D_2$	0.63	0.60	0.54
XV	415.6	$2s\ ^2S_{1/2} - 2p\ ^2S_{1/2}$	1.01	0.95	1.0
XV	384.0	$2s\ ^2S_{1/2} - 2p\ ^2S_{3/2}$	0.76	0.76	0.71
XIV	286.2	$2s2p\ ^3P_2 - 2p^2\ ^3P_2$	0.16	0.16	
XIV	237.8	$2s^2\ ^1S_0 - 2s2p\ ^1P_1$	0.14	0.15	

Table 1. Lifetimes in Cl XIV - Cl XV

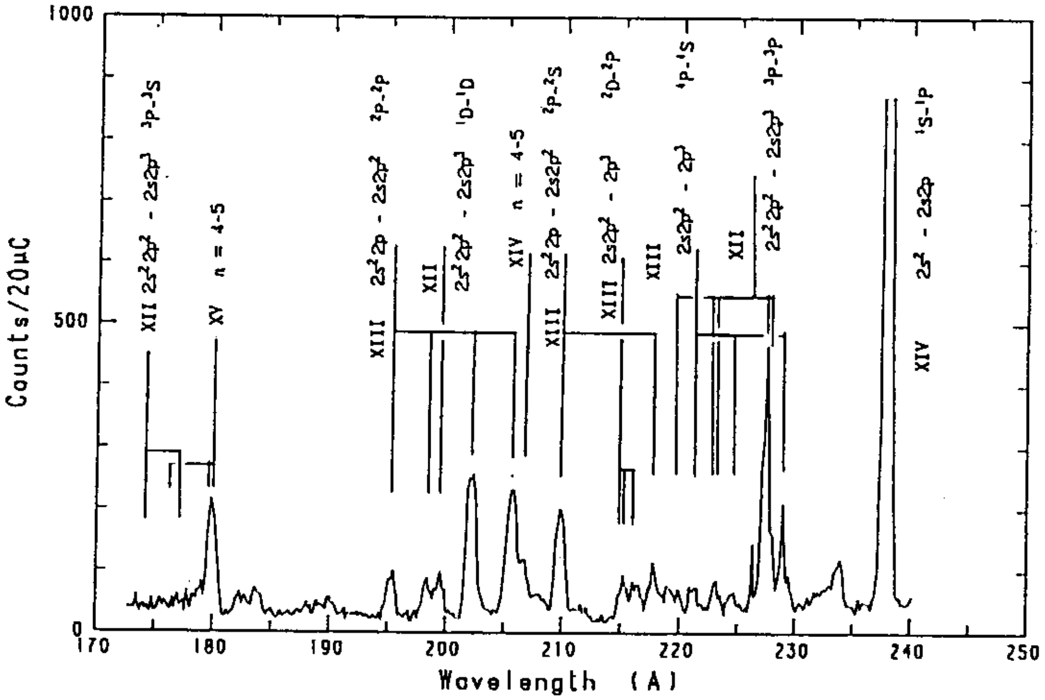

Fig. 1 Portion of the spectrum of multi-charged chlorine ions at 80 MeV beam energy.

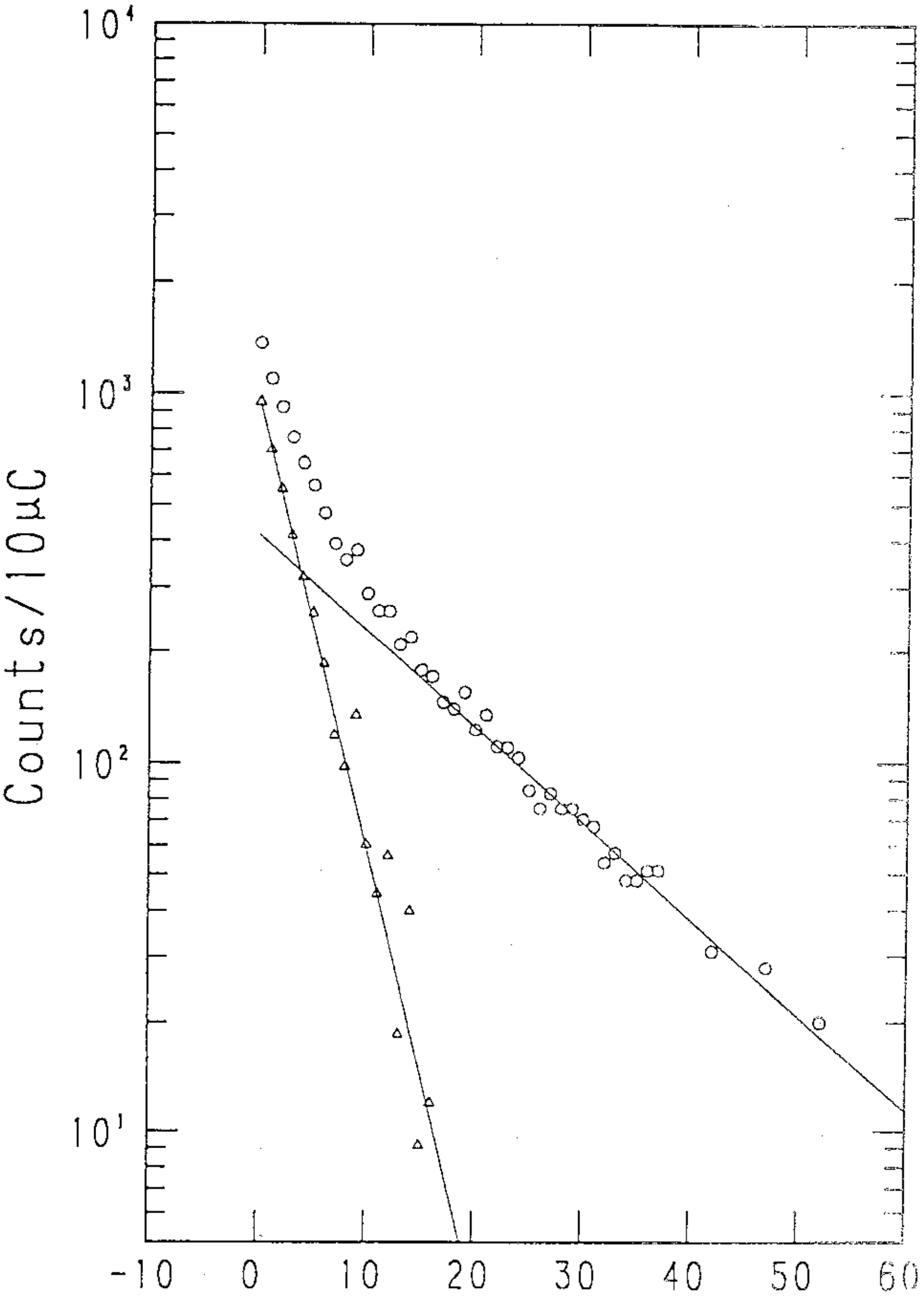

Fig. 2 Intensity decay curve for 2s2p $^1P_1$ level in the Cl XIV (237.8 Å) measured at 120 MeV. The decay curve is decomposed into two exponentials.

2.4 ABSENCE OF STAGE I RECOVERY PEAK IN NICKEL IRRADIATED WITH HEAVY IONS IN ENERGY RANGE 100-120 MeV

Akihiro IWASE, Shigemi SASAKI, Tadao IWATA and Takeshi NIHIRA*

Department of Physics, JAERI, *Faculty of Engineering,
Ibaraki University

Introduction

High energy heavy ions in energies of MeV/amu lose almost all of their energies by the interactions with electrons in solids, (inelastic collision). In some materials, the energy transfered to electrons causes atomic motions, as observed in electronic sputtering1), damage tracks in insulators2) and so on. In metals, however, it has been presumed from the fact of no observations of damage tracks except in very thin metal films, that the coupling between lattice and electrons is sufficiently loose, and that the inelastic collisions have little effect on the atomic motion.

This paper presents the extremely small amount of the stage I recovery irradiated with 100-120 MeV heavy ions, and shows that this anomaly is related to the contribution of the electron excitation by ions to the damage production process, that has not been considered in metals so far.

Experimental procedure

The specimens were thin Ni foils about 0.24μm thick, which were grown onto the Al_2O_3 coated Al substrates by vapor deposition at a pressure of $< 1.2\times10^{-7}$ Torr. The irradiations were performed with 100-120 MeV Cl, Br and I ions respectively from the JAERI tandem accelerator. The temperatures of the specimens were held below 14K during irradiations. After the irradiations, the annealing treatments were performed up to 300K in order to obtain the defect recovery spectra. The defect recoveries were measured at a constant heating rate of 1.5deg/min.

Results and discussion

Fig. 1 shows the recovery spectra of Ni irradiated with 100 MeV I ions and 120 MeV Cl ions, together with the results for 0.5 MeV H and 1.8 MeV Ar irradiatiions3). As can be seen in Fig. 1, the stage I recovery is remarkably reduced for Cl irradiation, and the complete absence of the recovery is found for I irradiation. Similar result was obtained for Br irradiation.

In the case of the low energy ion(0.5-2 MeV) irradiations, the amount of the stage I recovery and the structure of the stage I are well characterized as a function of the PKA(primary knock on atom) median energy $T_{1/2}$[3). This means that the damage structure related to the stage I recovery can be explained within the framework of the elastic collisions for the low energy ion irradiations. Fig. 2 shows the amount of the stage I recovery for both high and low energy ion irradiations, as a function of the PKA median energy. The amount of the stage I recovery for Cl, Br and I irradiatons are extremely small as compared with the low energy ion irradiations. This fact shows that the other machanism besides the lattice agitation by PKA enhances the mutual annihilations of Frenkel pairs during irradiation.

Fig. 3 shows the amount of the stage I recovery as a function of the electronic stopping power. The annihilations of Frenkel pairs during irradiation, which lead to the reduction of the stage I recovery, increase with increasing the amount of the electron excitation by ions. The dependence of the stage I recovery on the amount of the electron excitation suggests that the electrons excited by ions interact with the lattice, and that the energies transfered from electrons to the lattice cause the enhancement of the annihilations of Frenkel pairs. In a more naive view, it can be drawn that "a local heating" occurs along the ion path. "The temperature increase" due to the local heating is, however, too small to produce ion tracks in the specimen.

References

1) L. E. Seiberling, J. E. Griffith and T. A. Tombrello: Radiat. Eff. 52 (1980) 201.
2) R. L. Fleischer, P. B. Price and R. M. Walker: Nuclear Tracks in Solids (Univ. of Calif. Press, Berkeley, 1975).
3) A. Iwase, S. Sasaki, T. Iwata and T. Nihira: J. Nucl. Mater. to be published.

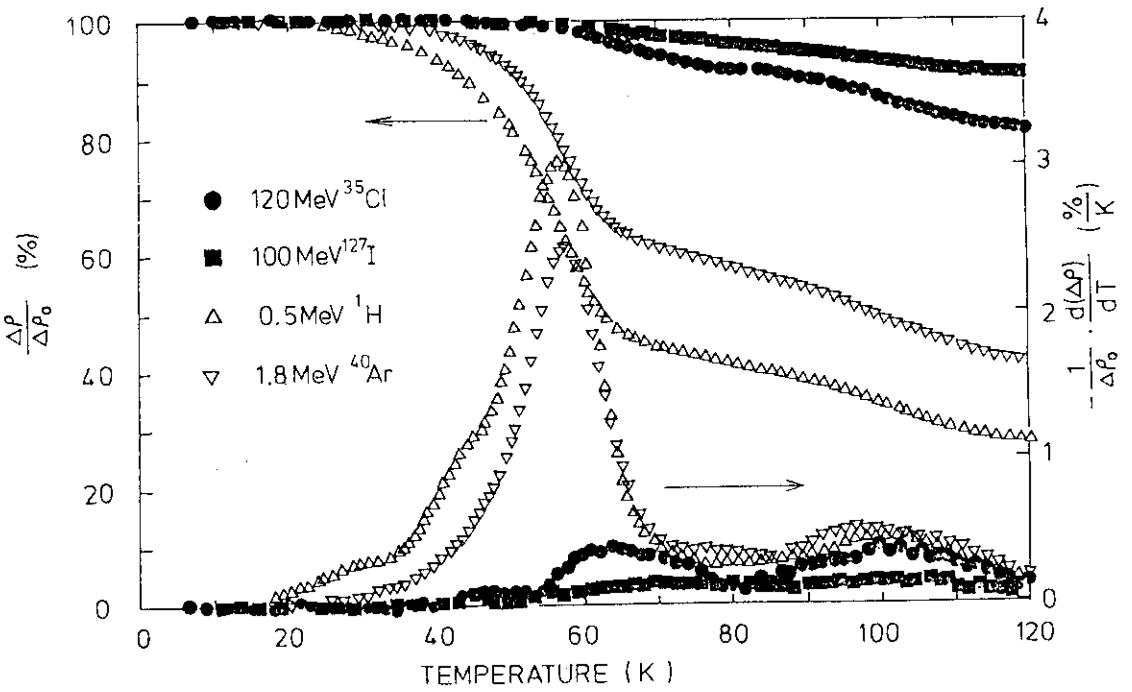

Fig. 1 Recovery spectra of Ni irradiated with 100MeV I and 120MeV Cl ions. For comparison, the results for H and Ar irradiations are also shown.

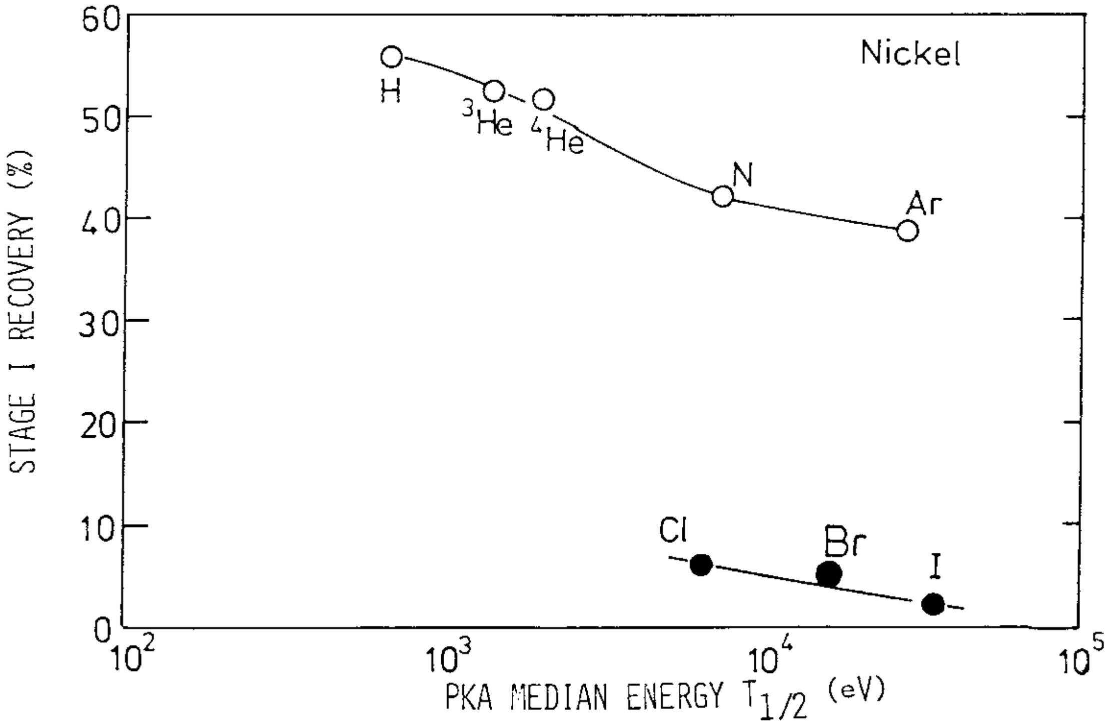

Fig. 2 The amount of the stage I recovery of Ni for high energy ion irradiations (closed circles) and for low energy ion irradiations (open circles) as a function of the PKA median energy $T_{1/2}$.

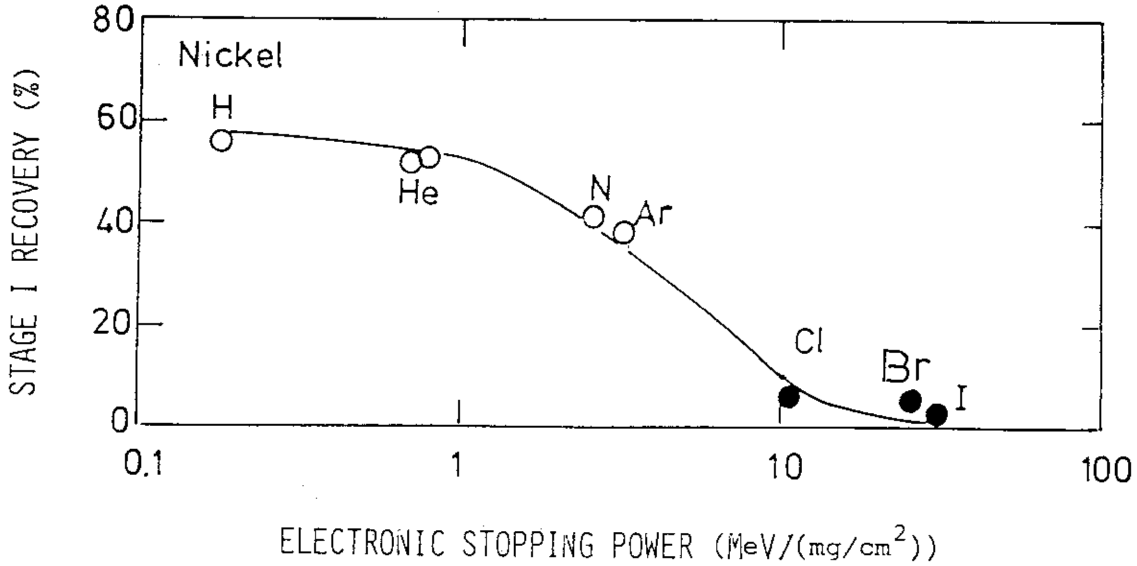

Fig. 3 The amount of the stage I recovery of Ni for high energy ion irradiations (closed circles) and for low energy ion irradiations (open circles) as a function of the stopping power.

2.5 RADIATION EFFECTS OF NEGATIVE THERMAL EXPANSION IN SEMICONDUCTORS BY HEAVY ION IRRADIATION

Hiroshi MAETA, Katsuji HARUNA*, Kazutoshi OHASHI*,
Takuro KOIKE* and Fumihisa ONO**

Department of Physics, JAERI, *Faculty of Engineering,
Tamagawa University, **College of Liberal Arts and
Sciences, Okayama University

1. Introduction

In the usual materials, the linear thermal expansion coefficient is always positive. However, many of the semiconductors show negative thermal expansion coefficient, so that the Gruneisen parameters are negative. These phenomena in the semiconductors which are tetrahedraly bonded solid, have been explained to be associated with transverse acoustic (TA) phonon mode at low temperatures$^{1)}$. Up to date, however, there are few experiments in which the value of the negative expansion coefficients changed by the irradiations and tried to investigate these phenomena from phonon mode characters.

In the present paper, we reports the effects of heavy ion irradiation on negative thermal expansion coefficient in Si and InP semiconductors by measuring lattice parameter. Furthermore, to look into the structure of the defects after heavy ion irradiation, the measurements of x-ray diffuse scattering were carried out at room temperatures.

2. Experimental Procedures

The specimens were formed of thin rectangular plates of Si and InP single crystals with the area of 3x10 mm^2 and thickness of 0.2 mm and 0.3 mm, respectively. These specimens were bombarded with 120 Mev Cl^{+10} ion to 10^{14} ion/cm^2 at about liquid nitrogen temperature. After the irradiation, the specimens were warmed up to room temperature. By using a CuKα beam through a fine slit of 0.2 mm in width, the Bragg reflections were measured by the Bond method in which two counters were placed symmetrically. Measurements of the thermal expansion of the lattice parameter were made between at 4.2 K and room temperature. The diffuse scattering measurements were also carried out at room temperature using a monochromatized $CuK\alpha_1$ radiation and a solid state detector(pure Ge).

3. Results

Typical results of these experiments are shown in figures 1, (a) and (b) for Si and InP specimens bombarded by Cl^{+10} ion. In these figures, the lattice parameters are plotted against temperatures for Si and InP after the bombardments . The experimental results are summarized in table 1, in addition to the irradiation condition .

Characteristic features of the results are as follows :

1) Very large increment of lattice parameters, $\Delta a / a_0$, by the irradiation were observed to be 2.0 % for Si and 7 % for InP.

2) Remarkable changes of negative thermal expansion coefficients in Si and InP after heavy ion irradiation were found. Temperature corresponding to the minimum values of the lattice parameters decreased from 130 to 80 K, for Si and increased from 70 K to 130 k for InP.

4. Discussion

It is very surprising that the values of the lattice parameter after the heavy ion irradiation increases up to 2 % in Si and 7 % in InP. The heavy ion irradiation is expected to produce larger number of the defects than that of the neutron irradiation. In the case of Si specimen, we estimated the concentration of the induced defects by Cl^+ bombardments to be about a few percent from a calculation using by the E-DEP-1 code, and it is assumed that the number of the survived defects at room temperatur is a half of the total number of the defects $^{2)}$. The increment of lattice parameter is due to the induced defects by heavy ion bombardment and it

Table 1 Increased lattice parameter of pure Si, and InP single crystals bombarded by Cl^{+10} ion at liquid nitrogen temperature. Measurements were carried out at room temperature.

specimens	ion	energy	range	thickness of specimen	increase of lattice parameter $\Delta a/a_0$
Si	Cl	120 MeV	32 μm	0.2 mm	1.88 %
InP	Cl	120 MeV	20 μm	0.3 mm	6.91 %

will be expected possibly for these defects to change the thermal expansion coefficients noticeably .

The Grüneisen constant γ is determined from the measurements of the thermal expansion coefficients α by using the following relation,

$$\gamma = 3\alpha B_T V/C_V, \qquad (1)$$

where B_T, V and C_V are the isothermal bulk modulous, the crystal volume and the specific heat at constant volume, respectively. Theoretically, using a model Grüneisen parameters γ_i defined by $\gamma_i = - d(\ln \nu_i)/d(\ln V)$ is for i-th mode with phonon frequency ν_i . The averaged Gruneisen constant $\langle \gamma \rangle$ is given by $\langle \gamma \rangle = \sum \gamma_i C_i/C_i$, where C_i is the heat capacity of the corresponding harmonic oscillator of frequency ν_i. All quantities contained in $\langle \gamma \rangle$ are positive except γ_i. In order that $\langle \gamma \rangle$ is negative in a certain temperature range, some of γ_i must satisfy the condition ;

$$d\nu_i/dV > 0 . \qquad (2)$$

This condition is usually strange. As the volume increases with temperatures, the frequency should decrease for simple material. In the case of materials which have negative thermal expansion coefficients, we must take into account the increasing frequencies with measuring the temperatures or expanding volume. Barron$^{1)}$ has pointed out that the normal mode which satisfies the above condition must be the transverse acoustic one in the short wave length region.

The result of the diffuse scattering is that the half width of the Bragg profiles are very sharp and no significant change could be seen, so that the defects may not be so complicated. Most of the defects in Si may be not only interstitial clusters and/or large dislocation loops, but many of these are cut down the bonding chains, other results the atoms can vibrate easily and the TA mode will be enhanced at low temperatures. It is also reasonable that decrease of the minimum temperature of the lattice thermal expansion to consider from 130 K to 80 K is due to the shear mode vibration (so called TA modes) in the cut-bonding specimen which is like to occur. On the other hand, in InP specimen the minimum temperature shifts to higher temperature, from 70 K to 130 K. It may be considered that for the InP specimen the displaced In and P atoms by the irradiation of the ion migrate and precipitate with each other. By the x-ray diffraction , some profiles were observed at lower angle side which can be considered to associate with the precipitation of the In atoms. From present discussion it can be considered that the shift of the temperatures at which the lattice parameter takes the minimum values is due to the softening of the TA mode by the precipitation of the In and/or P atoms. This argument is in good agreement with the calculated result that the effect of high pressure on phonon dispersion curves in InP is shown to lead 'softening' in the TA phonon mode[3].

A more detailed analysis of the present results and a further experimental study are currently in progress and will be published elsewhere.

References

1) T.H. Barron, Philos. Mag., **46**, (1955) 720.

2) C. Patel, W.F. Sherman and G.R. Wilkinson, Phys. Status Solidi, **b 114** (1982) 169.

3) W. Fuhs, U. Holzhauer, S. Mantl, F.W. Richter and R. Sturm, Phys. Status Solidi, **b 89**, (1978) 69.

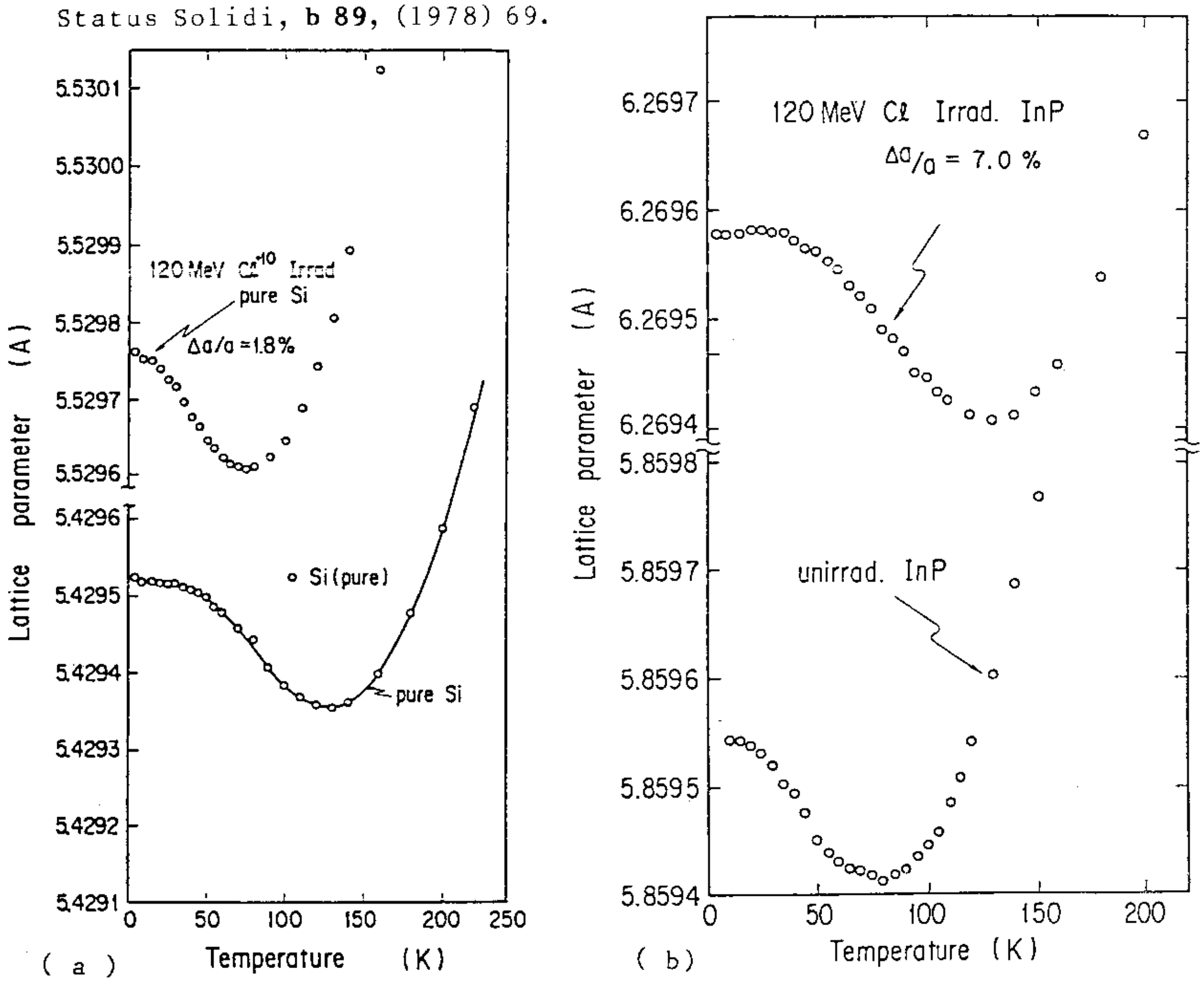

(a) (b)

Figs. 1 Temperature dependence of lattice parameter in Si, (a) and InP, (b) after tandem Cl^{+10} ion (120 MeV) irradiation.

2.6 DAMAGE PROFILES IN METALS IRRADIATED WITH HIGH ENERGY IONS

Saburo TAKAMURA, Mamoru KOBIYAMA* and Kiyotomo NAKATA**

Department of Physics, JAERI, *Faculty of Engineering,
Ibaraki University, **Hitachi Research Laboratory,
Hitachi Ltd.

1. Introduction

Few experimental works have been made to study about the distribution of radiation induced defects and implanted atoms in high energy ion-irradiation$^{1,2)}$, although there have been much studies in low energy ion-irradiation. There are two theoretical approaches for the depth profiles of defect production. The first is the analytical method, for example E-DEP-1 code$^{3)}$. In the second one, the Monte Carlo simulation code, TRIM, have been applied. The theoretical values of depth profiles depend on the choice of the available stopping power, particularly the electronic one.

In the present work, C ions at 90 MeV and Cl ions at 150 MeV are irradiated to multi-foil specimens of Al, Fe, Ni or Ag foils. With these foils isochronal annealings in electrical resistivity are made in order to study a amount of radiation induced defects. The depth profiles are obtained from a change in electrical resistivity. Comparison of the experimental depth profiles with the theoretical predictions of the modified E-DEP-1 and the TRIM codes are performed.

2. Experimental procedures

Foils of 99.5% Al, 99.85% Fe, 99.95% Ni and 99.97% Ag obtained from Goodfellow Metals Ltd. were used for the experiments. The foils were cut to 20 mm length and 20 mm width and the thickness of the foils was determined by weighing. The foils cut to about 2 mm width were piled up and were set to the specimen holder and were irradiated by means of low temperature ion-irradiation cryostat. The apparatus used in irradiation were described in the previous paper$^{4)}$. A description of the apparatus is not repeated here. The ion current during irradiation experiments was of the order of 10^{14} particle/m^{2}. The irradiation temperature was not obviously determined but the foils seems to be held at a temperature below liquid nitrogen temperature under the ion beam.

After irradiation, the foils were taken from the specimen holder in liquid nitrogen. The electrical resistance was measured at liquid helium temperature by using the special device where the ends of a foil were pressed to electrical terminals. Correction of the electrical resistivity for thin film effect was estimated from the table calculated by Dworschak et al.$^{5)}$. However, the correction factor for the specimens having the small value of the residual resistant ratio between room temperature and 4.2 K was below 2 so that the correction was not made in the present work. The isochronal annealings with temperature steps of about 50 K were performed between 80 and 220 K. The amount of resistivity changes of each foil was plotted against the depth which was the distance between the center of foil and the surface. The main source of error in the value of depth was due to uncertainties in measuring value of the length and width of foils, if the influence of thickness was not taken into account since the uniformity of foil thickness was good for the used foils. The error is within 1 %.

3. Results and discussion

The depth profiles due to analytical calculation are obtained as follows. The energy loss of ion consists of two parts. One is called electronic stopping which is energy loss to electrons of target and the other is energy loss in collisions to target nuclei, called nuclear stopping. In the high energy region, all electrons in the incident ions are stripped. However, when the ion velocity is less than the velocity of orbital electrons all the electron is not stripped. In the theoretical calculation, the most important problem is to know the degree of ionization of the ion. The electronic stopping of ions with medium energies has been the subject of theoretical calculation. In the low energy region, the theory of LSS is widely used for the calculation. The modified E-DEP-1 code was used in the present calculation$^{3)}$. The electronic energy loss is obtained by Ziegler's formula in high energy region and by Sugiyama's formula in medium energy region and by LSS theory in low energy.

Fig.1 shows the experimental depth profiles for C ions at 90 MeV to Al, Fe and Ni together with the defect distribution obtained by modified E-DEP-1 and TRIM codes. Experimental values are shifted to deeper distance as compared with the theoretical one. The difference of both depth profiles is considered to be attributed to uncertainties of electronic stopping in the theoretical calculation. The theoretical value depends on the choice of the available electronic stopping. Fig.2 shows the depth profiles for Cl ions at 150 MeV to Al, Fe and Ag. The overall agreement between the experimental and the theoretical values in Cl ion irradiation is approximately good. These experiments are in progress.

References

1) S.Hamada, T.Sawai and K.Shiraishi, J. Nucl. Mater. 133&134 (1985) 370.

2) T.Sasaki, Y.Baba and K.Hojou, JAERI Tandem, Linac & V.D.G. Annual Report 1984, JAERI-M85-104(1985) 37.

3) K.Nakata, T.Aruga and K.Shiraishi, private communication. T.Aruga, JAERI-M83-226(1984) 1.

4) S.Takamura, H.Maeta and M.Kobiyama, in ref.2) 97.

5) F.Dworschak, W.Sassin, J.Wick and J.Wurm, KFA-Report Jül-575-FN(1969).

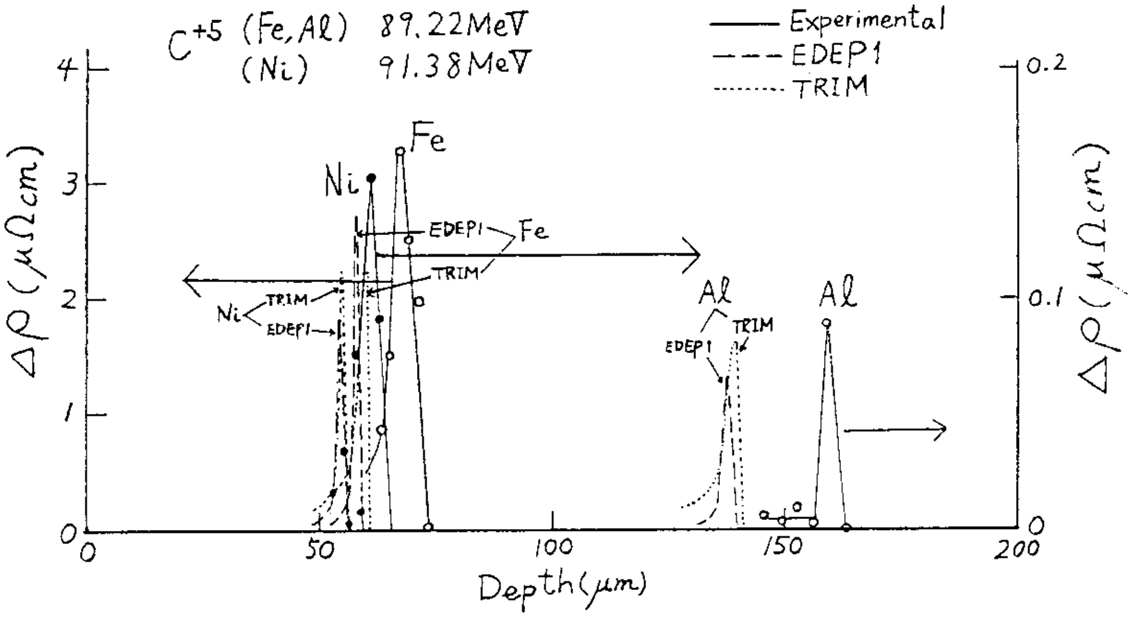

Fig.1 Relation between electrical resistivity changes and depth in Al, Fe and Ni foils after C ion irradiaiton. Curves calculated by E-DEP-1 and TRIM codes are also shown.

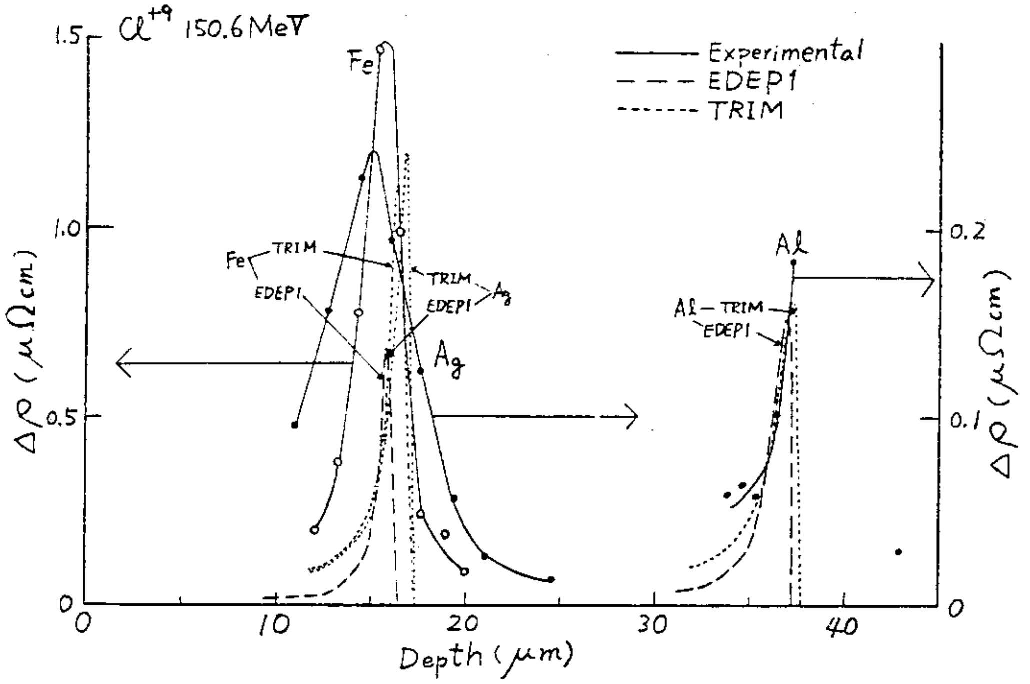

Fig.2 Relation between electrical resistivity changes and depth in Al, Fe and Ag foils after Cl ion irradiation. Curves calculated by E-DEP-1 and TRIM codes are also shown.

2.7 TRANSMISSION SPUTTERINGS OF COPPER AND SILVER BY 114 MeV F^{7+} IONS

Teikichi A. SASAKI and Yuji BABA

Department of Chemistry, JAERI

1. Introduction

Transmission-sputtering experiments of heavy ions have been performed to investigate depth distribution of the energy deposition[1,2] and to elucidate the mechanisms responsible for very small yields for far beyond the range predicted.[3-5] Although the sputtering yield provides information about sequences of nuclear collision cascades which are directly related to the energy-deposition distribution, the experiments have not been popular because of difficulty in preparation of a thin target appropriate for the ion bombardment.

This communication presents an expression in semi-quantitative analysis of the transmission-sputtering yield which is more general than that previously reported.[6] Auger electron spectroscopy (AES) was employed to obtain information about the depth profile of the sputtered particles and sputtering yield for Cu/Nb and Ag/Nb systems.

2. Experimental

Target materials were stack-foils of pure Cu and Ag metals (99.9 % up) from Furuuchi Chemicals and Goodfellow Metals, respectively. The thickness was determined by means of a gravimetric method within an accuracy of ± 0.2 μm. Nb foils with a thickness of ∿ 120 μm were used as catcher foils of the sputtered particles and were mechanically polished with diamond paste of 1/4 μm to make a mirrorlike plane. The stack-foils were set in a target holder made of copper together with the catcher foils. In some cases, 8 keV Ar^+ ion-etching was employed prior to the bombardment for the reduction of carbon and/or oxygen containing adsorbates.

Bombardments were carried out by means of Tandem accelerator at JAERI. The F^{7+} ions of ∿ 250 nA at the energy of 114 MeV from the accelerator impinged the target at normal incidence under a pressure of ∿ 7 x 10^{-7} Pa. The other details on the bombardments were described elsewhere.[2]

Information about the transimission sputtering was obtained with the AES technique by use of 5 keV electrons. The sputtering yields were estimated from the signal intensities of the Cu (LMM, 920 eV), Ag (LMM, 358 eV) and Nb (LMM, 167 eV) Auger lines. Ion etching for the depth profile of the sputtered particles trapped on the catcher surface was carried out with 8 keV Ar^+ ions from a PIG gun. The beam current in the etching was 0.3-1 $\mu A/cm^2$, determined by use of a small Faraday cup in an analyzer chamber of a VG ESCALAB-5 electron spectrometer.

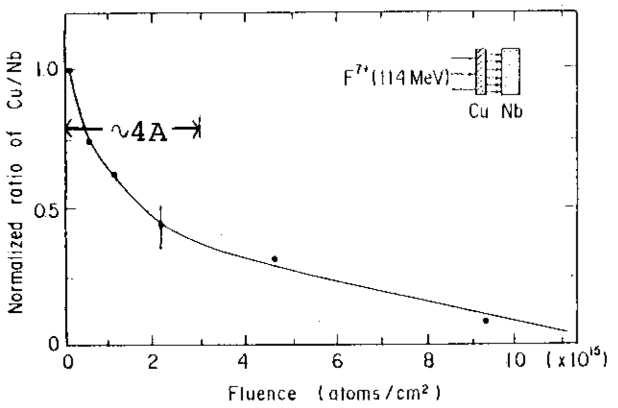

Fig. 1 Etching profile of the sputtered Cu particles deposited on near surface of the Nb catcher foil.

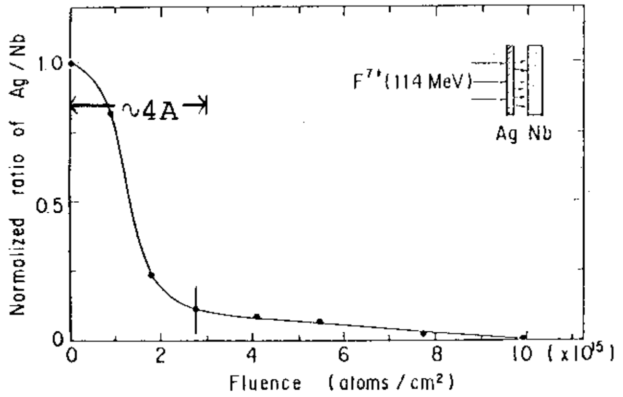

Fig. 2 Etching profile of the sputtered Ag particles deposited on near surface of the Nb catcher foil.

3. Results and discussion

Figs. 1 and 2 show etching profiles of the particles sputtered on the Nb foils. Since etching rate in the present experiment was 0.2 nm per an Ar^+ fluence of 1 x 10^{15} ions/cm^2, the deposition of the sputtered atom is estimated to be within 3 atomic layer for the Cu target and monoatomic layer for the Ag target, respectively. A tailing of the etching profile to the higher fluence for the Cu/Nb system is due to the surface roughness of the Nb foil which impeded uniformal Ar^+-ion etching. Detailed examination of Nb (LMM) and Ag (LMM) Auger spectra gave an evidence that the Ag particles sputtered are trapped in the oxideoverlayer of the catcher foil, Nb_2O_5, and that their chemical state is not oxide but metallic one. Similar result was obtained for the Cu particles

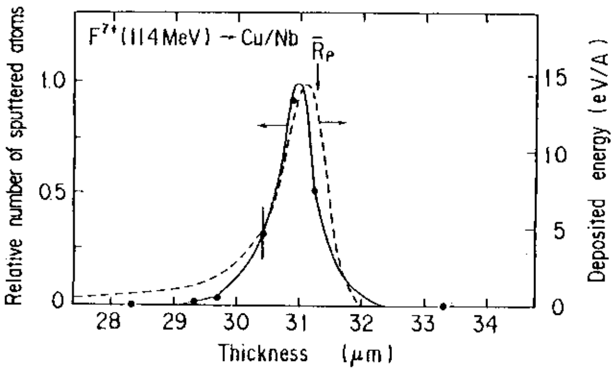

Fig. 3 Relative number of sputtered Cu atoms as a function of the target thickness. Total fluence was 1.7 x 10^{15} ions/cm^2. ——— : experimental, - - - - - - : energy-deposition distribution by the EDEP-1 code.

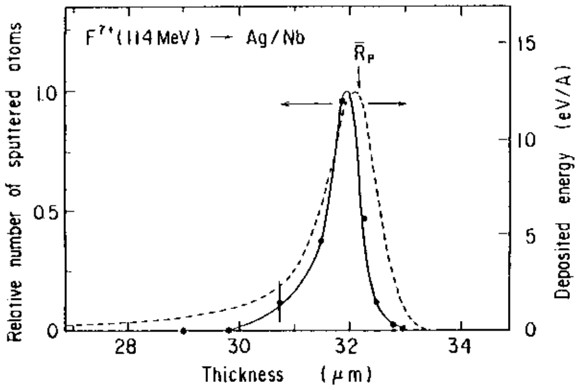

Fig. 4 Relative number of sputtered Ag atoms as a function of the target thickness. Total fluence was 4.0 x 10^{15} ions/cm^2. ——— : experimental, - - - - - - - : energy-deposition distribution by the EDEP-1 code.

sputtered on the Nb catcher foil.

Relative numbers of the sputtered atoms are represented as a function of target thickness in Figs. 3 and 4 for the Cu/Nb system and Ag/Nb system, respectively. The peak positions of the experimental curves obtained locate by $\sim$ 1 % shallower than that of the nuclear energy-deposition distribution by the EDEP-1 code7) modified for high-energy ions. Furthermore, the sputtering scarcely occurs in the region where the target thickness is less by 2.5 um than the mean projected range, though considerable amount of the incident energy is dissipated in a form of the nuclear stopping.

The absolute yield for the transmission sputtering at target thickness t is estimated as,

$$Y(t) = N_s/N_f \qquad (1)$$

where N_s and N_f are the numbers of the sputtered atoms and incident ions per cm^2, respectively. On the other hand, the Auger peak ratio h_t/h_c is approximately correlated with the layer thickness x of the sputtered atoms,

$$h_t/h_c = S_t(1-e^{-\mu_1 x})/S_c e^{-\mu_2 x} \qquad (2)$$

where S is the elemental sensitivity factor of the Auger spectra, μ_1 and μ_2 the absorption coefficients of the respective Auger electrons. The subscripts t and c denote the target and catcher foils, respectively. Eq.(2) is an expression fairly improved for the higher h_t/h_c ratio (≥ 1) which was not taken into account in the previous work.$^{6)}$ The absorption coefficients of the present Auger electrons are estimated to be 2×10^7/cm from the mean free paths of low energy electrons.$^{8)}$ Then the values of N_s can be estimated from the density of sputtered atoms and the layer thickness which is determined in eq.(2). Since the N_s values at the peak positions of the experimental curves are 3.8×10^{15} atoms/cm^2 for the Cu target and 1.4×10^{16} atoms/cm^2 for the Ag target, the maximum values of the sputtering yield are estimated to be 2.3 for the Cu/Nb system and 3.5 for the Ag/Nb system, respectively. Nuclear stopping calculations by the EDEP-1 code with the surface binding energy$^{9)}$ of 3.5 eV for the Cu target and 2.9 eV for the Ag target provide the sputtering yields of 2.0 and 3.1, respectively. The experimental data are in resonable agreement with these calculated values.

References

1) A.D. Marwick: Nucl. Instrum. Methods 132 (1976) 313.
2) T.A. Sasaki, Y. Baba, K. Hojou and T. Aruga: J. Nucl. Mater. 132 (1985) 95.
3) H.L. Bay, H.H. Anderson, W.O. Hofer and O. Nielsen: Appl. Phys. 11 (1976) 313.
4) K.H. Ecker and K.L. Merkle: Phys. Rev. B18 (1978) 1020.
5) H.L. Bay, H.H. Andersen and W.O. Hofer: Rad. Effects 28 (1976) 87.
6) T.A. Sasaki, Y. Baba and K. Hojou: "JAERI TANDEM, LINAC & V.D.G. Annual Report", JAERI-M 85-104 (1985) 37.
7) I. Manning and G.P. Mueller: Computer Phys. Commun. 7 (1974) 85.
8) C.R. Brundle: J. Vac. Sci. Technol. 11 (1974) 212.
9) R. Hultgren, P.D. Desai, D.T. Hawkins, M. Gleiser, K.K. Kelley, D.D. Wagman: Selected Values of the Thermodynamic Properties of the Elements (American Society for Metals, Metals Park, Ohio, 1973).

2.8 ION BEAM ANALYSIS OF $Nb_{0.8}Mo_{0.2}$ ALLOY
I. LATTICE LOCATION OF DISSOLVED DEUTERIUM

Hiroshi NARAMOTO, Kunio OZAWA+, Kiyoshi KAWATSURA,
Masao SATAKA, Sadae YAMAGUCHI*, Yutaka FUJINO* and
Matto AOKI**

Department of Physics, JAERI, *Faculty of Engineering,
Tohoku University, **The Institute for Solid State Physics,
The University of Tokyo

1. Introduction

Energetic ions interact with atoms in solid through the processes like electronic excitation, elastic scattering and nuclear reactions. Which of the processes is more operative is dependent on the projectile energies and the projectile-target combination. In crystalline solids, these ions interact with axial and planar potential arising from the systematic atomic configuration, and the anomalous transmission of incident ions, channeling, is caused along the crystallographic directions and planes. The combination of the channeling phenomena with the above processes gives us powerful tool to analyse the lattice location of relevant atoms distinguishing atomic species.

The location of hydrogen isotopes is of considerable interests for understanding their diffusional behaviour in transition metals1). However, the mechanism of site preference has not yet been clarified satisfactorily. The effect of substitutional solute atoms on hydrogen solubility has been studied in Nb based solid solutions, which suggested the strong interaction of hydrogens with the solutes2). The present report is concerned with the Mo alloying effect on site preference of D atoms in Nb, and the ion beam analysis which utilizes the electronic and the nuclear reaction process is employed to distinguish Nb, Mo and D atoms in $(Nb_{0.8}Mo_{0.2})D_{0.075}$.

2. Experimental procedure

$Nb_{0.8}Mo_{0.2}$ alloy single crystals were grown by an electron beam zone melting technique under the ultra high vacuum, and the solute content of Mo in Nb was determined to be about 20 % in atomic fraction through the process of ion beam analysis detecting the characteristic X-Rays. The

---

+Present address: Energy Research Laboratory, Hitachi Ltd.

details of experimental arrangement were already described elsewhere$^{3)}$.

Two kinds of ion beams were employed to detect three different components distinguishably in $(Nb_{0.8}Mo_{0.2})D_{0.075}$ alloy. The atomic masses of Nb and Mo atoms are almost the same, and a conventional Rutherford scattering analysis is not effective. 80 MeV ^{35}Cl ions from a tandem accelerator were bombarded to the specimen to induce the characteristic Kα X-Rays from Nb and Mo atoms, effectively. The dissolved D atoms in the specimen were detected employing the nuclear reactions $D(^{3}He, \alpha)H$ with the incident energy of 750 keV ^{3}He ions.

3. Results and discussion

Figure 1 shows the results of angular scans around the <100> axis for Kα X-Rays from Nb and Mo atoms in pure Nb and $Nb_{0.8}Mo_{0.2}$ crystals bombarded with 80 MeV ^{35}Cl ions. The full width at the half maximum in the channeling dip curves are the same within the experimental error for Mo and Nb elements in the alloy specimen, and these values are much smaller than that in pure Nb crystal as depicted by a solid curve($2\Psi_{1/2}$(Nb)=0.68°). The elements of Nb and Mo form a solid solution in an entire region of the solute contents, and the addition of the solute Mo atoms to the Nb matrix decreases the lattice constant of pure Nb by amount of about 1.3 %$^{4)}$. This decrease should result in the increase of the width of channeling dip curve considering a channeling theory $^{5)}$. The above change in the dip curve width is also confirmed in the same specimen using the Rutherford backscattering process of 1.6 MeV protons. The present result can be explained by the atomistic disorder induced by alloying.

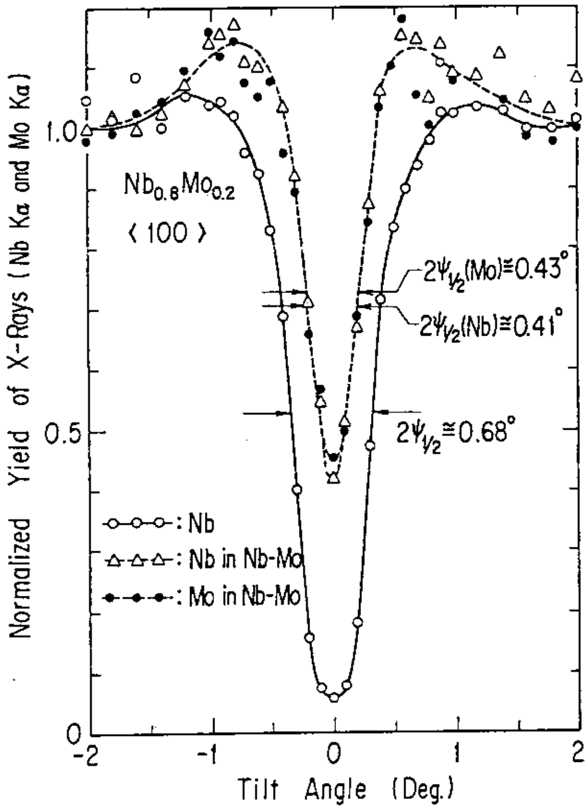

Fig. 1 Angular scans of Kα X-Rays yields around the <100> axis in Nb(solid line) and $Nb_{0.8}Mo_{0.2}$ specimens.

Figure 2 is the same kind of the <100> channeling dip curve as in the previous figure for $Nb_{0.8}Mo_{0.2}$ alloy after deuterium loading to the amount of 7.7 %. Data points with open and solid circles correpond to the X-Ray yields from the Nb matrix and the solute Mo atoms, respectively. The data points with triangles are from the channeling behaviour of Bremsstrahlung, but these are not discussed here. In this figure, it is observed that the widths of the dip curves are widened up almost to that of pure Nb specimen, and that some notable difference is induced between the dip curves for Nb and Mo. The atomic radius of solute Mo atom(1.36 Å) is smaller than that of Nb (1.43 Å) for bcc metallic bonding system, and the lattice shrinkage is expected to be caused by the addition of Mo atoms. The above result presumably reflect the attractive interaction of interstitial D atoms with substitutional solute Mo atoms. The introduction of D atoms could relieve the internal strain around the smaller Mo atoms. This interpretation is consistent with the dramatic increase of the terminal solubility of hydrogens in Nb-Mo system2).

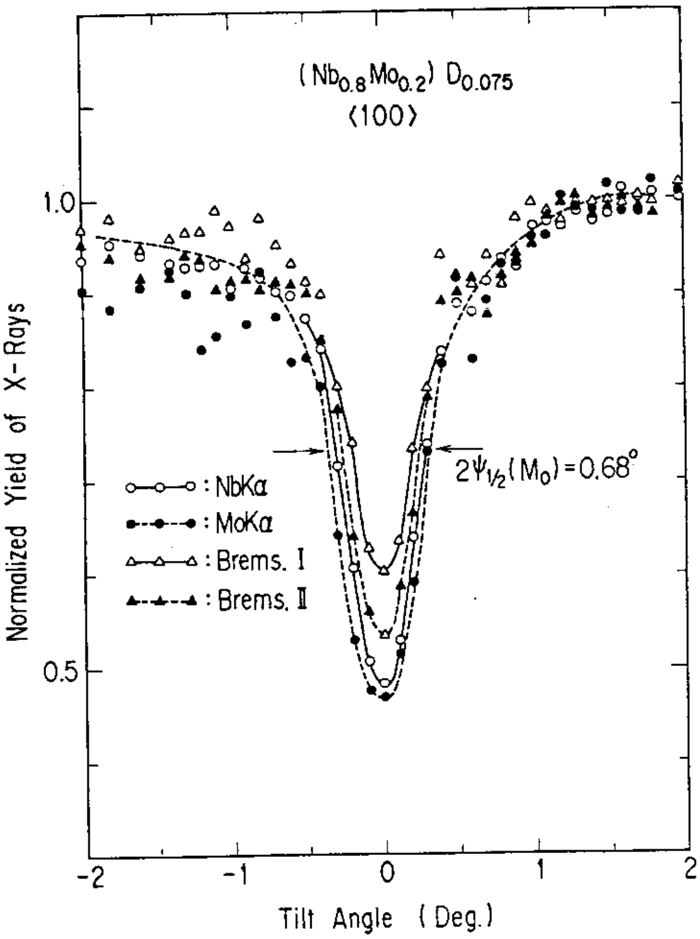

Fig. 2 Angular scans of X-Ray yields around the <100> axis in $(Nb_{0.8}Mo_{0.2})D_{0.075}$. Data with solid circles for Nb Kα X-Rays and data with open ones for Mo Kα X-Rays.

Figure 3 shows two kinds of the channeling dip curves around the <100> axis in $(Nb_{0.8}Mo_{0.2})D_{0.075}$ specimen for the incident 0.75 MeV ^{3}He ions. The solid line with open circles is the backscattering yield from Nb and Mo atoms,and any discrimation is impossible as described already. The dotted curve with solid circles is the nuclear reaction yield from D atoms. With angular scanning from -6° to 6°, the nuclear reaction yield is increased by about 2.7 times the starting yield. This result is reasonably explained by deuterium trapping by the defected induced through the probing process. The backscattering yield shows the clear minimum just at 0°, and on the contrary, the nuclear reaction yield forms the maximum at 0° even if the existence of deuterium trapping by the induced defects. This result indicates the interstitial location of the original D atoms and the random location of trapped D atoms. In order to locate the original D atoms exacly, the planar channeling measurements for 0.75 ^{3}He ions were made on the (110) and the (100) plane in the same specimen. The main features are as follows: the backscattering yields have the minimum at 0° on the (110) and the (100) plane, and the nuclear reaction yields from D atoms show the maximum and the small minimum in the (110) and the (100) plane, respectively. These results with figure 3 conclude the octahedral occupation of original D atoms and the substitutional occupation of solute Mo atoms. The octahedral occupancy of D atoms is totally different from the tetrahedral one in pure Nb crystal, which can be attributed to the Mo-D interaction again.

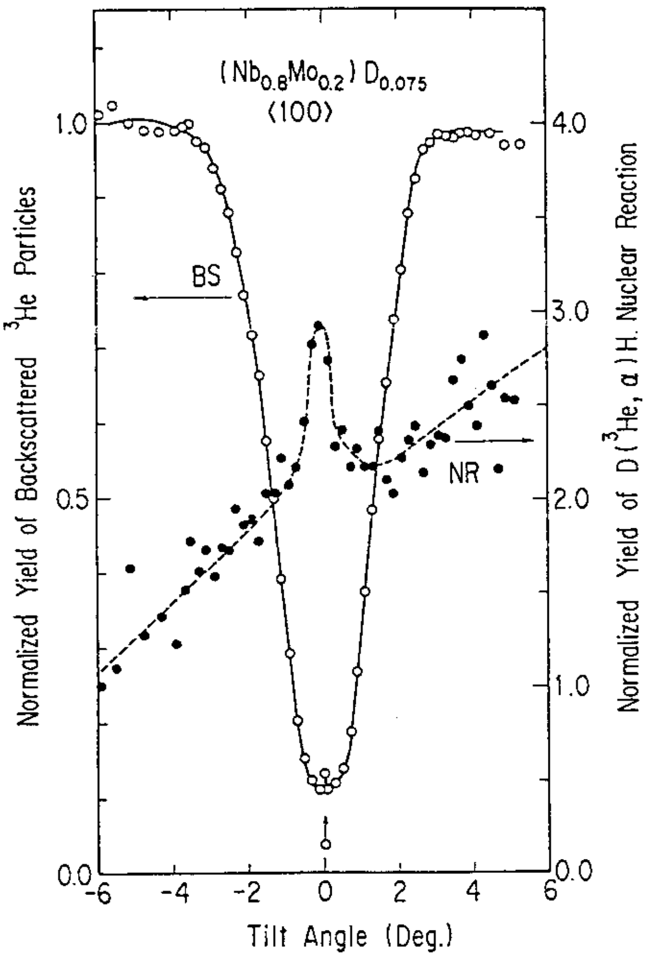

Fig. 3 Angular scans around the <100> axis of backscattering yield(solid line) and $D(^3He, \alpha)H$ nuclear reaction yield(dotted line) in $(Nb_{0.8}Mo_{0.2})D_{0.075}$.

References

1) For example: Y. Fukai, J. Less-Common Met. 101(1984)1.
2) T. Matsumoto, Y. Sasaki and M. Hihara, J. Phys. Chem. Sol. 36(1975)215.
3) JAERI TANDEM, LINAC & V.D.G. Annual Report 1984, JAERI-M 85-104(1985)p29.
4) Lattice Spacing and Structures of Metals and Alloys, ed. W. B. Pearson, Pergamon Press, London, 1956)p757.
5) For example: Channeling, ed. D. V. Morgan, John Wiley & Sons, New York, 1973).

2.9 X-RAY DIFFRACTION TOPOGRAPHIC OBSERVATION OF SILICON SINGLE CRYSTALS IRRADIATED WITH ENERGETIC HEAVY IONS (4)

Hiroshi TOMIMITSU, Yukio KAZUMATA and Eiji SAKAI*

Department of Physics; *Department of Reactor Engineering, JAERI

1. Introduction

The lattice disorder induced by ion-bombardments has been studied by X-ray diffraction topography (XDT). Schwuttke et al[1)] have shown that disorders concentrates in the very thin layers corresponding to the range stragglings of projectiles, when Si single crystals are bombarded by 2 MeV N^+, B^+ and P^+ ions with doses more than 10^{15} ions/cm^2, and the upper and lower parts of the specimen crystal separated by the disordered thin layer remain perfect. More refined study by Bonse, Hart and Schwuttke[2)] found the interference fringes arising from the two perfect regions separated by the very thin disordered layer.

One of the present authors(HT) has also reported[3)] the following results by the conventional XDT-observation in Si single crystals irradiated with 150 MeV Ni^{9+} and Cl^{9+} ions; 1) the specimens were deformed as a whole, 2) they sustained heavy strains which concentrated at the irradiation boundaries, and 3) systematic fringes were observed in the irradiated areas. The present authors subsequently reported[4,5)], from the XDT-observation of the Si wafers irradiated with 58 MeV B^{3+}, 70 MeV B^{4+}, 100 MeV C^{5+}, 120 MeV O^{7+}, 150 MeV Si^{9+} and 169 MeV Au^{13+} ions, that (1) only faint black-and-white contrasts were found at the irradiation boundaries by the irradiation of light ions; (2) on the other hand, besides these black-and-white contrasts, the systematic fringes within the irradiated areas and the macroscopic crystal deformation appears in the case of the irradiation with heavier ions (Cl^{9+}, Ni^{9+} and Au^{13+}).

In order to confirm the results mentioned above, we have made further measurements on the specimens irradiated with various kinds of energetic ions in the fiscal year 1985. The present article briefly summarizes the results of the XDT-observation on those heavy-ion-irradiated Si single crystals.

2. Experimental Results

2.1 Dependence of the Irradiation Effects on the Projectile Mass

As already described in section 1, two different types of irradiation= effects have been revealed[3,4,5] through XDT-observation. The very faint, black-and-white contrasts, indicating the lattice strains, were observed at the irradiation boundaries in the case of the irradiation with light ions. Besides this characteristic contrasts, the systematic fringes in the irradiated area and the macroscopic deformation of the specimen crystal were found on the bombardment with heavy ions. On the basis of these results, some Si wafers under various specified irradiations were examined to ascertain how the types of irradiation effects are conditioned.

The results together with the irradiation conditions are summarized in Table 1. The effects of the projectile mass are clearly seen in the Table.1

Table 1. Summary of the XDT-Observation without Beam-Scanning

Ions	Energy	Dose	Results**		
	(MeV)	x10^{14} ions/cm^2	**Marginal-Strain**	**Deformation**	**Fringe**
$^{11}\mathrm{B}^{4+}$	58	0.2	No	No	No
* $^{10}\mathrm{B}^{4+}$	66	6	**Yes**	No	No
$^{10}\mathrm{B}^{4+}$	70	1	**Yes**	No	No
$^{12}\mathrm{C}^{5+}$	100	5	**Yes**	No	No
* $^{12}\mathrm{C}^{5+}$	100	43	**Yes**	No	No
$^{16}\mathrm{O}^{7+}$	120	7	**Yes**	No	No
* $^{19}\mathrm{F}^{7+}$	120	3	**Yes**	No	No
$^{28}\mathrm{Si}^{9+}$	150	1	**Yes**	No	No
* $^{32}\mathrm{S}^{10+}$	165	1	**Yes**	**Yes**	No
$^{35}\mathrm{Cl}^{9+}$	150	6	**Yes**	**Yes**	**Yes**
* $^{35}\mathrm{Cl}^{9+}$	150	4, 8	**Yes**	**Yes**	**Yes**
$^{58}\mathrm{Ni}^{9+}$	165	0.5	**Yes**	**Yes**	**Yes**
* $^{79}\mathrm{Br}^{6+}$	90	10	**Yes**	**Yes**	**Yes**
$^{197}\mathrm{Au}^{13+}$	169	1	**Yes**	**Yes**	**Yes**

* The irradiation was made during the fiscal year 1985.

** The visibility was compared on the topographs taken by 333, 004 and 220 reflections.

2.2 Effect of the Beam Scanning on the Fringe Patterns in XDT

As for the origin of the interference fringe, Bonse, Hart and Schwuttke have attributed it to the inhomogeneity of the cross-sectional distribution of the projectile ions$^{2)}$. In order to confirm this assumption, we investigated the specimen crystals irradiated with homogeneous- and inhomogeneous beam distribution.

The homogeneous irradiation was realized by the beam-scanning in the horizontal direction with application of the alternative electric field with the saw-toothed shape of several kV, after the cross-section of the beam was shaped into a vertically elongated form.

The results are summarized in Table 2 together with the experimental conditions. The interference fringe could not be observed in the case of homogeneous irradiation, and consequently the assumption mentioned above was apparently proved.

Table 2. Effect of the Beam Scanning on the Fringe Pattern

Ions	Energy (MeV)	Dose x10^{14} ions/cm^2	**Scanning** Yes/ No	**Fringe****
* $^{32}\mathrm{S}^{9+}$	150	28	**Yes**	**No**
* $^{32}\mathrm{S}^{10+}$	165	1	No	Yes
* $^{35}\mathrm{Cl}^{8+}$	120	1	**Yes**	**No**
$^{35}\mathrm{Cl}^{8+}$	150	6	No	Yes
* $^{35}\mathrm{Cl}^{9+}$	150	4, 8	No	Yes
$^{58}\mathrm{Ni}^{9+}$	150	0.5	No	Yes
* $^{58}\mathrm{Ni}^{9+}$	192	3	**Yes**	**No**
$^{197}\mathrm{Au}^{13+}$	169	1	No	Yes
* $^{197}\mathrm{Au}^{13+}$	210	1	**Yes**	**No**

* The irradiation was made during the fiscal year 1985.

** The visibility was compared on the topographs taken by 333 reflection.

2.3 Effect of the Ion Energy on the Fringe Patterns in XDT

The observation of the interference fringe may depend on the length of the range of the projectile ions to the specimen crystal. We saw how the visibility changed with the ion energy, i.e. the range value, in the case of $^{32}S^{7+}$, $^{32}S^{8+}$ and $^{32}S^{10+}$ ions.

The experimental conditions and the results are summarized in Table 3 together with the range values, and, as expected, the interference fringes are apparently affected by the ion energy, i.e. the range length.

Further investigation is now in progress, especially for the dependence on the dose and the energy of ions.

Table 3. Effect of the Ion Energy on Fringe Pattern

Ions	Energy (MeV)	Dose $\times 10^{14}$ ions/cm^2	Range** (μm)	Fringe***
* $^{32}S^{7+}$	50	2	15	Yes
* $^{32}S^{8+}$	100	18	29	Yes
* $^{32}S^{10+}$	165	1	52	No

* The irradiation was made during the fiscal year 1985.

** The values were interpolated from the table in Ref.6.

*** The visibility was compared on the topographs taken by 333 reflection.

References

1) G.H.Schwuttke, K.Brack, E.E.Gardner and H.M.DeAngelis: Proc. Santa Fe Conf.Radiation Effects in Semiconductors, ed. F.Vook,(Plenum Press,N.Y., 1968) pp.406.
2) U.Bonse, M.Hart and G.H.Schwuttke: Phys.Stat.Solidi 33 (1969) 361.
3) H.Tomimitsu: Jpn.J.Appl.Phys. 22 (1983) L674.
4) H.Tomimitsu: JAERI-M 84-129 (1984) pp.47.
5) H.Tomimitsu, Y.Kazumata and E.Sakai: JAERI-M 85-104 (1985) pp.93.
6) U.Littmark and J.F.Ziegler: Handbook of Range Distributions for Energetic Ions in All Elements (Pergamon Press, N.Y., 1980).

2.10 LATTICE DEFECTS IN SILICON CARBIDE

Yukio KAZUMATA, Hiroshi NARAMOTO and Akira KIKUCHI*

Department of Physics, JAERI, *Faculty of
Engineering, Ibaraki University

1. Introduction

The change in phonon spectrum will affect the fundamental physical properties such as specific heat, thermal conductivity, infrared absorption and so on. The effect of lattice defects on phonon spectrum is an essential problem to be clarifyed for the study of radiation damage, nevertheless only a few attempts have been made1). The experimental difficulty in tackling this problem arises from the insufficient sensitivity of conventional neutron scattering which is a standard method for the observation of phonon spectrum. Raman scattering is favorable in sensitivity although detectable phonons (normal modes) are usually restricted to optical phonons at the center of the Brillouin zone. By use of polytype crystals, however, additional phonons at the intermediate and boundary in the Brillouin zone will be observable in the large zone schema.

6H SiC has wurtzite structure but more atoms (12 atoms) per unit cell and therefore has additional weak modes accessible to Raman scattering besides the optical modes at the zone center. The purpose of this paper is to study the effect of lattice defects on phonon spectrum by Raman scattering and also to determine models of paramagnetic defects by esr.

2. Experimental procedures

Four different specimens were used in this experiment. Three of them are single crystals with 6H structure. Two of these single crystals are transparent in pale green and another is opaque in dark brown. The rest is polycrystal grown by CVD method and contains both α and β phases. By esr, the green single crystals show three well-resolved hyperfine lines due to N impurity ions, but the brown one has many partially-resolved lines presumably associated with a large amount of the impurity ions. By Raman scattering, few differences are observed among these single crystals. In the polycrystal, a broad band is observed by esr and also some characteristic differences from single crystals are found in Raman spectrum.

Ion bombardments were carried out by a 2 MV Van de Gaaff and a tandem accelerator at the temperature at about -150°C. After bombardments the specimens were warmed up to room temperature , and then the measurements by esr and Raman scattering were made.

3. Results and Discussion

Preliminary experimental results will be described below since the experiments are now on the way for conclusion.

(a) Raman scattering: Typical Raman spectrum for a single crystal is shown in Fig.1. The representations of the Raman lines in normal modes were determined with polarized light in the reference of Loudon's paper$^{2)}$ as indicated in Fig.1. The Raman lines at lower wave number below 600 cm^{-1} belong to acoustic branches and the strong lines between 700 and 1000 cm^{-1} are due to optical branches. The E_2 and E_1-modes of the acoustic branch were assigned to the values of x=0.67 and 0.33 in the large zone, respectively, where $x=q/q_{max}$ and $q_{max}=6\pi/c$, pseudomomentum vector.

Raman spectra after ion bombardments are shown in Fig.2(a) and (b). Only optical modes are shown in these figures because acoustic modes can not be detected on account of broadening and reduction of the intensities of the lines. Even the lines of the optical modes suffer from an increase in widths. No symptom of recovery is observed after annealing at 730 C. Clearly further experiments dealing with lower doses will be needed to study the detailed change of Raman lines by lattice defects.

(b) ESR: As described above, the differences in esr spectrum are observed depending on the concentration of N ions contained in specimens. Fig.3 represents esr spectrum observed at NT after the bombardment of C^{+5} ions. The strong line at 0.33 T comprised several lines, which is seen by the enlargement of the magnetic field around the line. These lines are presumably associated with carbon vacancies or carbon clusters. Two of these lines decayed out after annealing at 250°and 750° C. The weak lines with large separation from 0.28 to 0.38 T show angular dependence, that is, change their locations in the magnetic field with the angles between the crystal axis and the direction of magnetic field. These weak lines will be caused by the spin-spin interaction of two dangling bonds or by the hyperfine interaction between a Si-nucleus and an unpaired electron.

More elaborate experiments are now in progress and a complete paper will be published soon.

References.

(1)B.S. Elman, H.S. Dresselhauss, G. Dresselhauss, E.W. Maby and H. Mazurek: Phys. Rev. B24 (1981) 1027.

(2)R. Loudon: Advan. Phys. 13 (1964) 423.

Figures

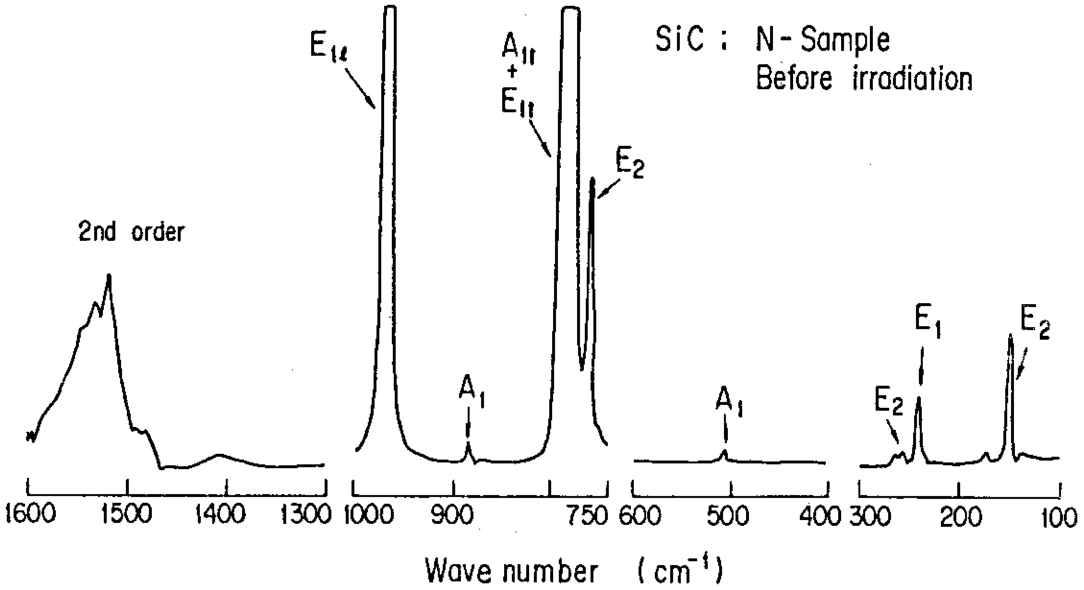

Fig.1. Raman spectrum of 6H SiC, before irradiation. This spectrum was observed by the optical configuration of X(ZZ+ZX)Y, where the symbols inside the parenthesis are, left to right, the polarization of the incident (Z) and of the scattered light (Z and X), while the ones to the left and right of the parenthesis are the propagation direction of the incident (X) and of the scattered light (Y), respectively. Reference axes X, Y and Z are fixed in the crystal, with Z along the C axis.

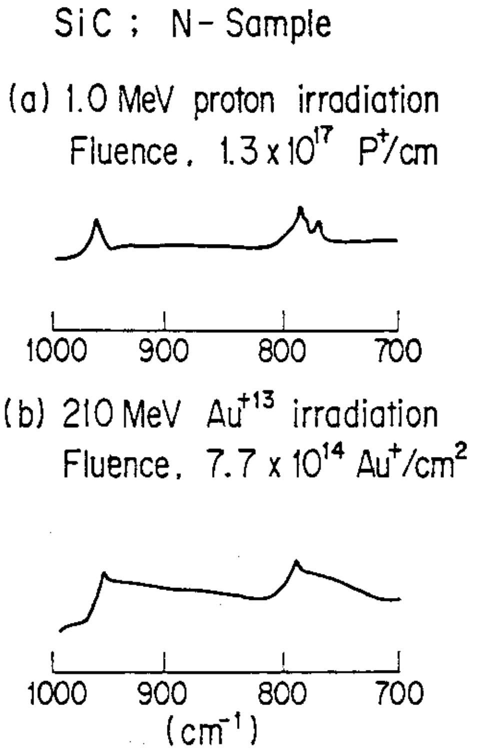

Fig.2 (a) Raman spectrum after 1.0 MeV P^+ ion bombardment. Optical modes are shown.
(b) Raman spectrum after 210 MeV Au^{+13} ion bombardment.

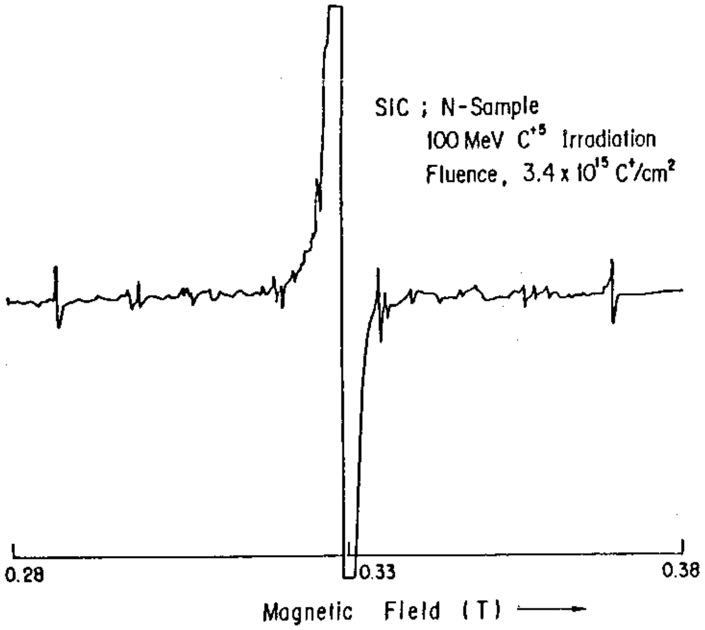

Fig.3. Esr spectrum measured at NT after 100 MeV C^{+5} ion bombardment. The strong line at the center (0.33 T) consists of several lines.

2.11 FURTHER MEASUREMENTS OF INDUCED RADIOACTIVITIES IN SILICON AND GERMANIUM IRRADIATED WITH HIGH-ENERGY HEAVY IONS

Eiji SAKAI

Department of Reactor Engineering, JAERI

Semiconductor detectors are known to be sensitive to radiation damage which may be annealed by heating at an elevated temperature. In high-energy heavy-ion detection with semiconductor detectors, nuclear reactions in the semiconductor materials themselves are expected to introduce radioactive nuclides which increase background counting rates of the detectors during and after the irradiation. These radioactive nuclides can not be removed by heating and the only method to remove these nuclides is etching. The production of radioactive nuclides is also important in manufacturing dopant layers buried deep into semiconductor materials by the ion implantation since the radioactivities may result in noisy devices and also the nuclides with their daughters may change the type of the materials.

In order to evaluate the amount of background counting rate increase in semiconductor heavy-ion detectors, the author started measuring the induced radioactivities in Si and Ge after the irradiation with various high-energy heavy ions. Gamma-ray spectra from irradiated wafers of Si and Ge were measured using a high-purity Ge spectrometer to obtain the induced gamma-ray-emitting nuclides, their radioactivities, their numbers of atoms at the end of the irradiation and the numbers of the atoms per incident heavy-ion. Some of the results were already published[1,2].

In this fiscal year(1985), irradiations with 90 MeV $^{79}Br^{6+}$, 120 MeV $^{19}F^{7+}$, 165 MeV $^{32}S^{10+}$, 66 MeV $^{10}B^{4+}$, 150 MeV $^{32}S^{9+}$, 50 MeV $^{32}S^{7+}$and 100 MeV $^{32}S^{8+}$ were carried out and some of the results are summarized in Table 1.

References

1) E. Sakai: IEEE Trans. Nucl. Sci., NS-31 (1984) 316.

2) E. Sakai: IEEE Trans. Nucl. Sci., NS-33 (1986) 651.

Table 1 Residual gamma-ray-emitting nuclides induced in Si and Ge irradiated with heavy ions, their radioactivities at the end of irradiation, corresponding numbers of atoms, numbers of atoms per incident ion, resultant stable daughter nuclides and the calculated threshold energies for compound nucleus formation

Heavy ions (Range)	Number of particles	Irradiated materials	Residual nuclide	Radioactivity(nCi)	Number of atoms	Number of atoms per particles	Stable daughter nuclide	Threshold energy(MeV)
120MeV $^{19}F^{7+}$	5.66E14	Si	Sc-44m(2.44d)	1360	1.54E10	2.78E-5	Ca-44	34.21
(94.8 μm)	/3.14cm^2		Sc-44m→Sc-44(3.93h)				Ca-44	
120MeV $^{19}F^{7+}$	6.21E14	Ge	Ga-67(78.9h)	22.6	3.41E8	5.56E-7	Zn-67	50.06
(61.8 μm)	/3.14cm^2		Ge-69(39.0h)	118	8.81E8	1.46E-6	Ga-69	
			As-71→Ge-71(11.2d)				Ga-71	
			As-71(61h)	121	1.42E9	2.32E-6	Ga-71	
			As-74(17.78d)	38.8	3.18E9	5.14E-6	Ge-74,Se-74	
			As-76(26.3h)	417	2.11E9	3.54E-6	Se-76	
			Se-75(118.5d)	4.9	2.66E9	4.28E-6	As-75	
			Br-77(57.0h)	136	1.49E9	2.44E-6	Se-77	
			Kr-79(35.0h)	333	2.24E9	3.72E-6	Br-79	
			Sr-83→Rb-83(86.2d)				Kr-83	
			Sr-83(32.4h)	1800	1.12E10	1.87E-5	Kr-83	
			Y-87→Sr-87m(2.80h)				Sr-87	
			Zr-86→Y-86(14.74h)				Sr-86	
			Y-87(80.3h)	1560	2.40E10	3.92E-5	Sr-87	
			Zr-88→Y-88(106.6d)				Sr-88	
			Zr-86(16.5h)	1970	6.25E9	1.07E-5	Sr-86	
			Zr-88(83.4d)	33.0	1.27E10	2.05E-5	Sr-88	
			Zr-89(78.4h)	736	1.11E10	1.81E-5	Y-89	
			Nb-90(14.6h)	1070	3.01E9	5.21E-6	Zr-90	
50MeV $^{32}S^{7+}$	~5.29E13	Si	None					70.74
(15 μm)	/0.72cm^2							
100MeV $^{32}S^{8+}$	~4.46E14	Si	Cr-51(27.7d)	6.1	7.74E8	~1.74E-6	V-51	70.74
(29.3 μm)	/0.72cm^2		Mn-52(5.59d)	5.0	1.29E8	~2.93E-7	Cr-52	
			Co-55→Fe-55(2.7y)				Mn-55	
			Co-55(17.5h)	112	3.76E8	~9.45E-7	Mn-55	
			Ni-56→Co-56(77.12d)				Fe-56	
			Ni-57→Co-57(271.77d)				Fe-57	
			Ni-56(6.10d)	1.8	5.10E7	~1.16E-7	Fe-56	
			Ni-57(36.0h)	221.5	1.53E9	~3.63E-6	Fe-57	
150MeV $^{32}S^{4+}$	~8.56E14	Si	Cr-48(15.976d)→V-48(15.976d)				Ti-48	70.74
(47.4 μm)	/0.3cm^2		Cr-48(21.56h)	66.7	2.77E8	~3.74E-7	Ti-48	
			Cr-51(27.70d)	25.3	3.24E9	~3.80E-6	V-51	
			Mn-52(5.59d)	143.7	3.70E9	~4.43E-6	Cr-52	
			Co-55→Fe-55(2.7y)				Mn-55	
			Co-55(17.54h)	265.6	8.95E8	~1.25E-6	Mn-55	
			Ni-56→Co-56(77.12d)				Fe-56	
			Ni-57→Co-57(271.77d)				Fe-57	
			Ni-56(6.10d)	8.0	2.24E8	~3.13E-7	Fe-56	
			Ni-57(36.0h)	124.6	8.62E8	~1.10E-6	Fe-57	

Heavy ions (Range)	Number of particles	Irradiated materials	Residual nuclide	Radioactivity(nCi)	Number of atoms	Number of atoms per particles	Stable daughter nuclide	Threshold energy(MeV)
165MeV $^{32}S^{10+}$	1.05E14	Si	Sc-44m(2.44d)	3.4	3.78E8	3.72E-7	Ca-44	70.74
(54 μm)	/0.98cm²		Sc-44m→Sc-44(3.93h)				Ca-44	
			Cr-48→V-48(15.976d)				Ti-48	
			Cr-48(21.56h)	69	2.86E8	2.97E-6	Ti-48	
			Cr-51(27.70d)	18	2.31E9	2.20E-5	V-51	
			Mn-52(5.59d)	102	2.62E9	2.53E-5	Cr-52	
			Co-55→Fe-55(2.7y)				Mn-55	
			Co-55(17.54h)	130	4.39E8	4.65E-6	Mn-55	
			Ni-56→Co-56(78.8d)				Fe-56	
			Ni-57→Co-57(271d)				Fe-57	
			Ni-56(6.10d)	1.8	5.10E7	4.92E-7	Fe-56	
50MeV $^{32}S^{7+}$	~1.96E14	Ge	None					94.25
(10.9 μm)	/3.0cm²							
100MeV $^{32}S^{4+}$	~1.38E15	Ge	As-71→Ge-71(11.2d)				Ga-71	94.25
(20.6 μm)	/2.88cm²		As-71(61h)	1.0	1.18E7	~8.86E-9	Ga-71	
			Y-87→Sr-87m(2.80h)				Sr-87	
			Y-87(80.3h)	0.4	5.56E6	~4.15E-9	Sr-87	
			Ru-97(2.88d)	0.8	1.02E7	~7.64E-9	Mo-97	
			Pd-100→Rh-100(20.8h)				Ru-100	
			Rh-101m(4.34d)	4.5	9.03E7	~6.69E-8	Ru-101	
			Pd-100(3.63d)	2.0	3.43E7	~2.55E-8	Ru-100	
150MeV $^{32}S^{4+}$	2.46E15	Ge	Ga-67(78.3h)	6.3	9.53E7	3.97E-8	Zn-67	94.25
(30.9 μm)	/2.15cm²		Ge-69(39.0h)	50.4	3.77E8	1.62E-7	Ga-69	
			As-71→Ge-71(11.2d)				Ga-71	
			As-71(61h)	34.4	4.03E8	2.65E-7	Ga-71	
			Se-72→As-72(26.0h)				Ge-72	
			As-74(17.8d)	53.7	1.82E8	8.26E-8	Ge-74,Se-74	
			As-76(26.32h)	33.4	1.69E8	7.42E-8	Se-76	
			Se-72(26.0h)	102	5.10E8	2.24E-7	Ge-72	
			Se-75(118.5d)	0.85	4.66E8	1.90E-7	Ge-75	
			Br-77(57.0h)	10.5	1.15E8	4.84E-8	Se-77	
			Zr-89→Y-89m(16.1s)				Y-89	
			Zr-89(78.4h)	3.3	4.90E7	2.04E-8	Y-89	
			Tc-95(20.0h)	430	1.65E9	7.43E-7	Mo-95	
			Tc-96(4.35d)	11.0	2.21E8	9.16E-8	Mo-96	
			Tc-99m(6.0h)	4178	4.82E9	2.71E-6	Ru-99	
			Ru-97(2.88d)	238	3.17E9	1.32E-6	Mo-97	
			Rh-99(15.0d)	2.3	1.61E8	6.56E-8	Ru-99	
			Pd-100→Rh-100(20.8h)				Ru-100	
			Pd-101→Rh-101m(4.34d)				Ru-101	
			Pd-100(3.63d)	43	7.25E8	3.02E-7	Ru-100	
			Pd-101(8.47h)	1294	2.11E9	1.08E-6	Ru-101	

Heavy ions (Range)	Number of particles	Irradiated materials	Residual nuclide	Radioactivity(nCi)	Number of atoms	Number of atoms per particles	Stable daughter nuclide	Threshold energy(MeV)
165MeV $^{32}S^{10+}$	3.56E14	Ge	Ga-67(78.3h)	4.9	7.36E7	2.11E-7	Zn-67	94.25
(35.6 μm)	/3.14cm²		Ge-69(39.0h)	48	3.62E8	1.06E-6	Ga-69	
			As-71→Ge71(11.2d)				Ga-71	
			As-71(61h)	29	3.43E8	9.93E-7	Ga-71	
			Se-72→As-72(26.0h)				Ge-72	
			As-73(80.3d)	0.4	1.32E8	3.70E-7	Ge-73	
			As-74(17.78d)	3.0	2.46E8	6.95E-7	Ge-74,Se-74	
			Se-72(8.40d)	6.5	2.5 E8	7.1 E-7	Ge-72	
			Se-75(118.5d)	0.7	3.75E8	1.11E-6	As-75	
			Br-77(57.0h)	12.5	1.37E8	3.97E-7	Se-77	
			Y-87→Sr-87m(2.80h)				Sr-87	
			Y-87(80.3h)	2.2	3.41E7	9.78E-8	Sr-87	
			Zr-89(78.4h)	5.5	8.31E7	2.39E-7	Y-89	
			Nb-95(35.0d)	16.1	2.60E9	7.31E-6	Mo-95	
			Tc-96(4.35d)	10.9	2.18E8	6.22E-7	Mo-96	
			Tc-99m(6.0h)	35600	4.10E10	1.52E-4	Ru-99	
			Ru-97(2.88d)	188	2.50E9	7.20E-6	Mo-97	
			Rh-99(15.0d)	1.8	1.21E8	3.42E-7	Ru-99	
			Pd-100→Rh-100(20.8h)				Ru-100	
			Rh-101m(4.34d)	100	2.01E9	5.75E-6	Ru-101	
			Pd-100(3.6d)	58	9.61E8	2.76E-6	Ru-100	
90MeV $^{79}Br^{6+}$	3.05E15	Si	None					226.35
(15.5 μm)	/3.14cm²							
90MeV $^{79}Br^{6+}$	3.66E15	Ge	None					253.83
(11.8 μm)	/3.14cm²							

Ⅲ RADIATION EFFECTS IN MATERIALS

3.1 CROSS-SECTIONAL TEM OBSERVATION OF 316 STAINLESS STEEL IRRADIATED WITH 90 MeV Br-ion

Tomotsugu SAWAI, Shozo HAMADA, Kenji SUZUKI and Akimichi HISHINUMA

Department of Fuels and Materials Research, JAERI

The heavy-ion irradiation experiments have been performed to simulate the neutron irradiation damage for fusion reactor materials. The radiation damage produced by ions is not uniform along the depth. Cross-section method for stainless steel developed by Hamada1) is very advantageous for the direct observation of depth-dependent damage profile and here has been applied it to Type 316 stainless steel irradiated with 90 MeV Br ions.

The plates of Type 316 stainless steel (2.5 mm^w x 12 mm^l x 0.2 mm^t) annealed for 1.8×10^3 s at 1373 K were irradiated with Br^{6+} ions in the JAERI tandem accelerator at the particle current of 50 nA/cm^2 to 23 dpa at the peak damage region. During the irradiation, the specimen had been heated only by the incident beam and the temperature had not been measured. After the irradiation, the sample was electroplated with nickel and then sliced in a plane normal to the irradiated surface. The sliced sample was mechanically and then electrolytically polished to the specimen for transmission electron microscopy(TEM). Further detailes of specimen preparation have been described elsewhere1,2).

Figure 1 shows typical cross-sectional electron micrograph showing the damage structure in the range from the incident surface to the damage peak region, which was taken originally at the magnification of x5000. The mean projected range of 90 MeV Br in Type 316 stainless steel was measured on the micrograph to be 6.75 ±0.15 μm. Because of the image distortion at low magnification and the poor reliability of magnification in conventional TEM micrograph, mean projected ranges had been measured in the cross-section method only by the optical microscopy2-4) whoes accuracy could not surpass 0.5 μm. The well designed microscope JEM-2000FX was examined with a grating of 28800 lines/inch and no harmfull image distortion was detected at the magnification of x5000. The exact magnification is also measured and its reproducibility is maintained by the minute adjustment of specimen hight to the objective lens with the equiped Z-axis controller. The application of transmission electron microscopy could remarkably improved the accuracy of range measurement.

90 MeV Br-ion in stainless steel belongs to the energy region around the maximum in the stopping power versus energy curve, where the estimations of stopping power have not been well established yet. Figure 2 also contains two lines calculated by extended E-DEP-1 code$^{5)}$ using the stopping power of Ziegler$^{6)}$ and modified value of Northcliffe and Schilling$^{7)}$. From the value originally given by Northcliffe and Schilling for nickel target, S_{Ni}^{NS}, that for iron target, S_{Fe}, was obtained by the following equation$^{2)}$;

$$S_{Fe}(E) = S_{Ni}^{NS}(E) \times (S_{Fe}^{Zig}(E) / S_{Ni}^{Zig}(E))$$

where S_{Fe}^{Zig} and S_{Ni}^{Zig} are the stopping powers of Fe and Ni target by Ziegler, respectively. It can be seen that the range calculated using S_{Fe} gives the better approximation than that using Zieler, which was also reported for the case of 45.7 MeV Ar in 316 stainless steel$^{2)}$.

Defect clusters around the mean projected range is shown in Fig. 3 at higher magnification. Defect clusters were also seen in the shallow region within the depth of about 1μm from the irradiated surface(Fig. 4) and near the grain boundary in the intermediate region of peak but no defect was observed in the grain(Fig. 5). These might be formed by the flow of point defect to the sink, but detailed discussion requires further experiments, especially with precise control of irradiation temperature.

References

1) S. Hamada: to be published in J. Nucl. Sci. & Tech.
2) S. Hamada et al: JAERI-M 85-104 (1985) p.45.
3) S. Hamada, T. Sawai and K. Shiraishi: J. Nucl. Mater. 133&134 (1985) 370.
4) K. Shiraishi and K. Fukai: J. Nucl. Mater. 117 (1983) 85.
5) I. Manning and G. P. Mueller: Comp. Phys. Comm. 7 (1974) 85.
6) J. F. Ziegler: Handbook of Stopping Cross-Sections for Energetic Ion in All Elements (Pergamon Press, New York, 1980).
7) L. C. Northcliffe and R. F. Schilling: Nucl. Data Tables, Sec. A7 (1970) 233.

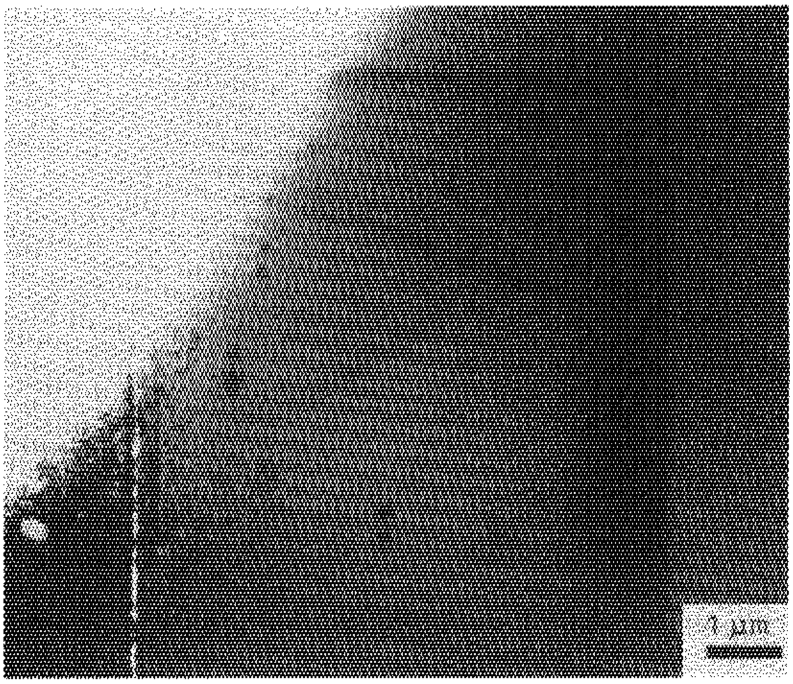

Fig. 1 Cross-sectional transmission electron micrograph of Type 316 stainless steel irradiated with 90 MeV Br-ion.

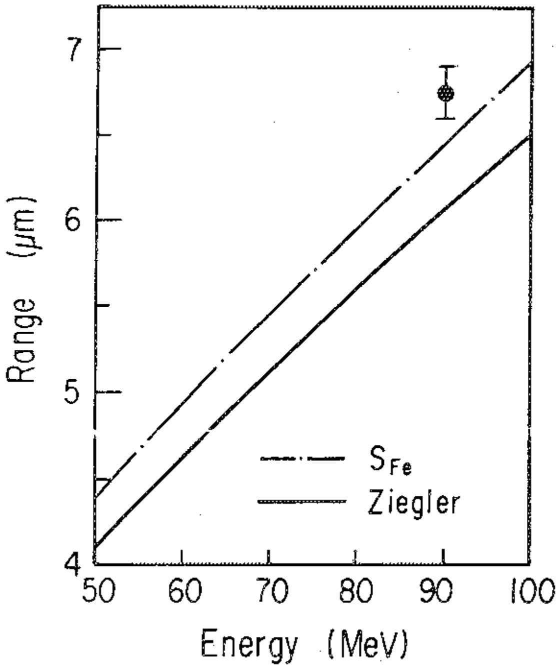

Fig. 2 Comparison of the measured(close circle) with the calculated(solid and dash line) in the mean projected range of Br-ion to iron.

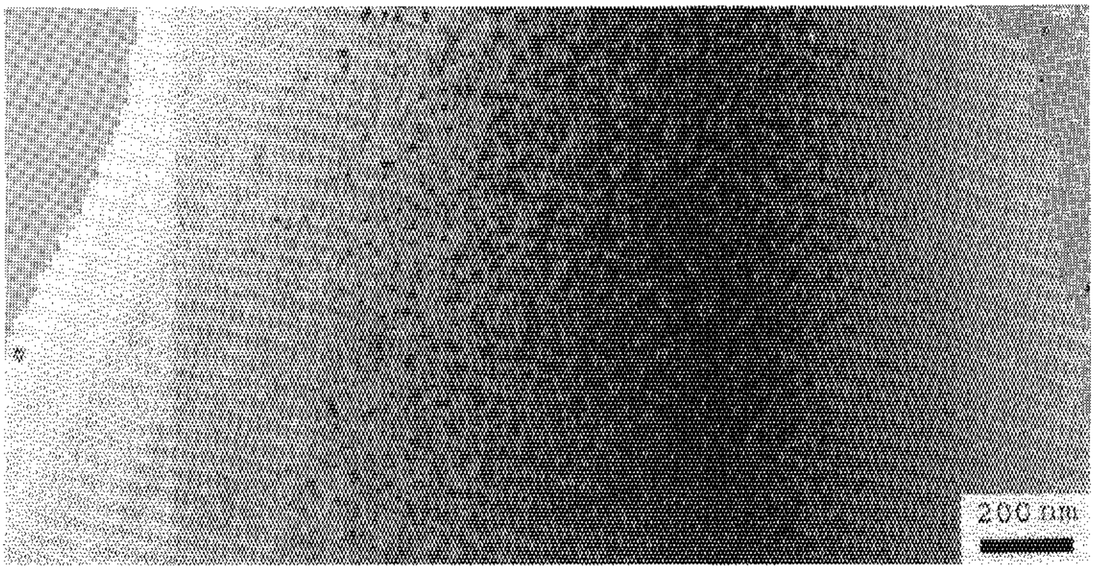

Fig.3 Microstructure of highly damaged region around the mean projected range.

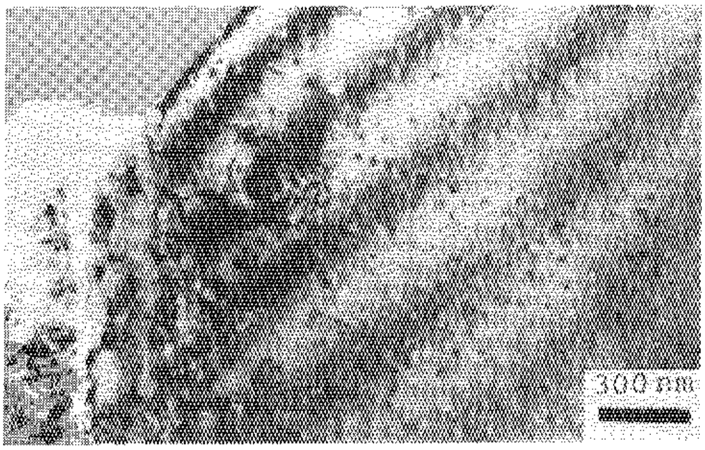

Fig.4 Defect clusters in the shallow region within the depth of about 1 μm.

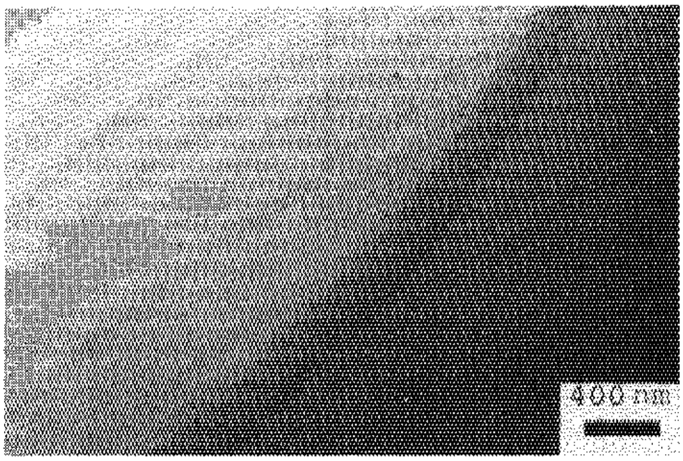

Fig.5 Defect clusters near the grain boundary within the range.

3.2 EFFECT OF INJECTED HELIUM ON MICROSTRUCTURE IN Ti-MODIFIED TYPE 316 STAINLESS STEELS IRRADIATED WITH HELIUM IONS

Kenji SUZUKI, Yoshio KATANO, Takeo ARUGA and Kensuke SHIRAISHI*

Department of Fuels and Materials Research and *Radioisotope and Nuclear Engineering School, JAERI

It has been reported that solute carbon affects the distribution of helium bubble and dislocation loop in Ti-modified Type 316 stainless steels containing high concentration of helium from microstructural observation of Ti-modified Type 316 stainless steel (PCA) irradiated with helium ions1). In the present report, the effect of injected helium on the distributions of precipitate and dislocation loops is investigated in PCA irradiated with helium ions to clarify the governing factor and mechanism for microstructure evolution.

The materials used in this study were Ti-modified Type 316 stainless steel1). All the samples of 3 mm diameter and 0.2 mm in thickness were solution annealed for 0.5 h at 1373 K in a vaccum of 1×10^{-4} Pa. Some samples were further aged for 24 h at 1023 K after the solution treament. The samples were irradiated for 1 h at 350 or 1023 K with 1.0 MeV He-ions using a 2MV Van de Graaff accelerator2) to a dose of 5×10^{19} He/m^2 at a current density of 2 mA/m^2. The injection produced a maximum helium concentration of 2×10^3 appm and displacement damage of 0.08 dpa. Calculation with the E-DEP-81 code3) shows that the injected helium is distributed in the range from 1.4 to 1.9 µm from the ion-incident surface of the specimen. Some samples irradiated at 350 K were annealed for 1 or 24 h at 1023 K in vacuum.

The microstructure of the PCA irradiated with He-ions at 1023 K is shown in Fig. 1 together with those for the unirradiated specimens which are solution annealed and given a thermal history similar to the irradiation. The dislocations are seen around the undissolved coarse TiC in the specimens after solution annealing for 0.5 h at 1373 K (Fig.1a). Fine TiC particles precipitate along the dislocations on additionally annealing for 1 h at 1023 K (Fig.1b). However, such precipitation could not be revealed in the specimen irradiated with He-ions for 1 h at 1023 K but helium bubbles are seen along the dislocation lines as well as in the matrix (Fig.1c). In Fig.2, the microstructure of the PCA, which are further aged for 24 h at 1023 K after solution treatment, irradiated with He-ions for 24 h at 1023 K is compared in Fig.2 with those for the specimens aged and given a thermal history similar to the irradiation. The size distribution of TiC particles precipitate along the dislocation in the specimens is presented in Fig.3. Since the distributibution curve of the irradiated sample is in agreement with that of the as-aged sample, TiC particle is not deduced to dissolve during the irradiation. The dominant factor governing the nucleation and growth of titanium carbide along the dislocation is considered to be diffusion of titanium atoms to the dislocation. When the dislocation line already has a carbon atmosphere, the precipitation of fine TiC particles along the dislocation is controlled by titanium diffusion through a vacancy mechanism. The available vacancies for titanium diffusion are reduced by helium atoms trapping the vacancies when the helium is injected into the matrix4). Thus, the helium injected into the PCA suppresses the nucleation and growth of titanium carbide along the dislocation.

The microstructure of PCA specimen annealed for 1 and 24 h at 1023 K after irradiation at 350 K is shown in Fig.4 along with that of the Type 316 stainless steel with boron injected with 3 MeV He-ions to a peak concentration of 1×10^3 appm and annealed for 24 h at 1023 K5). It is expected from the results obtained by the in-situ experiment using high voltage electron microscope that the interstitial loops are removed by absorption of vacancies during the anneal at 1023 K6,7). Nevertheless, many dislocation loops are observed with helium bubbles in the specimen annealed for 1 h at 1023 K after irradiation at 350 K (Fig.4a). Dislocation loops still remain in the matrix of the PCA and Type 316 stainless steel with boron after annealing for 24 h at 1023 K(Fig.4b and c). A high density of helium bubbles is formed along the loops8) and the recovery of the interstitial loops is, thus, strongly retarded by the presence of such helium bubbles along the loops; the vacancies diffusing to the loops are absorbed by the helium bubbles along the dislocation loops. Surprisingly, interstitial loops grew in helium-preinjected PCA during thermal annealing for 24 h at 1023 K(Fig.4b). The work on helium preinjected SA 316 by Mazey and coworkers9,10) revealed similar results. In summary, the observation indicates that the helium injection into the

PCA retards carbide precipitation along the dislocations during irradiation at 1023 K, and also stabilizes the dislocation loops during annealing at 1023 K after the irradiation at 350 K.

Reference

1) K. Suzuki. Y. Katano, T. Aruga, S. Hamada and K. Shiraishi: JAERI-M 85-104 (1985) 114.

2) K. Suzuki, Y. Katano, T. Aruga and K. Shiraishi: JAERI-M 84-181 (1984).

3) T. Aruga; JAERI-M 83-226 (1984) 1.

4) D.J. Reed: Radiat. Eff. 31(1977) 129.

5) K. Shiraishi, K. Fukaya and K. Fukai: J. Nucle. Mater. 119(1983) 268.

6) B.L. Eyre: J. Phys. F:Metal Phys. 3(1973) 442.

7) M. Kiritani and H. Takata: J. Nucle. Mater. 69&70(1978) 277.

8) A.I. Ryazanov, G.A. Arutyunova, V.A. Borodin, Yu. N. Sokursky and V.I. Chuev: J. Nucl. Mater. 110(1982) 65.

9) D.J. Mazey and S. Francis: AERE-R-7934(1975).

10) D.J. Mazey and R.S. Nelson: CONF-750989, Vol.1(1976).

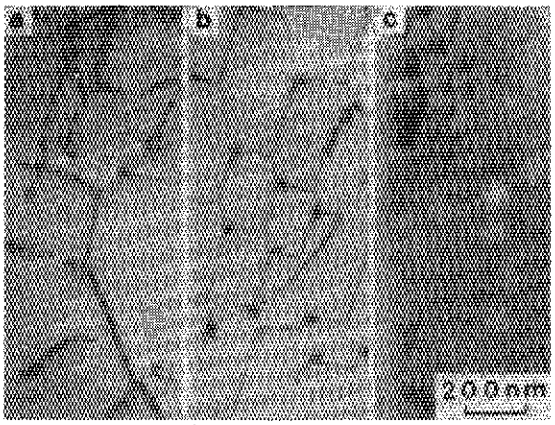

Fig. 1 Development of microstructure in the PCA; (a) as-annealed for 0.5 h at 1373 K, (b) unirradiated and annealed for 1 h at 1023 K, and (c) irradiated with 1.0MeV He-ions at 1023 K.

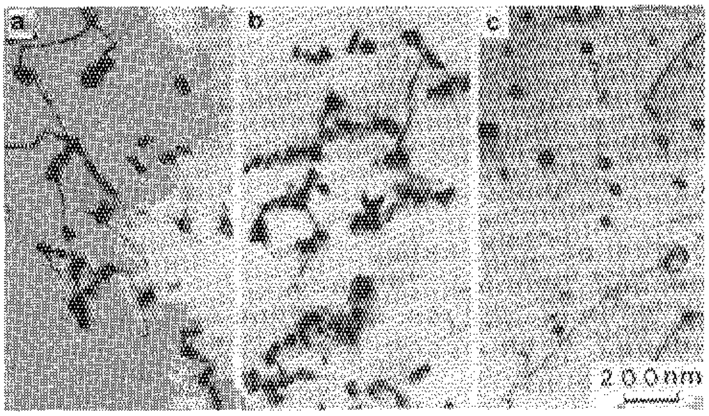

Fig. 2 Development of microstructure in the PCA; (a) as-annealed for 24 h at 1023 K, (b) unirradiated and annealed for 25 h at 1023 K, and (c) irradiated with 1.0 MeV He-ions at 1023 K.

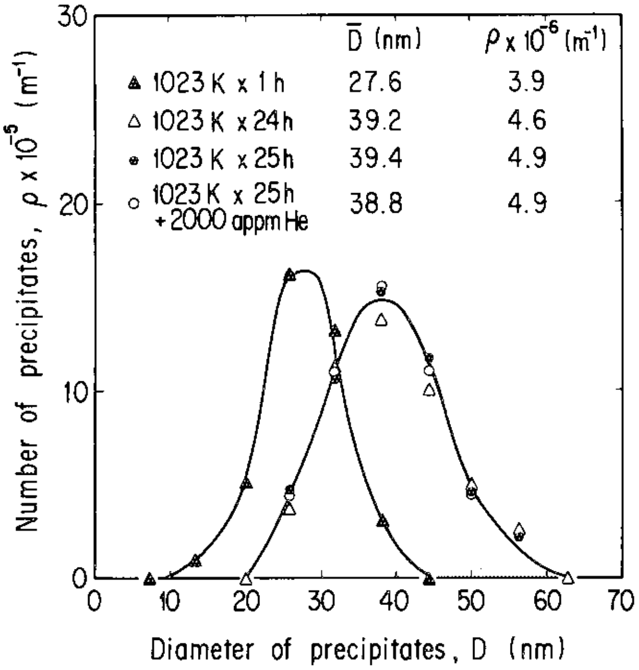

Fig. 3 Size distribution of TiC particles precipitate along the dislocation in the PCA under various condition.

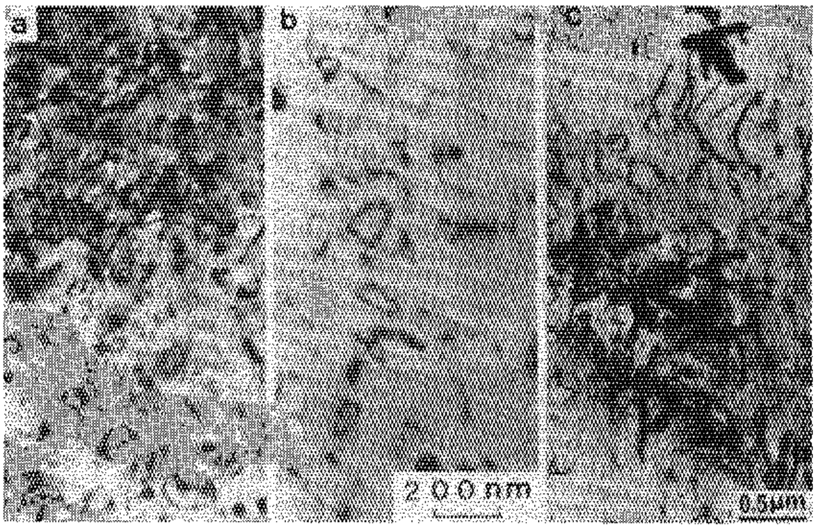

Fig. 4 Development of microstructure in the PCA annealed for 1 h (a) and annealed for 24 h (b), and in the Type 316 stainless steel with boron annealed for 24 h (c) at 1023 K.

3.3 MICROSTRUCTURE AND MECHANICAL PROPERTIES OF He IRRADIATED STAINLESS STEEL

T. Sawai, S. Hamada, A. Hishinuma, K. Miyahara*, N. Igata+ and Y. Hosoi*

Department of Fuels and Materials Research, JAERI, *Faculty of Engineering, Nagoya University, +Faculty of Engineering, University of Tokyo

Ductility loss and/or brittle fracture of Type 316 stainless steel due to the helium generated by fusion neutron is one of important problems in the development of fusion reactor materials. Helium implantation by accelerators can be used to simulate the helium effect on the mechanical property changes through the microstructural evolution. Helium concentration in the irradiated specimen is not uniform along the depth and peaks at the mean projected range with almost Gaussian distribution. Cross-section method for stainless steel developed by Hamada1) in JAERI is very advantageous for the transmission electron microscope(TEM) observation of this depth-dependent microstructure affected by helium and then applied to the foil tensile specimen of Type 316 stainless steel irradiated with 30 MeV He-ion.

Two small size tensile test specimens(100 μm thickness) of Type 316 stainless steel were set one upon another on a specimen holder at once, and irradiated with 30 MeV He-ion in the SF syclotron of University of Tokyo to 1.3×10^{17} ions/cm^2. The mean projected range of 30 MeV He in iron is calculated by the extended E-DEP-1 code2) to be 160 μm. Hereafter, we call the front specimen He through specimen and the back specimen He deposit specimen. One set of He through and He deposit specimen was annealed at 1023 K for 7.2×10^3 s in order to coarsen the He bubbles. Tensile tests are performed at room temperature and cross-sectional TEM specimens were prepared. Further detailes of experiment has been described elsewhere1,3).

The stress-strain curves of tensile tests for as-irradiated specimen(Fig. 1) showed that the flow stress increased but total elongation decreased with the He irradiation. Especially the decrement of the total elongation of the He deposit specimen is larger than that of the He through specimen. Figure 2 also shows the stress-strain curves of specimens which were annealed for 7.2×10^3 s at 1023 K after the irradiation. Same as the as-irradiated specimen, strength increased and ductility decreased with He irradiation. However, the ductility decrement of He deposit specimen is less than that of the as-irradiated specimen. Scanning electron microscope(SEM) observation of fracture surfaces revealed that intergranular fracture occurred only on the as-irradiated He deposit specimen while other specimens showed transgranular fracture.

Helium bubbles in He deposit specimens are shown in TEM micrographs(Figs. 3 and 4). The depth profiles of the bubble number density and the swelling in annealed specimen are given in Fig. 5 with the calculated He deposition profile(Fig.6). The microstructure of the as-irradiated He deposit specimen(Fig. 3) was changed through the annealing (Fig. 4). Figures 3 and 4 shows that He bubble diameter and bubble spacing in the matrix are smaller in the as-irradiated specimen than in the post-irradiation-annealed specimen. The as-irradiated He deposit specimen which have smaller bubble spacing(~50nm) than that of annealed He deposit specimen showed less elongation and intergranular fracture, which was in good accordance with the result of Bennetch and Jesser4) who discussed the fracture mode of 316 stainless steel with the bubble spacing.

References

1) S. Hamada: to be published in J. Nucl. Sci. & Tech.

2) I. Manning and G. P. Mueller: Comp. Phys. Comm. 7 (1974) 85.

3) N. Igata et al: to be published in J. Nucl. Mater.

4) J. I. Bennetch and W. A. Jesser: J. Nucl. Mater. 102 (1981) 809.

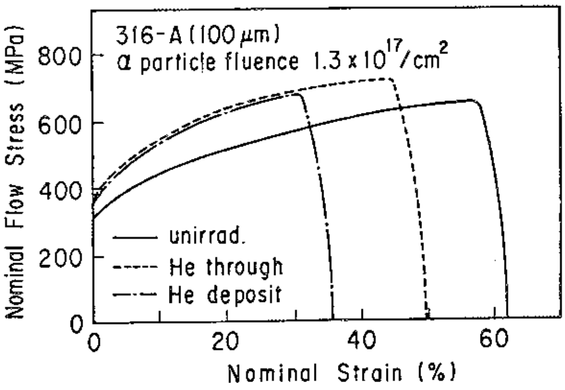

Fig.1 Stress-strain curves of as-irradiated specimen.

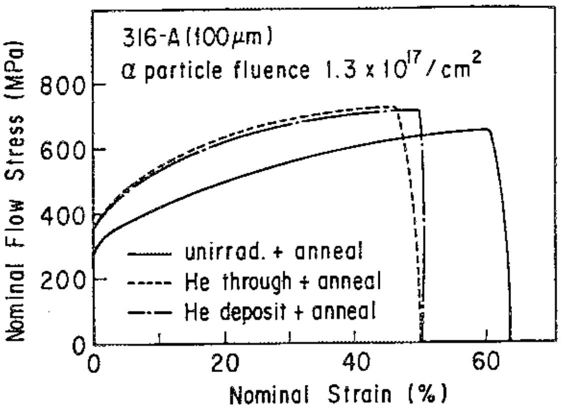

Fig.2 Stress-strain curves of irradiated and annealed specimen.

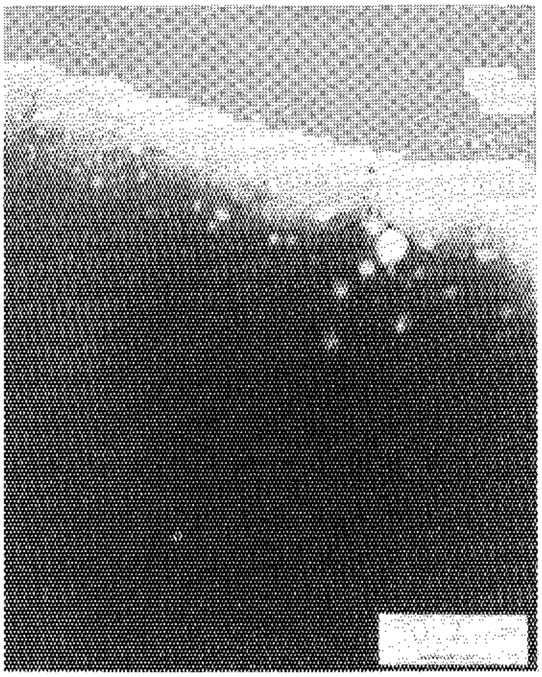

Fig.3 TEM micrograph of as-irradiated He deposit specimen.

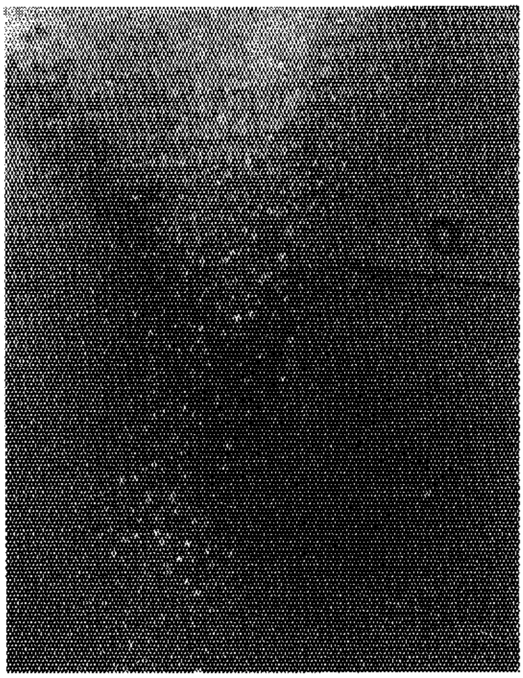

Fig.4 TEM micrograph of annealed He deposit specimen.

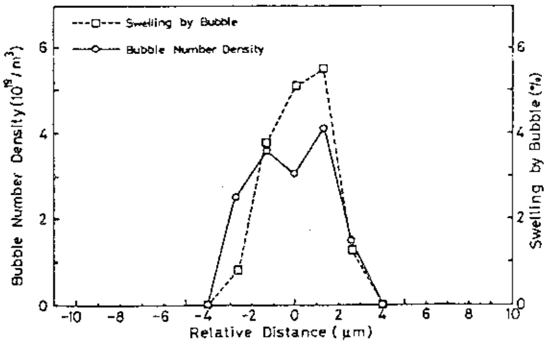

Fig.5 Depth profiles of the bubble number density and the swelling in annealed He deposit specimen.

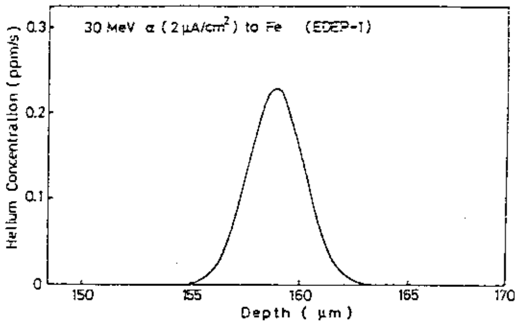

Fig.6 Implanted He concentration profile calculated by E-DEP-1 code.

3.4 EFFECT OF IMPLANTED-HELIUM DEPTH PROFILE ON DAMAGE STRUCTURE IN ELECTRON-IRRADIATED STAINLESS STEEL

Takeo ARUGA and Yoshio KATANO

Department of Fuels and Materials Research, JAERI

Helium bubbles in metals have been recognized to deteriorate the mechanical properties and induce the dimensional instability. It has been reported that the helium bubble formation in stainless steels is substantially affected by the solute segregation and the phase instability[1,2)], and that about a hundred appm of the cold implanted helium remarkably surppresses the cavity formation in the steel irradiated by nickel-ions at higher temperatures[3)]. Recently, much attention has been paid on the behaviors of helium implanted into metals to a high content at lower temperatures[4,5)], for the understanding of the mechanisms of helium bubble nucleation and growth under a displacement damage at both low and high temperatures.

In this report are described the results of in-situ cross sectional observation of the microstructural evolution in Type 316 stainless steel pre-injected by helium at ambient temperature and subsequently irradiated by electrons at a high temperature.

The 3.0 MeV He-ions were injected into the solution-annealed Type 316 stainless steel sample of 0.20 mm thickness using a Van de Graaf in JAERI at 433 K with a beam current of 10 mA/m^2 to a dose of $9 \times 10^{19}/m^2$. The injected sample was electroplated with nickel and specimens were prepared for the cross sectional observation of the damaged region by a transmission electron microscope. Then, the specimen was irradiated at 823 K with electrons in a JEM-1000D high voltage electron microscope operated at 1 MV. The irradiation flux was $4.0 \times 10^{23}/m^2.s$, which corresponds to a damage rate of 1.8×10^{-3}dpa/s for the steel. The irradiation was continued for 5 h to a dose of 32 dpa with an electron beam of about 5 μm in diameter. During the irradiation, changes in the microstructure were continuously observed and the depth-dependent analysis for defect clusters was performed.

Cross sectional microstructure produced in the Type 316 steel by 3.0 MeV He injection at 433 K is characterized by the defect clusters observed in black-dot contrasts with sizes of 2 to 5 nm and in depths from 4.6 to 5.5 μm from the He incident surface. The calculational results by TRIM85 computer code[6)] for the present 3 MeV He-ions on the steel give a peak depth of the projected range to be between 5.0 and 5.1 μm, as presented in Fig. 1. The peak helium content and displacement damage by the injection are predicted to be about 3000 appm and 0.2 dpa, respectively. The defect cluster densities measured in each 0.1 μm depth increment increase gradually with an increase in depth from 4.6 to 5.1 μm, beyond there, the density decreases sharply to zero, as shown in Fig. 1. As a result, the depth profile of the defect cluster density, which is asymmetric around the ion-rage and observed only within a limited depth region of 4.6–5.5 μm, is in fairly good agreement with the predicted range distribution, not with the displacement damage depth profile which is predicted to give one-tenth of the peak damage at depths of 3-4 μm. The fact indicates that the defect clusters observed in the sample implanted with helium at 433 K would nucleate through the formation of agglomerates of heliums and point defects produced by the injection.

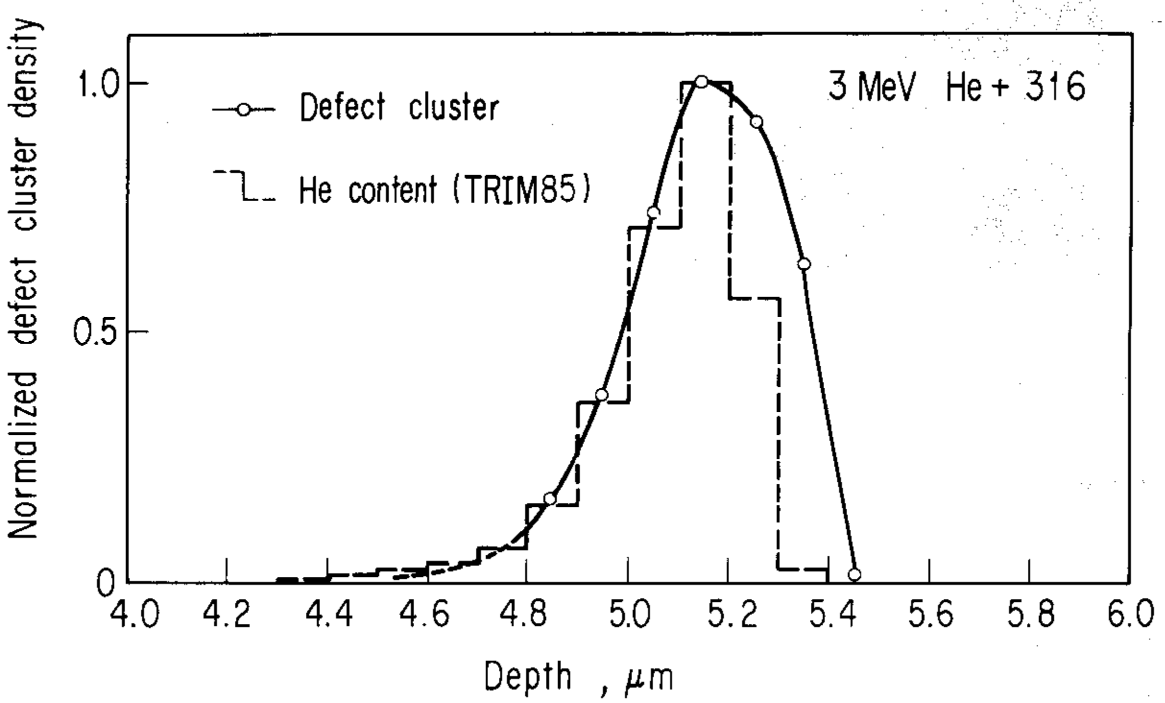

Fig. 1 Depth profile of the defect cluster density in Type 316 stainless steel injected with 3.0 MeV He-ions to 9 x $10^{19}/m^2$ at 433 K, compared with the ion-range distribution for 3.0 MeV He-ions calculated by TRIM85 computer code.

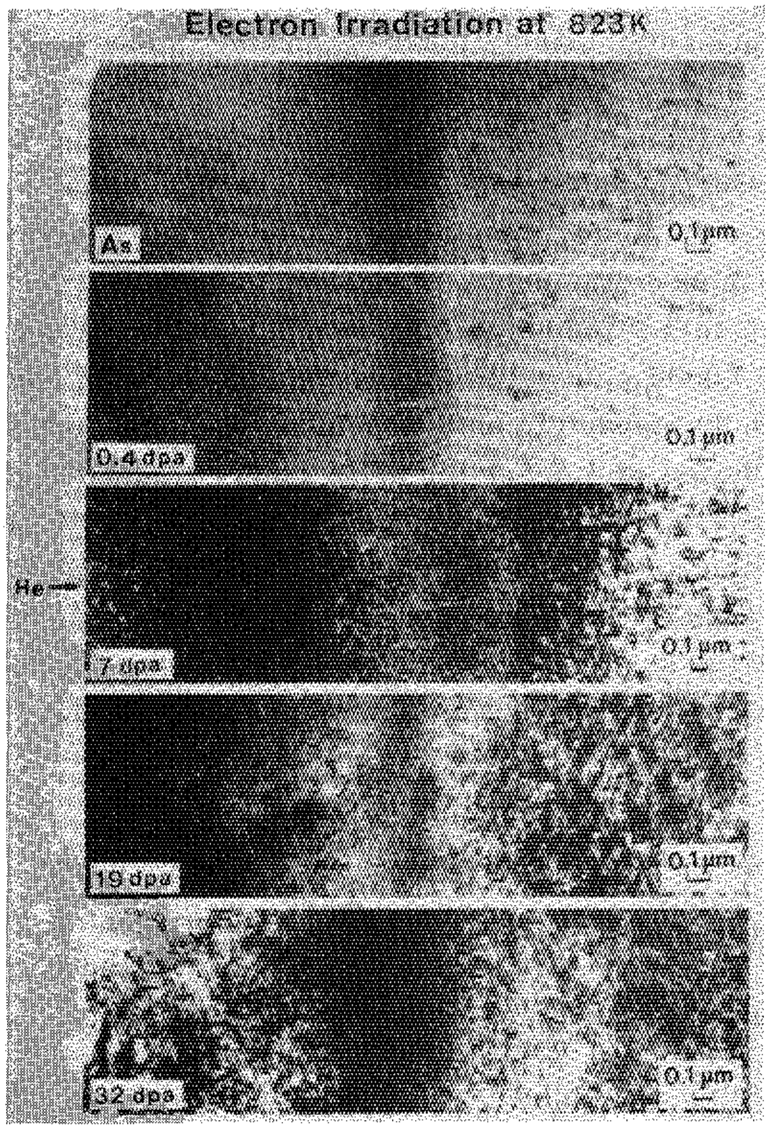

Fig. 2 Cross sectional microstructure produced in Type 316 stainless steel pre-injected with 3.0 MeV He-ions to 9 x $10^{19}/m^2$ at 433 K and then irradiated with 1.0 MeV electrons at 823 K to 32 dpa.

Typical microstructures produced in He-injected sample by 1 MeV electron irradiation at 823 K up to 32 dpa are shown in Fig. 2. For doses to 0.4 dpa, the size of the black dots which were observed in the as-injected sample, is seen to increase slightly while the density decreases a little. Furthermore, the evolution of damage structure under the electron irradiation is considerably sluggish even in the region more distant from the ion-range than a few micrometers, compared with that in the un-injected sample. When the irradiation proceeds from 7 to 19 dpa, it is noticed that two regions with a lower dislocation density than that of the surrounding regions appear; both are in band pararell to the ion-incident surface and one is in the front and the other is in the rear of the ion-range, as shown in Fig. 2. The width of the band for the front side is larger to be about 0.7 μm than 0.3 μm for the rear side of the ion-range. This asymmetry in the band width of low dislocation density region appears to be well correlated with that noticed in the depth profile of the predicted distribution for the ion-range (Fig. 1). It seems, therefore, that the presence of helium in the steel with a certain level of concentration may suppress the development of the dislocation structure under the electron irradiation at 823 K. In the present study, the helium content for the region of lower dislocation density is estimated to be about 200-300 appm, with no helium diffusion assumed during the pre-injection and the electron irradiation.

For the prolonged irradiation to 32 dpa, the band structure of lower dislocation density becomes blurred, but the highly tangled dislocation network could be observed widely around the ion-range. It should be noted that the formation of visible cavity is completely suppressed up to 32 dpa over the whole electron-irradiated area, which is in marked contrast with the highly swollen Type 316 steel sample with the same heat but without He pre-injection; 8 % of the void swelling was observed at 30 dpa in the uninjected sample irradiated with electrons at 823 K with an average void diameter and a void density to be 80 nm and $2\text{x}10^{20}/\text{m}^3$, respectively. The inhibition of visible cavity formation observed in the pre-injected sample is considered to be due mainly to an enhanced anihilation of radiation-induced point defects at the sites of submicroscopic helium-point defect complexes which would be formed over the electron-irradiated area by helium atoms diffused under the irradiation at 823 K.

References

1) T. Aruga, Y. Katano and K. Shiraishi: J. Nucl. Mater. 122&123 (1984)1401.
2) P. J. Maziasz: J. Nucl. Mater. 122&123 (1984) 236.
3) E. A. Kenik: J. Nucl. Mater. 122&123 (1984) 659.
4) H. Van Swygenhoven, G. Knuyt and L. M. Stals: J. Nucl. Mater. 127 (1985) 97.
5) Z. H. Luklinska and P. J. Goodhew: J Nucl. Mater. 135 (1985) 201.
6) J. F. Ziegler, J. P. Biersack and U. Littmark: Stoppings and Ranges of Ions in Matter vol. 1 (ed., Ziegler, Pergamon, New York, 1985).

3.5 CONDUCTIVITIES OF A Li_2O SINGLE CRYSTAL IRRADIATED BY OXYGEN IONS

Kenji NODA, Yoshinobu ISHII, Hisayuki MATSUI*,
Mikio HORIKI*, Satoshi SUZUKI*, Naomi OBATA*
and Hitoshi WATANABE

Department of Fuels and Materials Research, JAERI, *Faculty
of Engineering, Nagoya University

1. Introduction

During operation of fusion reactors, a huge number of irradiation defects will be introduced in Li_2O as a tritium breeding blanket material by fast neutrons with energies up to 14 MeV, tritons (2.7 MeV) and helium ions (2.1 MeV) produced by $^6Li(n,\alpha)^3H$ reactions. The irradiation defects will induce swelling and change of properties such as ion and thermal conductivities etc.

Li_2O irradiated by thermal neutrons and oxygen ions has been investigated by electron spin resonance (ESR) and optical absorption methods to study the behavior of individual irradiation defects 1-5). However, studying the behavior of irradiation defects as a whole is also necessary to complement the above mentioned studies.

Recently, the ion conductivity of Li_2O was investigated in the temperature range from 570 to 1420 K, to evaluate the self diffusion of Li 6,7). In the studies the self diffusion of Li was found to be associated with the tritium diffusion.

In this experiment the preliminary "in-situ" measurement of ion conductivity of Li_2O irradiated with oxygen ions was done to establish an experimental method for studies of the whole behavior of irradiation defects and the irradiation effect on the diffusion process.

2. Experimental

The specimen used was a thin plate of Li_2O single crystal (4x3x0.3 mm). The specimen was annealed at 1270 K for 5 h in vacuum better than 1×10^{-3} Pa to eliminate OH^- ions in the specimen, and then it was mounted on the specimen holder for the measurement of ion conductivity, which was attached in the irradiation chamber having an infrared imaging furnace.

By using a tandem accelerator at JAERI, the specimen was irradiated to

2.4×10^{19} ions/m^2 by oxygen ions with a energy of 100 MeV. The measurements of ion conductivity were conducted "in-situ" in the irradiation chamber not only before and after the irradiation but also at the times when the ion irradiation was sometimes interrupted during the irradiation. The conductivity was determined by measuring the complex impedance in the range from 1 to 100 kHz with two-terminal AC method using YHP Model 4192 A.

Li_2O absorbs easily OH^- ions during the handling in the air, and the OH^- ions have a large influence on the ion conductivity$^{6)}$. Therefore, the "in-situ" measurement is essentially important to measure the conductivity without the influence of OH^- ions absorbing after the irradiation.

3. Results and discussion

Impedance of the Li_2O specimen before the irradiation was measured in the temperature range from 390 to 470 K, after the specimen was annealed at 470 K for about 3 h in vacuum of the irradiation chamber (better than 1×10^{-4} Pa). Fig. 1 shows the complex impedance plot of the Li_2O specimen at 470 K from 1 to 50 kHz as a typical example of them measured in the temperature range from 390 to 470 K before the irradiation. The bulk resistance is identified from the intersecting point of a semicircular with real axis (abscissa of Fig. 1). In the measurements of this study, the bulk resistances were determined by drawing a semicircle fitted with the data in an extrapolating manner, as shown in Fig. 1.

Fig. 2 shows the relationship between the conductivity σ multiplied by temperature T and the inverse of temperature 1/T for the Li_2O single crystal specimen in the temperature range from 390 to 470 K before irradiation. The measurements of the conductivity in the temperature range were conducted twice (i.e., the first and the second runs). The values of the second run were smaller than those of the first run. This implies that the contribution of OH^- ions in the specimen for the ion conductivity lowered by the decrease of OH^- ions due to the heating during the first run. So, it was seen that the specimen measured had some content of OH^- ions.

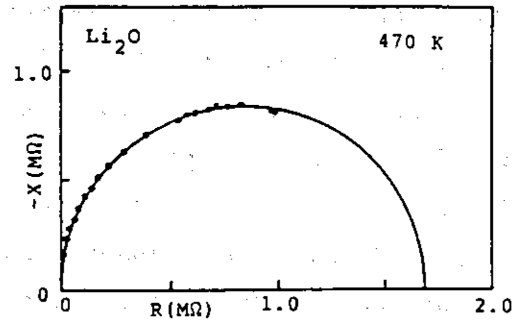

Fig.1 Complex impedance plot for Li_2O at 470 K.

A broken and a dotted lines in Fig. 2 show the σT-1/T relationships extrapolated from the previous data obtained above 720 K for as-received Li_2O single crystals and those in which OH^- ions were almost completely eliminated by heating-up to 1070 K in dry argon atmosphere⁶⁾. The present data σT were in fairly good agreement with the extrapolated data for as-received Li_2O single crystals. This is consistent with the fact that the specimen contained some content of OH^- ions, since the as-received specimen had some content of OH^- ions.

The present data in Fig. 2 lay on the lines expressed by $\sigma T = A\exp(-E/KT)$. From the gradient of the lines, the activation energy E could be determined to be about 60 kJ/mol in the present study. On the other hand, the activation energies of both extrapolated relationships (the broken and dotted lines) were about 50 kJ/mol. Thus, the value obtained in the present study was also similar to that of the previous works⁶,⁷⁾.

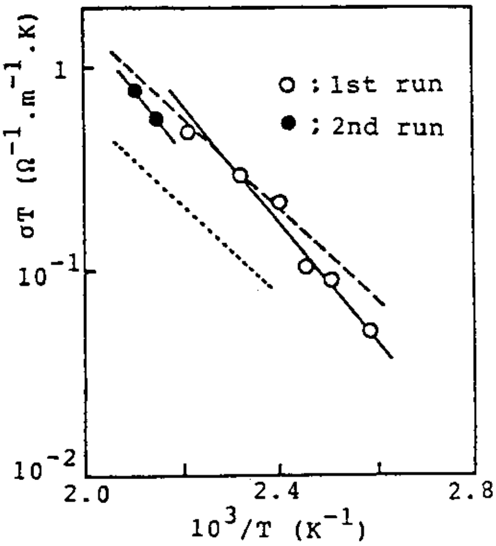

Fig.2 Temperature dependence of conductivity of Li_2O. Broken and dotted lines were extrapolated from data by Ohno et al. for as-received and well-annealed Li_2O crystals, respectively.

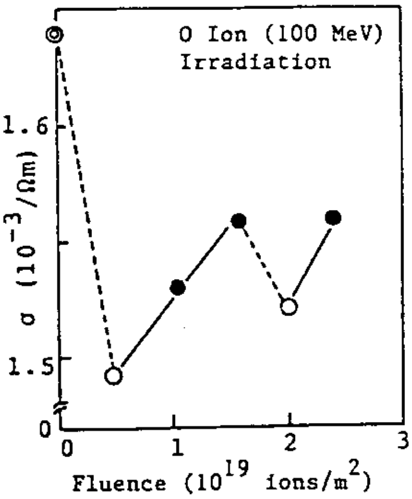

Fig.3 Irradiation effect on ion conductivity at 470 K. Irradiation Temperature, ○; 310-370 K, ●; 420 K.

Fig. 3 shows a relationship between the conductivity at 470 K and the oxygen-ion fluence. The conductivity increased in the irradiation periods shown by full lines (i.e., $0.5\text{-}1.5\times10^{19}$ ions/m^2, $2.0\text{-}2.4\times10^{19}$ ions/m^2), where the specimen was irradiated at 420 K and the conductivity indicated by closed circles was measured at 470 K after heating-up for about 20 min. On the contrary, the conductivity decreased in the period shown by broken lines (i.e., $0\text{-}0.5\times10^{19}$ ions/m^2, $1.5\text{-}2.0\times10^{19}$ ions/m2), where the irradiation temperature was in the range from 310 to 370 K and the conductivity indicated by open circles was measured at 470 K after the heating-up for about 1h. Thus, the behavior of ion conductivity during irradiation was quite different in the above two kinds of irradiation temperature and heating-up mode. This complicated behavior of conductivity may be due to decrease of contribution of OH^- ions in the specimen for the conductivity during the heating-up. In case of the data indicated by open circles the increment of the conductivity arising from the irradiation effect such as irradiation damages and implanted oxygen ions seemed to be smaller than the decrement due to the decrease of OH^- ions during the heating-up for the measurement. On the other hand, the increment was considered to be larger than the decrement in the case of the data indicated by closed circles.

In this study, it could be found that the ion conductivity of Li_2O was raised by the oxygen ion irradiation, but the evaluation and analysis of the the conductivity change in terms of irradiation defects and mobility (diffusion) of atoms could not be done. To investigate the behavior of irradiation defects and the irradiation effect on diffusion, further experiments will be conducted using a new specimen stage for measuring the ion conductivity, which will be attached a powerful heater to eliminate completely the residual OH^- ions in the specimen before irradiation.

References

1) K. Uchida, K. Noda, T. Tanifuji, S. Nasu, T. Kirihara and A. Kikuchi: phys. Status Solidi (a) 58 (1980) 557.
2) K. Noda, K. Uchida, T. Tanifuji and S. Nasu: J. Nucl. Mater. 91 (1980) 234.
3) K. Noda, K. Uchida, T. Tanifuji and S. Nasu: Phys. Rev. B 24 (1981) 3736.
4) K. Noda, T. Tanifuji, Y. Ishii, H. Matsui, N. Masaki, S. Nasu and H. Watanabe: J. Nucl. Mater. 122 & 123 (1984) 908.
5) K. Noda, Y. Ishii, H. Matsui and H. Watanabe: J. Nucl. Mater. 133 & 134 (1985) 205.
6) H. Ohno, S. Konishi, K. Noda, H. Takeshita, H. Yoshida, H. Watanabe and T. Matsuo: J. Nucl. Mater. 118 (1983) 242.
7) H. Ohno, S. Konishi, T. Nagasaki, T. Kurasawa and H. Watanabe: J. Nucl. Mater. 133 & 134 (1985) 181.

3.6 MICROSTRUCTURE OF ION-IRRADIATED Si_3N_4

Kenji NODA, Yoshinobu ISHII, Kotaro KURODA*,
Hiroyasu, SAKA*, Masayuki ARITA*, Masaya, HASHIMOTO*,
Toru, IMURA* and Hitoshi WATANABE

Department of Fuels and Materials Research, JAERI,
*Faculty of Engineering, Nagoya University

Use of refractory low-Z ceramic materials at the surface of the first wall in fusion reactors is necessary to decrease influences of plasma contamination due to the material of the first wall. Such materials will be subjected to not only surface erosion but also irradiation damage due to 14 MeV neutrons. In this study, microstructures of ion-irradiated Si_3N_4 were observed by a transmission electron microscope (TEM), to understand the irradiation damage in Si_3N_4 as one of the candidate of the low-Z materials for fusion reactors.

The specimens used were sintered β-Si_3N_4 including 8%-Y_2O_3 as a binder and single crystalline α-Si_3N_4 whiskers. The sintered Si_3N_4 was thinned by ion beam milling, to make TEM specimens. The TEM specimens of sintered β-Si_3N_4 and the single crystalline α-Si_3N_4 whiskers were irradiated with Ar (400 keV) or Cl(150 MeV) ions using 2 MeV VDG or a tandem accelerator at JAERI. Before and after the irradiation, microstructures of the specimens were observed with 200 kV TEM.

Before irradiation, the sintered β-Si_3N_4 specimens consisted of β-Si_3N_4 grains and other phases precipitated among the grains (($Y_{10}(SiO_4)_6N_2$ and WC phases etc.), and all of them were crystalline. Fig. 1 shows microstructure of a β-Si_3N_4 grain in the sintered specimen irradiated to 2.2×10^{21} ions/m^2 by Ar ions with an energy of 400 keV. Many small spots due to strain were observed in the crystalline β-Si_3N_4 grain. High resolution micrograph of the β-Si_3N_4 grain is shown in Fig. 2, and it reveals some localized disorder regions (surrounded by circles in Fig. 2) in the lattice image. The localized disorder regions corresponded to the spots observed in Fig. 1. In such disorder regions, crystalline-to-amorphous transformation was considered to occur locally by the Ar-ion irradiation. On the other hand, most phases other than β-Si_3N_4 crystalline grains were

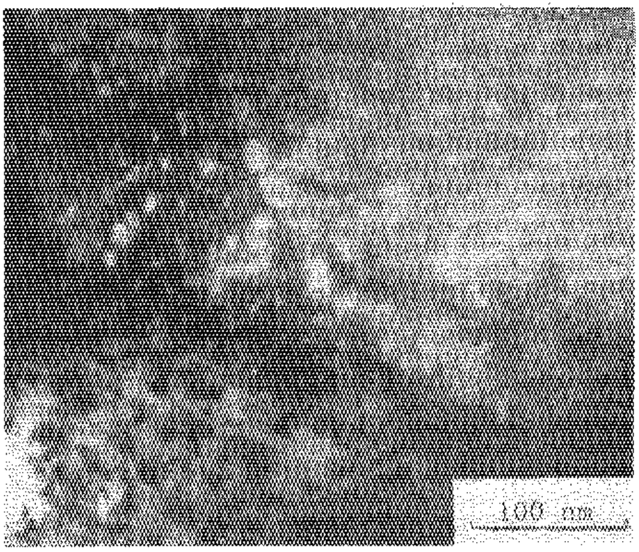

Fig.1 A micrograph of a sintered β-Si_3N_4 irradiated to $2.2x10^{21}$ ions/m^2 by Ar ions with an energy of 400 keV.

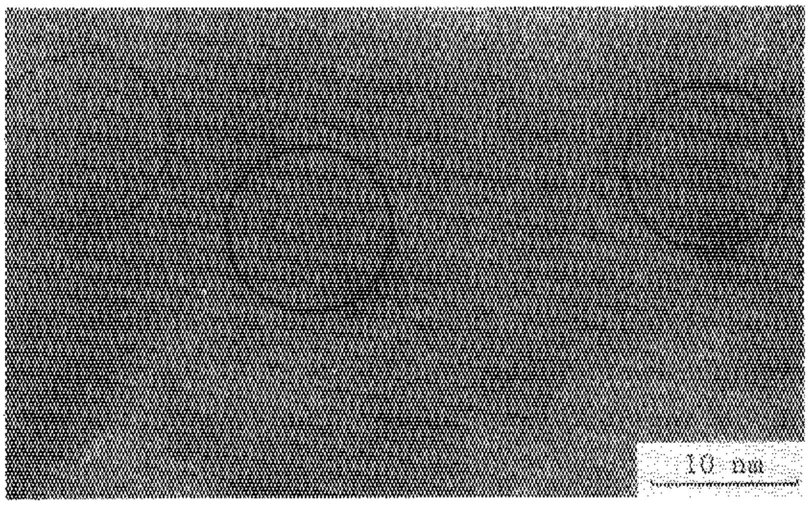

Fig.2 A high resolution micrograph showing local disorder in a β-Si_3N_4 crystalline grain.

observed to change entirely into amorphous state at the same Ar ion fluence and many voids were found in them, as reported previously$^{1)}$.

Fig. 3 shows electron micrographes of a single crystalline α-Si_3N_4 whisker and the electron diffraction patterns before and after Ar ion irradiation. The irradiation energy and the fluence were 400 keV and 2.2×10^{21} ions/m^2, respectively. Before the irradiation, many grown-in defects in the whisker and the diffraction spots were observed, and these shows that the whisker was crystalline. On the other hand, the micrograph and the diffraction halos after the irradiation reveal that the whisker has been entirely transformed into the amorphous state by the irradiation. Thus, the single crystalline α-Si_3N_4 whisker was easily damaged by Ar ion irradiation, in comparison with the β-Si_3N_4 crystalline grains. So, the difference in resistance for irradiation damage may be assumed to be attributed to the difference of phases. However, further systematic and detailed studies are required to know the origin of the difference in resistance for the irradiation damage.

Fig. 4 shows a microstructure of sintered β-Si_3N_4 irradiated to 6.5×10^{17} ions/m^2 by Cl ions with an energy of 150 MeV. In case of the Cl-ion irradiation at 150 MeV, the electronic stopping power is very large in the thin specimens for TEM observation but the nuclear stopping power is negligibly small, in contrast with the case of Ar-ion irradiation at 400 keV. Therefore, the effect of high electronic excitation such as formation of tracks was expected to occur rather than formation of displacement damages due to elastic collision. However, neither displacement damage (including transformation into amorphous state and formation of voids etc.) nor track was observed, as shown in Fig. 4. The magnitude of electronic excitation depends on mass and energy of incident ions, and they have a large influence on formation of tracks$^{2)}$. To investigate the effect of electronic excitation on formation of tracks in Si_3N_4, further experiments using some kinds of incident ions heavier than Cl ions are now planning.

References

1) K. Noda, Y. Ishii, K. Kuroda, H. Saka, Y. Nakata, M. Arita, T. Imura and H. Watanabe: "JAERI TANDEM, LINAC & V.D.G. Annual Report 1984" p. 81.
2) S. Furuno, K. Izui and Y. Komaki: JAERI-M 85-125 (1985) p. 165.

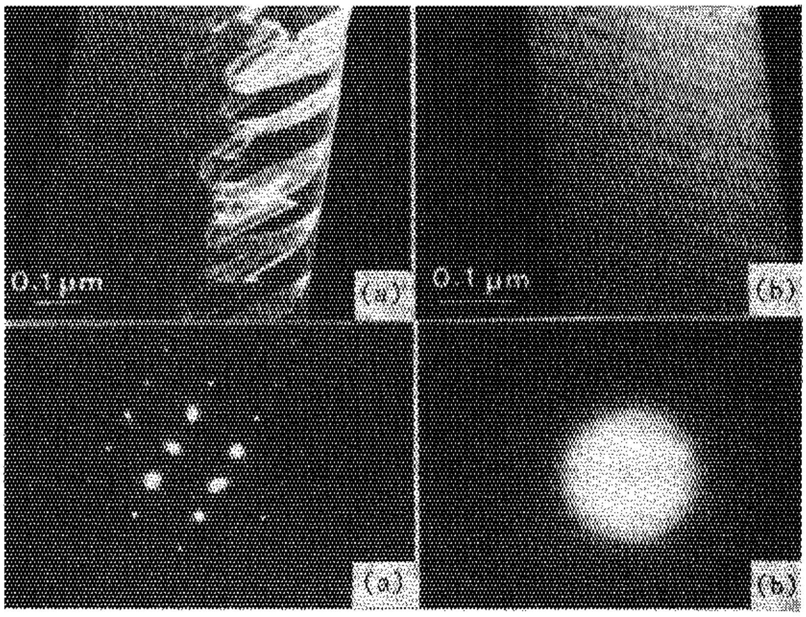

Fig.3 Microstructures of a single crystalline α-Si_3N_4 whisker and the electron diffraction patterns before (a) and after (b) Ar-ion irradiation.

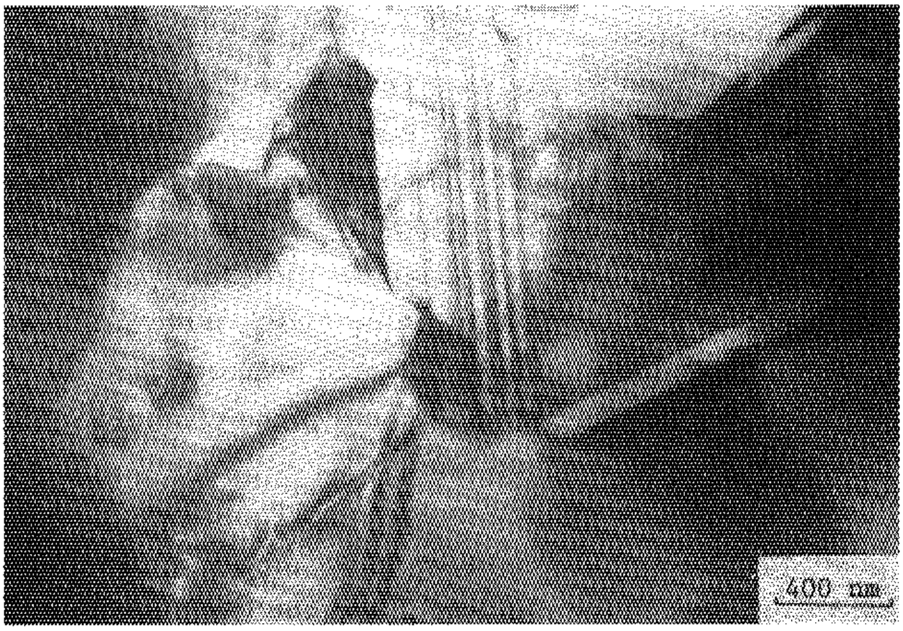

Fig.4 A microstructure of a sintered β-Si_3N_4 irradiated to 6.5×10^{17} ions/m^2 by Cl ions with an energy of 150 MeV.

3.7 IRRADIATION EFFECT ON SOME CERAMICS

Hideo OHNO,Yoshio KATANO and Hiroji KATSUTA

Function Materials Laboratory,Department of Fuels and
Materials Research, JAERI

Ceramics such as Al_2O_3,$MgAl_2O_4$, BeO and Si_3N_4 have increased importance in fusion power reactors. The ceramics for radiofrequency heating windows and neutral beam injector insulators require high quality in electrical , mechanical and radiation resistant property.

Partially stabilized zirconia(PSZ) with MgO or Y_2O_3 has been attracted special attention primarily because of its high strength and high resistance to fracture. The fracture toughness of PSZ is believed to originate from stress induced transformation of tetragonal ZrO_2 to monoclinic phase. However, the fracture toughness of PSZ has been reported to be greatly decreased by annealing related to the tetragonal to monoclinic phase transformation. Ions and neutron irradiation also affect the phase stability.

In this work, the phase stability of PSZ with 1 MeV O^+ ion was studied. Raman spectroscopy has been mainly used to analyze the phase stability of PSZ. Fig.1 shows the Raman spectra of non-irradiated PSZ aged at 573K and 673K for up to 148h in air. All of the observed peaks for starting material fit to tetragonal structure. After aging, typical peaks for monoclinic phase at 180-190 cm^{-1} and 385 cm^{-1} were observed in annealed specimens. The peaks of monoclinic phase become larger with aging time. However, neutron diffraction on the same samples with Raman spectra measurements has no noticeable phase change. The results indicates that the phase change of PSZ at these temperatures occurs only at surface area.

Fig.2(a) shows the preliminary analysis of Raman spectra for the specimen which was irradiated to 1.9×10^{20} ions/m^2 at an ambient temperature by O^+ ions with an energy of 1 MeV. Fig.2(b) shows the Raman spectra of non-irradiated part for the same specimen as Fig.2(a). These results indicate the tetragonal phase trnsform to monoclinic one with ion-irradiation. The analyssi of microstructures with TEM are now underway.

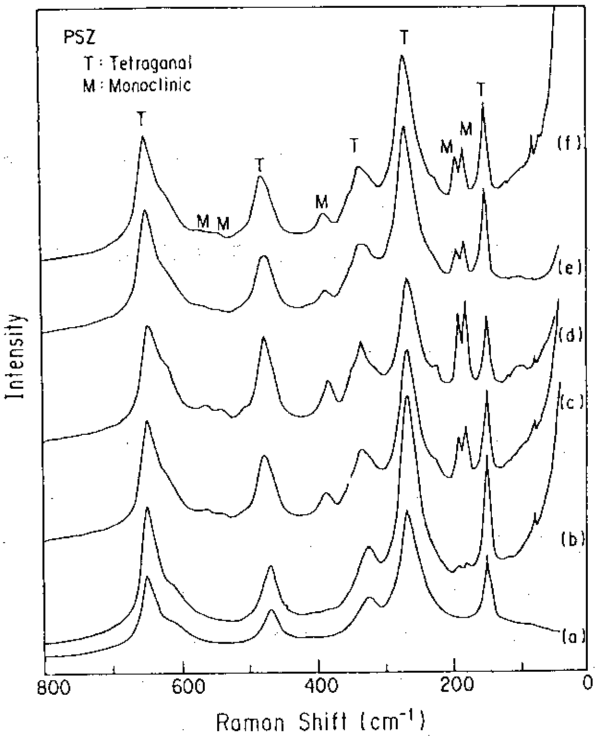

Fig.1 Raman spectra of PSZ with different annealing temperature and time. (a) as received, (b) 473 K-26 h, (c) 473 K-74 h, (d) 473 K-147 h, (e) 523 K-30 h, and (f) 523 K-51 h.

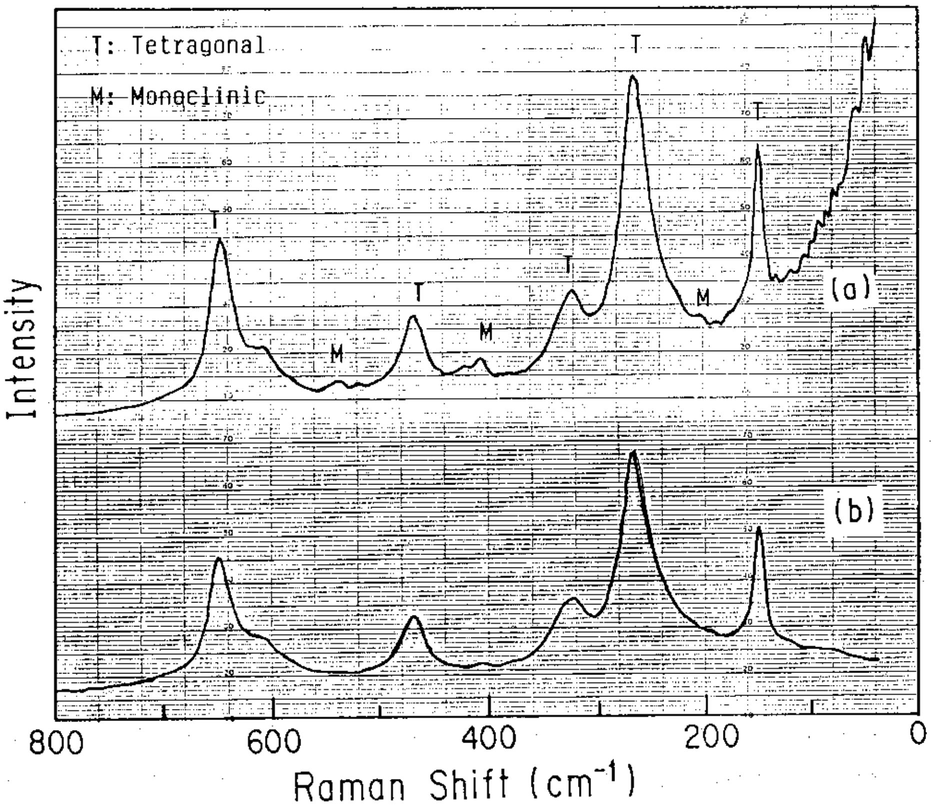

Fig.2 Raman spectra of PSZ with O^+ ion irradiation
(a) O^+ ion irradiation: 1.9×10^{20} ions/m^2 at an ambient temperature. (b) as received.

3.8 CHEMICAL REACTIONS INDUCED BY ENERGETIC PARTICLES

Takeshi SOGA, Katsutoshi FURUKAWA and Shin-ichi OHNO

Department of Chemistry

Recent results in atomic collision physics studies$^{1)}$ suggest that slow-moving particle collisions (in the energy range of 10 to 1000 keV) may result in such primary processes as inner shell or multiple excitations of an atom or molecule, which would involve an energy transfer per event much larger than outer shell or single excitations. Thus, low-energy particle collisions may induce chemical reactions different from those induced by γ-irradiations. At still lower impact energies (keV region), elastic collisions leading to atomic displacements are more and more frequent$^{2)}$. The energy transferred from incident ions to atomic constituents is often so high compared to the binding energy for a molecular and crystalline structure that a chemical reaction may take place in the solid.
The objectives of the present work are (1) to find a chemical consequence of a highly inelastic collision in solid iron(II) complexes and (2) to clarify the relative importance of electronic and atomic displacement excitations in chemical reactions in potassium nitrate.

1. An EPR Study of Highly Inelastic Processes in Potassium Hexacyanoferrate(II).

Single crystals of potassium hexacyanoferrate(II) trihydrate were irradiated in vacuum (ca. 10^{-5} Pa) with energetic ion beams or γ-rays. Ions in the energy range of 0.4 to 2 MeV were from a Van de Graaf accelerator. Ions with lower energies were from a small accelerater$^{4)}$. Potassium hexacyanoferrate(II) trihydrate, a low spin Fe(II) complex, is a diamagnetic compound and shows no EPR signals. On exposure to a beam of 1.8 MeV Ar^+ or 450 keV Ar^+ ion, the sample was decomposed to give EPR absorption spectra. (In Fig. 1) The central absorption at g=2.0 has previously been ascribed as due to the formation of cluster of Fe^{3+} ions coupled by a strong exchange interaction$^{6)}$. The signal intensities of this absorption grows linearly with irradiation time, the linewidths ranging from 100 to 300 G. Irradiation of the sample with 40 or 20 keV Ar^+

ions and with 0.4 or 1.6 MeV H^+ ions produced no remarkable EPR signals. γ-irradiations at room temperature at doses below 10^9 rad were found to produce a line due to isolated Fe^{3+} ions at g=4.3 alone. Further irradiations with γ-rays up to 10^{10} rad produced a single absorption line at g=2.0 of the linewidth 5G at room temperature. This spectrum remained unchanged when treated at temperatures below 100 °C for an hour or so. When treated at temperatures above 150 °C, however, it disappeared to produce a strong absorption at g=2.0 with a large width as is shown in Fig. 2. We may conclude that collisions between Ar^+ ions and Fe(II) in the energy range of 0.4 to 2 MeV will be highly inelastic due to inner shell or multiple excitation , they may lead to a violent destruction of the complex, as has been discussed by Stocklin in the case of biological compounds[3) , and that Fe^{3+} cluster are formed as the result of such collisions. Irradiations with γ-rays , protons, or helium ions alone did not induce this reaction, nor did a thermal activation.

2. Chemical Effectiveness of Elastic and Inelastic Collisions in the Decomposition of Potassium Nitrate[7-9).

The potassium nitrate, pressed into a disk of the diameter of 10 mm, was irradiated at ambient temperature in vacuum (ca. 10^{-5} Pa) with energetic ions. The concentration of nitrite ions produced was determined spectrophotometrically. The yields of nitrite ion are plotted as a function of incident ion dose. From the initial slope of the curves, the yields (G-value) for the formation of nitrite ion per 100 eV of the energy absorbed may be calculated. The results are included in Table 1, together with $G(NO_2^-)$'s reported in the literature for other radiation sources. On the other hand, we have calculated the electronic (S_e) and nuclear (S_n) stopping power of KNO_3 for these 100 keV ions according to the LSS theory. The ratio S_e/S_n gives a relative amount of electronic and nuclear (elastic) energy deposition. Some relevant value of $S_e/(S_e + S_n)$ are included in Table 2. There may be seen a correlation between $G(NO_2^-)$ value and $S_e/(S_e + S_n)$ value. It should be remembered that ionizing radiations, e.g.α, β and γ-rays and protons, lose most of their energy by electronic excitations. Thus, it may be concluded that the energetic ion induced decomposition of nitrate leading to the formation of nitrite is mainly through electronic excitations.

Table 1. Comparison of G(NO_2^-) from KNO_3 obtained by various radiations.

a) 100 kev

D^+, D_2^+, D_3^+	He^+	N_2^+	O^+, O_2^+
1.8±0.2	1.8±0.2	0.5±0.1	0.5±0.2

b) 1 MeV N^+ 2.0±0.3

c) Literature value

10 keV He^+	3.4 MeV α	1.5 MeV e^-	^{60}Co γ
1.54	2.2	1.48	1.46

Table 2. Some values of $S_e/(S_e + S_n)$ for the ions traversing KNO_3.

Energy /keV	D^+	He^+	N^+	O^+
1000	1.0	1.0	0.99	0.98
500	1.0	1.0	0.95	0.96
100	1.0	0.99	0.74	0.75
50	0.99	0.97	0.67	0.58
20	0.98	0.91	0.42	0.39

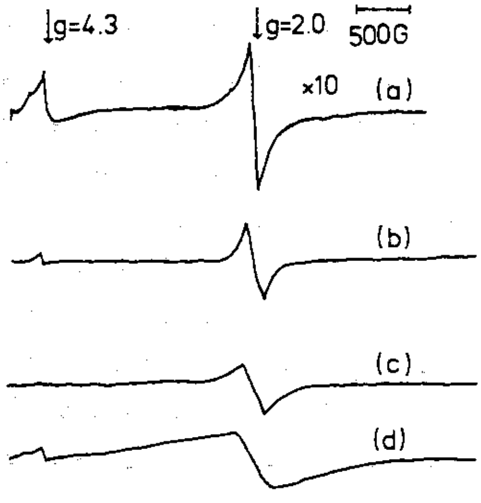

Fig. 1. EPR spectra of 1.8 MeV Ar^{2+}-irradiated (010) surface of $K_4[Fe(CN)_6]\cdot3H_2O$. Current density: 0.75 $\mu A\,cm^{-2}$; irradiation time: (a) 10 s, (b) 1 min, (c) 5 min, and (d) 15 min.

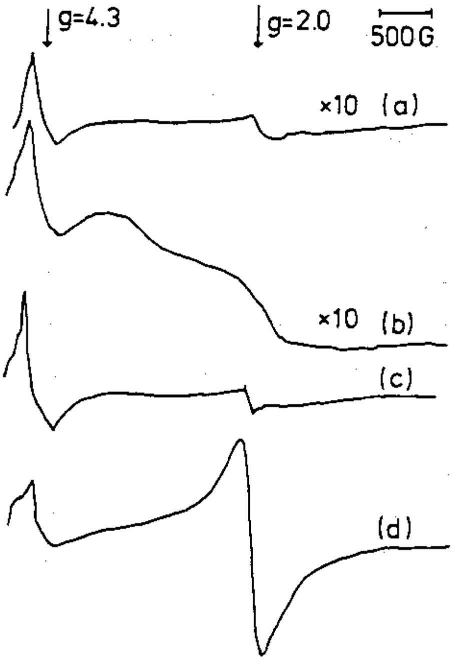

Fig. 2. EPR spectra of irradiated pellets of $K_4[Fe(CN)_6]\cdot3H_2O$.
(a) 40 keV Ar^+-bombarded at 10 $\mu A\,cm^{-2}$ for 10 min,
(b) 40 keV Ar^+-bombarded at 10 $\mu A\,cm^{-2}$ for 30 min,
(c) 1.45 MeV H^+-bombarded at 1.5 $\mu A\,cm^{-2}$ for 10 min, (d) ^{60}Co-γ irradiated at 4×10^9 rad followed by heating at 150 °C for 30 min.

References

1) F. T. Smith and A. Salop, "Radiation Research," ed. by O. F. Nygaard et al., Academic Press, New York (1975), p.242.

2) J. Kistemaker, F. J. DeHeer, J. Sanders and C. Snock, "Radiation Research," ed. by G. Silini, North-Holland, Amsterdam (1967), p.68.

3) G. Stocklin, "Radiation Research," ed. by S. Okada et al., Tokyo (1980), p.382.

4) K. Furukawa and S. Ohno, "100 keV-Ion Accelerator for Study of Chemical Reactions," JAERI-M 85-110 (1985).

5) S. R. Logan and W. J. Moore, J. Phys. Chem., 67, 1042 (1963).

6) S. Ohno and K. Furukawa, Bull. Chem. Soc. Jpn., 58, 1100 (1985).

7) K. Furukawa and S. Ohno, Bull. Chem. Soc. Jpn., 58, 1831 (1985).

8) S. Ohno, K. Furukawa and T. Soga, Bull. Chem. Soc. Jpn., 59, 1947 (1986).

9) T. Soga, K. Furukawa and S. Ohno, Proc. 52th Ann. Conf. Chem. Soc. Jpn., I, p.322 (1986).

IV NUCLEAR CHEMISTRY

4.1 PRODUCTION OF ACTINIDES IN REACTIONS OF ^{242}Pu WITH ^{12}C AND ^{238}U WITH ^{16}O

Nobuo SHINOHARA, Shigekazu USUDA, Shin-ichi ICHIKAWA,
Toshio SUZUKI, Masaaki MAGARA, Hiroshi OKASHITA,
Hideki YOSHIKAWA*, Yousei IWATA**, Takayoshi HORIGUCHI**,
Seiichi SHIBATA*** and Ichiro FUJIWARA****

Department of Chemistry, JAERI, *Department of Chemistry,
Tokyo Metropolitan University, **Department of Physics,
Hiroshima University, ***Institute for Nuclear Study,
University of Tokyo and ****Faculty of Economics,
Otemongakuin University

Actinides produced in bombardments of ^{242}Pu with ^{12}C and ^{238}U with ^{16}O ions at energies near the Coulomb barriers have been studied using radiochemical methods$^{1-3)}$. Both reactions form the same compound nucleus by a complete fusion reaction:

$$^{12}_{6}\mathrm{C} + {}^{242}_{94}\mathrm{Pu} \longrightarrow {}^{254}_{100}\mathrm{Fm}^*$$
$$^{16}_{8}\mathrm{O} + {}^{238}_{92}\mathrm{U} \longrightarrow {}^{254}_{100}\mathrm{Fm}^*$$

The investigation of the production of identical actinides in the reactions is an effective way to clarify such heavy-ion-induced reactions. In the previous report$^{2)}$ we informed that the isotopes of ^{250}Fm, $^{244-246}$Cf and ^{242}Cm are produced in both reactions as above. This report deals with a comparative study of the reactions between ^{242}Pu(^{12}C,4n)^{250}Fm, ^{238}U(^{16}O,4n)^{250}Fm, ^{232}Th(^{22}Ne,4n)^{250}Fm$^{4)}$, and ^{241}Pu(^{13}C,4n)^{250}Fm$^{5)}$.

The experimental excitation functions for ^{250}Fm produced by the ^{12}C + ^{242}Pu and the ^{16}O + ^{238}U reactions are shown in Fig. 1. The solid lines connect the measured values. The yield curves appear to be symmetric in both reactions. The formation cross section of ^{250}Fm from the ^{12}C + ^{242}Pu reaction is several times larger than that from the ^{16}O + ^{238}U reaction. The maximum of the excitation function for the ^{16}O + ^{238}U reaction occurs at a projectile energy about 20 MeV (lab. system) higher than for the ^{12}C + ^{242}Pu reaction and the difference in the Coulomb barriers between the two reactions is calculated to be also 20 MeV (lab. system). This agreement seems to be ascribable to the roughly same excitation energy (E^*) of the compound ^{254}Fm nuclei at the maximum cross sections for the two systems, which are also shown in Fig. 1 along with the energy of the bombarding particles. The maximum cross sections are determined to be 6 and 1.5 μbarn ($E^* = 42$ and 48 MeV) for the $^{12}C + {}^{242}Pu$ and the $^{16}O + {}^{238}U$ systems, respectively, while the $^{22}Ne + {}^{232}Th$ and the $^{13}C + {}^{241}Pu$ reactions give the values of 0.25^4) and 5^5) μbarn ($E^* = 44$ and 43 MeV). It is found from the comparison between these results that the maximums increase with increasing Z and/or A in the targets, namely, with decreasing Z and/or A in the projectiles.

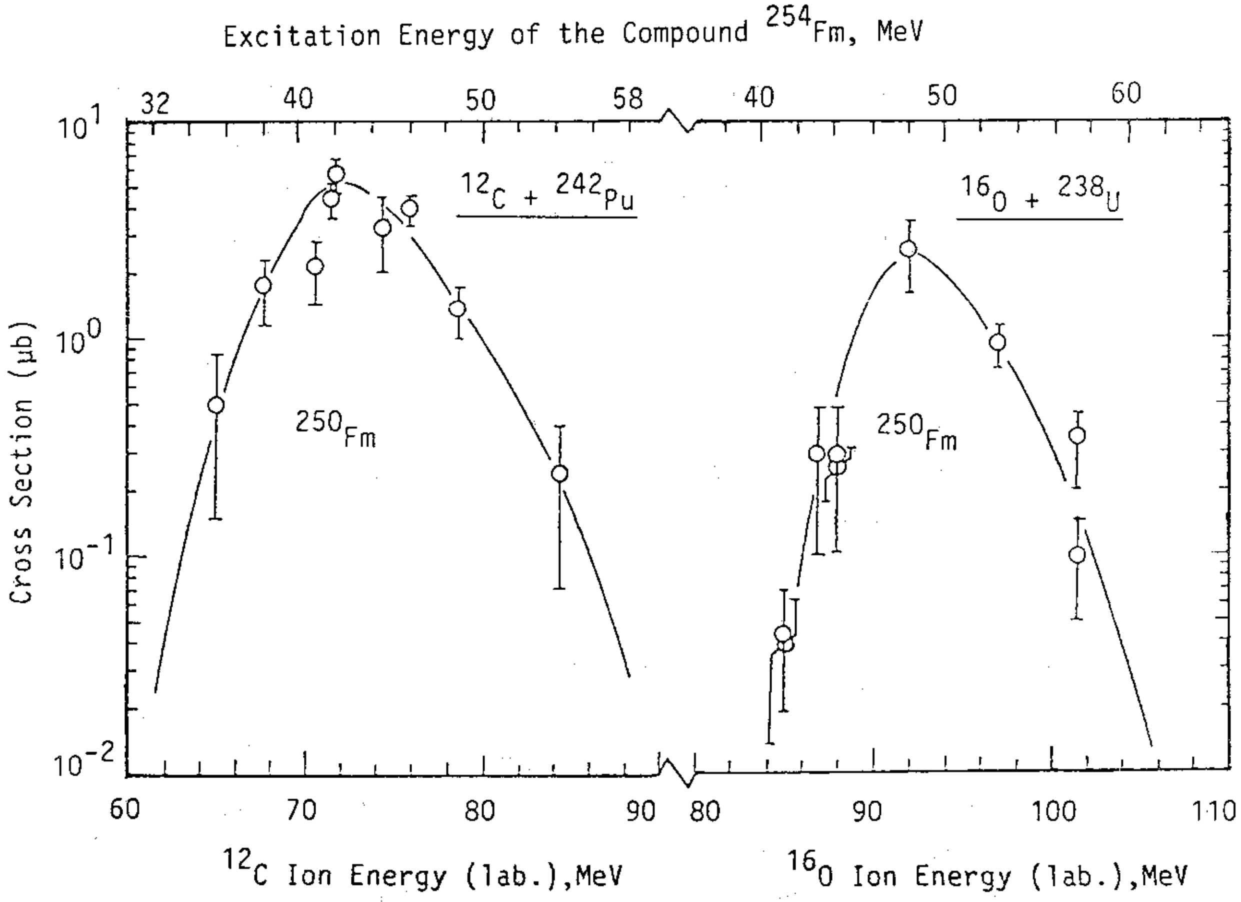

Fig. 1 Excitation functions of ^{250}Fm produced by the $^{12}C + {}^{242}Pu$ and the $^{16} + {}^{238}U$ reactions.

References

1) N. Shinohara et al.: Americium and Curium Chemistry and Technology (N.M.Edelstein, et al.(eds.), D.Reidel Publishing Co., Dordrecht, 1985) pp.251-260.
2) N. Shinohara et al.: JAERI-M 85-104 (1985) 129.
3) S. Usuda et al.:JAERI-M 86-067 (1986) 99.
4) E. D. Donets et al.: Sov. Phys.-JETP 16 (1963) 7.
5) V. V. Volkov et al.: Sov. Phys.-JETP 37 (1960) 859.

4.2 TRANSFER REACTIONS IN 105-MeV ^{16}O + ^{197}Au

Kentaro HATA, Yuichiro NAGAME, Toshiaki SEKINE, Sumiko BABA,
Akihiko YOKOYAMA**, Shin-ichi ICHIKAWA*, Hiroshi BABA**,
Tadashi SAITO**, Atsushi SHINOHARA**

Department of Radioisotopes, *Department of Chemistry,
JAERI, **Faculty of Science, Osaka University

Introduction

Deep inelastic reaction induced by heavy ions is characterized by a large dissipation of relative kinetic energy and a large number nucleon transfer between two interacting nuclei. The diffusion model1),2) which treats statistically these processes has been successfully applied to explain the features and to reproduce the kinetic energy spectra and the mass (or element) distributions of reaction products. This model, however, was found to be unable to be apply to very mass-asymmetric reaction systems. The damped reaction products in ^{197}Au + ^{16}O reaction system have been investigated in order to understand the characteristics of deep inelastic reaction in very mass-asymmetric reaction system.

Experimental and Results

The target of self-supporting Au foil about 1 mg/cm^2 was used. The ^{16}O bombardment was performed at JAERI tandem accelerator with an incident energy of 105 MeV. The projectile-like fragments were measured using a ΔE-E Si solid state counter telescope to determine the kinetic energies, and to identify the atomic numbers of the products. The center-of-mass angular distributions of the products with $Z = 4$ to 7 are shown in Fig.1. The differential cross section of each element has its maximum at an angle smaller than the grazing angle. The distributions of the smaller Z have peaks at much smaller angles and become broader. The energy spectrum of the products with $Z = 7$ exhibits distinctly two components. On the other hand, the energy spectra which have asymmetric and structureless broad component were observed for the others. We divided all these spectra into two components assuming that they were contributed by two different reaction processes. Figure 2 shows the most-probable total kinetic energy of each element and its width (FWHM) obtained from the energy spectrum as a function of the scattering angle. The measured energies are compared with the calculated values of Coulomb repulsion energies between two touching spheres in exit channel.

Discussion

As shown in Fig.2, the average total kinetic energies for the low-energy component are found to be almost independent of angle and roughly correspond to the Coulomb repulsion energies for the products with $Z < 7$. This suggests that the kinetic energy dissipation is almost complete and that the process is quickly terminated as soon as the composite system begins to rotate. This is characteristic for very mass-asymmetric systems.

The angular distributions of the projectile-like products have been analyzed in terms of the diffusion model. The differential cross sections calculated by this model are shown in Fig.1. For the calculation, the following three parameters were assumed; drift velocity, diffusion coefficient and half life of the composite system. As listed in Table 1,the best fit parameters were obtained to reproduce the experimental angular distributions. Although the general trend of the distributions could be explained by this model, with increasing angle, the larger discrepancies between the experimental values and the calculated ones have been observed. However, we can understand from the angular distributions that the life time of the composite system is much shorter than its one rotation time(1.2×10^{-20}s). Agarwal[2] has proposed that the life time of the composite system depends on the mass-asymmetry of the entrance channel. The life time of the composite system obtained in the present work is consistent with his systematics, as shown in Fig.3.

References

1) G.Wolschin and W.Nörenberg: Z. Phys. A284 (1978) 209.
2) S.Agarwal: Z. Phys. A297 (1980) 41.
3) R.Bass: Nucl. Phys. A231 (1974) 45.

Table 1 Parameters used in diffusion model calculation

grazing angular momentum : 43 ℏ
*critical angular momentum : 48 ℏ
**Diffusion coefficient : 3.7 X 10^{21}/sec
**Drift velocity : -4.5 X 10^{21}/sec
Half life : 2.0 X 10^{-22} sec

* calculated by Bass model3). ** for mass transfer.

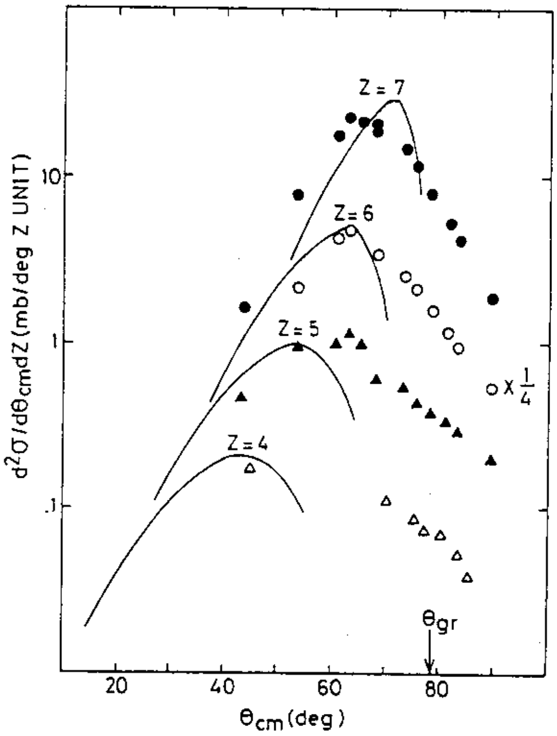

Fig.1 Experimental(dots) angular distributions for fragments with the Z values indicated at the data sets. The curves are calculated values by using the diffusion model with the parameters in Table 1. The experimental cross sections for Z = 6 are multiplied by the factor of 1/4.

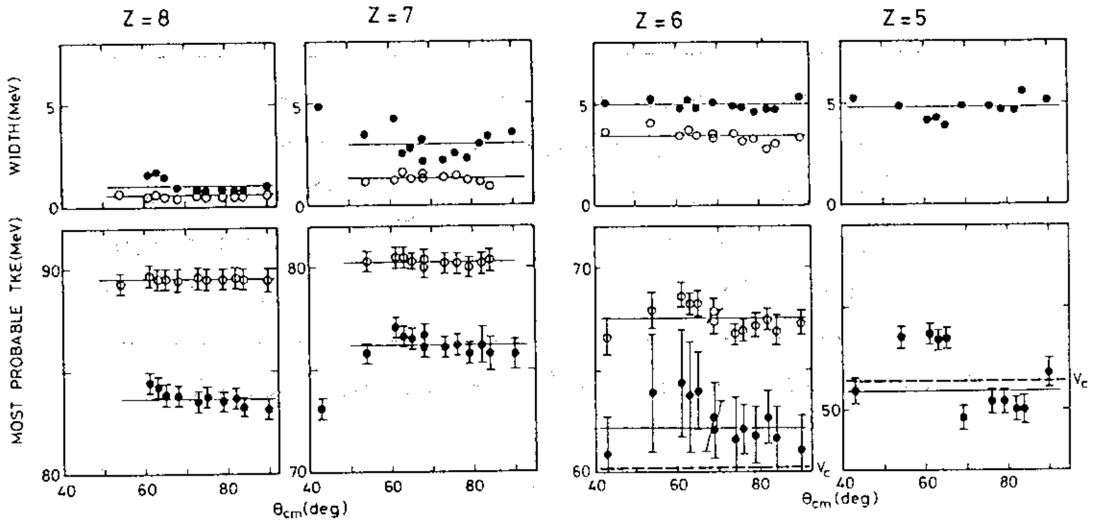

Fig.2 Most probable total kinetic energies and FWHM's of the particle energy spectra are plotted as a function of the reaction angle. Open circles are the data for high-energy components and close circles for low-energy components. The straight lines are drawn through the data to guide the eye. The dashed lines illustrate the exit Coulomb repulsion energy between two touching spheres.

Fig.3 Half lives of the composite systems are plotted vs. mass asymmetry of the reaction system A_L / (A_L + A_H) where A_L is mass number of the light partner and A_H mass number of the heavy partner. Open circles are for entrance channels ^{52}Cr +^{56}Fe, ^{40}Ca + ^{64}Ni and ^{16}O + ^{92}Mo.(2) A closed circle is the data obtained in this work.

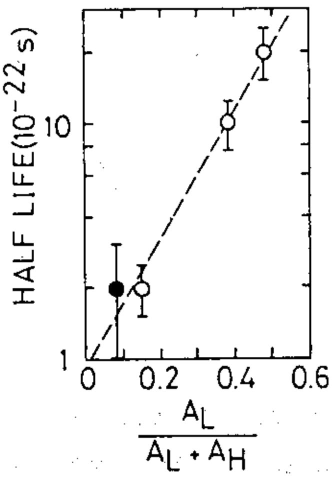

4.3 NEUTRON TRANSFER REACTION IN THE SYSTEM ^{37}Cl + ^{103}Rh

Sumiko BABA, Kentaro HATA, Toshiaki SEKINE and
Yuichiro NAGAME

Department of Radioisotopes, JAERI

The number of neutrons evaporated from fragments produced in heavy-ion collisions gives an important information about the energy dissipation in the reaction. In this work we attempted to evaluate the excitation energies of primary fragments in a neutron-transfer reaction, by comparing the secondary distribution of the target-like isotopes and that of the complementary projectile-like ones obtained radiochemically, and thus by estimating the average number of the evaporated neutrons.

The reaction system of ^{103}Rh target and ^{37}Cl projectile was adopted, since the Rh isotopes of mass numbers from 99 to 105 (excluding 103 and 104) have decay properties suitable for radiochemical determination. Furthermore, their independent yields can be easily measured, as the Pd and Ru nuclides are all stable or long-lived. As for the projectile-like products, the yields of ^{38}Cl and ^{39}Cl were measured.

The ^{103}Rh target of 0.5 mg/cm^2 thick was bombarded with 165-MeV ^{37}Cl ions from the JAERI tandem accelerator. The products recoiling out of target were collected in a gold catcher foil with a thickness of 50 mg/cm^2, which was thick enough to stop the primary 165-MeV Cl beams; it was checked beforehand that no Cl radioactivities were found in a blank gold foil. The γ rays of the Cl isotopes and the short-lived Rh isotopes in the target and the gold catcher foil were measured by a Ge(Li) detector. (More than 95% of the products were found in a catcher.) Instead of the Au catcher foil, an Al catcher foil was used for the determination of the long-lived Rh isotopes, such as ^{101g}Rh and ^{102m,g}Rh. After irradiation, Rh was separated chemically from the other reaction products and aluminum, and was subjected to the γ-ray measurement. Rhodium-101m ($T_{1/2}$ = 4.34 d), observable both in the gold catcher and in the chemically separated Rh fraction, was used to normalize the cross sections.

The formation cross sections obtained for the Cl and the Rh isotopes are plotted in Fig.1 against a number of neutrons lost or gained in reaction. One must note two components in the Rh isotope distribution: a damped-collision component with a large width and a quasi-elastic few-nucleon transfer component, mainly consisting of the low-spin isomers. From the experimental results, the average number of neutrons evaporated from the primary products was deduced by the analysis based on the following approximations;

1) Low-spin Rh isotopes are formed via the quasi-elastic collision without obtaining sufficient excitation energies to evaporate any neutron.

2) In the deep-inelastic collision, high-spin Rh products with some excitation energies are formed, but the deexcitation by the evaporation of charged particles are negligible.

3) The primary and secondary isotope distributions are described by gaussian for both Rh and Cl.

The isotope yields for high spin-state Rh nuclides were fitted to a gaussian function as Fig.1 shows. In the case of ^{100}Rh and ^{105}Rh, only the ground-state nuclides were detected. The cross sections were attributed to the high spin-state yields. The cross sections of quasi-elastic collision for ^{38}Cl and ^{39}Cl are equivalent to those for low spin-state ^{102}Rh and ^{101}Rh, respectively, according to the approximation 1). The deep-inelastic component in the yields of ^{38}Cl and ^{39}Cl was obtained by subtructing the quasi-elastic component from them and plotted in Fig.1. The secondary isotope distribution for Cl produced via damped process was constructed so as to give a gaussian including these two points with an area identical to that for Rh. It is represented with dashed line in Fig.1. The centroids are very close to zero as shown by arrows in Fig.1. It means that no neutron evaporation from the fragments occurred and the most probable neutron transfer is zero.

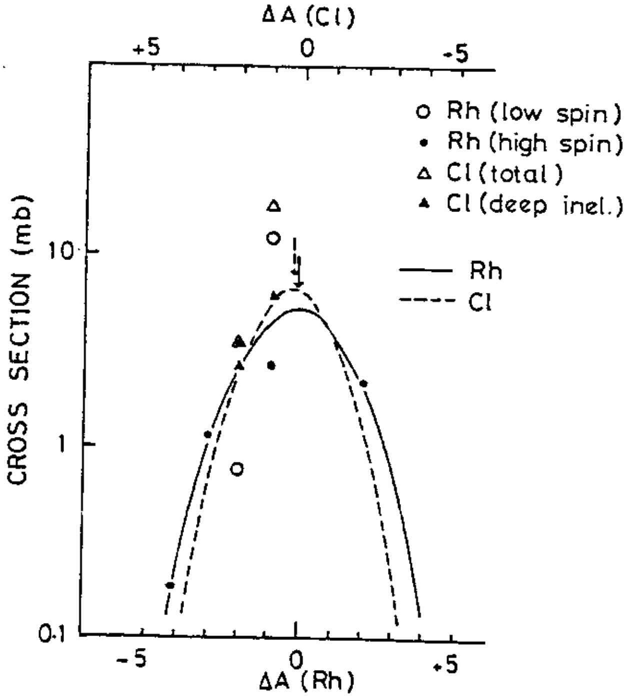

Fig.1. Distributions of Rh and Cl isotopes.

4.4 A STUDY OF NUCLEI FAR FROM STABILITY BY USING JAERI ISOL

Shin-ichi ICHIKAWA, Toshiaki SEKINE*, Masumi OSHIMA**,
Kentaro HATA*, Nobuo SHINOHARA and Naruto TAKAHASHI***

Department of Chemistry, *Department of Radioisotopes,
**Department of Physics, JAERI, ***Osaka University

A study of nuclei far from beta stability has been continued by using an isotope separator on-line (ISOL) to the JAERI tandem heavy-ion accelerator. The study of the ^{121}Ba decay started last year$^{1)}$ was extended to the measurements of beta-delayed protons, beta end-point energies and lifetimes of states. In addition, the surface-ionization ion source constructed earlier$^{2)}$ was tested in on-line operation with respect to hold-up times and ionization efficiencies for several isotopes.

A Study of the Decay of ^{121}Ba

A partial decay scheme of ^{121}Ba, including the levels up to 0.2 MeV, was proposed earlier$^{1)}$ from gamma singles and gamma-gamma coincidence measurements. This year, more detailed spectroscopic measurements were carried out with the reaction system ^{35}Cl + ^{93}Nb.

The beta-delayed proton measurement with a surface barrier detector 100 μm thick yielded 5.6×10^{-5} as a proton-X-ray ratio in the decay of ^{121}Ba. This value was found to be consistent with the proton branching reported by Bogdanov et al.$^{3)}$

The beta rays were measured with a plastic scintillation detector. The detector consists of a NE102A scintillator with a diameter of 76 mm and a length of 80 mm; its surface was coated with aluminum about 1000 Å thick. Using this detector, beta-gamma coincidence measurements were performed for products with the masses 121, 122 and 123. The beta-ray spectra gated by gamma rays were obtained and reduced to Kurie plots for ^{121}Ba as well as for ^{121}Cs, ^{122}Cs and ^{123}Cs. With the known Q_β values of these cesium isotopes, the beta-ray energy was calibrated. Using the same beta detector, the beta-gamma-t measurements were made to determine the lifetimes of the states in ^{121}Cs associated in the decay of ^{121}Ba.

The construction of the ^{121}Ba decay scheme is in progress, including all the results from the above measurements.

Characteristics of the Surface Ionization Ion Source

Efficiencies and hold-up times, which are crucial parameters for ion source, were measured, using 190-MeV ^{35}Cl beams with intensities from 30 to 40 particle nA. As a target, a niobum foil 3.4 mg/cm^2 thick was used to determine the hold-up times for ^{122}Cs and ^{122}Ba. In addition, a rhodium foil 1.8 mg/cm^2 thick was bombarded in the determination of efficiencies to produce ^{134}Nd and ^{134}Pm. Acting as a recoil catcher, a graphite or a tantalum foil of 100 μm thickness was placed inside the ion source; for both the catcher materials hold-up times and efficiencies were examined. For surface ionization of atoms, a rhenium foil was placed inside the ionizer heated together with the vaporizer by electron bombardment from filaments.

The overall efficiencies, containing ionization and transport efficiences, were obtained by comparing the source strengths collected on a movable tape with the production rates calculated on the basis of the reaction cross sections predicted by the statistical model code ALICE.$^{4)}$ Therefore, the resulting efficiencies are not very reliable as absolute values.

The results obtained are plotted in Fig. 1 as a function of the ionizer temperature. The ^{124}Cs isotope was found to have high efficiencies, as expected, for both the catcher materials. One should note that ^{124}Ba was observed to have an efficiency of at most 1% even at 2500 K for the tantalum catcher. The efficiencies obtained for ^{124}Ba are extremely low compared with a value of 18% observed in off-line operation for ^{126}Ba produced in the ^{37}Cl + ^{93}Nb reaction$^{2)}$; the cross sections predicted by the ALICE code or the nuclear data$^{5)}$ used in determination of the ^{124}Ba activity may be very erroneous. In conclustion, however, one can say that a tantalum catcher is more favorable than a graphite catcher for all the isotopes examined here.

The time needed to mass-separation in ISOL is determined almost by a hold-up time of atoms in an ion source. The hold-up time consists of the time of diffusion of recoil nuclei from a catcher foil and the time for the atoms to be ionized in an ionizer. Experimentally, the hold-up time was obtained as a release half-life, namely, a time needed for the amount of radioactivity to decrease to half of the initial one after the accelerator beam was swiched off. The half-life of a probe nucleus for this measurement must be much longer than a release half-life, so that a release profile is not obscured by its nuclear decay. In the present experiment, ^{122}Cs (4.2 min) and ^{122}Ba (117 sec) were chosen as probe nuclei. While the accelerator beam was switched on for 8 sec and switched off for 12 sec, eight X-ray spectra were recorded for the products with the mass 122. This process was repeated untill enough counting statistics were obtained. During experiment the ion source was operated at an ionizer temperature of 2700 K.

The release profiles obtained for ^{122}Cs and ^{122}Ba are shown in Fig. 2. In the case of ^{122}Cs, the hold-up time for the carbon catcher is twice as long as that for the tantalum catcher. The hold-up times for ^{122}Ba were found to be much shorter than those for ^{122}Cs, for both the catcher materials. From these observations, one can say that the hold-up time of ^{122}Cs depends strongly on a diffusion rate in a catcher, and that ^{122}Cs atoms diffuse more slowly than ^{122}Ba atoms in tantalum and graphite at the temperature given in this experiment, since both the ^{122}Cs and the ^{122}Ba nuclei were expected to be impalnted into almost the same depth in a catcher.

References

1) S.Ichikawa et al. : JAERI TANDEM LINAC & V.D.G Annual Report 1984, JAERI-M 85-104 (1985), p.139

2) S.Ichikawa et al. : JAERI TANDEM Annual Report 1983, JAERI-M 84-129 (1984), p.60

3) B.D.Bogdanov, A.D.Demanov, V.A.Karnaukov, L.A.Petrov and J.Voboril: Nucl. Phys. A303 (1978) 145

4) M.Blann: Report COO-3494-29 (1976)

5) U.Reus and W.Westmeier: Atomic Data and Nuclear Data Tables 29(1983), p.275

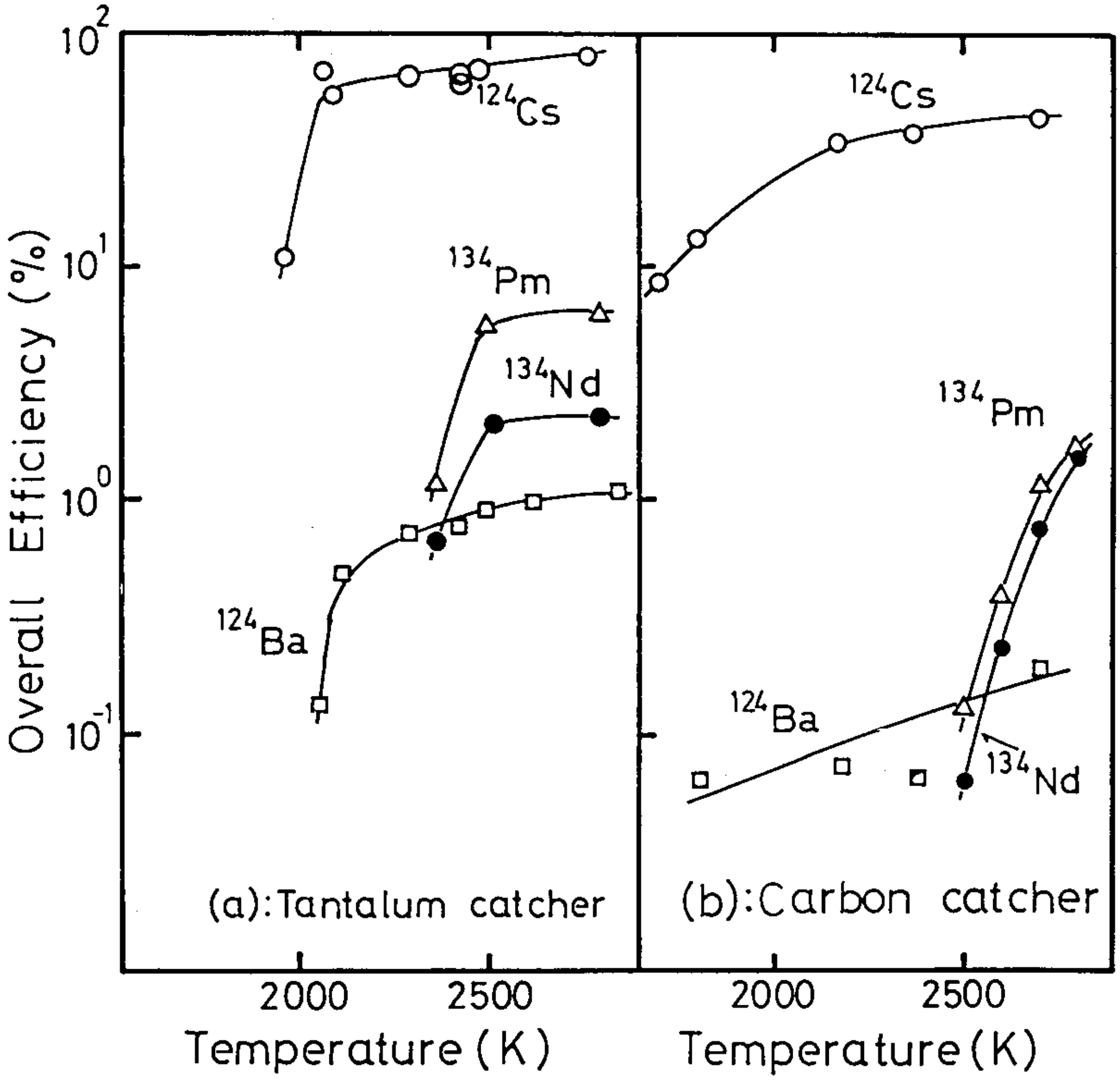

Fig.1 Overall efficiencies for ^{124}Cs, ^{124}Ba, ^{134}Pm and ^{134}Nd as a function of the ionizer temperature; in Part (a) a tantalum foil was used as a recoil catcher and in Part (b) a graphite foil. With respect to the low efficiencies observed for ^{124}Ba, see text.

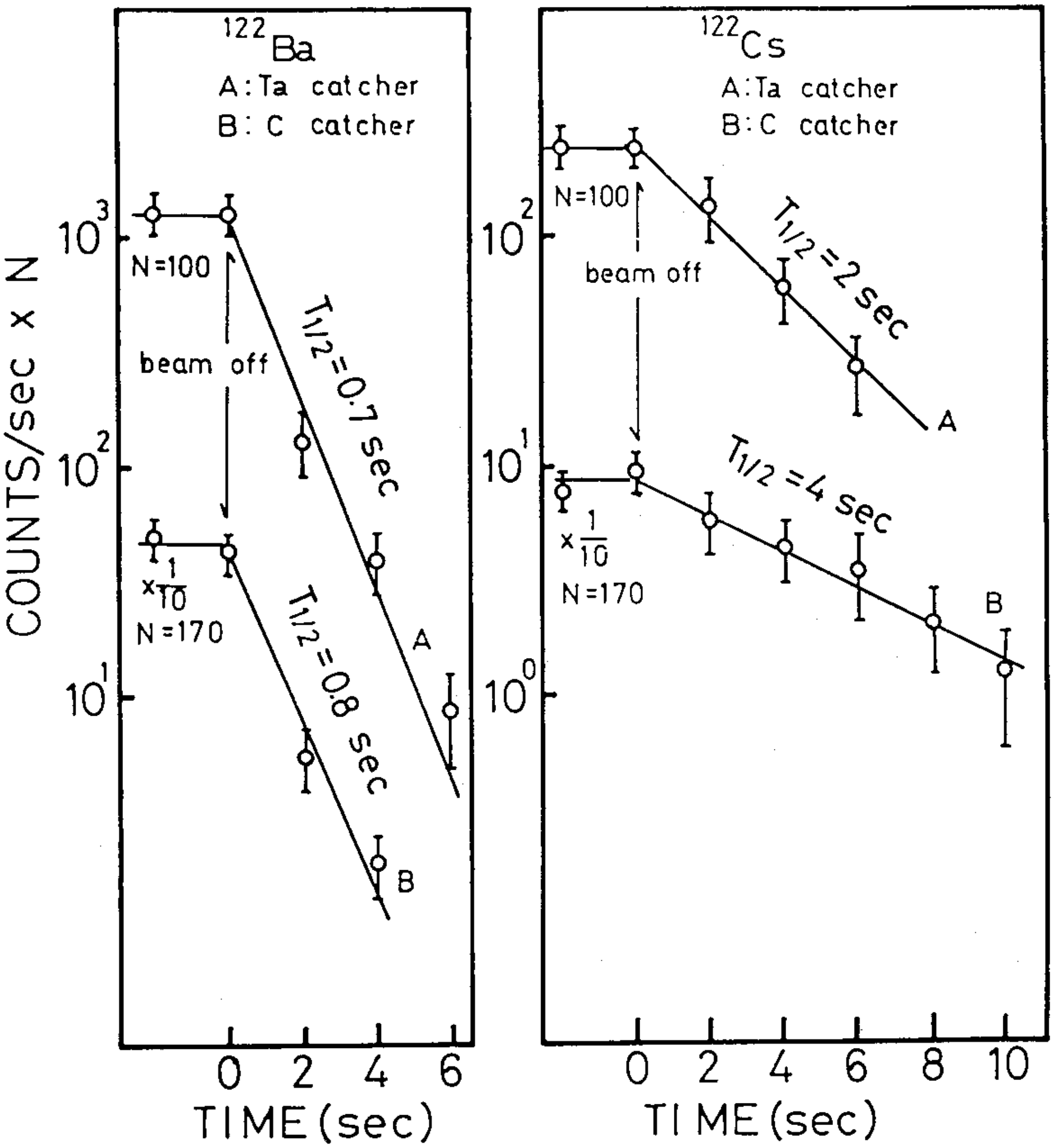

Fig.2 Release profiles of ^{122}Cs and ^{122}Ba in the intermittent accelerator beam. The origin of time is set at the time when the beam is switched off. The eight spectra were recorded in a cycle, 8-sec beam-on and 12-sec beam-off, and accumulated in the same cycles repeated N times, as indicated.

4.5 PREPARATION OF ^{211}Rn-^{211}At GENERATOR FROM ^{209}Bi IRRADIATED WITH ^{14}N

Hiromitsu MATSUOKA, Sumiko BABA, Kentaro HATA,
Yuichiro NAGAME, Takashi MORIYA, Terutomi MOKI,
Mishiroku IZUMO and Takami SORITA

Department of Radioisotopes, JAERI

An -emitting halogen ^{211}At ($T_{1/2}$ =7.2 h) is receiving much attention for its potential as a therapeutic medicine. In a general way, it is prepared directly by ^{209}Bi(α, 2n)^{211}At reaction. However, the radiochemical impurity ^{210}At ($T_{1/2}$ =8.0 h) with its long-lived daughter ^{210}Po ($t_{1/2}$ = 138 d) by ^{209}Bi(α , 3n)^{210}At reaction co-exists at the projectile energies higher than 28 MeV, where the cross section of the ^{209}Bi(α, 2n)^{211}At reaction is maximum.$^{1)}$ An indirect preparation route is through ^{211}Rn which decays to ^{211}At via E.C.decay. Radiochemical properties of ^{211}Rn ($T_{1/2}$ =14.2 h) are favorable to obtain a pure ^{211}Rn-^{211}At generator system. We intended in this work to search some useful reactions for preparation of ^{211}Rn.

The possible reactions producing ^{211}Rn are listed in Table 1. We adopted the ^{209}Bi + ^{14}N reaction first, because of availability of the projectile beam and the target material.

Table 1. The possible reaction to produce ^{211}Rn

Reaction	Required projectile energy (lab.)	ref.
^{209}Bi(^{14}N, 4n)^{219}Th $\xrightarrow{\alpha}$ ^{215}Ra $\xrightarrow{\alpha}$ ^{211}Rn ^{209}Bi(^{14}N, α4n)^{215}Ra $\xrightarrow{\alpha}$ ^{211}Rn ^{209}Bi(^{14}N, 2α4n)^{211}Rn	> 74 MeV	present work
^{209}Bi(^{7}Li, 5n)^{211}Rn	> 33 MeV	2)
^{204}Pb(^{12}C, 4n)^{215}Ra $\xrightarrow{\alpha}$ ^{211}Rn ^{204}Pb(^{12}C, α4n)^{211}Rn	> 63 MeV	
^{209}Bi(^{12}C, p5n)^{215}Ra $\xrightarrow{\alpha}$ ^{211}Rn	> 64 MeV	
^{198}Pt(^{16}O, 3n)^{211}Rn	> 80 MeV	
^{234}Th(p, x)^{211}Rn $^{nat.}$U(p, x)^{211}Rn	> 600 MeV (spallation)	3)

The targets of ^{209}Bi (1-2 mg/cm^2) were prepared by evaporating Bi metal(99.9% purity) onto 2 mg/cm^2 Al support discs. The ^{14}N bombardments were performed at the JAERI tandem accelerator with incident energies ranging from 75 MeV to 120 MeV. After bombardments, the ^{211}Rn radioactivities in each target-catcher pair were measured by a calibrated Ge(Li) detector.

Figure 1 shows the formation cross section observed for ^{211}Rn. A smooth curve was drawn to guide the eye. The subsequent calculation of thick-target yields was carried out by integration along this curve.

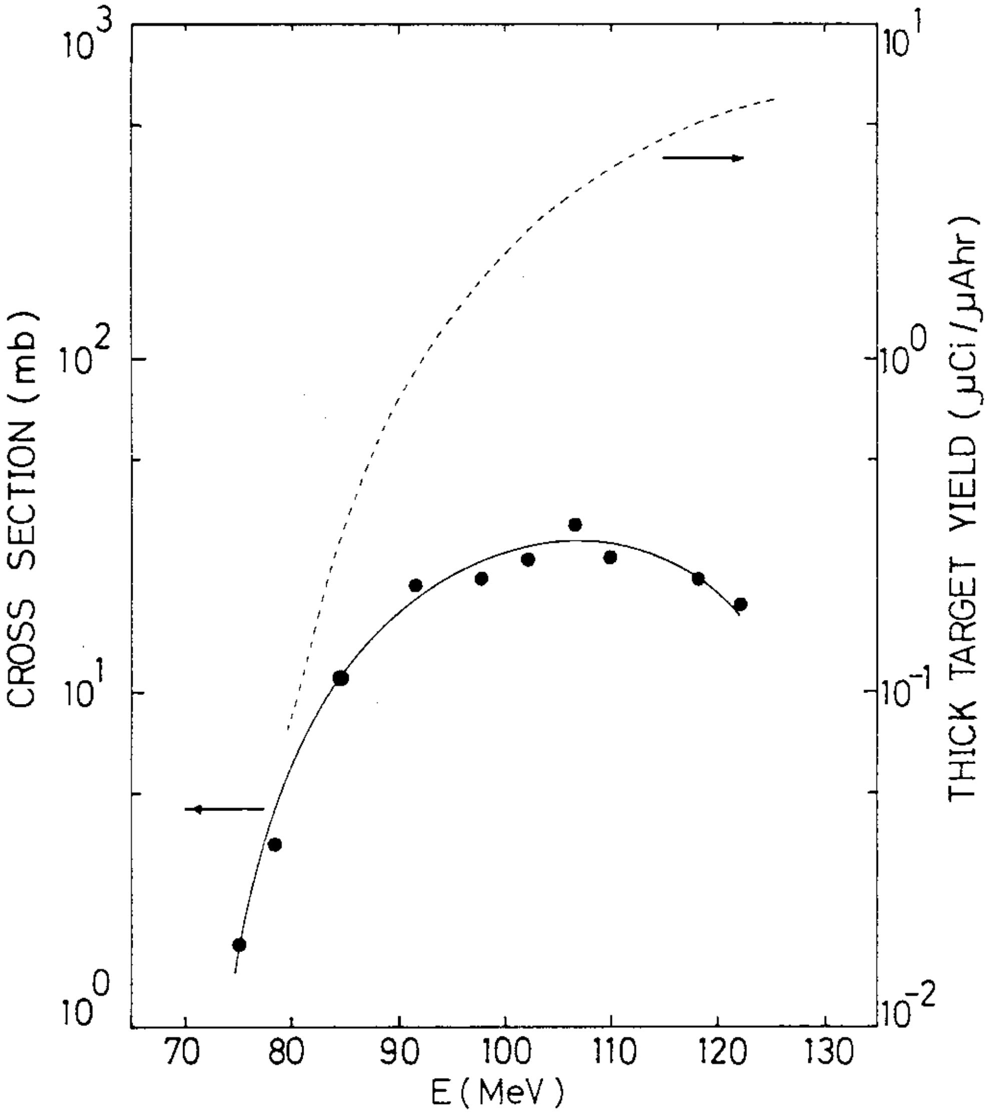

Fig.1 Formation cross section(solid line) and thick-target yield curve(dashed line) for the production of ^{211}Rn.

The cross section values are assumed to be the cumulative yields of the following four reaction channels;

(i) $^{209}\mathrm{Bi}(^{14}\mathrm{N},\ 4n)^{219}\mathrm{Th} \xrightarrow[0.1\mu s]{\alpha} {}^{215}\mathrm{Ra} \xrightarrow[1.6ms]{\alpha} {}^{211}\mathrm{Rn}$

(ii) $^{209}\mathrm{Bi}(^{14}\mathrm{N},\ \alpha 4n)^{215}\mathrm{Ra} \xrightarrow[1.6ms]{\alpha} {}^{211}\mathrm{Rn}$

(iii) $^{209}\mathrm{Bi}(^{14}\mathrm{N},\ 2\alpha 4n)^{211}\mathrm{Rn}$

(iv) $^{209}\mathrm{Bi}(^{14}\mathrm{N},\ x)^{211}\mathrm{Rn}$

where x is a number of transferred nucleons. The first three reaction paths are attributed to the compound nuclear reaction processes, whereas the last one results from the multi-nucleon transfer reaction. Although the reaction path through the compound nucleus formation has been expected to be the most probable reaction process, it has not been possible to deduce the reaction mechanism from the shape of this excitation function obtained in the present work. The detailed analysis about the reaction mechanism is in progress.

Thick-target yields calculated from the formation cross section are also shown in Fig.1 by a dashed line. With this energy range (target thickness $\sim$600mg/cm^2), the thick-target yield of ^{211}Rn was found to be about 6μCi/μA·h at the end of bombardment.

The development of the ^{211}Rn-^{211}At generator system and other production methods of ^{211}Rn listed in Table 1 are scheduled in following experiments.

References

1) R.M.Lambrecht and S.Mirzadeh: Int.J.Appl.Radiat.Isot. 36 (1985) 443.

2) G.-J.Meyer and R.M.Lambrecht: Int.J.Appl.Radiat.Isot. 31 (1980) 351.

3) R.Bimbot and M.F.Rivet: Phys.Rev. C8 (1973) 375.

V NUCLEAR PHYSICS

5.1 B(E2) ANOMALY IN GROUND-STATE BANDS OF CE-126 AND -124

Tetsuro ISHII, Masaru HOSHI*, Mitsuhiko ISHII
and Masao OGAWA*

Department of Physics, JAERI, *Tokyo Institute of
Technology (Yokohama)

We have studied high-spin states in ^{126}Ce and ^{124}Ce excited by reactions ^{92}Mo(^{37}Cl or ^{35}Cl, xp yn). The gamma-gamma coincidences, the gamma-ray angular distributions and the Doppler-shifted gamma-ray spectra have been taken with the help of a charged-particle multiplicity filter "silicon box": which discriminates between reaction channels by taking count of emitted charged particles [1,2,3].

The level schemes are shown in fig.1 together with the half lifetimes of some excited states. In the following the experimental results are summarized with a brief discussion:

(1) ^{124}Ce is one of the most well-deformed nuclei that have ever been observed in the very light rare-earth region. However an anomaly in B(E2) values takes place in the ground-state bands in ^{124}Ce as well as

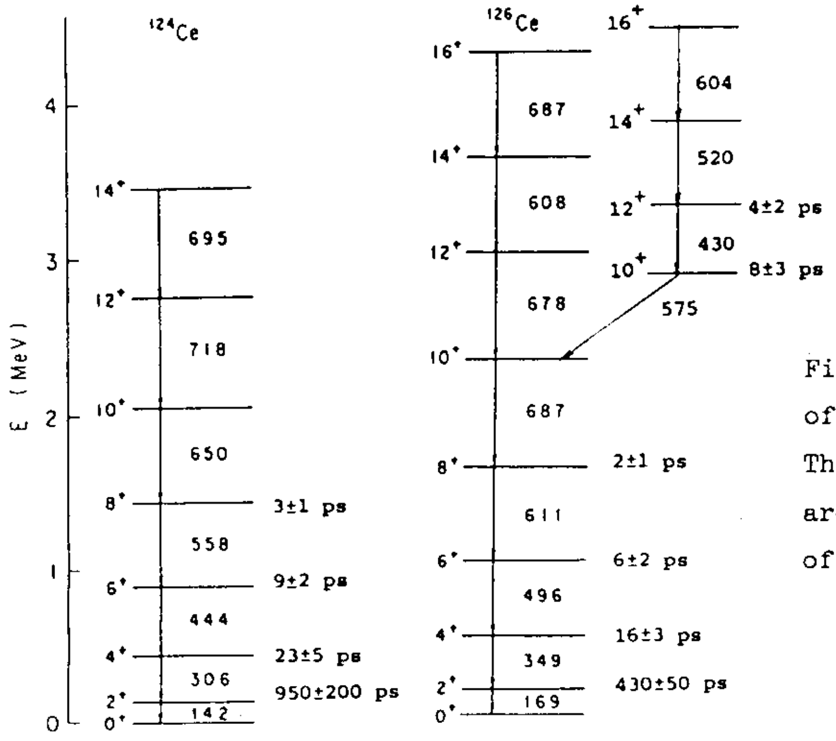
124Ce
126Ce
E (MeV)
0
1
2
3
4
0+
2+
4+
6+
8+
10+
12+
14+
16+
142
306
444
558
650
718
695
950±200 ps
23±5 ps
9±2 ps
3±1 ps
169
349
496
611
687
678
608
687
430±50 ps
16±3 ps
6±2 ps
2±1 ps
575
430
520
604
8±3 ps
4±2 ps

Fig.1. Level schemes of Ce-126 and -124. The half lifetimes are given in units of ps.

^{126}Ce: the 4^+, 6^+ and 8^+ states in ^{126}Ce have longer lifetimes than ones predicted by the IBM-2 [4], and so do the 6^+ and 8^+ states in ^{124}Ce. See fig.2.

(2) The yrast bands backbend in ^{126}Ce and ^{124}Ce. On the other hand no backbending was found up to the 12^+ state in $^{136,\,134}$Sm and up to the 14^+ state in ^{132}Nd [2,3].

(3) A side band was found in ^{126}Ce. In ^{138}Sm a collective band based on two quasi-protons: $(\pi h11/2)^2\ 10^+>$ follows the 8^+ state in the yrast band. Refer to related topics in this annual report. It is an interesting problem whether the side band in ^{126}Ce is proton-like or neutron-like. Further experiments are in progress.

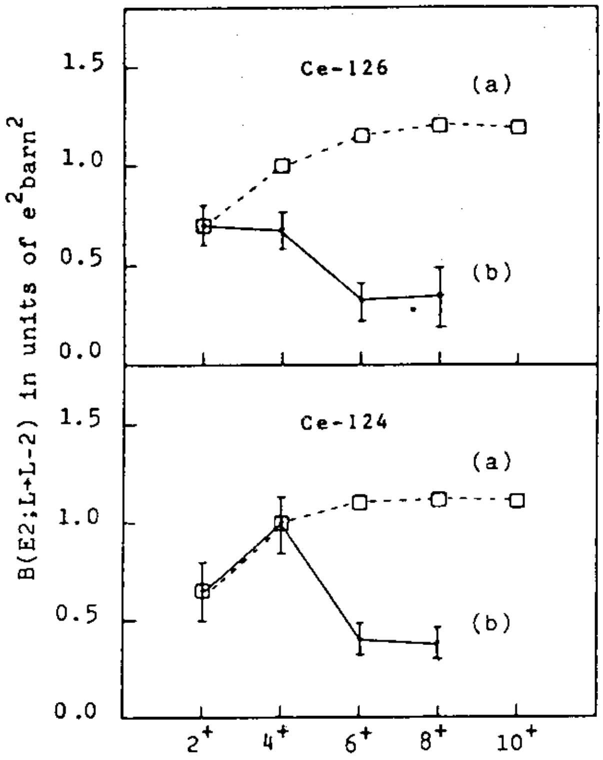

Fig.2. Experimental and theoretical B(E2) values for the ground-state bands in Ce-126 and -124. (a) the IBM-2 calculation and (b) the present results.

References

1) M. Ishii and A. Makishima: ed. K. Harada et al., REPORT OF JOINT SEMINOR ON HEAVY-ION NUCLEAR PHYSICS AND CHEMISTRY USING TANDEM ACCELERATORS, JAERI-M 84-085 (1984) p.75.
2) A. Makishima: Ph.D. Thises, Tokyo Institute of Technology (1985).
3) M. Ishii et al.: A SILICON BOX, a contributed paper to the symposium on RECENT ADVANCES IN THE STUDY OF NUCLEI OFF THE LINE OF THE STABILITY held in Chicago in 1985 by American Chemical Society.
4) T. Otsuka and N. Yoshida: Report JAERI-M 85-094.

5.2 YRAST STATES OF TWO QUASI-PROTONS COUPLED WITH BOSONS

Mitsuhiko ISHII, Tetsuro ISHII,
Akiyasu MAKISHIMA* and Masao OGAWA**

Department of Physics, JAERI, *National Defence Medical College, **Tokyo Institute of Technology (Yokohama)

We previously investigated nuclear structure of ^{138}Sm and established its level scheme shown in fig.1 1,2). On the basis of the B(E2,12$^+$→10$^+$) and the level spacings between the 10$^+$, 12$^+$ and 14$^+$ states, we suggested that these states belong to the band of two quasi-protons: (h11/2)^2 10$^+$>, coupled with the bosons 2). The present report describes a recent g-factor experiment to confirm this suggestion.

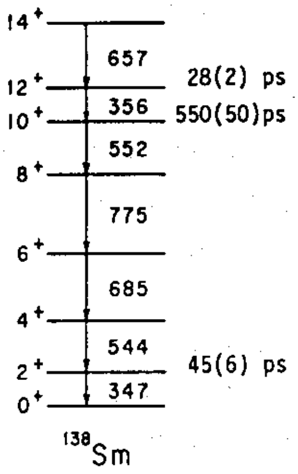

Fig.1. Level scheme of ^{138}Sm.

^{138}Sm nuclei were produced in a reaction ^{107}Ag(^{35}Cl,2p2n) and were implanted into a cooled, magnetized Gd foil. In order to observe Larmor precession, γ-ray spectra were taken in coincidence with two protons emitted with the silicon box 1,2) and four germanium detectors: which were placed at 90±45° and 180±45° with respect to tke beam axis. The angular distributions of the 356 keV transition as well as the 347 keV transition precessed in the positive direction with respect to the applied magnetic field, that is, in the negative direction to the internal field felt by Sm nuclei in the Gd foil. This means that the g-factors for both the 2$^+$ and 12$^+$ states are positive-valued, and gave a confirmation to the previous suggestion.

References

1) M. Ishii and A. Makishima: Report JAERI-M 84-085(1984)p.75.

2) A. Makishima: Ph.D. Thises, Tokyo Institute of Technology, May 1985. Also refer to C.J. Lister et al., Phys. Rev. Lett. 55 810(1985) and S. Lunardi et al., Z. Phys. A321 177(1985).

5.3 LARMOR PRECESSION OF EXCITED STATES IN SM-138 AND SM-136

Tetsuro ISHII, Mitsuhiko ISHII,
Akiyasu MAKISHIMA* and Masao OGAWA**

Department of Physics, JAERI, *National Defence Medical College, **Tokyo Institute of Technology (Yokohama)

We have observed Larmor precession of excited states in ^{138}Sm and ^{136}Sm. The respective nuclei were excited by reactions ^{107}Ag(150 MeV ^{35}Cl, 2p2n) and ^{107}Ag(150 MeV ^{32}S, p2n). Those nuclei were implanted into a cooled, magnetized Gd foil: a foil of 6 mg/cm^2 with a ^{107}Ag layer of 2 mg/cm^2. In-beam gamma-rays were observed by selecting reaction channels involved with a help of the silicon box. Four germanium detectors were placed at 90±45° and 180±45° with respect to the beam axis for ^{138}Sm and at 90±30° and 180±45° for ^{136}Sm. Magnetic fields of about ±350 gauss were externally applied to the foil by a pair of permanent magnets. The precession angles for the transitions of particular interest are given in table 1. We previously measured their lifetimes [1,2]. The g-factor of the first 2^+ state in ^{136}Sm has not yet been measured. So we assume that it takes a typical value of 0.35 for collective 2^+states. Then we can estimate the internal magnetic field felt by Sm nuclei in Gd and values of the g-factor for other excited states. The sign of the internal field and the precession is defined as positive or negative depending on whether they are parallel or antiparallel to the applied field, respectively.

Table 1.

	transitions	precession	lifetimes	g-factors	internal field
^{136}Sm:	$2^+ \rightarrow 0^+$	10°(1)	130(10)ps	0.35(assumed)	-550 k gauss
^{138}Sm:	$12^+ \rightarrow 10^+$	7°(0.5)	28(3) ps	1.1(0.15)	
	$10^+ \rightarrow 8^+$	170°(30)	550(50)ps	1.4(0.20)	

References

1) M. Ishii and A. Makishima: JAERI TANDEM ANNUAL REPORT 1984, p.151.
2) A. Makishima: Ph.D. Thises, Tokyo Institute of Technology, 1985.
To be published in Phys. Rev. C in 1986.

5.4 MULTIPLE COULOMB EXCITATION OF ^{161}DY

Masumi OSHIMA, Shiro KIKUCHI, Shin-ichi ICHIKAWA*,
Takeo ARUGA**, Takashi INAMURA***, Akira HASHIZUME***
and Hideshige KUSAKARI****

Department of Physics, *Department of Chemistry,
**Department of Fuels and Materials Research, JAERI,
*** The Institute of Physical and Chemical Research,
**** Faculty of Education, Chiba University.

It is well known that high-j orbits such as $i_{13/2}$ give rise to a large perturbation of the rotational levels of deformed nuclei. Recently, we have demonstrated such a rotational perturbation effect on M1 and E2 transitions as well as on level energies in ^{167}Er.[1] This perturbation effect is dependent on signature r: a quantum number classifying rotational spectra which is defined as $r = \exp(-i\pi\alpha)$, where $I = \alpha$ mod2; I is the spin value of the rotational state.[2] However, the investigations on ^{159}Tb[3] and ^{173}Yb[4] have revealed that the effect is rather weak in these nuclei. The ground states of these nuclei originate from the $d_{5/2}$ and $h_{9/2}$ orbits. Thus, this effect is expected to be strongly dependent on the single-particle orbits which characterize the bands. It is interesting to study systematically

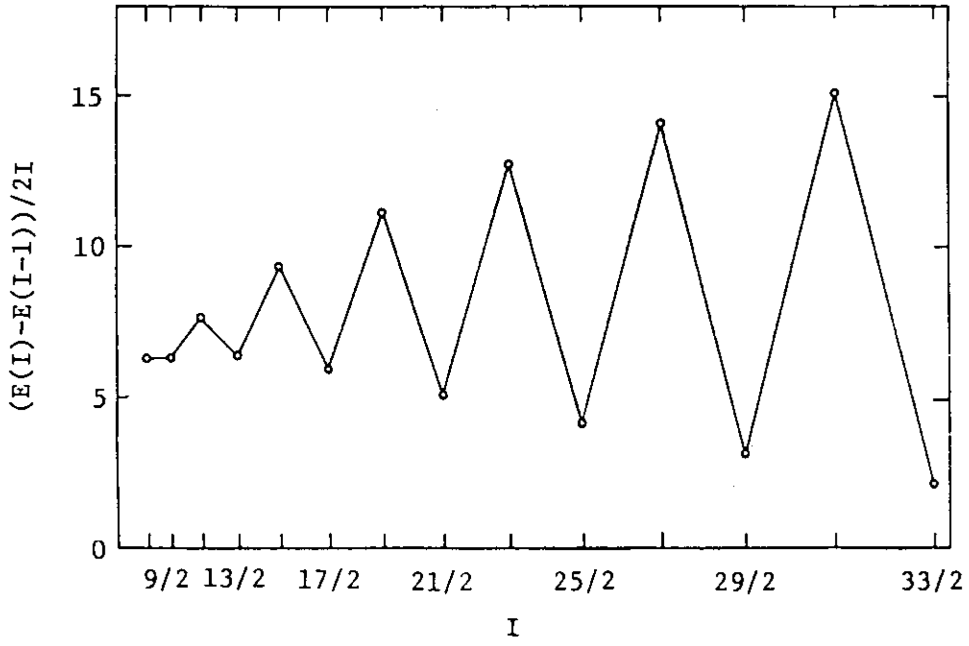

Fig. 1 Energy differences as a function of spin.

how the single-particle orbits affect the rotational states.

The nucleus ^{161}Dy is the one whose ground-state rotational band is built on the $i_{13/2}$ neutron orbit as is the case with ^{167}Er. Therefore we are interested in whether there is the same signature dependence in ^{161}Dy as observed for ^{167}Er. The ground-state rotational band of ^{161}Dy has been established up to spin 33/2,[5] and an energy plot: $(E(I) - E(I-1))/2I$ vs I^2 depicted in Fig. 1 shows such a remarkable signature dependence as in ^{167}Er. However, nuclear lifetimes are not available for highly excited states with higher spins than 9/2. In order to measure their lifetimes, we are making multiple Coulomb excitation experiment on ^{161}Dy. Here we present our preliminary results.

The nucleus ^{161}Dy was multiply Coulomb-excited with a ^{81}Br beam of 305 MeV from the JAERI tandem accelerator. The target was a self-supporting metallic foil of 2.5 mg/cm^2 in thickness. Deexcitation γ rays were measured with a germanium detector placed at 45° to the beam in coincidence with backward scattered projectiles which were detected at θ = 100°-150° to the beam with a plastic scintillator(Ω = 0.5 sr). Nuclear lifetimes were measured by the recoil distance method.[6] It should be stated that the Doppler-shift attenuation method[1,6] is inadequate for ^{161}Dy because some γ rays are too closely distributed to permit the lineshape analysis.

We have for the first time measured lifetimes of the $11/2^+$, $15/2^+$,

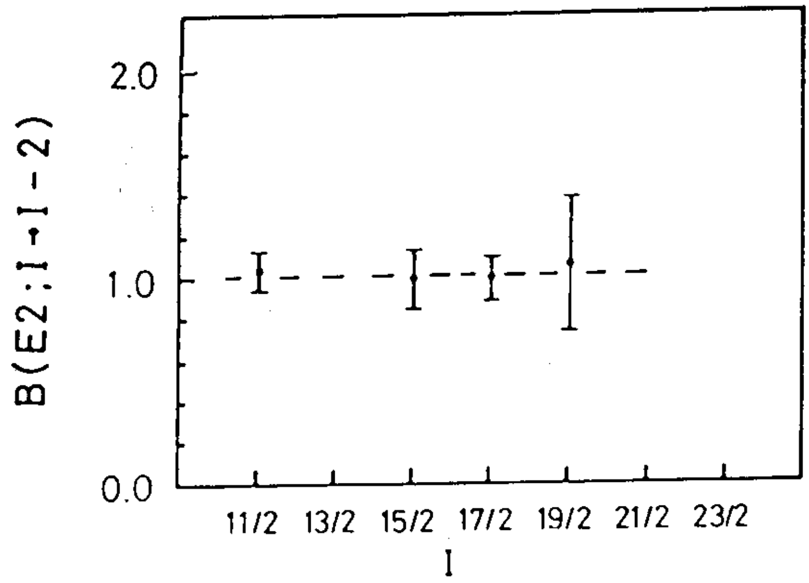

Fig. 2 B(E2;I→I-2) values of ^{161}Dy in unit of rigid-rotor values (Q_0 = 6.4 b).

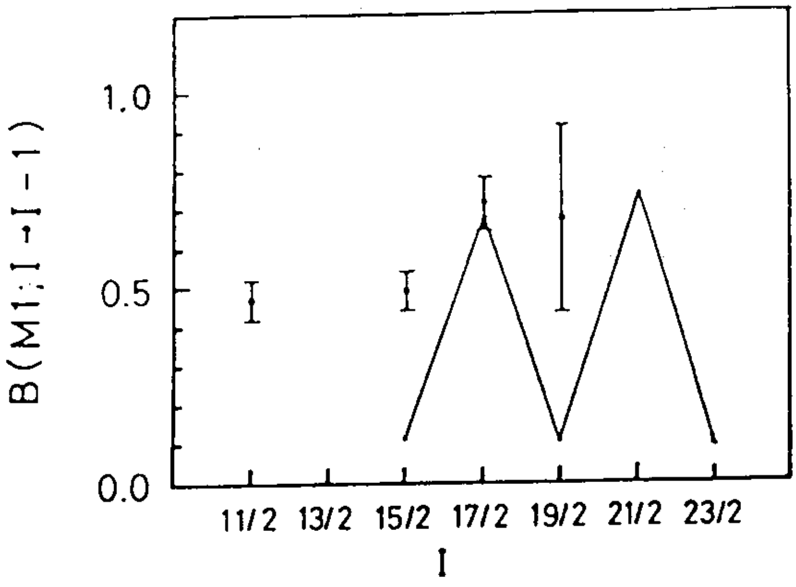

Fig. 3 B(M1;I→I−1) values of ^{161}Dy in unit of rigid-rotor values which are obtained by adopting $g_K - g_R = -0.55$.7) The solid line shows an extended particle-rotor model calculation8) performed by Hamamoto.

$17/2^+$ and $19/2^+$ states. (For the $13/2^+$ state intruder γ rays make it hard to deduce the true lifetime.) Preliminary results of stopover B(M1) and crossover B(E2) values are plotted in Fig. 2 and 3. It is obvious that crossover B(E2) values are close to the predictions of the Bohr-Mottelson model7) as seen from Fig. 2, where an intrinsic quadrupole moment of Q_0 = 6.4 b was adopted. The B(M1) values, however, appear to have some signature dependence, which is similar to that found earlier for ^{167}Er. This trend is qualitatively in agreement with the extended particle-rotor model calculation8) performed by Hamamoto but the oscillation amplitude of experimental values is much smaller than the calculated ones. In order to clarify this point, higher spin states will be studied through multiple Coulomb excitation with beams of ^{58}Ni or ^{81}Br.

References

1) M. Ohshima, E. Minehara, M. Ishii, T. Inamura, and A. Hashizume, Nucl. Phys. A436 (1985) 518.

2) M.J.A. de Voigt, J. Dudek, and Z. Szymanski, Rev. Mod. Phys. 55 (1983) 949.

3) R. Chapman, J.R. Leslie, M. Maynard, P. Skensved, D. Ward and J.F. Sharpey-Schaffer, Nucl. Phys. A397 (1983) 296.

4) A. Hashizume et al., priv. comm.

5) R.G. Helmer, Nuclear Data Sheets 43 (1984) 1.

6) for example, D.B. Fossan and E.K. Warburton, Nuclear Spectroscopy and Reactions, ed. J. Cerny, Part C (Academic Press, New York and London, 1974) p.307.

7) A. Bohr and B.R. Mottelson, Nuclear Structure Vol.2 (W.A.Benjamin, inc.,1975).

8) I.Hamamoto, Phys. Lett. 106B (1981) 281.

5.5 SIGNATURE DEPENDENCE OBSERVED IN ROTATIONAL LEVELS BASED ON A $f_{7/2}$ SINGLE-PARTICLE STATE IN ^{163}Dy

Masumi OSHIMA, Eisuke MINEHARA, Shiro KIKUCHI,
Takashi INAMURA* and Akira HASHIZUME*

Department of Physics, JAERI, *The Institute of Physical and Chemical Research

The Coriolis interaction acts most effectively on particles in high-spin orbits such as $i_{13/2}$ and $h_{11/2}$, leading to strong perturbation to a rotational band. So far this perturbation effect has been discussed mainly through the excitation energies and branching ratios and, recently, valuable data of E2 and M1 intraband transition probabilities of such high-spin rotational bands are being obtained.1-3) Rather few data, however, are available for lower-spin orbits. The rotational perturbation effect on such orbits are believed to be rather weak. However, in order to identify this effect, it is important to study systematically how the single-particle orbits affect the rotational levels.

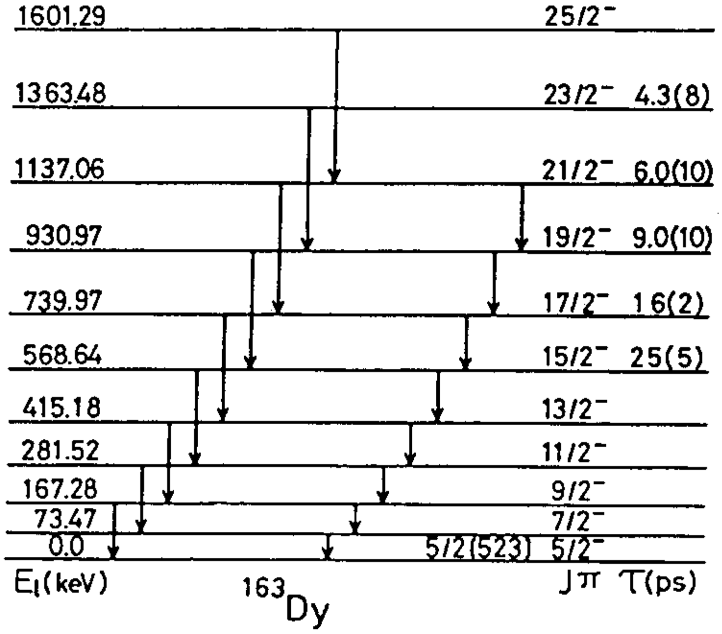
1601.29
25/2⁻
1363.48
23/2⁻ 4.3(8)
1137.06
21/2⁻ 6.0(10)
930.97
19/2⁻ 9.0(10)
739.97
17/2⁻ 16(2)
568.64
15/2⁻ 25(5)
415.18
13/2⁻
281.52
11/2⁻
167.28
9/2⁻
73.47
7/2⁻
0.0
5/2(523) 5/2⁻
Eₗ(keV)
163Dy
Jπ τ(ps)

Fig. 1 A level scheme of the ground-state rotational band of ^{163}Dy.

For this purpose we undertook a Coulomb-excitation experiment on ^{163}Dy of which ground-state rotational band is based on $f_{7/2}$ single-particle orbit.

A self-supporting metallic target of ^{163}Dy (92.3 % enriched and about 30 mg/cm^2 thick) was bombarded with beams of 160-MeV ^{35}Cl and 250-MeV ^{58}Ni from the JAERI tandem accelerator. γ-γ coincidence measurements were performed with three conventional germanium detectors which were placed at 0°, 90° and -90° to the beam. A level scheme for the ground-state rotational band was constructed on the basis of the coincidence results as shown in Fig. 1. The levels higher than the $17/2^-$ member were newly established.

To make spin assignments, angular distributions of γ-rays were measured at seven angles between 0° and 90° to the beam. E2/M1 mixing ratios have been extracted as follows. Since all crossover transitions decaying from the $9/2^-$ to $23/2^-$ states are of pure E2, ratios of the experimental A_2 values and calculated ones for complete alignment give attenuation factors of nuclear alignment for these states. Mixing ratios of the M1+E2 stopover transitions were extracted from analysis of the angular distributions utilizing the attenuation factors for individual states. For the $17/2^- \rightarrow 15/2^-$ transition the mixing ratio was not available from the analysis of the angular distribution in the situation discussed above. Thus we adopted a mean value of δ's for the $9/2^- \rightarrow 7/2^-$ and $13/2^- \rightarrow 11/2^-$ transitions, which have the same signature ($\alpha=1/2$) as the $17/2^- \rightarrow 13/2^-$. This may be justified by the fact that the mixing ratios can be classified into two distinct groups, i.e., the mixing ratios are close to -2.7 and -1.7 for the favoured ($\alpha=1/2 \rightarrow \alpha=-1/2$) and the unfavoured ($\alpha=-1/2 \rightarrow \alpha=1/2$) transitions, respectively.

The experimental branching ratios and mixing ratios were converted to ratios of B(M1)/B(E2), which are plotted in Fig. 2. Here a signature dependence is clearly observed. This is very interesting because so far no significant signature dependence was observed for the bands built on such a low-spin single-particle orbit as $f_{7/2}$. In order to see which

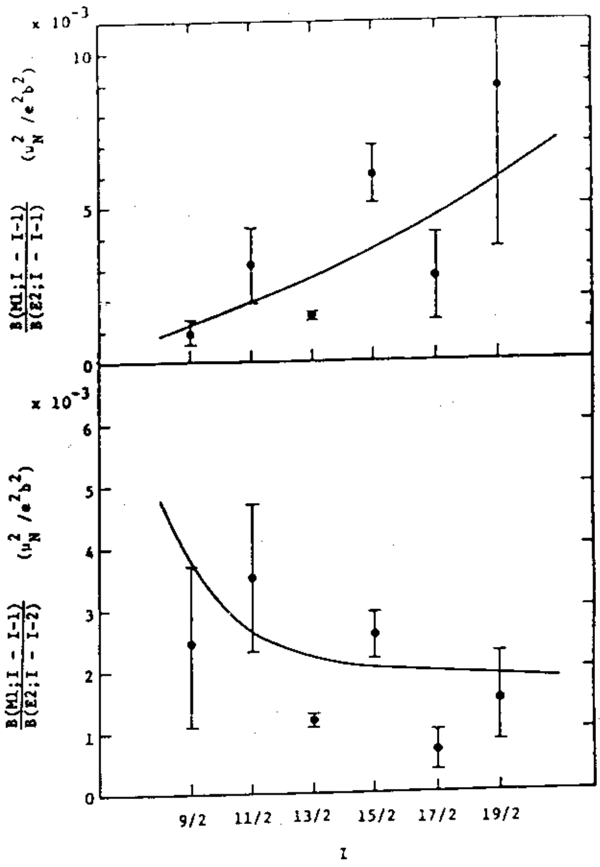

Fig. 2 a) B(M1;I→I-1)/B(E2;I→I-1) ratios obtained from mixing ratios. b) B(M1;I→I-1)/B(E2;I→I-2) ratios obtained from branching and mixing ratios.

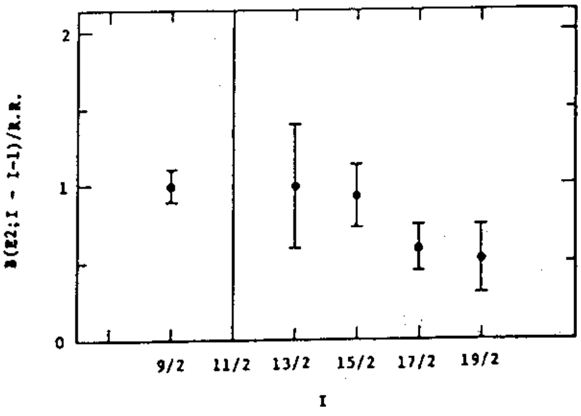

Fig. 3 B(E2;I→I-1) values for stopover (M1+E2) transitions devided by rigid-rotor values(see the text).

type of transition, M1 or E2, causes such a dependence, absolute transition probabilities have been deduced from the measurement of nuclear lifetimes. The nuclear lifetimes were determined from analysis of Doppler broadened γ-ray lineshapes. A γ-ray singles spectrum used for the analysis was taken with a Compton-suppression spectrometer that was placed at 0° to the beam. The detailed formulation of the analysis is described in ref. 4. The lifetimes obtained for the $13/2^-$ to $23/2^-$ states are summarized at the right side of Fig. 1.

The experimental B(M1) and B(E2) values were extracted from the nuclear lifetimes, branching ratios and E2/M1 mixing ratios and are presented in Figs. 3, 4 and 5. The rigid-rotor values used in the figures are obtained by adopting g factors$^{6)}$ of g_K=0.25, g_R=0.27 for B(M1) values and an intrinsic quadrupole moment of Q_0=7.0 b for B(E2) values.

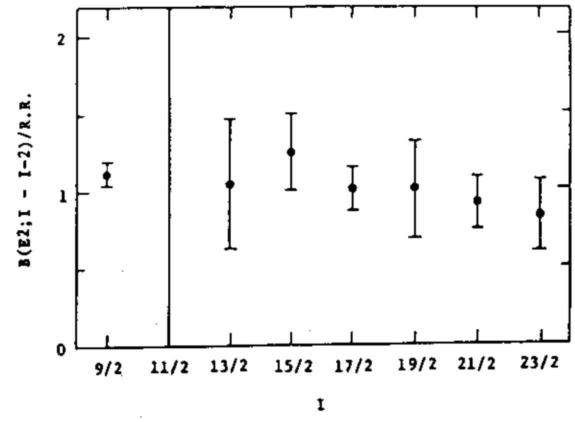

Fig. 4 B(E2;I→I-2) values for crossover (E2) transitions devided by rigid-rotor values(see the text).

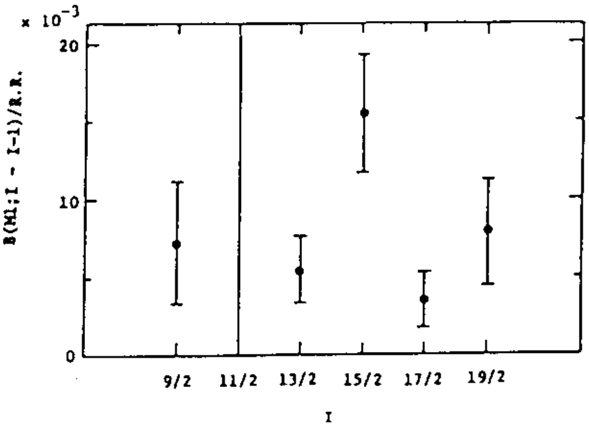

Fig. 5 B(M1;I→I-1) values for stopover (M1+E2) transitions devided by rigid-rotor values(see the text).

The B(E2;I → I-1) and B(E2;I → I-2) values in Fig. 3 and 4 seem to show a small tendency to decrease as spin, but it may be stated that the experimental values coincide with the prediction of the simple rotation-particle coupling model (cited as rigid-rotor values in the figure) within the experimental errors. Here we emphasize that there is no strong signature dependence in these values. Thus it is concluded that the remarkable signature dependence observed in the B(M1)/B(E2) ratios of Fig. 2 is primarily due to the B(M1). While absolute B(M1) value at spin 11/2 is lacking, the overall tendency seen in Fig. 5 is consistent with the B(M1)/B(E2) ratios, supporting the above statement. The phase of the oscillation coincides with those observed for $i_{13/2}$ or $h_{11/2}$ single-particle orbits,[1-3] i.e., a transition of the type I(α=1/2) → (α=-1/2) is reduced and the I(α=-1/2) → I-1(α=1/2) is enhanced.

The behavior of the B(M1) values presents a puzzle. There is neither signature dependence in the excitation energies nor in the B(E2) values. In many nuclei[1-3] where the perturbation effect of rotation is postulated, the signature dependence was observed for the excitation energies as well as the B(M1) values.

In summary, a significant signature dependence was observed for reduced M1 transition probabilities in the ground-state rotational band in ^{163}Dy. That is considered to be ascribed to the perturbation effect of rotation. It should be pointed out that the tendency observed for the B(M1) values coincides with the one predicted for the $i_{13/2}$ odd-A nuclei.1-3) Similar systematic data will be valuable for studying the rotational perturbation of nuclear system. It is of particular interest to study systematically whether the observed transition probabilities are reproduced quantitatively in a given model.

References:

1) J.Kownacki, J.D.Garrett, J.J.Gaardhoje, G.B.Hagemann, B.Herskind, S.Jonsson, N.Roy, H.Ryde and W.Walus, Nucl. Phys. A394 (1983) 269.
2) G.B.Hagemann, J.D.Garrett, B.Herskind, J.Kownacki, B.M.Nyako, P.L.Nolan and J.F.Sharpey-Schafer, Nucl. Phys. A424 (1984) 365.
3) M.Oshima, E.Minehara, M.Ishii, T.Inamura and A.Hashizume, Nucl. Phys. A436 (1985) 518.
4) T.Inamura, F.Kearns and J.Lisle, Nucl. Instr. Meth. 123 (1975) 529.
5) A.Bohr and B.R.Mottelson, Nuclear Structure Vol. 2 (Benjamin, New York, 1975).

5.6 TRANSFER CROSS SECTIONS FOR $^{28}Si+^{58,62}Ni$ REACTIONS

Yasuharu SUGIYAMA, Yoshiaki TOMITA, Hiroshi IKEZOE, Kazumi IDENO, Naomoto SHIKAZONO, Norihisa KATO*, Hiroshi FUJITA*, Tsuyoshi SUGIMITSU* and Shigeru KUBONO**

Department of Physics, JAERI, *Department of Physics, Kyushu University, **Institute for Nuclear Physics, University of Tokyo

Quasielastic reaction cross sections were measured[1)] for $^{28}Si+^{58,62}Ni$ at the JAERI tandem accelerator in order to investigate correlation between the quasielastic reaction strength and the enhanced subbarrier fusion cross section[2,3)]. The ^{28}Si beam energy was 110 MeV which was about 40% higher than the Coulomb barrier . The energy spectra were measured with an energy resolution of ~250 keV by using the heavy-ion spectrograph[4)] "ENMA". The spectrograph has the characteristic feature that the kinematic momentum shift k is compensated well, so that a high energy resolution is achieved over a wide range of k. The outgoing particles were momentum analyzed in the spectrograph ENMA and detected in the focal plane detector[5)]. The entrance slits of the spectrograph were opened 2.2° horizontally and vertically which corresponded to a solid angle of 1.6 msr. From a measurement of total energy E, energy loss δE and position $B\rho$ an unambiguous determination of mass, atomic number, Q value and atomic charge state q were possible. Four nuclei ^{29}Si, ^{30}Si, ^{27}Al and ^{26}Mg were observed in addition to elastically scattered ^{28}Si. Other reaction products could not be identified because of their small yields.

Energy spectra obtained for the 12^+ charge state at $\theta_{lab}=34.7°$ from the reactions $^{62}Ni(^{28}Si,^{29}Si)^{61}Ni$, $^{62}Ni(^{28}Si,^{30}Si)^{60}Ni$, $^{58}Ni(^{28}SI,^{29}Si)^{57}Ni$ and $^{58}Ni(^{28}Si,^{30}Si)^{56}Ni$ are shown in Fig.1. An energy resolution of ~250 keV made it possible to resolve transitions to low-lying discrete levels. In the reaction $^{62}Ni(^{28}Si,^{29}Si)^{61}NI$, however, transitions to the ground state and the $5/2^-$ state at 0.067 MeV in ^{61}Ni were not resolved. We labeled these transitions as the ground state transition for convenience. It is seen that the neutron-transfer strength is concentrated in transitions to a few final states. Peaks marked with ^{28}Si correspond to elastic scattering feed through the mass gate for ^{29}Si.

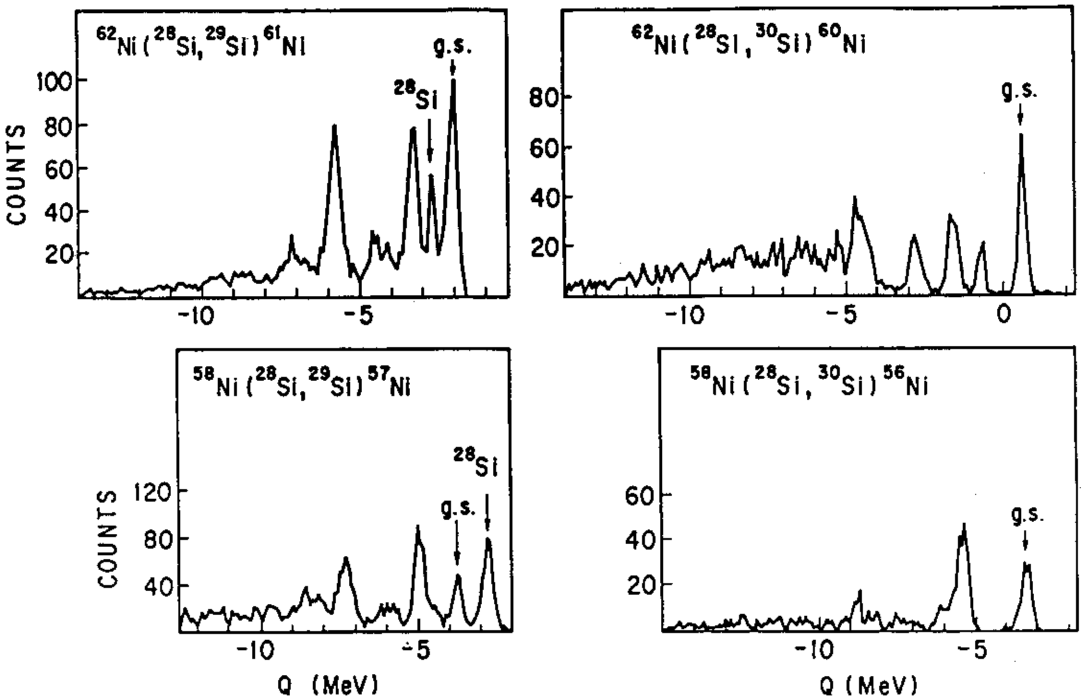

Fig.1 Spectra obtained for the 12^+ charge state from the (^{28}Si,^{29}Si) and (^{28}Si,^{30}Si) reactions on ^{58}Ni and ^{62}Ni at $\theta_{lab}=34.7°$.

Angular distributions for the elastic and inelastic scattering to the first 2^+ states in ^{58}Ni,^{62}Ni and ^{28}Si are shown in Fig.2. For these scattering the coupled-channels calculations were performed with the code Ptolemy$^{6)}$. The results are shown by solid lines in Fig.2. The potential parameters obtained are as follows: V=50 MeV, W=10 MeV, r_0=1.2 fm, a=0.65 fm. The imaginary potential depth W is reduced by one half compared to that obtained at E_{lab} =140 MeV$^{7)}$.

Angular distributions of the ground state transitions for the neutron-pickup reactions ^{58,62}Ni(^{28}Si,^{29}Si) and ^{58,62}(^{28}Si,^{30}Si) are shown in Fig.3. Absolute values of the

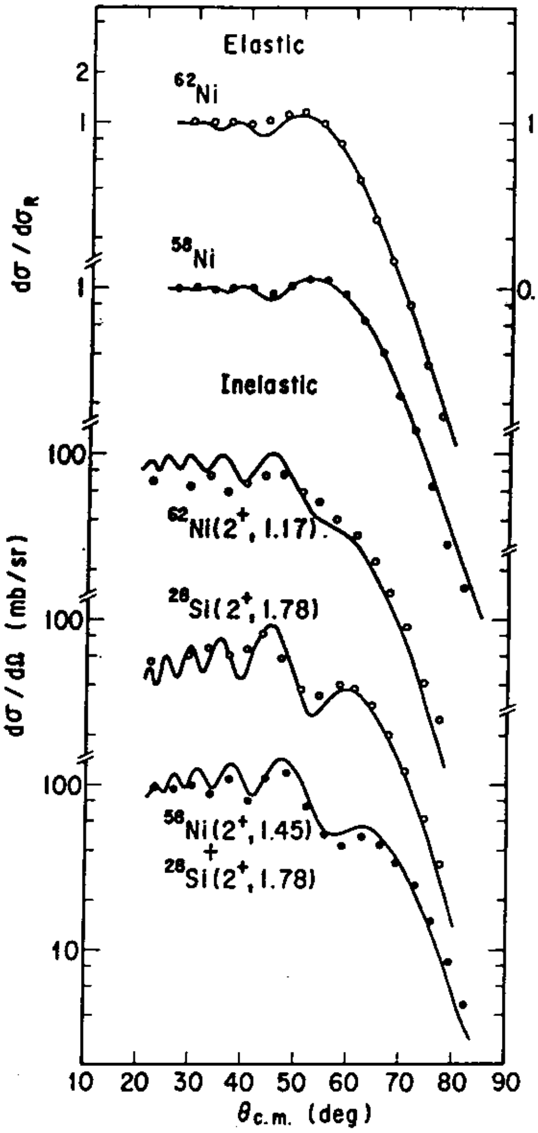

Fig.2 Angular distributions for the elastic and inelastic scattering. The solid lines are coupled-channels calculations.

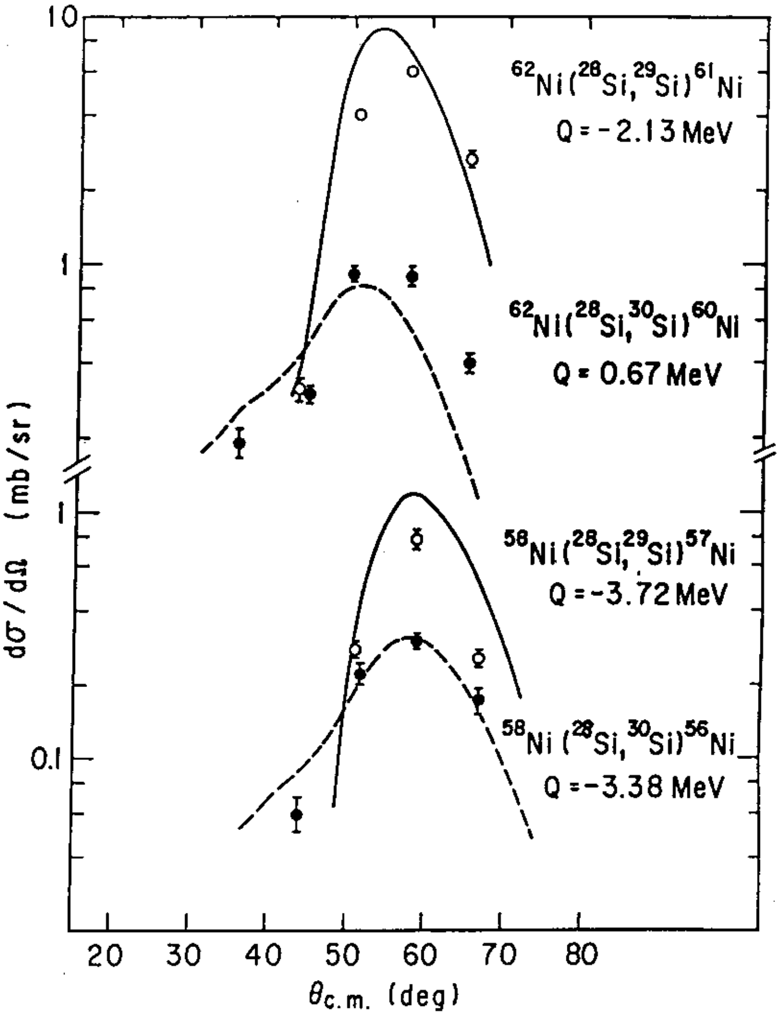

Fig.3 Angular distributions of the ground state transitions from the neutron-pickup reactions. Solid and dashed lines are DWBA calculations.

cross sections were derived by normalizing the yields of the pickup reactions to those of the elastic scattering which were measured simultaneously. A strong isotope dependence in the reaction cross sections is observed . The cross sections for the one-neutron and two-neutron pickup reactions in the system ^{28}Si+^{62}Ni are larger than those in the system ^{28}Si+^{58}Ni by factors of about 8 and 3, respectively. Despite of the positive ground state Q value of 0.67 MeV in the system ^{28}Si+^{62}Ni, the transition to the ground state in the reaction ^{62}Ni(^{28}Si,^{30}Si)^{60}Ni is smaller than that in ^{62}Ni(^{28}Si,^{29}Si)^{61}Ni by a factor of about 5. Angular distributions for transitions to others states in the neutron-pickup reactions were similar to those of their ground state transitions.

DWBA calculations for the ground state transitions were performed with the code Ptolemy. The results are shown by solid and dashed lines in Fig.3. The spectroscopic factors obtained from the (p,d) and (d,p) reactions are used for the one-neutron pickup reaction (^{28}Si,^{29}Si). For the two-neutron pickup reaction, we set the spectroscopic factors to one and used a cluster wave function for the transferred dineutron. The isotope dependence of the reaction cross sections results mainly from the different Q values between the systems ^{28}Si+^{58}Ni and ^{28} Si+^{62}Ni. Angle- and energy-integrated cross sections for the one-neutron pickup reaction (^{28}Si,^{29}Si) are also explained well by the DWBA calculations.

References

1) Y.Sugiyama et al., to be published.
2) S.G.Steadman,ed.,Intern.Conf.on Fusion Reactions below the Coulomb Barrier, Lecture Notes in Physics, Vol.219(Springer, Berlin, 1985).
3) A.M.Stefanini et al., Phys. Rev. C30(1984)2088.
4) Y.Sugiyama et al.,Nucl.Instrum.& Methods 187(1981)25; Z.Phys.A322(1985)579.
5) E.Takekoshi et al.,Nucl.Instrum.& Methods A237(1985)512.
6) D.H.Gloeckner et al., Argonne National Laboratory report No. ANL-76-11(1978), unpublished; M.J.Rhoades-Brown et al., Phys.Rev.C21(1980)2417,2436.
7) P.D.Bond et al., Phys. Lett. 114B(1982)423.

5.7 COINCIDENCE MEASUREMENTS OF LIGHT PARTICLES AND EVAPORATION RESIDUES IN THE SYSTEM $^{16}O + ^{27}Al$

Hiroshi IKEZOE, Naomoto SHIKAZONO, Yoshiaki TOMITA,
Yasuharu SUGIYAMA and Kazumi IDENO

Department of Physics, JAERI

Incomplete fusion in the reaction of 150 MeV ^{16}O with ^{27}Al¹⁾ was investigated by measuring light particles (proton and α-particle) in coincidence with evaporation residues (ER). Energy spectra of α-particles in coincidence with each ER are shown in Fig. 1 together with the results of the statistical model calculation (solid lines) using the program code LILITA 2). From the figure small but definite high energy components for each residue are seen at the most forward angle $\Theta_\alpha = -13^\circ$, where the negative angle indicates the opposite side of the detector position of ER with respect to the beam direction. The slopes of the energy spectra decrease monotonously in a high energy region and no energy bump corresponding to the beam velocity α-particles is seen in contrast to the results of ref. 3).

The energy-integrated angular distribution of the α-particles in coincidence with ER of mass numbers $28 \leqq A \leqq 38$ is shown in Fig. 2. Yields observed at the large negative angles ($\Theta_\alpha \leqq -40^\circ$) were small compared with the statistical model calculation (solid line). On the other hand, large yields were observed at the forward angles and the same side with the detector position of ER ($\Theta_{HI} = +8^\circ$). It was assumed that this enhancement of the α-particle yields was ascribed to the incomplete fusion process and the calculated line was multiplied by a factor of 0.8 to reproduce the data measured at the negative angles ($\Theta_\alpha \leqq -45^\circ$). An extra component (dashed-dotted line) was obtained after subtracting the complete fusion component (dotted line) from the data. It is noted that this extra component is forward peaked and roughly symmetric around the beam direction.

Energy spectrum of protons in coincidence with ER showed an enhanced low energy component, indicating that the effective potential barrier for the proton emission may be lower than the present calculation using the optical model potential of ref. 4). The angular distribution of protons in coincidence with ER showed a non-compound component at the forward angles, which was small compared with the forward peaked component of the α-particles.

The present results suggest that the incomplete fusion process observed in the reaction of 150 MeV $^{16}O + ^{27}Al$ is mainly caused by the forward emissions of the energetic α-particles. The ratio of the α-particle emission responsible for the incomplete fusion process to the total fusion process was estimated to be about 20%.

References

1) H.Ikezoe, N.Shikazono, Y.Tomita, K.Ideno, Y.Sugiyama and E.Takekoshi, Nucl. Phys. A444 (1985) 349.
2) J.Gomez del Campo and R.G.Stokstad, ORNL/TM-7295.
3) C.Gerschel, Nucl. Phys. A387 (1982) 297c.
4) F.G.Perey, Phys. Rev. 131 (1963) 745.

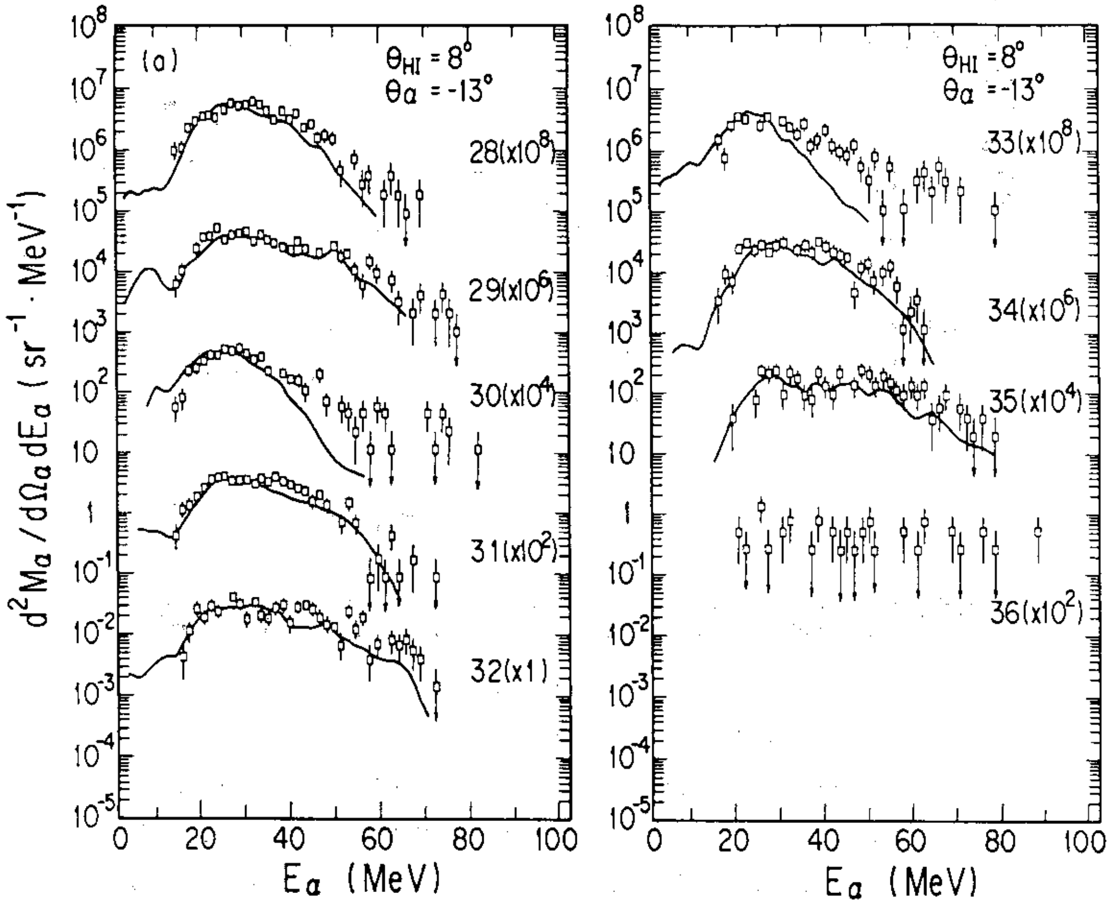

Fig. 1 Energy spectra of α-particles measured at $\Theta_{\alpha} = -13^{\circ}$ in coincidence with each evaporation residue, which was measured at $\Theta_{HI} = 8^{\circ}$. Numbers shown in the figure are the mass numbers of the residues. The ordinate shows the differential multiplicity and solid lines are the results of the statistical model calculation.

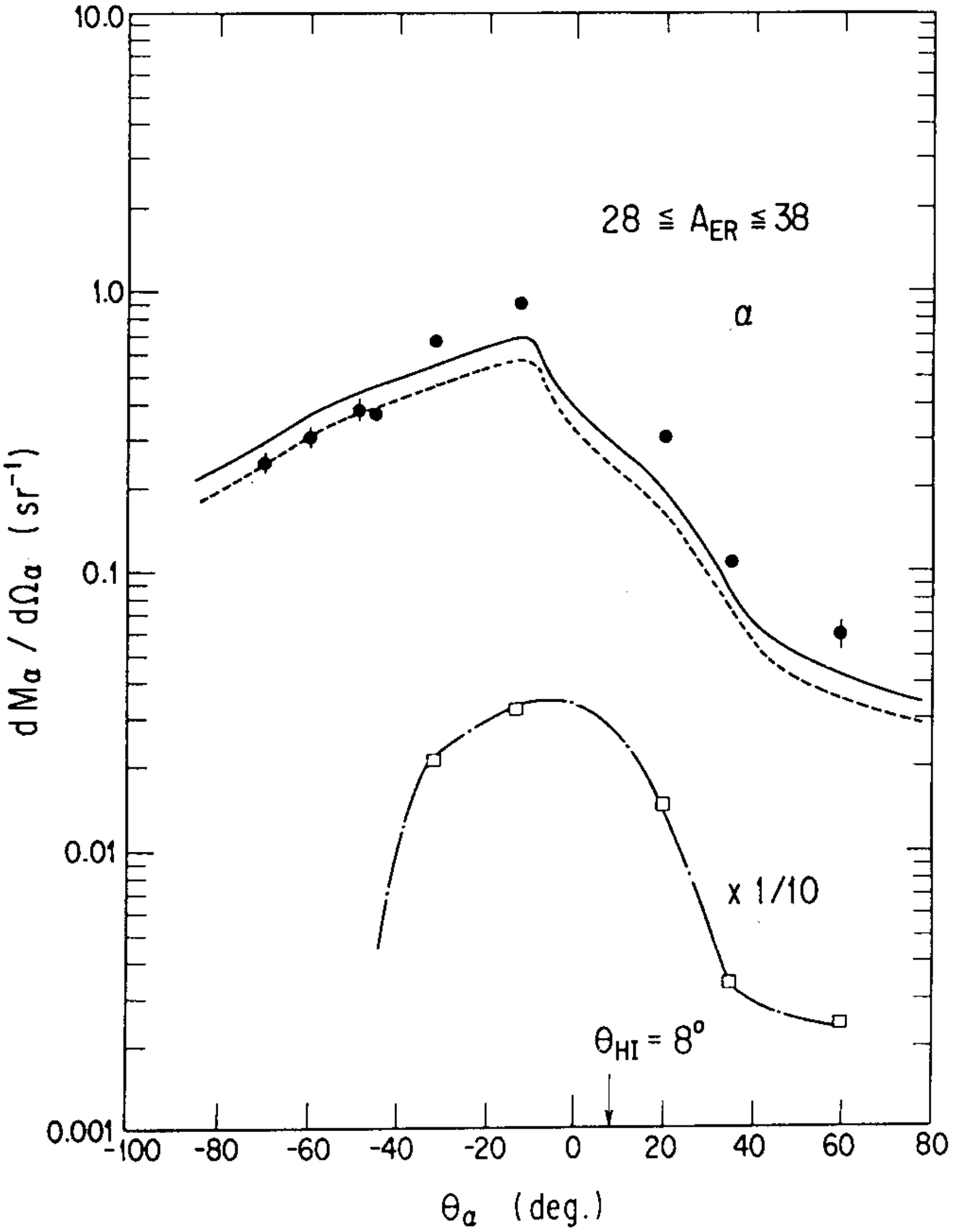

Fig. 2 Differential multiplicity of α-particles in coincidence with evaporation residues of mass $28 \leqq A \leqq 38$. Measured angle of the residue is shown by arrow. Solid line is the result of the statistical model calculation. Dashed line is multiplied by a factor of 0.8 of the calculated result (solid line). Dash-dotted line is obtained by subtracting the complete fusion component (dashed line) from the data.

5.8 COINCIDENCE MEASUREMENT OF DAMPED REACTION FRAGMENTS FOR THE SYSTEMS OF ^{35}Cl + ^{46}Ti and ^{37}Cl + ^{48}Ti

Kazumi IDENO, Yoshiaki TOMITA, Hiroshi IKEZOE, Yasuharu SUGIYAMA, Susumu HANASHIMA, Watalu YOKOTA*, Katsunori SUZUKI*, Mitsuhiko OGIHARA*, Tetsuro KOMATSUBARA*, S. M. LEE*, and Takashi MIKUMO*

Department of Physics, Japan Atomic Energy Research Institute, *Tandem Accelerator Center, University of Tsukuba

In the damped reaction a large fraction of incident energy is consumed by the excitations of the binary fragments from the composite system formed with the incident particle and target nucleus. For example, these excitation energies amount to about 50% of the incoming energy of 110 MeV for the ^{37}Cl + ^{48}Ti reaction$^{1)}$. Information on the transferred energies to the fragments is important to understand the energy damping process.

We determined the most probable Q-values and its widths ΔQ for various combinations of fragments for the systems of ^{35}Cl + ^{46}Ti and ^{37}Cl + ^{48}Ti at 180 and 200 MeV, using the JAERI tandem accelerator. For this purpose we measured the angular distributions of two coincident fragments in plane$^{1)}$. We also measured their kinetic energies and charges. Our inclusive measurement for the ^{37}Cl + ^{48}Ti system$^{2)}$ revealed a saturated behavior of the observed total kinetic energies (T.K.E.) of the fragments and a flat angular distribution at backward angles in the energy range of 160 to 200 MeV. In order to sample out such a general feature of the strongly damped reaction, we chose one of the coincident angles at θ_{lab} = 45 degrees. We used two sets of ΔE-E counter telescopes with ionization chambers. Isobutane gas of 17 torr was used. We built a position-sensitive Si-detector in one of the sets; this telescope covered the range of 25 to 50 degrees.

Fig. 1 shows the examples of the measured coincidence events. It is seen that missed charges from the fragments increase with

Fig. 1 Angular distributions of coincident events for the systems of ^{35}Cl + ^{46}Ti and ^{37}Cl + ^{48}Ti. One detector was placed at 45 degrees and the other one was moved. In the figure, z denotes the the charges of the fragments detected at the fixed angle of 45 degrees. The marks ●, ○, △, × and □ indicate the events with no charge missed, with one, two, three and four charges missed, respectively. The solid lines are to guide the eye.

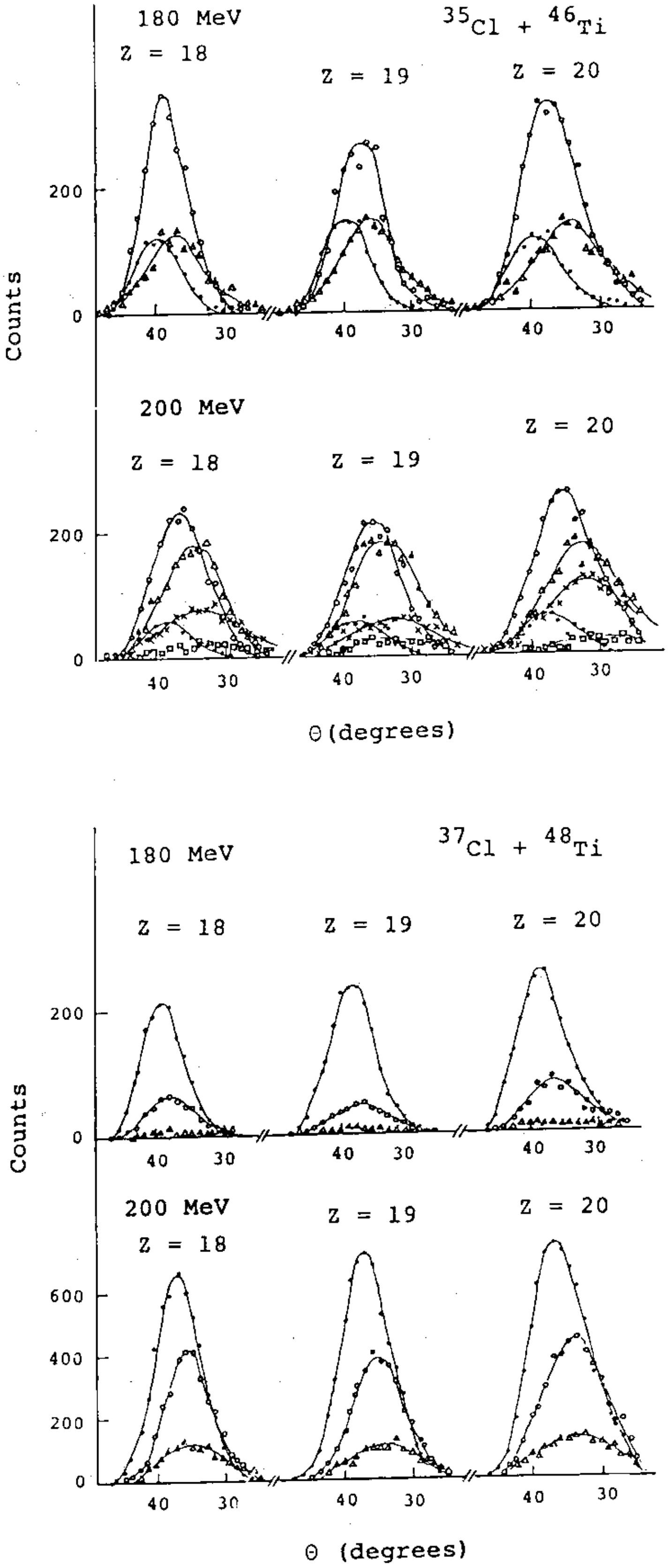

incoming energies. For the system of ^{35}Cl + ^{46}Ti a few charges are mainly missed, while for the system of ^{37}Cl + ^{48}Ti coincidence events with no charge missed are dominant. From these angular distributions we obtained the most probable Q-values, from which we deduced the T.K.E.

Fig. 2 shows the dependence of the T.K.E. on the charges of the fragments detected at 45 degrees. It is seen that the value of the T.K.E. decreases by about 5 MeV for each increment of the number of missed charges. It is naturally expected that from the states of the high Q-values more charges are likely to be emitted. The simple expression for the Coulomb energy is compared with the T.K.E. in the figure.

Fig. 3 shows the widths (FWHM) of the Q-values obtained from the angular distributions of the coincidence events shown in Fig. 1. The effect of the nucleon emissions from the fragments and the angular resolution to the observed widths was estimated to be 5 to 10%. We obtained $\Delta Q \approx 20$ MeV in the present cases.

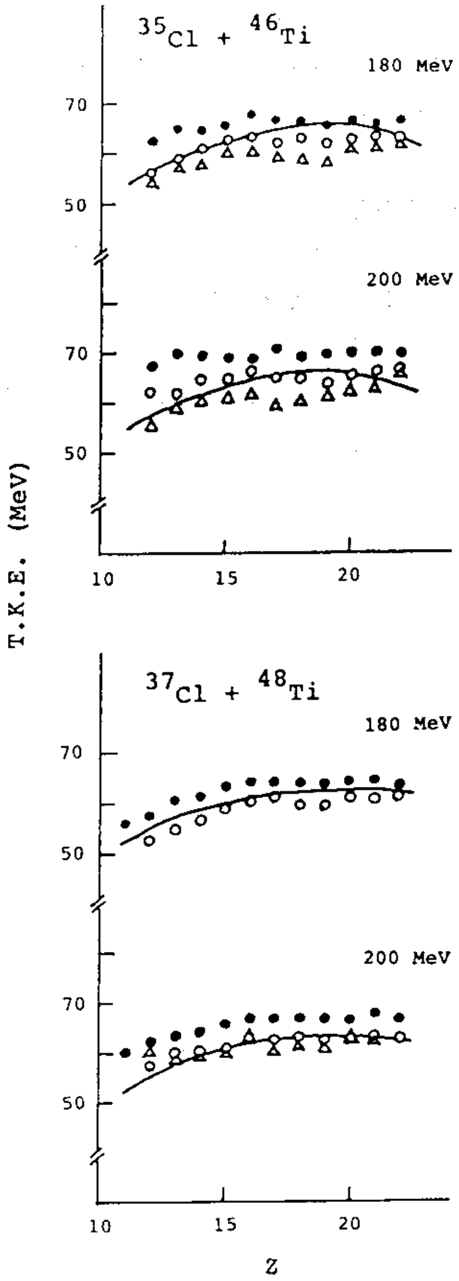

Fig. 2 The T.K.E. vs fragment charges detected at 45 degrees. The marks ●, ○ and △ have the same meaning as in Fig. 1. The solid lines represent the Coulomb energy for the two touched spheres with r_o = 1.2 fm.

More detailed comparison is being made between the two systems.

References

1) K. Ideno et al.: JAERI TANDEM Annual Report 1984, p. 155.

2) W. Yokota et al.: To be published.

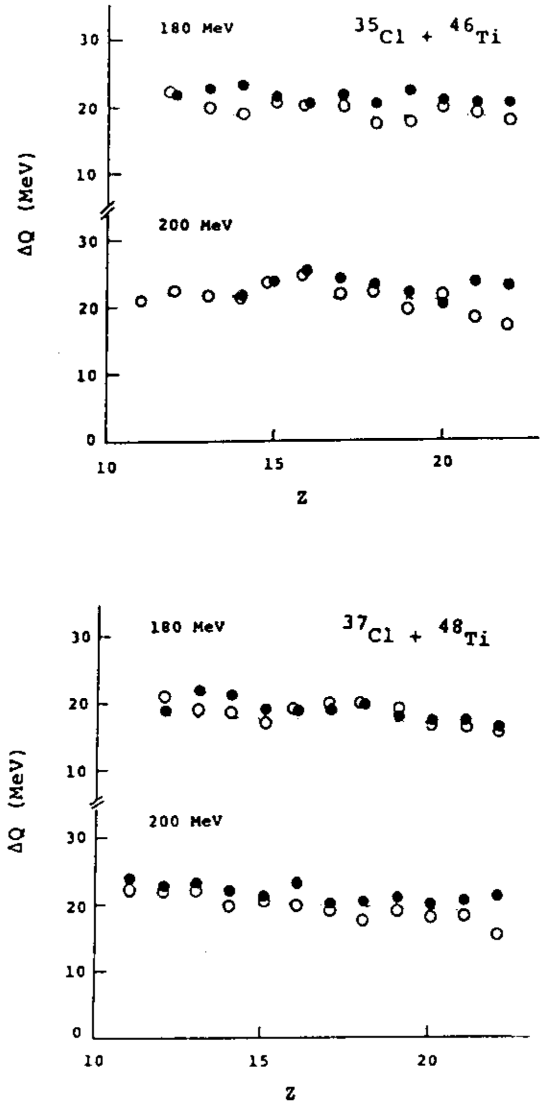

Fig. 3 ΔQ vs fragment charges detected at 45 degrees. The marks ● and ○ have the same meaning as in Fig. 1.

5.9 SHELL-MODEL EVIDENCE FOR THE EXCHANGE TERM IN THE INTERACTING BOSON-FERMION HAMILTONIAN

Takaharu OTSUKA, Nobuaki YOSHIDA,* Piet VAN ISACKER,**
Akito ARIMA** and Olaf SCHOLTEN***

Department of Physics, JAERI, *Department of Information Science, University of Tokyo, Hongo, Tokyo, **Department of Physics, University of Tokyo, Hongo, Tokyo, ***National Superconducting Cyclotron Laboratory, Michigan State University, East Lansing, Michigan, 48824, U.S.A.

The exchange term is the most important interaction between an odd particle and bosons in the Interacting Boson Fermion Model (IBFM), because it essentially determines excitation energies of band heads. The shell model origin of the exchange term has not been clarified, however. Consequently, it has not been known how large it should be from the microscopic point of view. We have recently succeeded in the microscopic formulation of the exchange interaction based on the OAI mapping method[2]. The quadrupole pairing interaction is shown to be the dominant source in and near spherical regions of the periodic table. The strength of this term calculated for the $0g_{9/2}$ orbit turns out to be in good agreement with the phenomenological fit. In fact, the IBFM energy levels obtained by the exchange term thus calculated are compared with the corresponding experimental levels in Fig. 1, demonstrating good agreement.

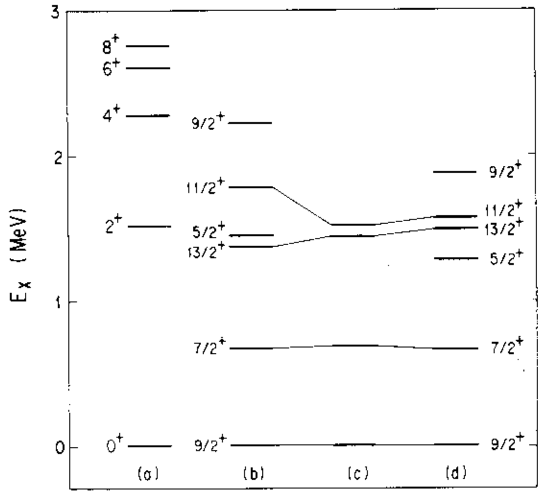

Fig. 1. Experimental energy levels of proton $0g_{9/2}$ states in (a) ^{92}Mo and (c) ^{93}Tc, compared with two IBFM calculations, (b) and (d), where Hamiltonians are derived from shell model Hamiltonians determined empirically from the experimental levels of ^{92}Mo. All multipole pairings of thus determined shell model Hamiltonian are included in (d), while only monopole and quadrupole pairings are taken in (b).

References

1. F. Iachello and O. Scholten, Phys. Rev. Lett., 43 (1979) 679.
2. T. Otsuka, A. Arima and F. Iachello, Nucl. Phys., A309 (1978) 1.

5.10 EXCITON MODEL APPROACH TO THE MOVING SOURCE MODEL

Akira Iwamoto

Department of Physics, JAERI

In the heavy-ion reaction with energies of 10-20 MeV par particle, energetic nucleons and light composite particles are emitted much more than those calculated from the evaporation model. Phenomenologically, the energy-angle double differential cross sections are fitted well by the moving source model[1]. To understand the physics of this model, we develop the model combining the exciton model and Fermi sphere consideration. The report on this work is given in Ref.2.

Systematics of the fast particle in incomplete fusion were examined in Refs.3 and 4 and it was found that the velocity of the light collision partner in cm frame is a good measure of the cross section and Fermi sphere consideration is useful. Thus we set up the initial condition of the exciton model by the Fermi sphere consideration where the reference frame is the compound nucleus. We define the projectile source and target source as independent emitters of the fast particles. In addition to the particle-hole numbers and excitation energies, we calculate the linear momenta of both sources by the phase space integration. In order to calculate the angular dependence, we generalize the emission rate expression used in the exciton model. The emission of the nucleon from the p-particle h-hole state of the parent nucleus which has the excitation energy E and momentum $\vec{P}$ is found proportional to $\omega(p-1,h,E-\varepsilon-Q,\vec{P}-\vec{q})$. This ω is the level density par linear momentum for the residual nucleus where $\vec{q}$ is the momentum of the emitted particles and Q is the Q-value of the reaction. Since ω is strongly decreasing function of the strength of the momentum, forward peaking of the fast particle is obtained naturally.

In figure 1, proton spectra of 215 MeV and 310 MeV incident energy ^{167}Au(^{16}O,p) reactions are shown. Data[1] and our calculation (solid line) are shown together with the evaporation calculation (dashed line). Addition of solid and dashed lines reproduces well the angle and incident energy dependence of the data. Such calculation was done for ^{90}Zr and

^{27}Al targets with several incident energies and similar good fitting was obtained. Our results resemble to those of the moving source model calculations. Thus we conclude that the present model is one way to understand the physics behind the moving source model. Instead of changing to the moving frame, use of the momentum dependent level density explains naturally the forward peaking of fast particles in the heavy-ion reactions.

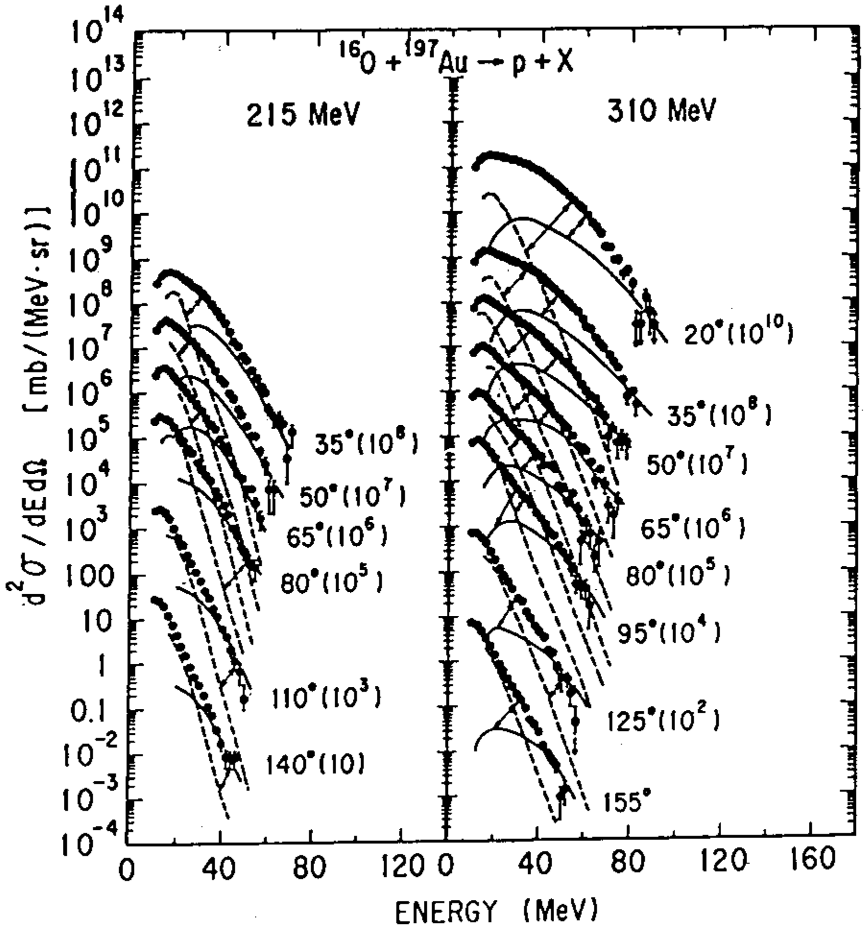

Fig.1. Double differential cross section for the reaction $^{197}Au(^{16}O,p)$.

References

1. T.C. Awes et al., Phys.Rev.,C25 (1982) 2361.
2. A. Iwamoto, JAERI- Internal Report
3. H. Morgenstern et al., Phys.Rev.Lett., 52 (1984) 1104.
4. G.S. Stephans et al., Phys.Lett., 161B (1985) 60.

Ⅵ NEUTRON PHYSICS

6.1 SCATTERING OF 14.9 AND 18.0 MEV NEUTRONS FROM ^{118}Sn

Satoshi CHIBA, Yoshimaro YAMANOUTI, Masayoshi SUGIMOTO,
Yutaka FURUTA, Motoharu MIZUMOTO, Mikio HYAKUTAKE*
and Shin IWASAKI**

Department of Physics, JAERI
*Faculty of Engineering, Kyushu University
**Faculty of Engineering, Tohoku University

Introduction

Using the JAERI tandem fast neutron time-of-flight(TOF) spectrometer, neutron elastic and inelastic scattering cross sections to low lying states of ^{118}Sn have been measured at incident neutron energies of 14.9 and 18.0 MeV.

The interaction of nucleons with tin isotopes has many interesting features because tin has a proton closed shell of Z=50[1,2,3]; (1)In the Lane consistent model, the optical potential has both isoscaler and isovector parts[4]. The parameter of the model have been payed strong attention in these years but not established well yet, especially for the isovector part. Because the tin isotopes have a wide variety of asymmetric coefficients, they are very sensitive to the isovector term. (2)Inelastic scattering of spherical even-even nuclei can be described by the vibrational model and the cross sections are calculated by distorted-wave Born approximation. Because the proton shell is closed, the deformation parameter deduced from neutron inelastic scattering will be different from that from proton scattering. The difference shows the extent to which the closed core is polarized.

The purpose of this study is to deduce the energy dependence of the optical potential and the deformation parameters for ^{118}Sn. Besides these interests, the neutron scattering cross section is very important because tin is one of the candidate materials for the superconducting magnets to be used in fusion reactor facilities.

Experiments

Neutrons were produced by the D(d,n)^{3}He reaction. The deuteron beam was extracted from the in-terminal ion source, chopped and bunched to 2ns and accelerated in single way. Average current was about 2 μA at a repetition rate of 2 MHz. A 1cm dia. and 3cm long deuterium gas target was used. The scattering sample was a metallic cylinder, 97.2% in ^{118}Sn, of 1.6cm in dia. and 3cm in height, loaned from ORNL. The sample was located at 12.5cm from the center of the gas target. The main detector system consisted of four 22cm diam and 35cm thick NE213 liquid scintillators contained in glass vessels. Two photomultipliers(RCA8854) viewed the rear and front end of the glass container for the purpose of time-compensation$^{5)}$. These detectors were placed in a shield collimator system with a 8m flight path.

Two monitor detectors viewed the neutron generating target directly for run-to-run flux normalization. Each monitor detector was 5cm dia. and 1.2cm thick NE213 scintillator coupled to the RCA8575 or Hamamatsu R594 photomultiplier(PM) tube.

The scattered neutron TOF spectra were taken at 25 laboratory angles between 15- and 160-deg. at 14.9 MeV, and 21 angles between 20- and 140-deg. at 18.0 MeV. Gas-out with sample-in spectra were also taken at 15- to 60- deg. at 14.9 MeV, but effect of the contaminant neutrons was negligibly small. Thus at other energy and angles gas-out measurements were not performed.

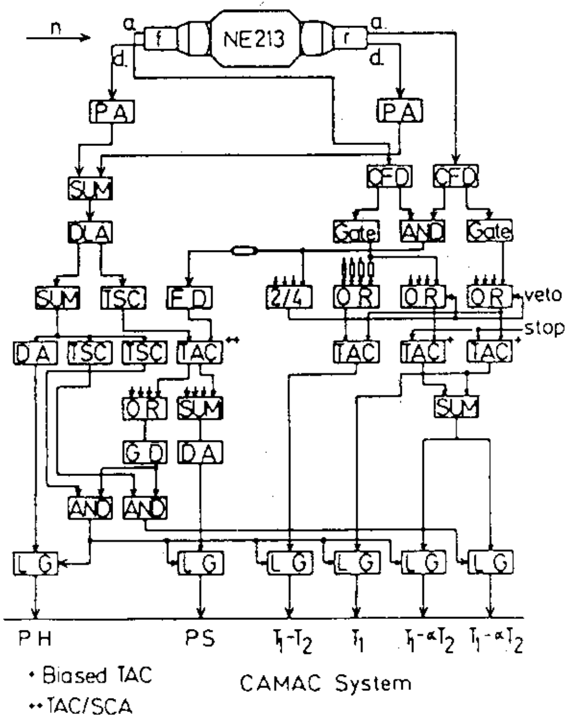

Fig.1 Block diagram of the electronics

The relative detection efficiency was measured by observing the angular distribution of the reaction D(d,n)^{3}He and comparing with previously measured values$^{6)}$. The incident neutron flux was measured at 0-deg. with the main detectors in order to normalize the relative cross sections.

The electronics circuitry used is shown in Fig.1. It consists of TOF unit, pulse shape discriminator and time-compensation circuitries. The time compensation was made by the formula$^{7)}$: $T=T_1-\alpha T_2$, where T_1 is the TOF of a event measured by the rear side PM, T_2 is that by the front one and α is the compensation constant which was determined experimentally. This is so-called "hardware" compensation. Other signals shown in this figure; PH, PS, T_1, T_1-T_2, are the same as those described previously7) and were used for "software" compensation. In the present study, however, the hardware compensation was enough to separate peaks.

The data were accumulated on magnetic tapes using the PDP 11/55-11/04-MBD(Microprogrammed Branch Driver)-CAMAC system.

Results

One of the TOF spectra, measured at E_n=14.9 MeV, 70-deg, is shown in Fig.2. In this figure background is already subtracted. The two peaks located at about 468 and 456 channels are those for elastically and inelastically scattered neutrons from the first 2^+ state, respectively. The third one at 442 ch. includes contributions from many levels. It is, however, a well known characteristic of inelastic nucleon scattering from even-even target nuclei that a one-phonon octupole vibrational state is strongly excited3). Hence we call this peak as the 3^- group. In Fig.3 shown is a TOF spectrum measured at E_n=18.0 MeV, 60-deg. Similarly, three peaks associated with elastic, first 2^+ and the 3^- group neutrons are seen. By fitting skewed Gaussian functions and linear background to these spectra, each peak yield was deduced. An example of the fitting is shown in Fig.3. By applying absolute normalization and corrections for finite geometry and dead time of ADC and TAC, cross sections were calculated. Theoretical analysis is now in progress.

References

1)J. Rapaport et al.:Nucl. Phys. A341(1980)56
2)R. W. Finlay et al.:Nucl. Phys. A338(1980)45
3)R. W. Finlay et al.:Nucl. Phys. A334(1980)257
4)A. M. Lane: Nucl. Phys. 35(1962)676
5)J. D. Carlson et al.:Nucl. Instr. Methods 147(1977)353
6)M. Drosg:Nucl.Sci. Eng. 67(1978)190
7)M. Sugimoto et al.:JAERI-M 85-104(1985)185

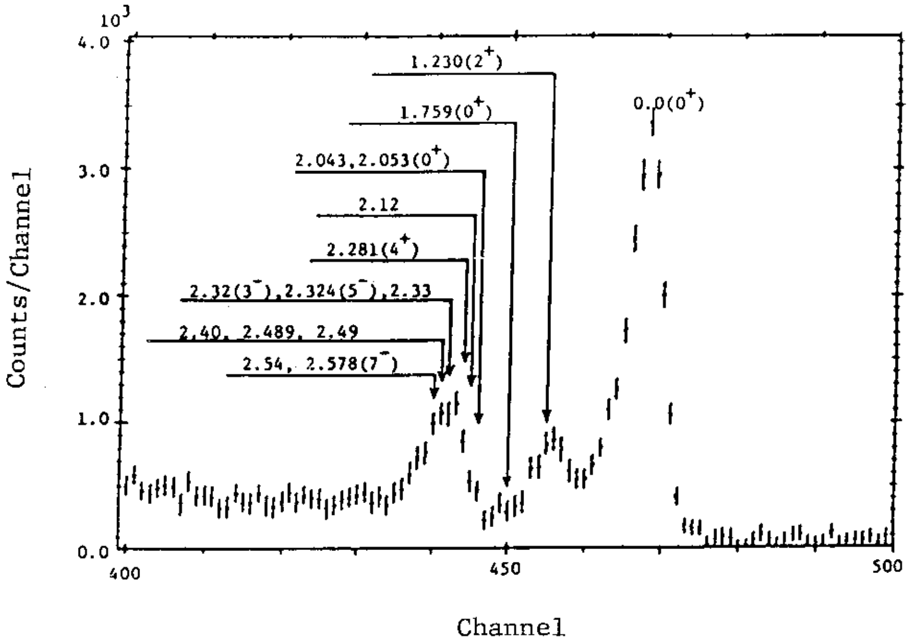

Fig.2 TOF spectrum measured at 14.9MeV, 70-deg.

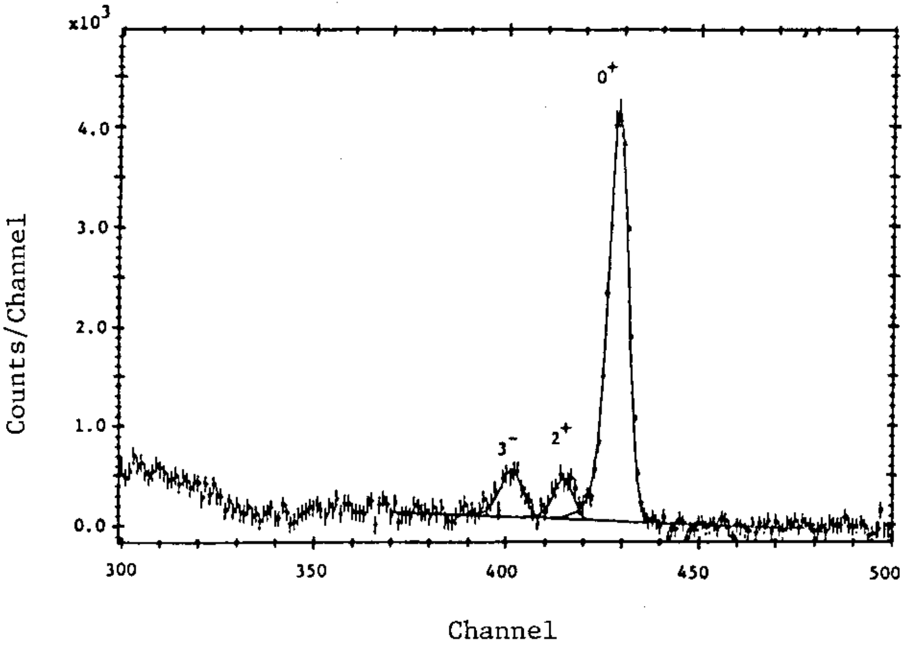

Fig. 3 TOF spectrum measured at 18.0MeV, 60-deg. Lines show the result of the peak fitting.

6.2 PRELIMINARY MEASUREMENTS FOR ELASTIC AND INELASTIC NEUTRON SCATTERING IN THE ENERGY REGION OF 30 MeV

Yoshimaro YAMANOUTI, Masayoshi SUGIMOTO
Satoshi CHIBA, Mikio HYAKUTAKE* and Shin IWASAKI**

Department of Physics, JAERI,
*Faculty of Engineering, Kyushu University
**Faculty of Engineering, Tohoku University

Differential cross sections for elastic and inelastic neutron scattering in the energy region above 10 MeV are very important to investigate the reaction mechanism for the neutron-nucleus interaction. Up to now, however, the elastic and inelastic neutron scattering cross sections have been obtained in the energy region below 26 MeV. Pulsed neutron beam in the energy region above 26 MeV is available from the JAERI tandem accelerator by using the ^{7}Li(p,n)^{7}Be reaction as an accelerator-based neutron source. The present neutron time-of-flight facility has been designed for the neutron scattering experiments in the energy region of 30 MeV, but has not been checked experimentally.

For the neutron scattering measurements in the energy region of 30MeV following properties of the neutron time-of-flight facility have been investigated experimentally.

1) Properties of the neutron producing target by using the ^{7}Li(p,n)^{7}Be reaction.
2) Shielding properties of the collimator and detector shield tank system.
3) Timing properties of the very large neutron detector.
4) Method to determine the neutron detection efficiency by the p-n scattering.

A pulsed beam of protons with burst duration of 2 nsec was provided by the tandem accelerator. The neutron detector is a 20 cm in diam. by 35 cm thick NE213 liquid scintillator viewed by photomultiplier tubes at both ends. Neutrons were observed by an array of these four neutron detectors. A lithium-metal target was used as a neutron producing target.

The zero degree neutron time-of-flight spectrum for the $^{7}Li(p,n)^{7}Be$ reaction was observed at an incident energy of 33 MeV. Fig.1 shows the time-of-flight spectrum. A main peak corresponding to the ground and 0.429 MeV excited states of ^{7}Be is seen in the figure. Neutron groups corresponding to the higher excited states of ^{7}Be are weakly excited in comparison with the main peak.

Measurements of elastically and inelastically scattered neutrons from carbon were made in order to check the shielding properties of the collimator and detector shield tank system. Fig.2 shows the time-of-flight spectrum for the scattering of 31 MeV neutrons from carbon at the 35° scattering angle. As is seen in fig.2, the neutron background without the sample is low compared with the sample-in spectrum.

Time-of-flight spectra for the H(n,n)H reaction using a polyethylene sample have been measured at 31 MeV for obtaining the detection efficiency. A typical time-of-flight spectrum for the H(n,n)H reaction is shown in fig.3. Neutron peaks corresponding to carbon are well resolved from that corresponding to hydrogen at this scattering angle.

The result of the preliminary experiment showed that the present time-of-flight facility was proved to be useful for the measurements of neutron scattering in the energy region of 30 MeV. Scattering measurements in this energy region will be made on light nuclei in the near future.

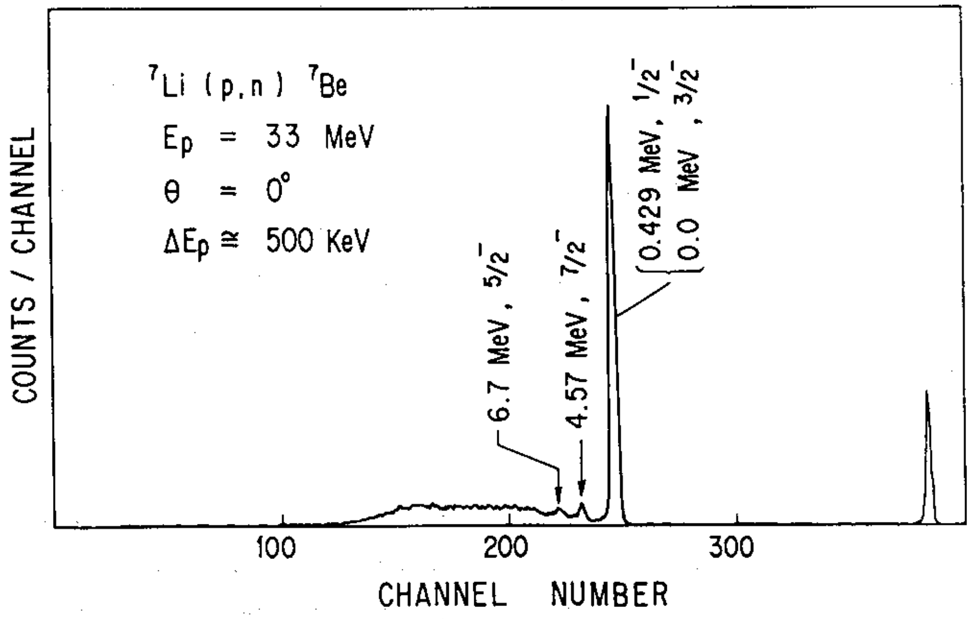

Fig.1 Zero degree time-of-flight spectrum for the $^{7}Li(p,n)^{7}Be$ reaction at E_p=33 MeV.

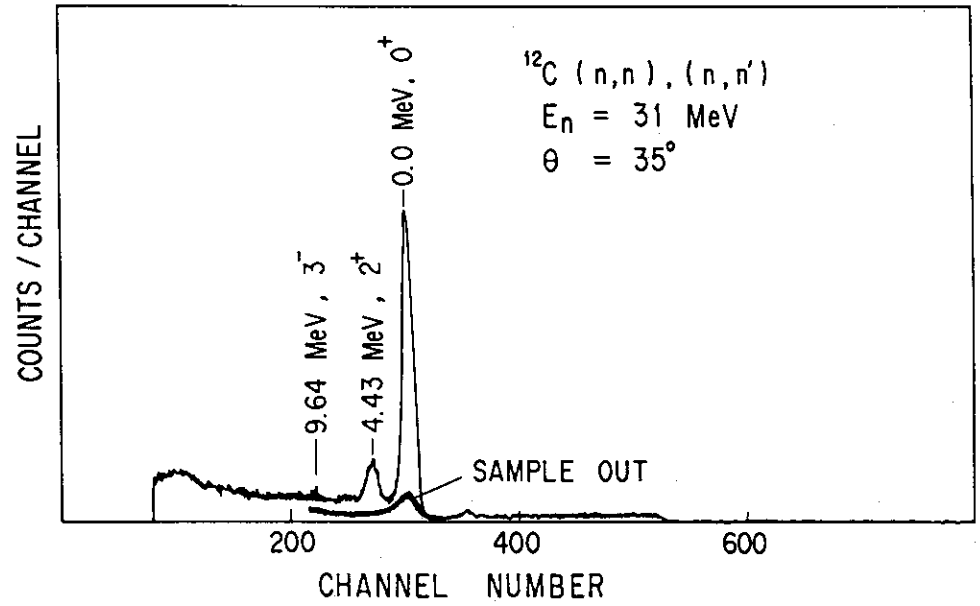

Fig.2 Time-of-flight spectrum of neutrons scattered from ^{12}C at E_n=31 MeV. Background spectrum without scattering sample is also shown in the figure.

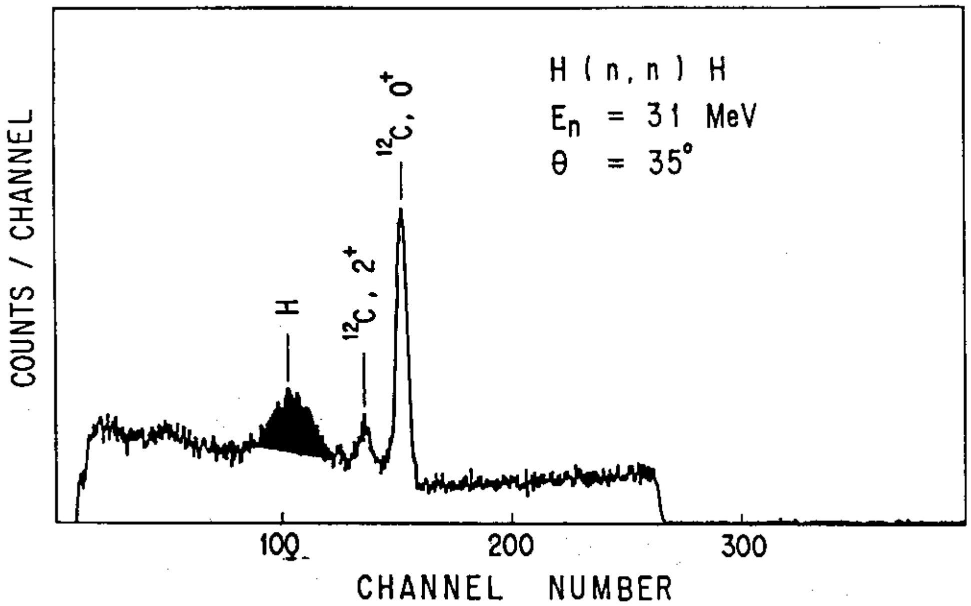

Fig.3 Time-of-flight spectrum from polyethylene. Peak with dark shading corresponds to neutrons for the H(n,n)H reaction at E_n=31 MeV.

6.3 MEASUREMENTS OF GAMMA-RAY PRODUCTION CROSS SECTIONS

Motoharu MIZUMOTO, Yoshimaro YAMANOUCHI, Masayoshi SUGIMOTO,
Satoshi CHIBA, Yutaka FURUTA and Yuuki KAWARASAKI

Department of Physics, JAERI

Importance of the gamma-ray production cross sections has been long recognized in the nuclear data committee for the evaluation of JENDL-3$^{1)}$. These nuclear data are necessary to calculate the radiation shielding and the gamma-ray heating both for fission and fusion reactors. The experimental data measured using the mono-energetic sources are still insufficient especially in the energy range between 5 to 14 MeV. In most of the previous experiments, attentions were paid only to discrete gamma-rays for the basic nuclear physics. Measurements to obtain whole gamma-ray spectra including continuum part have been carried out with the white neutron source up to 20 MeV$^{2)}$, but their absolute values are sometimes questionable due to the coarse neutron energy interval and the low counting statistics. Our aim is to provide accurate gamma-ray production data in the MeV region for the applied purposes.

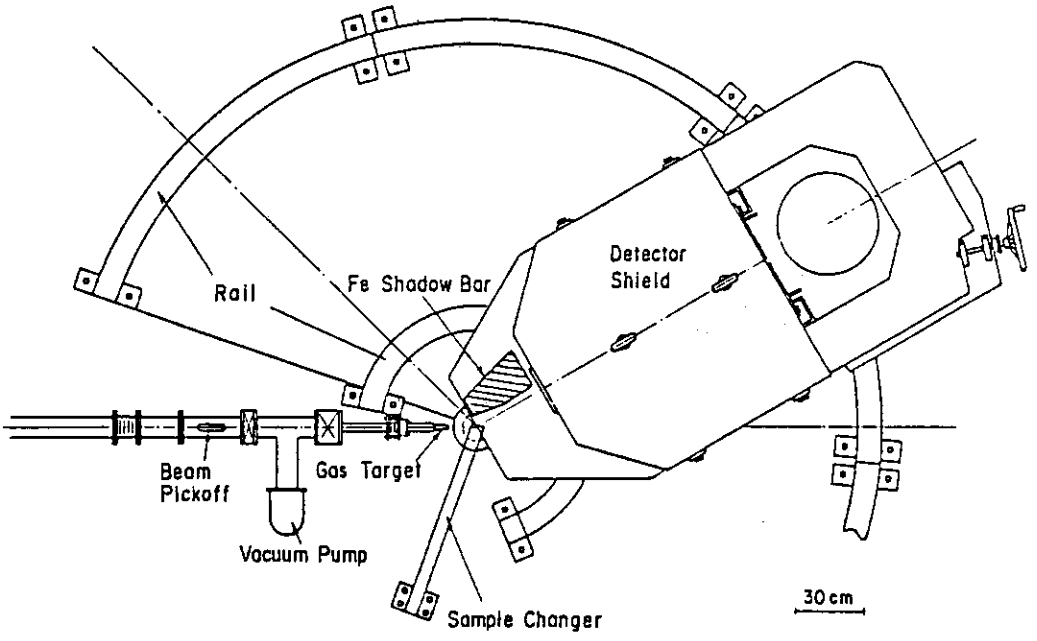

Fig.1 Schematic Layout of $(n\ n'\gamma)$ Experimental Arrangement

In the energy region of interest in our experiment, the reactions such as inelastic scattering $(n,n'\gamma)$, neutron capture (n,γ) and charged particle reactions of $(n,p\gamma)$ and $(n,\alpha\gamma)$ are important for gamma-ray emissions. In particular, the cross section of $(n,n'\gamma)$ reaction is dominant compared to other reactions.

The experimental arrangement is shown in Fig. 1. Neutrons were produced through the $D(d,n)^3He$ reaction. The in-terminal source of the Tandem accelerator was used to extract a deuteron beam bombarding a pressurized (0.2 MPa) deuterium target. With the d-d reaction, emitted neutrons are not mono-energetic due to the deuteron break-up in the high energy region. The test experiments were carried out using three different incident energies of 10, 7 and 5 MeV. The 5 MeV deuteron was finally chosen for our first experiment to elimanate the effects of break-up neutrons. The average beam current and pulse width were 0.8 A and 4 ns, respectively, at a 2 MHz repetition rate. The whole detector system with a heavy shield could be rotated around the sample to measure the angular distributions. To reduce the background, the detector shield was composed of lead and borated paraffin and the iron shadow bar was prepared between the gas target and the spectrometer. The sample was placed at 15 cm from the neutron target.

The gamma-ray detector was located at about 80 cm from the sample as shown in Fig. 2. Gamma-ray spectra were measured with a 7.6 cm diameter x 15.2 cm long NaI(Tl) detector, which was set in a 25.4 cm diameter x 25.4 cm long NaI(Tl) annular detector. These two detectors were operated in an anti-coincidence mode to suppress the Compton backgrounds and neutron capture gamma-rays in the detector. The TOF technique of

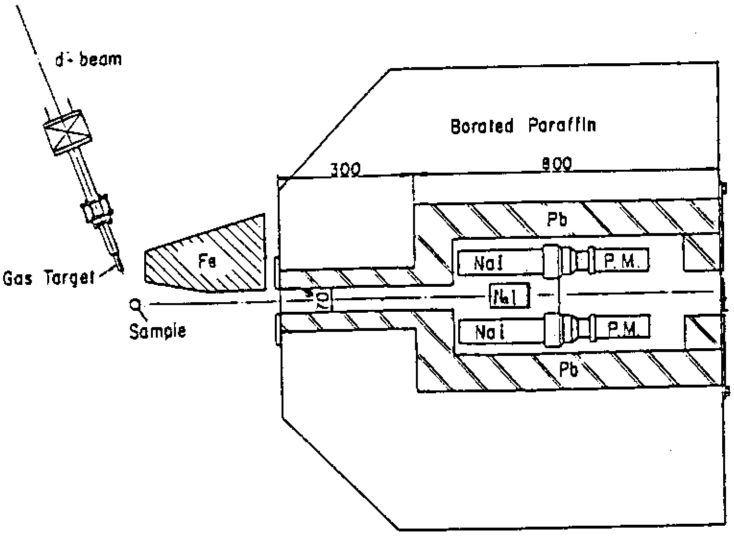

Fig. 2 $(n\ n'\gamma)$ Detector Schield

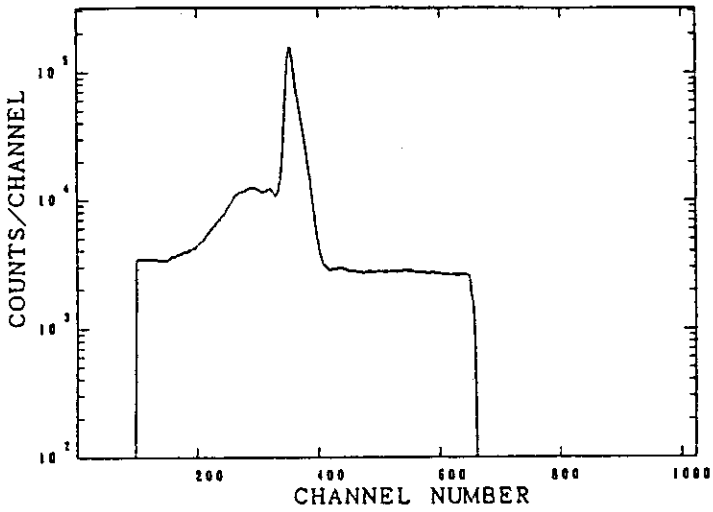

Fig. 3. The time spectrum observed with the gamma-ray detector.

the gamma-ray detection was used to improve the signal to background ratio. The example of the time spectrum is shown in Fig. 3. The neutron spectra were also measured at the same time employing a 5 cm diameter x 1.27 cm thick NE213 detector located at a distance of 2.2 m from the neutron source.

The response functions of this anti-Compton NaI detector have to be determined in order to obtain the absolute gamma-ray yields. The several standard gamma-ray sources such as ^{60}Co, ^{137}Cs and ^{22}Na were used to examine the response functions. Fig. 4 shows the spectrum obtained for the 4.43 MeV single gamma-rays from the ^{12}C(n,n'γ) reaction. The raw data of the gamma-ray pulse height spectrum for the structural material of Al are shown in Fig. 5. The several discrete gamma-rays from ^{27}Al(n,n'γ)^{27}Al and ^{27}Al(n,pγ)^{27}Mg are observed above the continuum part of the spectrum.

Since our own response functions have not been prepared, the published response values for TIT was applied to check the system. They have been used the similar detector system for the neutron capture gamma-ray spectrum measurements in the keV region$^{3)}$. After subtracting the backgrounds, the gamma-ray spectra were unfolded using the conventional computer program FERDOR$^{4)}$.

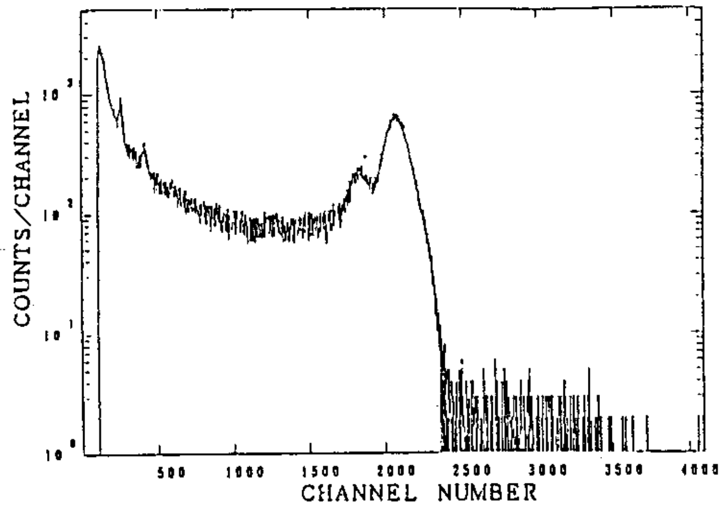

Fig. 4. Spectrum obtained for the 4.43 MeV single gamma-rays from the ^{12}C(n,n'γ) reaction.

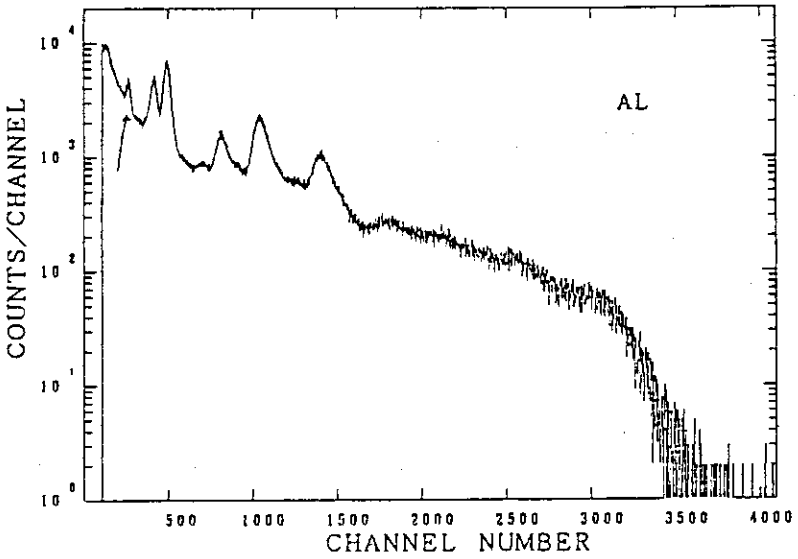

Fig. 5. Gamma-ray pulse height spectrum of Al(n,n'γ)

The result is shown in Fig. 6, together with the data taken at ORELA[5]. The agreement of the spectrum shape seems reasonable though our detector system has the better energy resolution.

The efforts are being made to estimate the response function and to improve the energy and time resolutions.

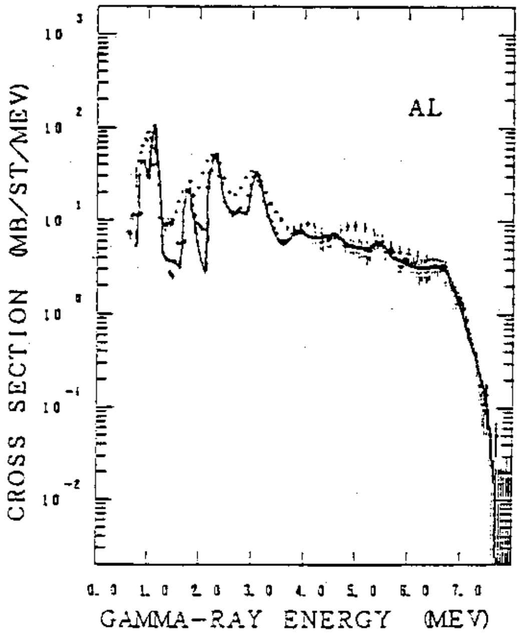

Fig. 6. Preliminary results of gamma-ray spectra of Al(n,n'γ) (–•–) compared with those by ORELA (▴).

References

1) Japanese Nuclear data Committee, Journal of Atomic Energy Society, 21, 377 (1979)
2) J.K. Dickens et al., Nucl. Sci. Eng. 62 (1977) 515
3) N. Yamamuro et al., Proc. Int. Conf. Sci. Eng., Geel, (1982) p152, M. Igashira, private communication
4) H. Kendric and S.M. Sperling, GA-9882 (1970)
5) G.L. Morgan and F.G. Perey, ORNL TM-5241 (1976)

6.4 NEUTRON TOTAL CROSS SECTION MEASUREMENTS ON OXYGEN, ALUMINUM AND CARBON BELOW 1.2 MEV

Makio OHKUBO
Department of Physics , JAERI

Abstract

Neutron total cross sections of oxygen, aluminum and carbon were deduced up to 1.2 MeV, by the transmission measurements at a TOF spectrometer of the JAERI linac.

1. Introduction

In the course of the neutron cross section measurements, we often encounter the cases where the available samples of nuclides aimed at are in chemical form of oxides. In such cases, the accurate cross section of oxygen is needed to correct the effects of oxygen in experimental data acquired.

Neutron cross section of oxygen is accurately known in thermal energy and in MeV energy region, and an evaluated file is available in JENDL3-PR2. However the experimental data are extraordinarily poor in the energy region from 0.1 keV to 300 keV.

We have made the transmission measurements on aluminum and aluminum oxide at a 47-m TOF station of the JAERI linac, and then deduced the total cross section of oxygen below 1.2 MeV by a subtraction method. In order to ascertain the accuracy of the measuring system, the total cross section of carbon were also measured in the same experimental conditions.

2. Measurements and Results

The aluminum samples were metallic plates or a lod, of 7, 32, and 105.5 mm thicknesses. The aluminum oxide sample was fine powder of 99.9 % in purity, heated to 160 °C in air for ~3 hrs to eliminate moisture. The powder was packed into aluminum cylindrical cases of 40 mm ϕ x 30 mmt and 65 mm ϕ x 128.5 mmt. The carbon sample was 20 mm thick plate made by Toyo Tanso Co.

The observed total cross sections σ_t of oxygen were deduced by subtracting σ_t of Al from that of Al_2O_3, and are shown in Fig.1 up to 1.2 MeV. The peak cross section of the lowest resonance of ^{16}O at 432 keV was obtained to be about 12.8 barn for thick sample measurement, whereas it was 15.6 barn for the thin sample measurement. The difference was caused by the saturation effect.

For the energy region below 200 keV, σ_t can be approximated by a linear function

$$\sigma_t(E) = 3.85 - 0.002\ E \quad \text{(barn)} \qquad (\ 1\ \text{keV} < E < 200\ \text{keV})$$

where E is in a unit of keV. The errors in the cross sections are rather large at 35, 88 and 150 keV due to the resonances of aluminum.

At very low energy ($E \simeq 0$), σ_t was obtained to be 3.85 ±0.07 barn. This value is 2.6 % higher than the value 3.761 ± 0.006(barn) measured by Koester et al.[1] at thermal neutron energy. It is realized that the contamination with moisture in the sample must be avoided carefully. Because of large neutron cross section of hydrogen (20 barn at $E_n \sim 0$), inclusion of 1 mg of H_2O in 1 gram of Al_2O_3 is sufficient to rise the apparent oxygen cross section by 0.1 barn.

Observed total cross sections of carbon below 930 keV are in good agreement with the evaluated values JENDL3-PR2. This agreement ensures the accuracy of the system.

References

1. L.Koester, K.Knopf and W.Waschkowski: Z.Phys. A 292,95(1979)

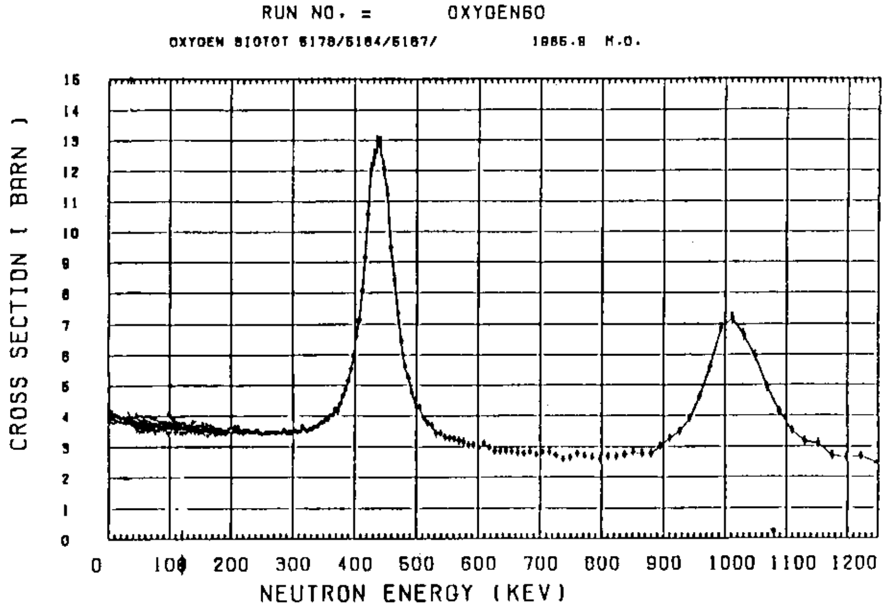

Fig.1 Observed total cross section of oxygen below 1.2 MeV.

6.5 NEUTRON RESONANCE PARAMETERS OF ^{148}Sm

Motoharu MIZUMOTO and ZHAO Wen Rong*

Department of Physics, JAERI, *Institute of Atomic Energy, China

Accurate values of resonance parameters, such as resonance energies, neutron widths and radiation widths for some of the high yielded fission product nuclei, are needed for reactor calculation and their systematic values are important for nuclear structure study. At JAERI linac, we have been continuously providing nuclear data of fission product nuclei$^{1)}$. In particular, nuclei as samarium isotopes in a mass region of A=150 have been extensively measured since they are located near a peak in the s-wave strength function and their contributions are significant to the neutron capture rate in the reactor core.

There have been no previous data available for ^{148}Sm resonance parameters except the potential scattering radius 8.3 fm and resonance energies of 5 lower resonance levels in BNL-325(84)$^{2)}$. A value of the s-wave strength function, about 3×10^{-4}, was deduced by Kirouac and Eiland$^{3)}$ based on the systematics of the measured results for some other Sm isotopes. For the evaluation of JENDL-1, a value of 3.11×10^{-4} has been used to evaluate the capture cross section in the keV region, which was calculated from the systematic values of spherical optical potentials.$^{4)}$ In the present work, the transmission measurements were performed and the resonance parameters were obtained in the neutron energy region from 40 eV to 9000 eV.

The experimental arrangement was similar to previous work for odd samarium isotopes of ^{147}Sm and ^{149}Sm$^{5)}$. The transmission data of ^{148}Sm were obtained by the neutron time-of-flight method using the 120 MeV JAERI Linac in the energy range of 40 - 9000 eV for a thick sample and from 40 to 3000 eV for a thin sample. The neutron producing Ta target and 5 cm thick polyethylene moderator were used for the pulsed neutron source, and the flight path length was 56.319 m. The linac was operated at 300 pps and 600 pps with 25 ns pulse width for the thin and thick sample, respectively.

The neutron transmissions were measured with an 11.1 cm diameter x

0.635 cm thick ^{6}Li-glass detector. Neutron flux was monitored by an additional ^{6}Li-glass detector at 47 m station. Beam filters were inserted permanently in the neutron beam; BN (boron nitrate) to absorb low energy neutrons and Pb to reduce the gamma flash. Some black resonance filters, such as Al, Na, W and Mn were used to determine time dependent backgrounds. The energy calibration was made by the energies of sharp resonances present in the filters of Al and Pb.

The enriched sample (96.49 %) of ^{148}Sm was oxide powder borrowed from the isotope division of Oak Ridge National Laboratory. The abundance values of minor samarium isotopes were checked by Analytical Chemistry Laboratory of JAERI and agreed well with those given by ORNL. An amount of the water absorbed in the oxide sample was also measured and used for sample thickness correction.

The transmission data were analyzed with a multi-level Breit-Wigner formula incorporated in a least squares fitting program SIOB$^{6)}$, which includes level-level interference, Doppler broadening and instrumental resolution. Since there are no previous values of radiation width available, Γ_γ= 60 meV was assumed on the basis of the experimental data for ^{147}Sm(69 meV), ^{149}Sm(62 meV) and ^{150}Sm(60 meV)$^{2)}$. The statistical spin factor g = 1 was used, assuming that all the resonances observed are s-

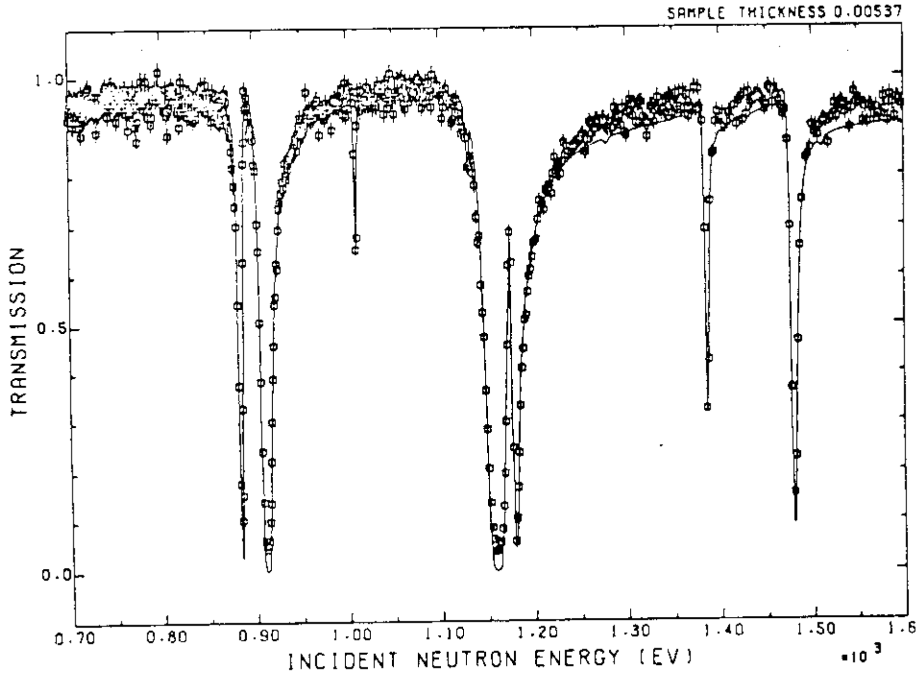

Fig. 1 Example of resonance analysis of the transmission data for ^{148}Sm. The solid line is a multi-level Breit-Wigner fit.

wave. The transmission data of the two samples were analyzed at the neutron energy below 1500 eV, while above that energy only the thick sample data were fitted.

Fig. 1 shows the comparison of the experimental transmission data with those calculated from the resonance parameters of the thick sample. The value of the potential scattering radius determined in this work agrees well with the systematic value 8.3 fm given by BNL-325. Resonance energies and neutron widths for more than 70 resonances of ^{148}Sm were newly determined in this experiment. A part of the results is given in Table 1 below 1500 eV. The resonance energies of five resonances recommended by BNL-325 were found to be in good agreement with our energy values. In the low energy region, there are many small resonances coming from ^{147}Sm, ^{149}Sm and ^{152}Sm. The good fitting results were also obtained for these small resonances, which were calculated with the recommended resonance parameters in BNL-325.

Our values of the neutron width may be slightly changed due to the assumption of the radiation width especially for low energy resonances. With the different assumed values of Γ_γ= 120 meV, fitted neutron widths for the lowest two resonances at 94.86 and 140.3 eV are changed from 443 to 416 meV and from 27 to 25 meV, respectively.

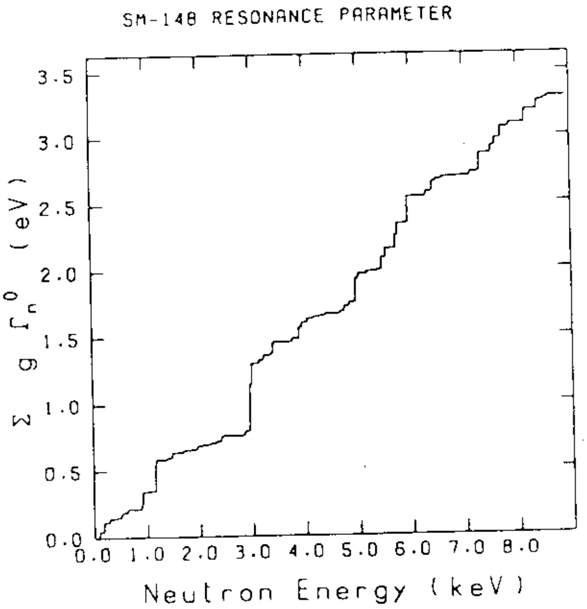

Fig. 2 The cumulative sum of the observed reduced neutron widths for ^{148}Sm.

The cumulative sums of the observed reduced widths are plotted against neutron energy in Fig. 2. This plot is insensitive to weak levels which might be missed in this experiment. From the mean slope in this figure, the value of s-wave strength function is obtained to be (3.8 ± 0.7) x 10^{-4}. Without any missing small resonance correction, the average level spacing is about 100 eV. This value is 50 % larger than the values of

70 eV used for the evaluation of the capture cross section in the keV region$^{4)}$.

Further transmission measurements were made with the thicker sample and high energy resolution. The analysis is still in progress to obtain better radiation widths using the thick-thin method in the resonance area analysis and to get more precise neutron widths in the higher neutron energy region.

References

1) M. Mizumoto et al., Proc. of the NEANDC Topical Conference, JAERI M 84-182 (1984) p75

2) S.F. Mughabghab, M. Divadeenam and N.E. Holden, Neutron Cross Sections, vol.1B, Neutron Resonance Parameters and Thermal Cross Sections, BNL-325 (4th ed.) (1984)

3) G.J. Kirouac and H.M. Eiland, Phys. Rev. C11 (1975) 859

4) S. Iijima et al., Proc. of the Specialist Meeting of Neutron Cross Sections of Fission Product Nuclei NEANDC (E)209 "L" p317

5) M. Mizumoto, Nucl. Phys., A357 (1981) 90

6) G. de Saussure, D.K.Olsen and R.B. Perez, ORNL-TM-6286 (1978)

Table 1 A part of resonance parameters of ^{148}Sm determined in this experiment.

Energy (eV)	Δ Energy (eV)	Γn (eV)	$\Delta\Gamma$n (eV)
94.864	0.012	0.443	0.003
140.30	0.01	0.0268	0.0010
184.61	0.02	0.879	0.007
288.54	0.01	0.432	0.004
422.41	0.01	0.189	0.005
514.14	0.02	0.755	0.009
557.75	0.02	0.085	0.003
623.78	0.02	0.593	0.010
884.84	0.05	0.916	0.03
910.82	0.07	2.99	0.04
1009.6	0.17	0.059	0.008
1158.6	0.11	7.08	0.07
1178.9	0.07	1.19	0.04
1386.2	0.11	0.46	0.03
1479.4	0.08	1.48	0.05

6.6 MEASUREMENTS OF NEUTRON TOTAL REFLECTIONS ON METALLIC SURFACES

Masatoshi SUZUKI, Yuji KAWABATA, Hidetake TAKAHASHI,
Masanobu SAKAMOTO*

Department of Research Reactor Operation and *Department
of Physics, JAERI

The upgraded JRR-3 project has includes the installation of the neutron guide tubes with the rectangular cross section which are constructed of borosilicate glass plates deposited with nickel on their inside surfaces. They are expected to transport collimated neutron beams over distances up to several tens of meters and permit to install much greater number of neutron reseach instruments in much larger external experimental hall. In the case of the curved guide, they can separate thermal and cold neutron beams from fast neutron beams and gamma rays which are sources of background noises. This report describes the results of measurements on the total reflectivities of neutrons from the metallic mirror surfaces which play the most important role in the neutron guide tubes.

The three different kinds of mirror planes are studied. First ones are the nickel surfaces deposited on the polished plates of borosilicate glass. They are expected to be used for the guide tubes in the upgraded JRR-3 project. Secondly the polished surfaces of nickel plates with three different degrees of surface roughness are examined, in order to make sure whether they have enough reflectivities of neutrons. They are intended to be used under the severe radiation field of neutrons and gamma rays near the reactor core, instead of the deposited nickel surfaces. Thirdly the surfaces of the ordinary float-glass, i.e. soda-lime glass, are checked in order to make a comparison with the other cases. The maximums of surface roughness Rmax and the average values Ra for the mirror surface of the five samples are given in Table. 1.

The measurements of the total reflection have been made by using the thermal neutrons from the JAERI electron linac. The experimental arrangement is shown schematically in Fig. 1. The neutron spectra reflected from the mirror surfaces are measured by means of the time-of-flight method at the glancing angle of 3.5×10^{-3} rad. for nickel surfaces and 2.3×10^{-3} rad. for float-glass surface, which are the critical angles on the total reflection for neutron wavelength 2Å. The reflectivities are obtained from the reflected neutron spectra normalized by the incident neutron spectra.

The measured spectra and the derived reflectivities for the surfaces of nickel deposited on polished borosilicate glass plate and float-glass are shown in Fig. 2 The reflectivities for the three nickel plates and the nickel deposited glass plate are given in Fig. 3. The results show that the reflectivities on the nickel surface deposited on the polished surface of borosilicate glass plate and the float-glass plate are almost unity above 2Å in neutron wavelength. However, in the case of the polished surfaces of nickel plates, Fig. 3 shows that the reflectivities decrease as the surface roughness increases.

Therefore it is evident that the reduction of reflectivities on the total reflection of neutron largely depends on the degree of surface roughness of mirror plane. Smaller values than about 150Å in average of surface roughness are required for the mirror planes to be used for neutron guide tubes. Although the reflectivities on the deposited nickel surface and the float-glass surface are almost unity, the gain of neutrons transmitted through the guide tube of the nickel surface is larger than the case of the glass surface, due to the difference of the critical angles for the both materials.

Table.1 surface roughness of mirror plates

surface roughness sample	Ra(A)	Rmax(A)
Ni deposited glass plate	100	800
Float-glass	150	1300
Ni plate-1	190	1700
Ni plate-2	270	4000
Ni plate-3	760	7500

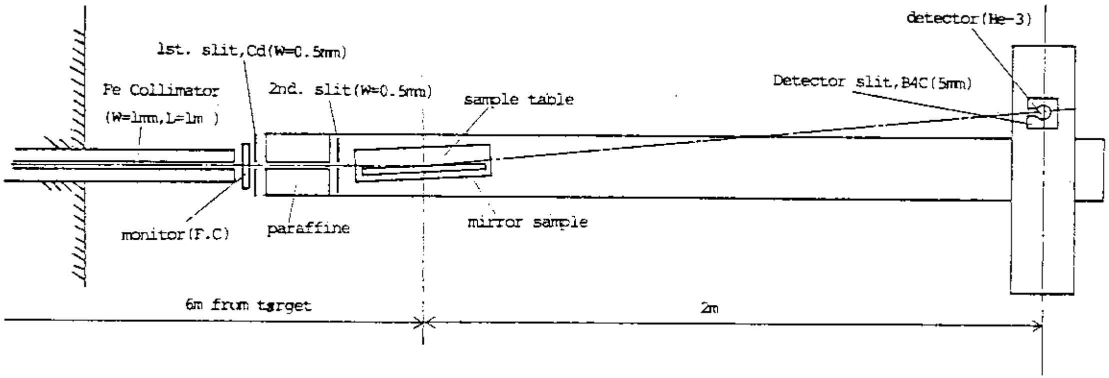

Fig.1 Schematic geometry of experimental equipments

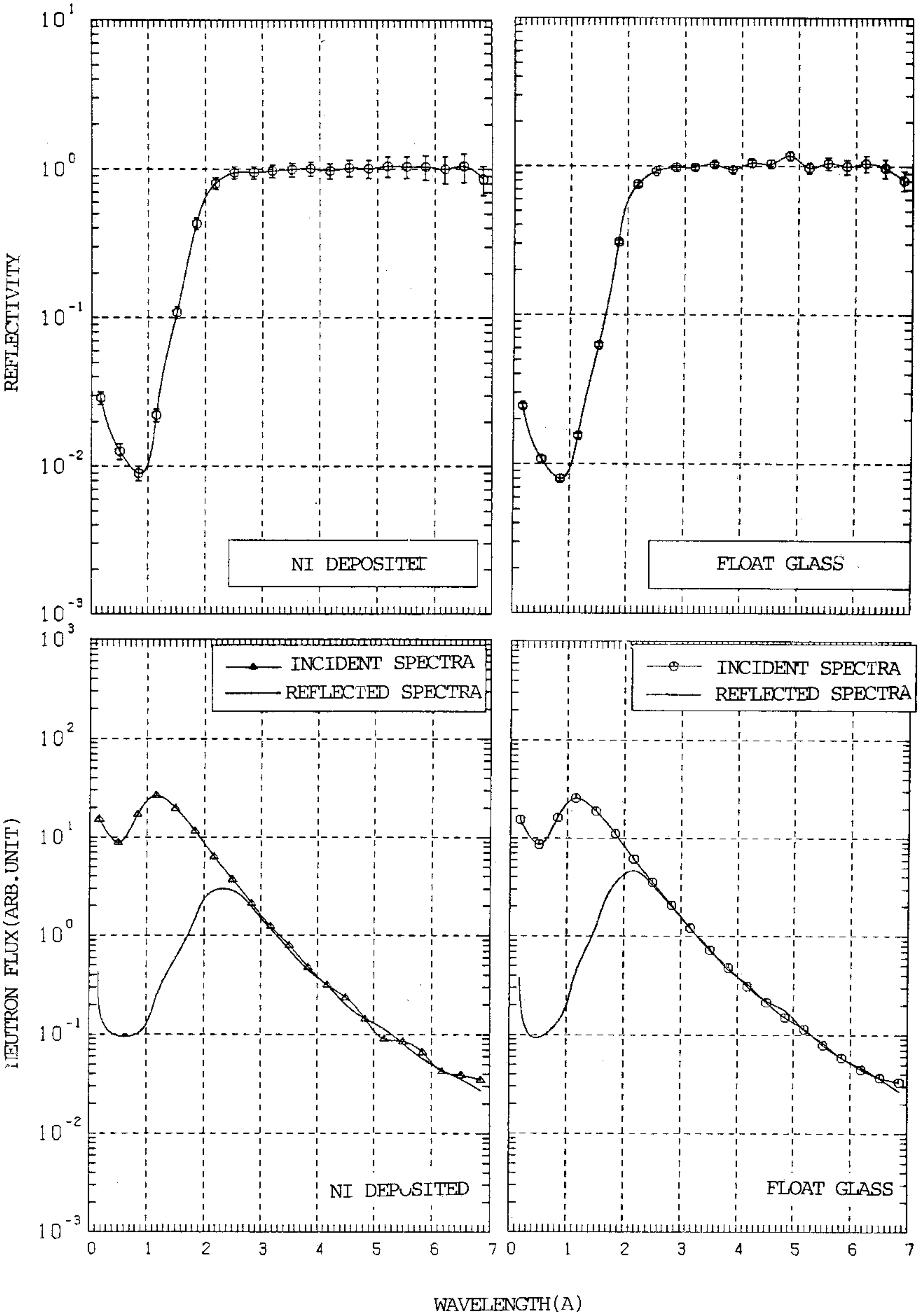

Fig.2 The measured spectra and reflectivities for deposited Ni float-glass

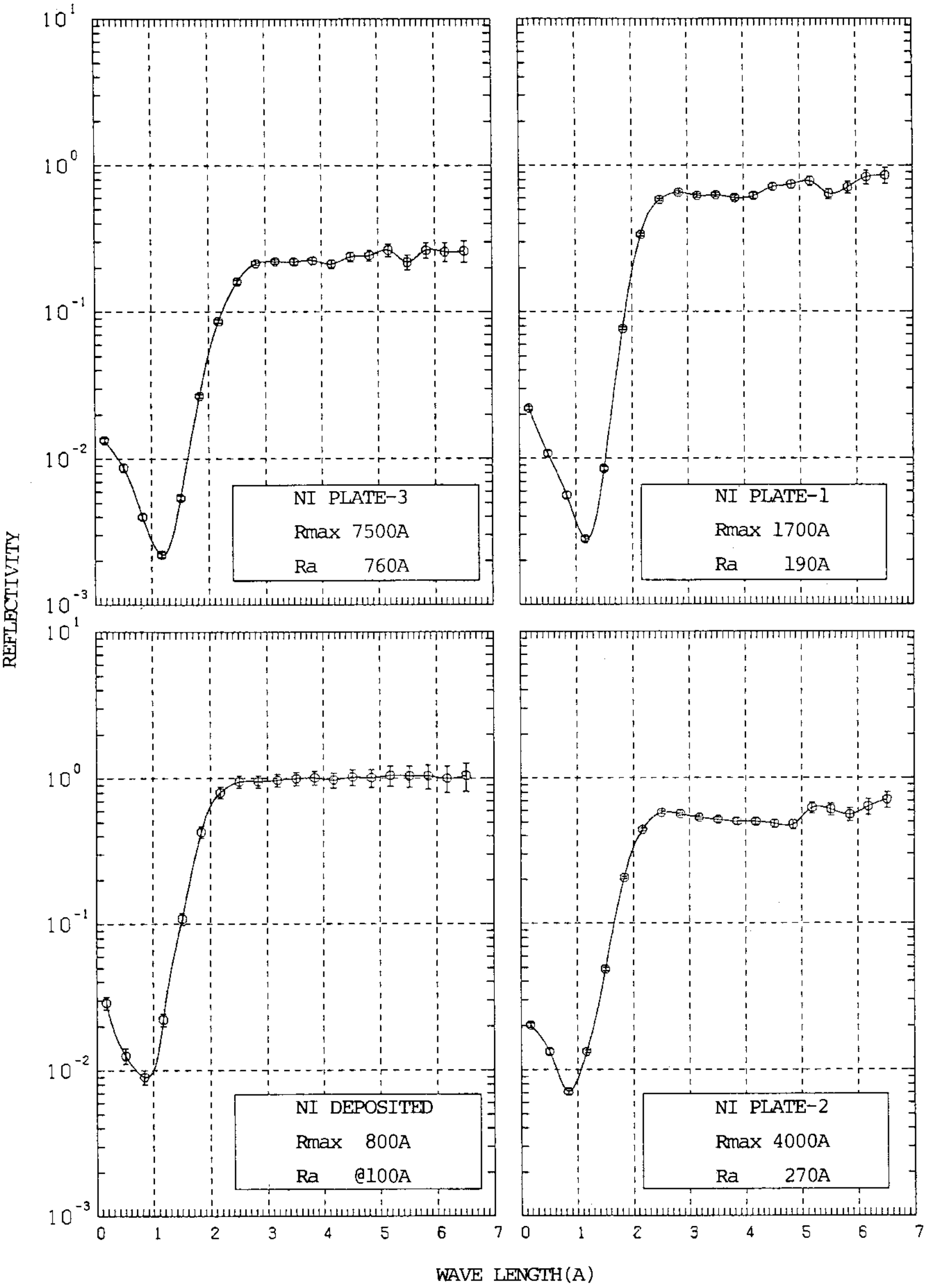

Fig.3 Reflectivities for three kinds of Ni plates and Ni deposited glass

6.7 NEW INFORMATIONS CONTAINED IN THE PULSE SHAPE OF AN NE213 LIQUID ORGANIC SCINTILLATOR

Yutaka FURUTA

Department of Physics, JAERI

Instrumentaion

In the present study, a 2" diam. by 2" long NE213 scintillator was used and the shape of voltage pulse of amplifier output was observed. A delay line amplifier was used to amplify signals keeping their shape as faithfully as possible.

To measure the rise time, a RISE TIME TO PULSE HEIGHT CONVERTER (RHC)$^{1)}$ developed in JAERI was used. It has a special characteristic so as to measure the rise time or slope between any two points of the pulse shape, by selecting the values of the lower pickoff and the upper pickoff. When values of the both pickoffs are selected closely, a local slope at any point of the pulse shape can be obtained. In such case the difference of the pickoff values is defined as the differential pickoff and the corresponding rise time is defined as the differential rise time in the present study.

Experiments and results

1. Rise time distribution

Figures from 1-A to 1-C show the rise time distribution obtained for an Am-Be neutron source under the same conditions except the values of lower and upper pickoffs represented by % of the height.

Figure 1-A was obtained by 20.0 % lower and 81.2 % upper pickoffs. In the figure, a sharp peak with a fast rise time shows the rise time distribution of gamma-ray pulses and a lower hill with a slower rise time is that for neutrons. This is a well known typical pattern of the gamma-neutron rise time distribution.

Figure 1-B shows a rise time distribution obtained by 26.0 % lower and 90.0 % upper pickoffs. It can be seen in this figure, that the rise time distribution for gamma rays is also faster than that of neutrons. In this case, the rise time difference between gamma rays pulses and neutrons' is large and it was estimated as about 130 ns.

Figure 1-C shows the rise time distribution for 90.8 % lower and 100.0 % upper pickoffs. These pickoff conditions are corresponding to observing the rise time of the top part of the pulse while Fig.1-A and Fig.1-B are observing the rise time for the fast rising part.

It can be seen from the figure that the rise time relation between the sharp peak and the lower hill becomes inverse and the sharp peak is positioned at a slower rise time. It was confirmed by further experiments using Na-22 gamma rays that the sharp peak was surely made by gamma-ray pulses, of which result is shown in Fig.1-D.

In this case(Fig.1-C), the rise time difference between gamma-ray pulses and those of neutrons was very large and was estimated about 150 ns.

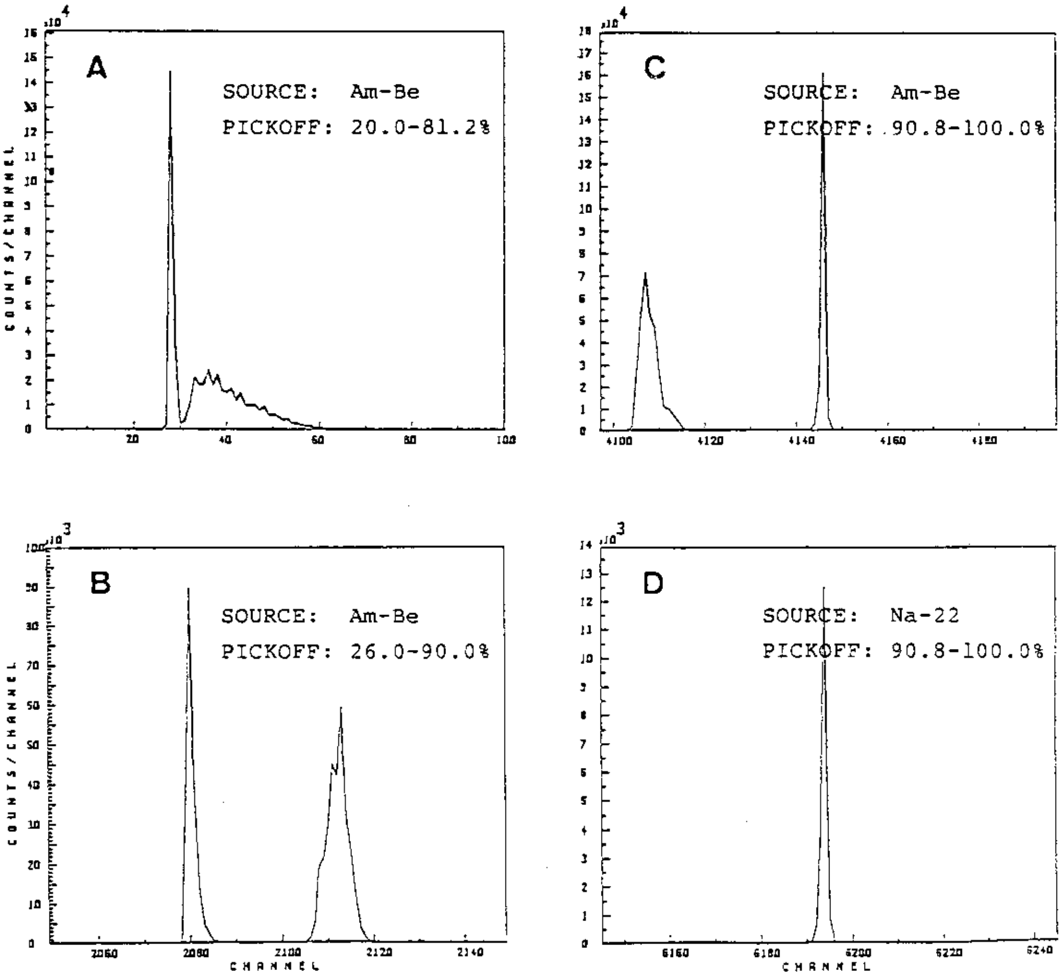

Fig.1 Rise time distributions under several pickoff conditions.

These situations can be clarified from Photo.1 showing the voltage pulse of amplifier output; bottom two show the wave forms of gamma-ray pulses and upper one shows neutron pulse. The gamma-ray pulse has a flat top while that of neutron is curved with a slant.

Further experiments were made and the result is shown in Fig.2, which shows a rise time distribution for Am-Be gamma rays and neutrons measured by fixing the lower pickoff at 5.0 % and varying value of the upper pickoff. Under such pickoff condition, a profile of the pulse shape can be obtained, and the figure shows the pulse shape above 20.0 % of the height. It can be seen from the figure, that gamma-ray pulses rise promptly until about 90.0 % of the height nearly straight and turn rapidly to a flat top with a gentle slope.

On the contrary, neutron pulses rise slower than that of gamma rays, and then, turn gently from about half height to a top, which is consistent with Photo.1.

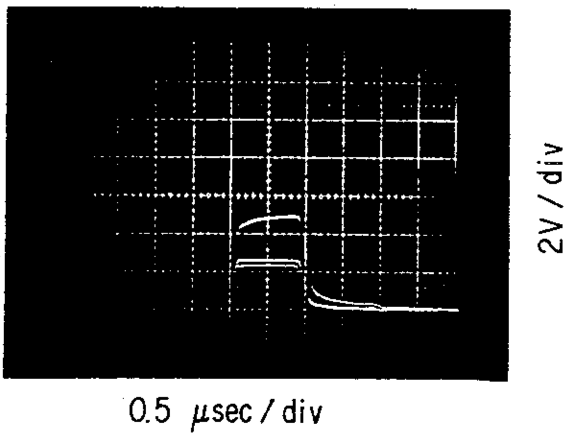

Photo.1 Wave forms of the voltage pulse.

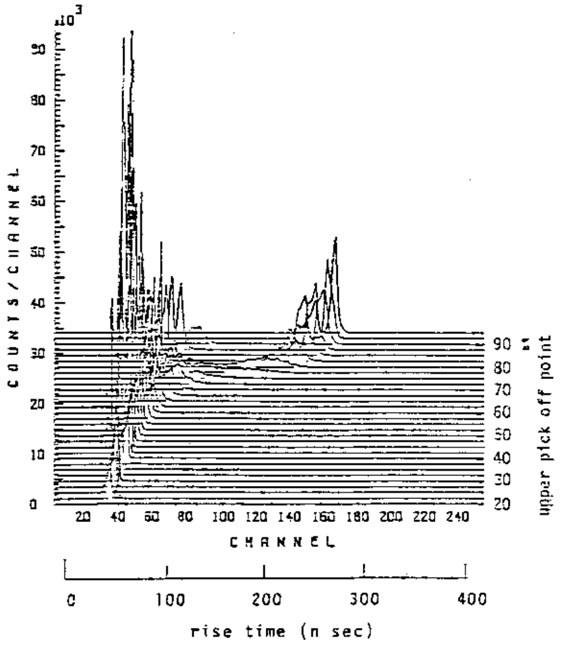

Fig.2 Rise time distribution of Am-Be gamma rays and neutrons as a function of upper pickoff with fixed (5.0 %) lower pickoff.

2. Differential rise time

To study the pulse shape of the NE213 scintillator more precisely, the differential rise time was measured. Upper half of Fig.3 shows the differential rise time distribution for only gamma rays obtained by the Na-22 gamma-ray source, and bottom of the figure is for gamma rays and neutrons from the Am-Be source. Both figures were obtained as a function of the lower pickoff value, with constant differential pickoff of 2.0 %.

From the figure, the following can be seen.

The differential rise time distribution of gamma-ray pulses is very simple, thus, the pulse shape of gamma rays is considered to be simple and smooth. On the contrary, that of the neutron pulses is very complicated at about 80 % of their height. It is considered that there happen something on the neutron pulse at this turning part, and the pulse shape of neutrons is not always smooth and is different from one another at the turning part.

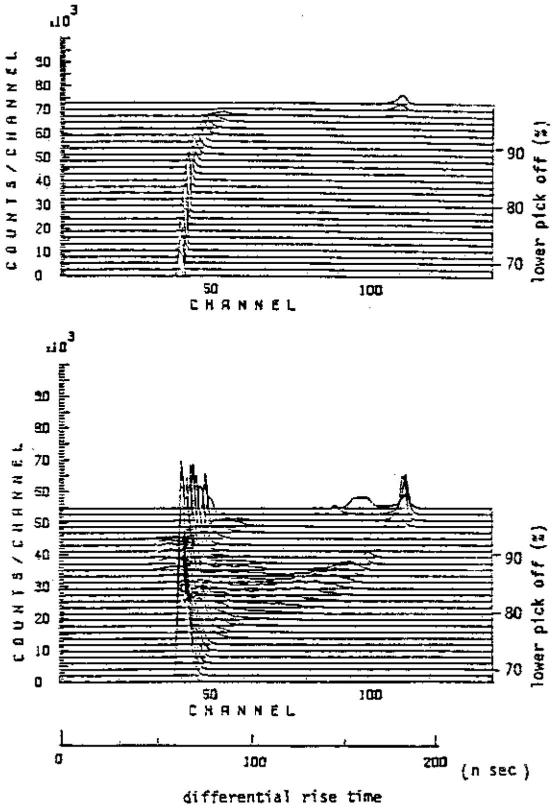

Fig.3 Differential rise time distribution as a function of lower pickoff for fixed (2.0 %) differential pickoff.

Considerations

We can summarize the experimental results on the shape of the voltage pulse as follows:

1) While gamma-ray pulses rise faster than those of neutrons initially, the rise time of gamma-ray pulses becomes slower than those of neutrons at the top part of the pulse.
2) While gamma-ray pulses have a flat top, neutron pulses have a curved one.
3) While the shape of the gamma-ray pulses are smooth and same for each other, those of neutron are generally complicated and different from one another at the turning part from the initial fast rise to the curved top.

These experimental facts are considered to be caused by the difference of the decay time(slow component) of scintillation light of the NE213 scintillator between gamma rays' and neutrons'. Since we are observing the voltage pulse obtained by integrating the scintillation signal, the difference of scintillation decay time is converted into the difference of the rise time. In the gamma-ray scintillation, fraction of the slow component is very little, thus its voltage pulse rises straight and has a flat top. While in the scintillation of neutron, the fraction is larger and the voltage pulse rises slower than that of gamma rays and the pulse height increases even at the top part. These are the reason of the first and the second results.

For the third result, it is considered to be caused by neutrons multiply scattered in the scintillator.

The elastic scattering cross section of neutrons from hydrogen is very large and the velocity of the scattered neutrons is extended over several cm/ns. When further scattering would occur in the scintillator, the following pulse will be superposed on the preceding pulse with some time delay and it makes a step on the pulse shape. While, the velocity of gamma rays is very large and even if further scattering would occur, the time delay of the followed pulse is very small and resultant pulse will be observed as if single event occurred. This would be the reason of the third result.

The present study can be utilized for neutron measurements. One way is to use the top part of pulse for the pulse shape discrimination of gamma rays and neutrons. About 150 ns of the rise time difference was obtained in the present study.

Another is to use possibly to obtain the neutron spectrum without the unfolding process. The multiply scattered neutron losses almost all amount of its energy in the scintillator, and if we can select only such pulses, we can obtain a pulse height distribution nearly corresponding to the spectrum. Information about multiply scattered neutrons is considered to be contained in the turning part of the pulse shape of neutrons.

The differential rise time may serve for the purpose.

Reference

1)S. Kinbara and T. Kumahara: Nucl. Instr. & Methods 70(1979)173.

6.8 EFFECTS OF THE TIMING WALK ON THE TIME RESOLUTION OF THE LARGE VOLUME NEUTRON DETECTOR

Masayoshi SUGIMOTO and Yoshimaro YAMANOUTI

Department of Physics, JAERI

The recent version of the data processing program becomes to be able to estimate the effects of the timing walk on the time resolution of the large volume neutron time-of-flight(TOF) detector system that is used for the measurements of the neutron scattering in the energy rage 10-40 MeV by using the Japan Atomic Energy Research Institute tandem accelerator. The observed shift in the time spectrum for 11 MeV neutrons reached 1 ns for the pulse heights with more than 2 MeV electron equivalent, but the influence to the time resolution is about 0.5ns and is relatively small compared with the overall resolution, 3 ns.

Introduction

The data processing program$^{1)}$ was originally developed to derive a neutron TOF spectrum from the list mode event recorded data by correcting the time difference of the TOF obtained at each detection point that spreads over the 20 cm dia. and 35 cm thick detector. This process can be called "software" time-compensation method, because it calculates a size of the correction for the observed TOF to obtain the best time resolution and imposes the gates for each event by using a set of parameters: 1) T1, the TOF obtained from a photomultiplier attached at the flat end of the scintillator on the opposite side to the scattering sample, 2) t1-t2, the difference of the TOFs obtained from the photomultipliers attached at the ends of both sides, 3) PH, the pulse height amplitude summed up for all scintillators in the detector system, and 4) PS, the pulse shape (rise time) information to reject the undesirable gamma-ray events.

The derived TOF spectrum inevitably includes the timing walk due to the change of the rise time according to its pulse height. And it is very difficult to exclude it only by the experimental technique in the case of the large volume neutron detector. The effects of the timing walk on the time resolution can be checked by using the two dimensional map of TO vs. PH, where TO is the TOF derived from the "softeware" time-compensation method. If the timing walk is fully corrected, all TO spectra corresponding to each PH channel should have the same peak position for monoenergetic neutrons. Conversely, the shift of the peak positions of the TO spectra indicates the size of the timing walk and it can be corrected by adjusting these positions.

Data processing program

The data processing is performed using the DEC VAX 11/780 with the help of the interactive graphics, Evans & Southerland multi picture system. The fortran program is developed to execute the various phases of the data processing of the list mode data by selecting a command shown in the graphic display and hitting on the data tablet. The total number of the commands are 21 and they are grouped by their functions into: A) the manipulation of the files in the magnetic tape or disk storage, B) the preparation of the parameters for the "software" time-compensation and its execution, and C) the control of the job and the condition of the graphic display. The procedures for these commands are separated as the library modules and utilized in the other programs of the data processing.

The information needed for the time-compensation is provided from T1 and t1-t2 parameters in the list mode event data. The principle of the time-compensation is quite easily expressed that all TOF spectra observed at each detection point spreading over the scintillator volume are forced to converge to a referenced spectrum at the specific point, and the details are presented in the other article1). The resulting TOF spectrum, TO, is displayed and, if necessary, can be written on the magnetic tape or disk storage. The other parameters, PH and PS, are mainly used for imposing the gates to the TO spectrum. For the present purpose, the parameter, PH, is also used for the creation of the two dimensional map of TO vs. PH in the process of the time-compensation method, simultaneously.

Experimental result and discussion

Fig. 1 is a hardcopy of the map of TO vs. PH obtained from the measurement of the $^2H(d,n)^3He$ reaction at 35 deg with 10 MeV deuteron beam, and fig. 2 shows its time-compensated TOF spectrum. The peak shown in the figs. 1 and 2 corresponds to the monoenergetic neutrons with 11 MeV energy and has a 3 ns fwhm. The size of the time shift of the peak position in the map is 1 ns from the highest pulse height to the lowest one, that is about 2 MeV electron equivalent. This means that the actual effect on the time resolution of the timing walk estimated here is relatively small, less than 0.5 ns.

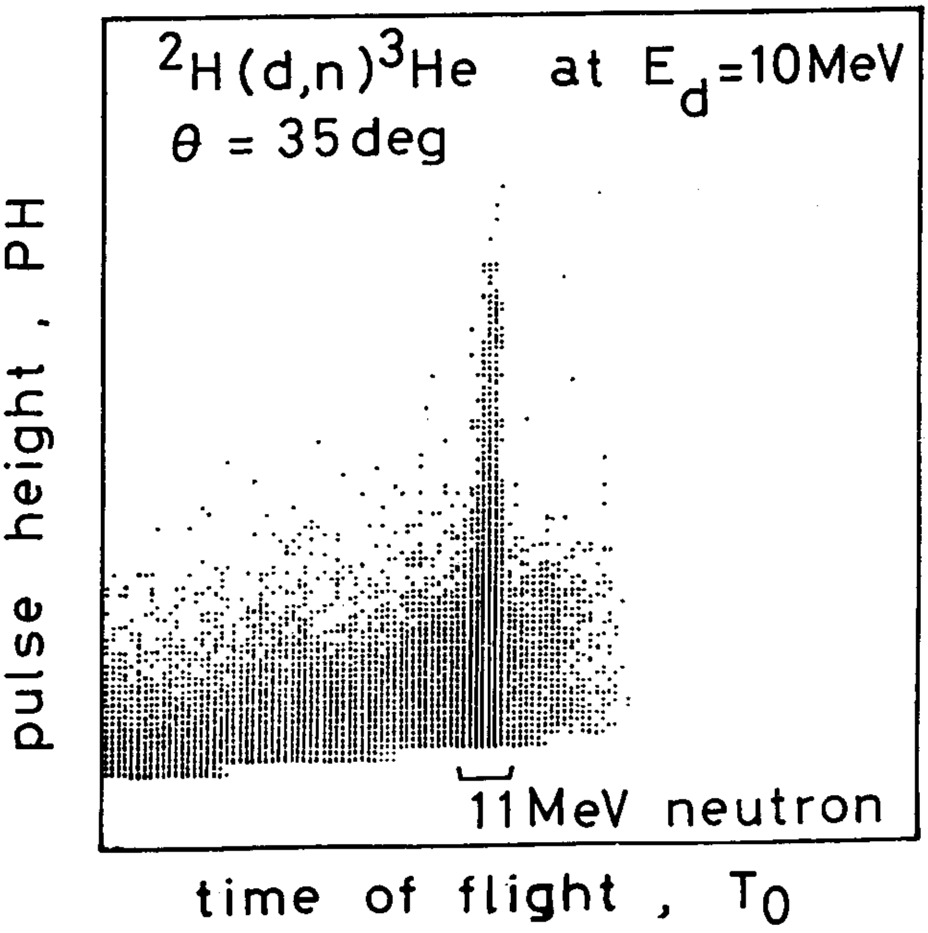

Fig. 1. Hardcopy plot of the two dimensional map of TO vs. PH, where TO represents TOF obtained from the "software" time-compensation method, and PH is the pulse height of the scintillator. The channel shift for the 11 MeV neutron peak in the TO spectrum is 1 ns from the highest PH to the lowest one.

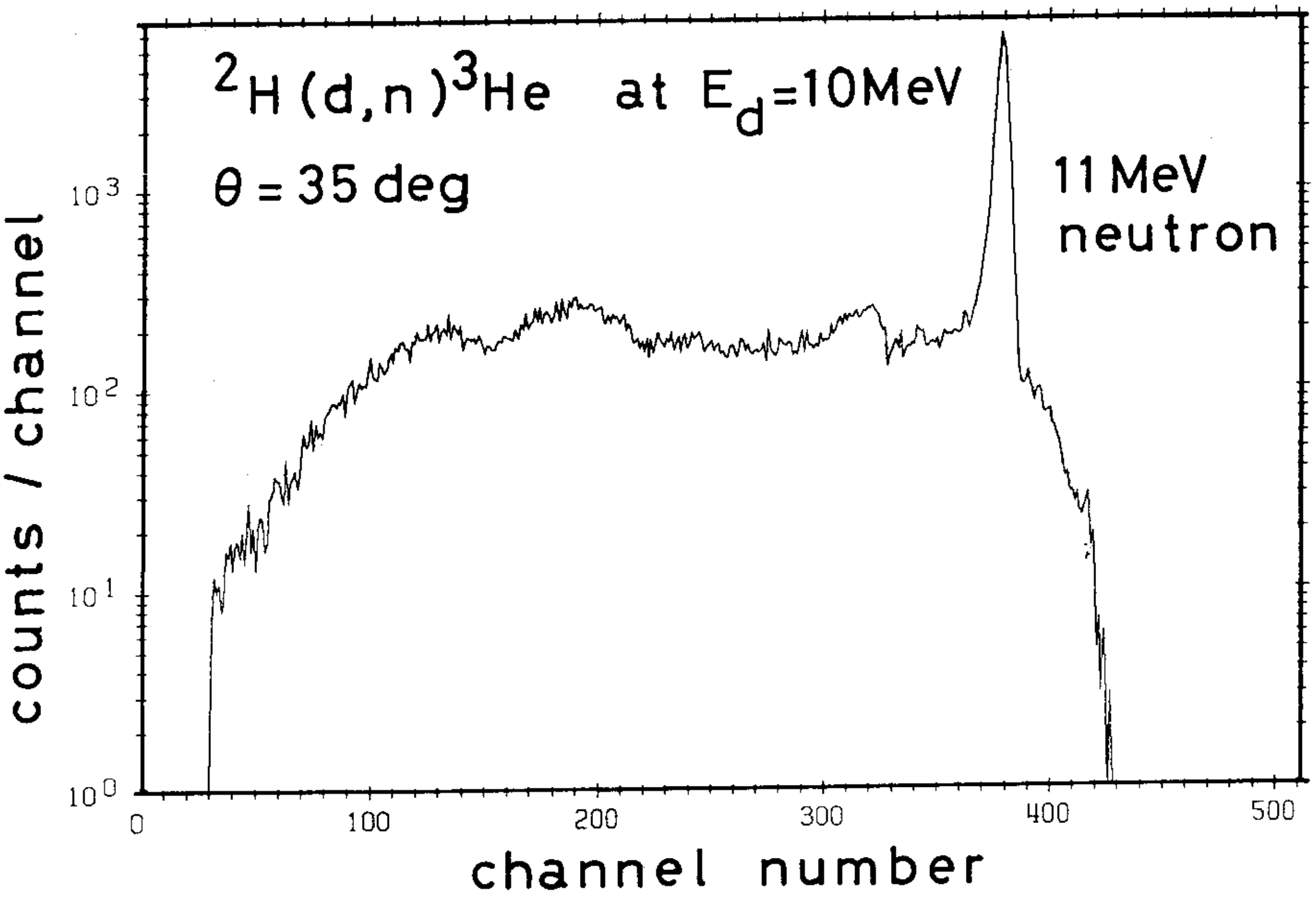

Fig. 2. Time-compensated TOF spectrum for the ^{2}H(d,n)^{3}He reaction at 35 deg with 10 MeV incident deuteron beam. The peak is corresponding to 11 MeV neutrons with 3 ns fwhm.

In contrast to the case of the small scintillators, the PH of the large volume scintillator is a sum of the outputs of two photomultipliers attached at the both end sides of the cylindical vessel and each pulse height output depends on the detection point due to the attenuation in the scintillator itself. So, that the events have the same PH is not always corresponding to that they have the same pulse heights for each photomultiplier and the same effects of the timing walk. Due to this fact the timing walk processed above is somewhat underestimated, however it is the only part that is correctable.

References

1) M. Sugimoto and Y. Yamanouti: JAERI-M 85-104 (1985) pp. 185-189.

6.9 REDUCTION OF DELAYED GAMMA RAY BACKGROUNDS FOR A PULSED NEUTRON SOURCE*

Makio OHKUBO
Department of Physics, JAERI

Abstract

Delayed gamma-ray backgrounds from a pulsed neutron source were measured with the TOF spectrometer of the JAERI linac. These gamma-rays, which were mainly due to neutron capture by hydrogen at the source, were appreciably reduced by loading boron-nitride in the cooling water of the neutron moderator of the target assembly.

1. Introduction

A neutron source with high intensity, short neutron pulse width and low gamma-ray background is essentially important for the high resolution neutron time-of-flight spectroscopy. A lot of calculations and measurements were already made on the properties of the neutron sources for this purpose,$^{1-6)}$ in which time dependences of the emitted neutrons as a function of neutron energy etc. were discussed. However, it seems that serious consideration was not taken on the 2.2 MeV delayed gamma-rays produced by the neutron capture by hydrogen in the moderator, which caused time dependent backgrounds for the neutron TOF measurements with ^{6}Li-glass scintillation detectors.

In the neutron total cross section measurements by the transmission method, this background is not only time dependent but dependent on the transmission sample thicknesses, and is troublesome for high accuracy measurements. To reduce the 2.2 MeV capture gamma-rays, inclusion of boron in the moderator is effective, where slow neutrons are captured predominantly by boron during slowing down process, and the accompanying 0.48 MeV gamma-rays can be cut off easily by a pulse height discriminator.

At the JAERI linac, the boron-loaded polyethylene moderator was used for more than 10 years. However, because of the improvement of the linac in recent years(increase in the beam current and the repetition to 600 pps) the radiation damage of the moderator became a serious problem; hydrogen evaporation and carbonization, the swelling and melting of polyethylene especially behind the target where the radiation density is extremely high.

---

* The following is a brief description of an article submitted to the Nuclear Instruments and Methods A, with the same title.

2 Boron-Nitride Loaded Water Moderator

To overcome these radiation damages, we have constructed an aluminum water box moderator in which boron-nitride(BN) loaded cooling water was circulated, as shown in Fig.1. In order to smear the fine structure dips observed in the neutron spectrum due to the aluminum resonances, two pieces of 1 cm thick boron loaded polyethylene plates were attached on both sides of the aluminum box, though the radiation damage was expected in the polyethylene side plates.

As the coolant of the moderator, BN powder of maximum 1.1 kg(after kneaded with water) was dissolved into the 6 liter water, which was circulated in a closed circuit including a heat exchanger.

The neutron TOF measurements were made by operating the linac. The electron beam energy was 125 MeV, the peak current 3A, the pulse width 25ns, and the repetition rates 300 or 600 pps. The neutron detector was a ^{6}Li-glass scintillator placed at a 47 m station, and the time analysis was made by an analyzer with a 31.25ns channel width and 4 k memory size.

A series of test was made by changing the BN contents in the coolant. The neutron energy spectrum shape was measured to be $E^{-0.74}$, which did not change in the neutron energy region from 0.3 eV to 10 keV region. The background was sufficiently small($<$ 2%) below 5 keV. The aluminum fine structures were not observed in the neutron beam from the source.

In high energy region, the time dependent backgrounds were measured by inserting two kinds of Al_2O_3 powder of 12 cm and 19 cm in the neutron beam. The neutrons of energies which coincided with the resonance energies of 35, 88 keV(Aluminum) and 432 keV(Oxygen) were stopped, whereas the delayed gamma rays from the neutron source transmitted through the Al_2O_3. They reached to the ^{6}Li-glass detector, and contributed to the background for the neutron counting. In Fig.2, TOF spectra of $E_n > 5$ keV are shown with insertion of 12 cm thick Al_2O_3,for pure water(A), and for BN loaded water (B)(1.1 kg of BN, n_B/n_H=0.053). In the figure, TOF spectrum without Al_2O_3 (open beam) are also shown. It is remarked that the background counts at these black resonances decrease systematically with neutron flight time and the content of BN, as shown in Fig.3. Decay half-lives $t_{1/2}$ of the background are extracted from Fig.3, which ranges from 9.2μsec for pure water to 2.8μsec for 1.1 kg of BN in the coolant. The decay speed of slow neutrons became about three times faster compared to the pure water, and the backgrounds were decreased correspondingly. In Fig.4, the decay half-life are shown as a function of atomic ratio of boron to hydrogen in the coolant.

This boron loaded water moderator seems to operate satisfactorily up to now, and it enable us to carry out the high precision TOF measurements in MeV energy region.

References

1) A.Michaudon: J.Nucl.Energy Part A-B 17(1963)165
2) R.L.Macklin : N.I.M. 91(1971)79
3) H.S.Camarda : N.I.M. 106(1973)205
4) A.Bignami, C.Coceva and R.Simonini: EUR-5157e (1974)
5) C.Coceva, R.Simonini and D.K.Olsen: N.I.M. 211(1983)459
6) J.M.Salome and R.Cools : N.I.M.179(1981)13

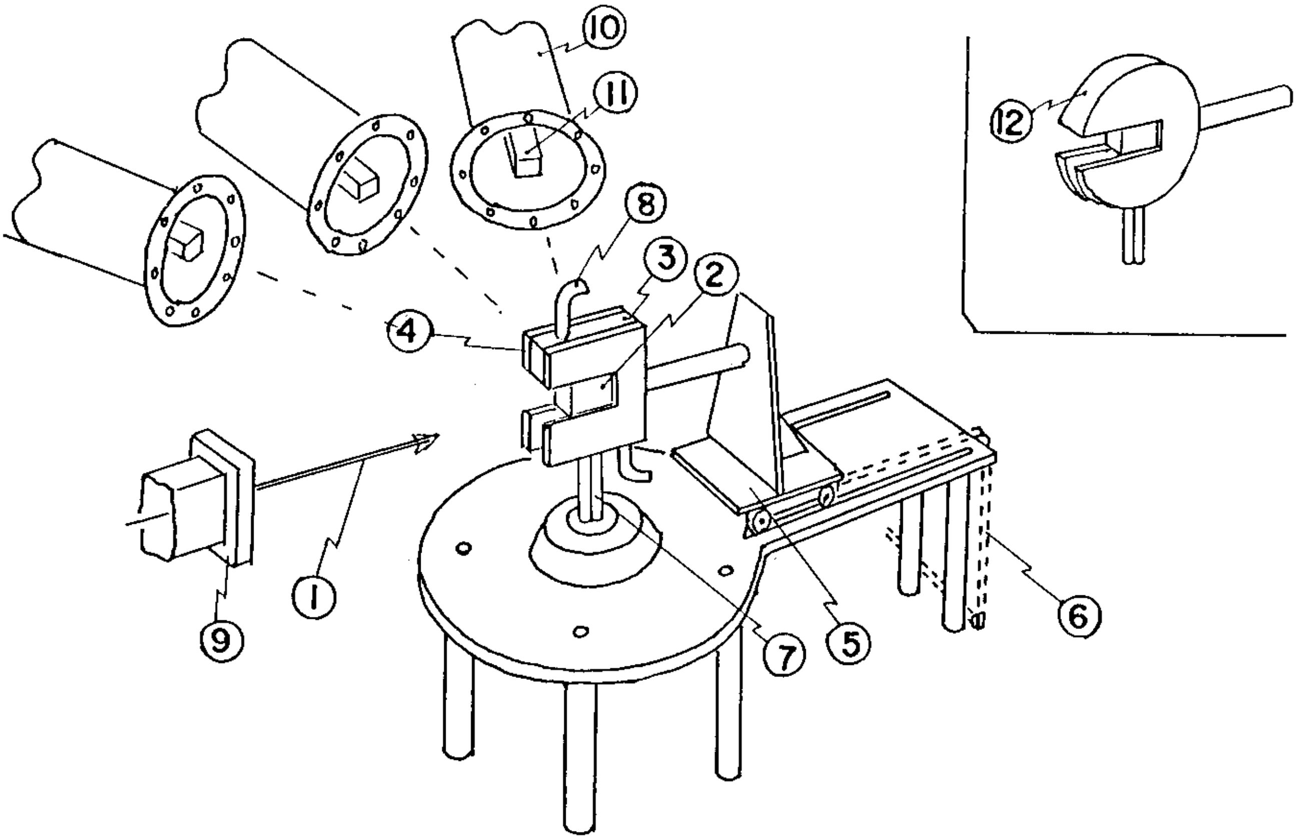

Fig.1
A sketch of the target moderator system for the linac.

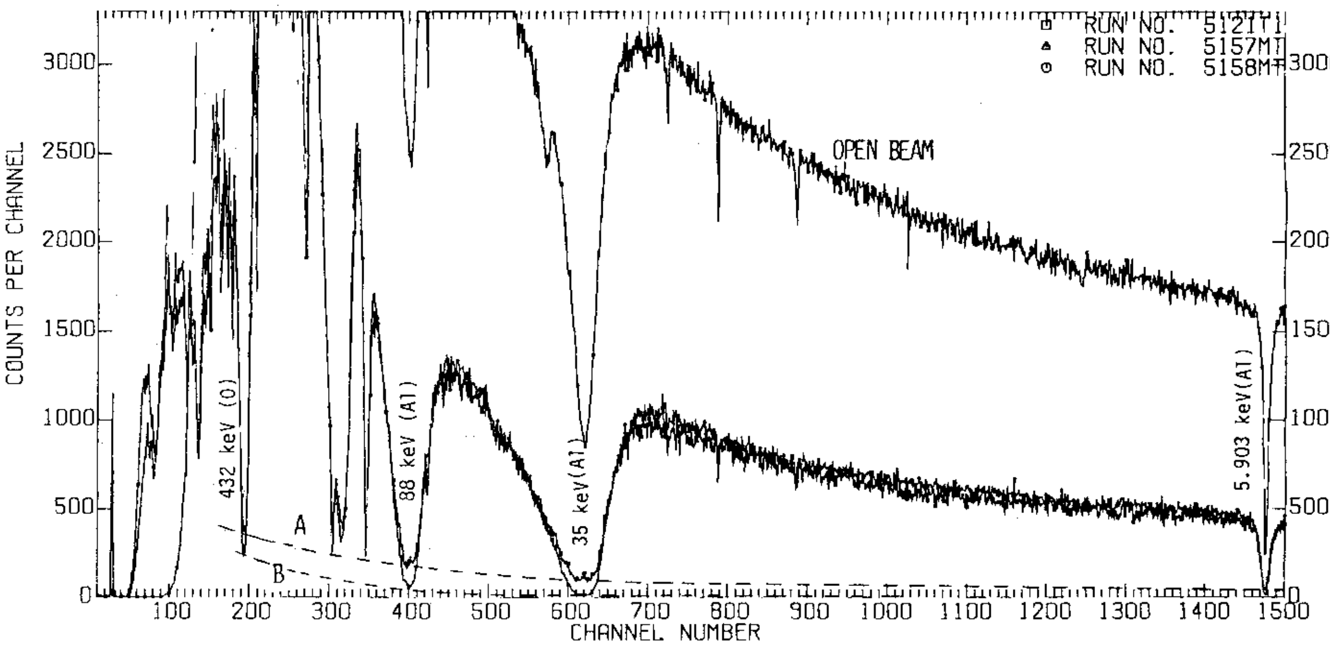

Fig.2 Neutron counts/channel versus TOF channel number measured by the ^{6}Li-glass detector. A open beam spectrum and the spectra with insertion of Al_2O_3 are shown. (A) Pure water, (B) 1.1 kg of BN in the water.

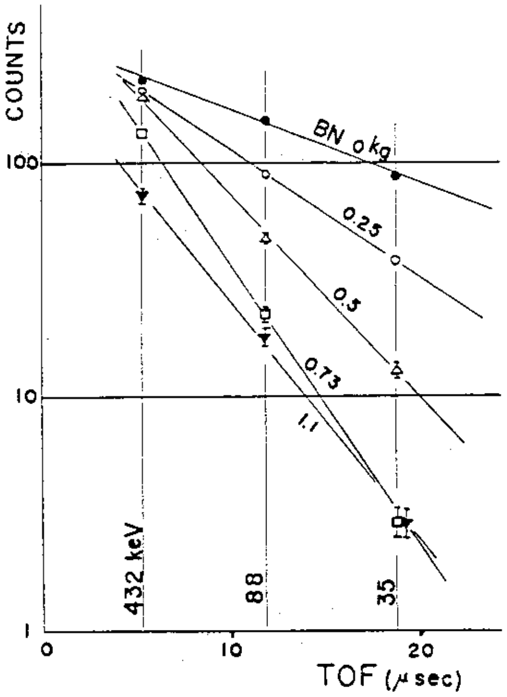

Fig.3

The background counts versus TOF as functions of BN contents.

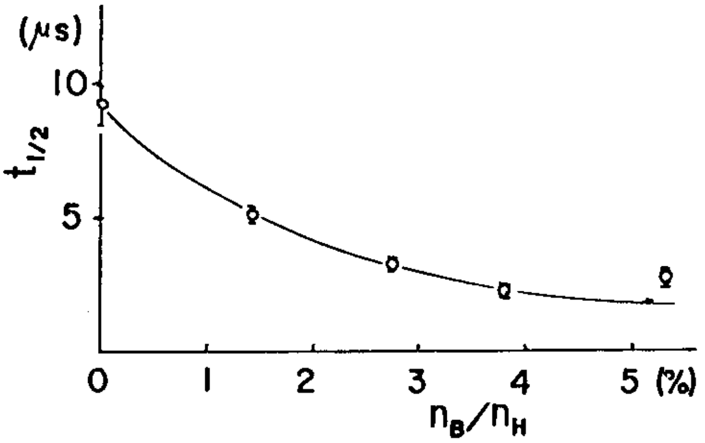

Fig.4

Decay half life of the backgrounds versus atomic ratio of born in the coolant.

VII PUBLICATIONS

7.1 Publications in Journals and Proceedings

1. Baba, Y. and Sasaki, T.
   Chemical States and Thermal Stability of Hydrogen-Implanted Ti and V Studied by X-Ray Photoelectron Spectroscopy.
   J. Nucl. Mater. 132 (1985) 173.

2. Baba, Y. and Sasaki, T.A.
   XPS Observations of Yttrium Surface Bombarded with Energetic Hydrogen-Ions.
   J. Nucl. Mater. 138 (1986) 149.

3. Electron Linac Group
   Electron Linac Operation and Improvements.
   JAERI-M 85-104 (1985) 19.
   L

4. Fujita, H., Kato, N., Tachikawa, T., Sugimitsu, T., Kimura, K., Ikeda, Y., Yamaguchi, H., Nakajima, Y., Sugiyama, Y., Tomita, Y., Ikezoe, H., Ideno, K., Shikazono, N., Kubono, S. and Tanaka, M.
   Phase Anomaly for Elastic and Inelastic Scattering of the $^{19}F + ^{16}O$ Systems.
   JAERI-M 86-067 (1986) 63.
   T

5. Furukawa, K. and Ohno, S.
   Decomposition of Solid Potassium Nitrate by Incident 100 keV Ions.
   Bull. Chem. Soc. Jpn., 58 (1985) 1831.

6. Furukawa, K. and Ohno, F.
   100 keV-Ion Accelerator for Study of Chemical Reactions.
   JAERI-M 85-110 (1985).

7. Ginocchio, J.N., Otsuka, T., Amado, R.D. and Sparrow, D.A.
   Medium Energy Probes and the Interacting Boson Model of Nuclei.
   Phys. Rev. C33 (1986) 247.

8. Hamada, S., Suzuki, K., Sawai, T. and Shiraishi, K.
   Temperature Dependence of Damage Profile in Helium Irradiated Stainless Steels.
   JAERI-M 85-104 (1985) 110.
   V

9. Hamada, S.
   The Specimen Preparation for Transmission Electron Microscopy by Cross-Section Method.
   J. Nucl. Sci. & Tech. in press.
   T, V

10. Horie, K. and Hanashima, S.
    Optically Coupled CAMAC Analog Input Output System.
    JAERI-M 85-132 (1985).
    T

11. Ikezoe, H., Shikazono, N., Tomita, Y., Ideno, K., Sugiyama, Y. and Takekoshi, E.
    Incomplete Fusion of the $^{16}O + ^{27}Al$ Reaction.
    Nucl. Phys. A444 (1985) 349.
    T

12. Inamura, T., Hashizume, A., Ohshima, M., Kikuchi, S., Aruga, T. and Ichikawa, S.
    Multiple Coulomb Excitation of ^{161}Dy.
    RIKEN Accelerator Progress Report (1985) in press.
    T

13. Ishii, M., Makishima, A., Hoshi, M. and Ishii, T.
    A Silicon Box: A New Tool for Ion-Beam Gamma-Ray Spectroscopy through Heavy-Ion Fusion Reactions.
    Symposium: Recent Advances of the Study of Nuclei off the Line of the Stability, Held by American Chemical Society in Cicago in September 1985.
    T

14. Ishii, M., Ishii, T., Hoshi, H. and Ogawa, M.
B(E2) Anomaly in Ground-State Bands of ^{126}Ce and ^{124}Ce.
Report of the Joint Seminar on Heavy-Ion Nuclear Physics and Chemistry in the energy range of Tandem Accelerators (II) JAERI-M 86-067 (1986) p.38.
T

15. Iwamoto, A.
Pre-Equilibrium Emission of Light Composite Particles in Light and Heavy Ion Reactions.
Proc. 4-th International Conference on Nuclear Reaction Mechanism, Varrenna, p.51 (1985).

16. Iwamoto, A.
Nucleon Clusterization.
Proc. 4-th International Symposium on Neutron Induced Reactions, Smolenice, in press.

17. Iwase, A., Sasaki, S., Iwata, T. and Nihira, T.
Calorimetric Measurements of Stopping Power of Al and Ni for ^{35}Cl and ^{12}C Ions.
J. Phys. Soc. Jpn. 54 (1985) 1750.
T

18. Iwase, A., Sasaki, S., Iwata, T. and Nihira, T.
Defect Production by Energetic Heavy Ions in Aluminum and Copper.
J. Nucl. Mater. 133 & 134 (1985) 365.
T, V

19. Iwase, A., Sasaki, S., Iwata, T. and Nihira, T.
Calorimetric Measurements of Stopping Power of Al and Ni for ^{35}Cl and ^{12}C Ions.
JAERI-M 85-125 (1985) 143.
T

20. Iwase, A., Sasaki, S., Iwata, T. and Nihira, T.
    Defect Production by Energetic Heavy Ions in Aluminum and Copper.
    JAERI-M 85-125 (1985) 248.
    T, V

21. Iwase, A., Sasaki, S., Iwata, T. and Nihira, T.
    Defect Production and Recovery in Nickel Irradiated with Energetic Ions.
    J. Nucl. Mater. to be published.
    V

22. Kawarasaki, Y.
    A Linked Microcomputer System: NODAL-Like Program in FORTH.
    Proc. 10th Meeting on Linac Technology, p.19, in Japanese (Sep. 5-7 1985, Sendai, Japan).
    L

23. Kazumata, Y., Yugo, S., Kimura, T., Sato, Y. and Nakano, T.
    ESR of Pyro-Graphite Irradiated by Ions I
    Low Energy Ion Bombardments.
    JAERI Internal Report (1986)
    V

24. Kazumata, Y., Yugo, S., Kimura, T. and Nakano, Y.
    ESR of Pyro-Graphite Irradiated by Ions II
    High Energy Ion Bombardments.
    JAERI Internal Report (1986)
    V, T

25. Kuroda, K., Noda, K., Ishii, Y., Saka, H., Imura, T. and Watanabe, H.
    Damage Structure in Ion-Irradiated Si_3N_4 Ceramics.
    Proceedings of 11th International Congress on Electron Microscopy, Aug. 31 - Sep. 7 1986, Kyoto, Submitted.
    V

26. Makishima, A., Adachi, M., Taketani, H. and Ishii, M.
    Yrast Bands in ^{138,136}Sm and ^{132}Nd.
    to be published in Phys. Rev. C. in 1986.
    T

27. Mashiko, K., Nobusaka, Y., Akiyama, N., Shoji, T., Ishizaki, N. and Kawarasaki, Y.
Status of the JAERI-LINAC.
Proceedings of the 10th Meeting on Linac in Sendai (1985) 16.
L

28. Mizumoto, M., Sugimoto, M., Ohkubo, M., Nakajima, Y., Furuta, Y. and Kawarasaki, Y.
Neutron Radiative Capture and Transmission Measurements of ^{135}Ba and ^{137}Ba.
Proc. Int. Conf. on Nuclear Data for Basic and Applied Science, Santa Fe (1985).

29. Mizumoto, M.
Standard Cross Section for Neutron Capture Measurements (in the keV Region).
Proc. of the 1985 Seminar on Nuclear Data, JAERI-M 86-080 (1986).

30. Noda, K., Ishii, Y., Matsui, H. and Watanabe, H.
Irradiation Damage in Lithium Oxide.
Radiat. Eff., in press.
T

31. Ohno, S. and Furukawa, K.
Decomposion of Crystalline Potassium Hexacyanoferrate (II) Trihydrate by Incident Energitic Argon Ions.
Bull. Chem. Soc. Jpn., 58 (1985) 1100.
V

32. Ohno, S., Furukawa, K. and Soga, T.
Elastic and Inelastic Collision in Decomposition of Poatssium Nitrate.
Bull. Chem. Soc. Jpn., 59 (1986) 1947.

33. Oshima, M., Kikuchi, S., Ichikawa, S., Aruga, T., Inamura, T., Hashizume, A. and Kusakari, H.
Multiple Coulomb Excitation of Deformed Odd Nuclei.
JAERI-M 86-067 (1986) 27.
T

34. Oshima, M., Johnson, N.R., McGowan, F.K., Baktash, C., Lee, I.Y., Schutz, Y., Ribas, R.V. and Wells, J.C.
An Investigation of the Evolving Collectivity at High Spins in ^{157}Er, ^{158}Er and ^{159}Er.
Phys. Rev. C (1986, in press).
T

35. Otsuka, T.
Microscopically Derived Interacting Boson Model.
Capture Gamma-Ray Spectroscopy and Related Topics - 1984, edited by S. Raman (AIP Conference Series No. 125, 1985).

36. Otsuka, T. and Ginocchio, J.N.
Renormalization of g-Boson Effects in the Interacting-Boson Hamiltonian.
Phys. Rev. Lett. 55 (1985) 276.

37. Otsuka, T. and Yoshida, N.
User's Manual of the Program NPBOS.
JAERI-M 85-094 (1985).

38. Otsuka, T. and Yoshinaga, N.
Fermion-Boson Mapping for Deformed Nuclei.
Phys. Lett., 168B (1986) 1.

39. Ozawa, K., Yamaguchi, H., Kawatsura, K., Sataka, M., Kitahara, T., Kikuchi, A., Komaki, K., Ootuka, A. and Fujimoto, F.
Beam-Foil Interaction of Highly Ionized Chlorine Ions in the High Energy Region.
Nucl. Instrum. & Methods B9 (1985) 621.
T

40. Ozawa, K. and Naramoto, H.
Ion Beam Analysis on Nb-Mo Alloy with High Energy Heavy Ions.
Proc. ISIAT'85.
T

41. Pardo, R., Kawarasaki, Y. and Wasniefski, K.
A CAMAC-Based Intelligent Subsystem for Atlas Example Application: Cryogenic Monitoring and Control.
Proc. 1985 Particle Acc. Conf., p.2017 (May 13-16 1985, Vancouver, BC, Canada).

42. Pittel, S., Scholten, O. and Otsuka, T.
Generalized Seniority in the Presence of Strong Shell Effects.
Phys. Lett. 157B (1985) 239.

43. Rao, M.N., Johnson, N.R., McGowan, F.K., Lee, I.Y., Baktash, C., Oshima, M., McConnel, J.W. and Wells, J.C.
Loss of Collectivity at High Spin in ^{172}W and a 3-Band Interpretation of First Yrast Upbends.
Submitted to Phys. Rev. C.
T

44. Sakai, E.
Further Measurements of Induced Radioactivities in Silicon and Germanium Irradiated with High-Energy Heavy Ions.
IEEE Trans. Nucl. Sci., NS-33 (1986) 651.
T

45. Sasaki, T.A., Baba, Y., Hojou, K. and Aruga, T.
Transmission Sputtering of Titanium by 114 MeV Fluorine Ions.
J. Nucl. Mater. 132 (1985) 95.
T

46. Sasaki, T.A. and Baba, Y.
X-Ray Photoelectron and X-Ray-Induced Auger Electron Spectroscopic Data, III -Graphite, Si, SiC, Si_3N_4 and SiO_2-.
JAERI-M 85-063 (1985).

47. Sasaki, T.A. and Baba, Y.
Surface Compositional and Chemical-State Changes of SiC, Si_3N_4 and SiO_2 by energetic Hydrogens.
J. Nucl. Mater. 138 (1986) 145.

48. Sataka, M., Ozawa, K., Kawatsura, K., Yamaguchi, H., Ishii, K., Kitahara, T., Masai, K., Ootuka, A., Komaki, K., Fujimoto, F. and Kikuchi, A.
    Beam-Foil Spectroscopy at JAERI Tandem.
    JAERI-M 85-125 (1985) 58.
    T

49. Scholten, O., Heyde, K., Van Isacker, P. and Otsuka, T.
    Mixed-Symmetry Interpretation of Some Low-Lying Bands in Deformed Nuclei.
    Phys. Rev. C32 (1985) 1729.

50. Semkow, T.M., Sarantites, D.G., Honkanen, K., Abenante, V., Adler, L.A., Baktash, C., Johnson, N.R. and Oshima, M.
    Spectroscopic Study of the High-Spin States in ^{135}Pr.
    Submitted to Phys. Rev. C.
    T

51. Shinohara, N., Ichikawa, S., Usuda, S., Suzuki, T., Okashita, H., Sekine, T., Hata, K., Horiguchi, T., Yoshizawa, Y., Shibata, S. and Fujiwara, I.
    Synthesis of Transuranium Nuclides from Interaction of ^{16}O with ^{238}U.
    Proceedings of the 1984 International Chemical Congress of Pacific Basin Societies, "Americium and Curium Chemistry and Technology", N.M. Edelstein et al.(Eds.), D. Reidel Publishing Co., Dordrecht, (1985) p.251-260.
    T

52. Shoji, T.
    The Trigger Pulsers Using SCR's to Drive the Large Thyratrons.
    JAERI-M 86-049 (1986).
    L

53. Soga, T., Furukawa, K. and Ohno, S.
    Effect of the Deposited Energy Density on the Chemical Reaction.
    Proc. 52th Ann. Conf. Chem. Soc. Jpn., I, p.322 (1986).
    V

54. Sugiyama, Y., Shikazono, N., Tomita, Y., Ikezoe, H., Tachikawa, T., Takekoshi, E., Kubono, S. and Tanaka, M.
Magnetic Substate Population in $^{12}C + {}^{12}C$ Inelastic Scattering.
Phys. Lett. 159B (1985) 90.
T

55. Sugiyama, Y., Tomita, Y., Ikezoe, H. and Shikazono, N.
Particle Line Shape after γ-Ray Emission in Flight.
Z. Phys. A322 (1985) 579.
T

56. Sugiyama, Y., Tomita, Y., Ikezoe, H., Ideno, K., Shikazono, N., Kato, N., Fujita, H., Sugimitsu, T. and Kubono, S.
Transfer Cross Sections for $^{28}Si + {}^{58,62}Ni$ Reactions near the Coulomb Barrier.
JAERI-M 86-067 (1986) 114.
T

57. Suzuki, K., Katano, Y., Aruga, T., Hamada, S. and Shiraishi, K.
Effect of Carbon on Microstructure in Ti-Modified Type 316 Stainless Steels Irradiated with Helium Ions.
J. Nucl. Mater., 133 & 134 (1985) 585.
V

58. Suzuki, K., Katano, Y., Aruga, T., Hamada, S. and Shiraishi, K.
Effect of Solute Carbon Content on the Distribution Helium Bubble and Dislocation Loop in Ti-Modified Type 316 Stainless Steels Irradiated with Helium Ions.
JAERI-M 85-104 (1985) 114.
V

59. Suzuki, K. and Hamada, S.
Effect of Degree of Cold Working before Annealing on the Distribution of Helium Bubble in Ti-Modified Type 316 Stainless Steel Irradiated with Helium Ions after Annealing.
JAERI Internal Report (1986)
V

60. Suzuki, M., Kawabata, Y., Takahashi, H. and Sakamoto, M.
Measurements of Neutron Total Reflections on Metallic Surfaces (in Japanese).
JAERI-M 86-037 (1986).
L

61. Takamura, S., Aruga, T. and Nakata, K.
Fission-Neutron Displacement Cross Sections in Metals.
J. Nucl. Mater. 136 (1985) 159.

62. Takeuchi, S. and Kanazawa, S.
Service Lives of Long-Life Carbon Stripper Foils in the First Three Years Operation of the JAERI Tandem Accelerator.
Nucl. Instr. and Meth. to be published.
T

63. Usuda, S., Yoshikawa, H. and Shinohara, N.
Ion Exchange Separation of Short-Lived Transplutonium Nuclides.
JAERI-M 86-067 (1986) 99.
T

64. Yoshida, T. and Hanashima, S.
A Current Logarithmic Amplifier for the JAERI Tandem Accelerator.
JAERI-M 85-085 (1985).
T

7.2 Contributions to Scientific and Technical Meetings

1. Baba, Y. and Sasaki, T.A.
   Surface Chemical Changes of TiC, TiN and TiO_2 by Light-Ion Bombardments.
   Annual Meeting of the Atomic Energy Society of Japan in Kyoto (Mar. 26-29, 1986).

2. Chiba, S., Baba, M., Nakashima, H., Ono, M., Yabuta, N., Yukinori, S. and Hirakawa, N.
   Interaction of Fast Neutrons with $^{6,7}Li$.
   International Conference on Nuclear Data for Basic and Applied Sciences, Santa Fe, May 1985.

3. Chiba, S. and Shibata, K.
   Revision of the Neutron Nuclear Data of Light Elements in JENDL-3PR1.
   Fall Meeting of Atomic Energy Society of Japan, Sendai, 1985.

4. Fujita, H., Kato, N., Tachikawa, T., Sugimitsu, T., Kimura, K., Ikeda, Y., Yamaguchi, H., Nakajima, Y., Sugiyama, Y., Tomita, Y., Ikezoe, H., Shikazono, N., Kubono, S. and Tanaka, M.
   Elastic and Inelastic Scattering of the $^{19}F + ^{16}O$ System.
   Fall Meeting of the Physical Society of Japan in Yamanashi (Oct. 12-15, 1985).
   T

5. Hanashima, S. and Minehara, E.
   Scaling of Optical Parameters for the JAERI Tandem Accelerator.
   Symposium of North Eastern Accelerator Personnel (SNEAP) 85 in Argonne, Illinois, U.S.A. (Oct. 21-24, 1985).
   T

6. Ichikawa, S., Sekine, T., Hata, K., Shinohara, N. and Takahashi, N.
   A Study of the Decay of ^{121}Ba.
   The 29th Symposium on Radiochemistry in Funabashi (Oct. 1-3, 1985).
   T

7. Ideno, K., Tomita, Y., Ikezoe, H., Sugiyama, Y., Yokota, W., Lee, S.M. and Mikumo, T.
   Coincidence Measurements of Heavy Fragments in the Deep Inelastic Collision of ^{35}Cl + ^{46}Ti.
   Spring Meeting of the Physical Society of Japan in Tokyo (Mar. 29 - Apr. 1, 1986).
   T

8. Igata, N., Miyahara, K., Tada, C., Blasl, D., Hamada, S., Sawai, T., Kayano, H. and Hosoi, Y.
   Microstructure and Mechanical Properties of α Particle Irradiated Stainless Steels.
   2nd International Conference on Fusion Reactor Materials in Chicago (Apr. 13-17, 1986).

9. Iwamoto, A.
   Subbarrier Fusion Reactions.
   Joint Seminor on Heavy-Ion Nuclear Physics and Nuclear Chemistry in the Energy Reagion of Tandem Accelerators (II) (Jan. 9-11, 1985).

10. Iwamoto, A.
    Pre-Equilibrium Emission of Light Composite Particles in Light and Heavy Ion Reactions.
    4-th International Conference on Nuclear Reaction Mechanism, Varrenna (June 10-14, 1985).

11. Iwamoto, A.
    Nucleon Clusterization.
    4-th International Symposium on Neutron Induced Reactions, Smolenice (June 17-21, 1985).

12. Iwase, A., Sasaki, S., Iwata, T. and Nihira, T.
    Defect Production and Recovery in FCC Metals Irradiated with Energetic Ions (II).
    Fall Meeting of the Physical Society of Japan in Chiba (Oct. 1-4, 1985).
    T, V

13. Iwase, A., Sasaki, S., Iwata, T. and Nihira, T.
Defect Production and Recovery in FCC Metals Irradiated with Energetic Ions (III).
Spring Meeting of the Physical Society of Japan in Tokyo (Mar. 29 - Apr. 1, 1986).
T, V

14. Iwase, A., Sasaki, S., Iwata, T. and Nihira, T.
Defect Production and Recovery in Nickel Irradiated with Energetic Ions.
Second International Conference on Fusion Reactor Materials in Chicago (Apr. 13-17, 1986).
V

15. Iwata, T.
Radiation Effect Studies in the Tandem Energy Region.
Beijing International Symposium on Physics at Tandem (May 26-30, 1986).
T

16. Kazumata, Y., Yugo, S. and Kimura, T.
ESR of Pyro-Graphite Irradiated by Various Particles.
Fall Meeting of the Physical Society of Japan in Chiba (Sep. 31 - Oct. 3, 1985).
V, T

17. Kuroda, K., Noda, K., Ishii, Y., Saka, H., Imura, T. and Watanabe, H.
Ion-Irradiation of Sintered Si_3N_4 Doped Y_2O_3.
Fall Meeting Japan Institute of Metals in Nigata (Oct. 4-6, 1985).
V

18. Mizumoto, M. and Sugimoto, M.
Neutron Capture Cross Section of ^{135}Ba and Its Uncertainty Analysis.
Fall Meeting of the Atomic Energy Society of Japan in Sendai, (Oct. 2-5, 1985).

19. Naramoto, H., Ozawa, K., Kawatsura, K., Sataka, M., Yamaguchi, S., Fujino, Y. and Aoki, M.
Ion Beam Analysis on Nb-Mo Alloy
(I) Lattice Location of Dissolved Deuterium Atoms.
Spring Meeting of the Physical Society of Japan in Tokyo (Mar. 30, 1986).
V, T

20. Ootuka, A., Fujimoto, F., Komaki, K., Kawatsura, K. and Ozawa, K.
Molecular Effect of Al and O X-Ray Yields from Aluminum Oxide Films for H and H_2 Ion Bombardment.
US-Japan Seminar on Physics with Fast Molecular Beam in Honolulu (Dec. 9-13, 1985).
V

21. Oshima, M.
Shape Change at High Spin States in $^{157,158,159}Er$.
Proc. of Kiken Seminar on Microscopic Aproach to the Nuclear Structure at High Spin (Kyoto, 1985).
T

22. Oshima, M.
Shape Change at High Spin States in $^{157,158,159}Er$.
Fall Meeting of Phisical Society of Japan (Tokyo, Oct. 12-15, 1985).
T

23. Oshima, M.
Shape Change at High-Spin States in Deformed Nuclei.
The 3rd Seminar on Science and Technology Sponcered by Interchange Association, Japan (Tokyo, Nov. 11-12).
T

24. Otsuka, T.
"Low-Lying Isovector Collective States and the IBM" and "Renormalization of G-Boson Effects in the Interacting-Boson Hamiltonian".
International Symposium on Particle and Nuclear Physics, September, 1985, Beijing (Peking), China.

25. Sataka, M., Ozawa, K., Kawatsura, K., Naramoto, H., Ishii, K., Ootuka, A., Komaki, K., Fujimoto, F., Kikuchi, A. and Kitahara, T.
Beam-Foil Spectroscopy of Multi-Charged Chlorine Ions (II).
Fall Meeting of the Physical Society of Japan (Oct. 1-4, 1985).
T

26. Shinohara, N., Usuda, N., Ichikawa, S., Suzuki, T., Magara, M., Okashita, H., Yoshikawa, H., Iwata, Y., Yoshizawa, Y., Shibata, S. and Fujiwara, I.
Transuranium Elements Produced by Heavy-Ion Nuclear Reactions (3) $^{16}O + ^{238}U$ and $^{12}C + ^{242}Pu$ Reactions.
The 29th Symposium on Radiochemistry in Funabashi (Oct. 1-3, 1985).
T

27. Sugimoto, M. and Yamanouti, Y.
Improvement of the Time Resolution of the Large Neutron Detectors.
Fall Meeting of the Physical Society of Japan in Kofu (Sep. 12-15, 1985).
T

28. Sugimoto, M., Yamanouti, Y., Nishihara, S., Mizumoto, M., Furuta, Y. and Hyakutake, M.
Measurements of the Neutron Elastic and Inelastic Scattering Cross Sections of Aluminum.
Fall Meeting of the Physical Society of Japan in Kofu (Sep. 12-15, 1985).
T

29. Sugimoto, M., Yamanouti, Y., Nishihara, S., Mizumoto, M., Furuta, Y. and Hyakutake, M.
Measurements of the $^{27}Al(n,n)$ and (n,n') Reactions at $E_n = 13$ MeV.
Annual Meeting of the Atomic Energy Society of Japan in Uji (Mar. 26-29, 1986).
T

30. Sugiyama, Y.
Spectrometer "ENMA".
KEK Workshop on Nuclear Physics Using Pions "Magnetic Spectrometer System for Pion Physics at KEK" (Apr. 19-20, 1985).
T

31. Sugiyama, Y.
Particle Identification for Heavy Nuclei.
Workshop on Focal Plane Counter for RIKEN Ring Cyclotron (Sep. 13-14, 1985).
T

32. Sugiyama, Y., Tomita, Y., Ikezoe, H., Shikazono, N., Takekoshi, E., Tachikawa, T., Kubono, S. and Tanaka, M.
Spin Alignment in $^{12}C + ^{12}C$ Inelastic Scattering.
Fall Meeting of the Physical Society of Japan in Yamanashi (Oct. 12-15, 1985).
T

33. Tomimitsu, H., Kazumata, Y. and Sakai, E.
XDT-Observation of Si Single Crystals Irradiated with Energetic Heavy Ions.
Fall Meeting of Phys. Soc. Japan in Chiba (Sep. 30 - Oct. 3, 1985).
T

34. Usuda, S., Shinohara, N. and Yoshikawa, H.
Anion Exchange Behaviour of Transplutonium Elements in Mineral Acid-Alcohol Mixed Solvents (II).
The 29th Symposium on Radiochemistry in Funabashi (Oct. 1-3, 1985).
T

35. Usuda, S., Yoshikawa, H. and Shinohara, N.
Ion Exchange Separation of Short-Lived Transplutonium Nuclides.
The Joint Seminar on Heavy-Ion Nuclear Physics and Nuclear Chemistry in the Energy Region of Tandem Accelerators (II) in Tokai (Jan. 9-11, 1986).
T

36. Yokota, W., Ideno, K., Suzuki, K., Ogihara, M., Nakagawa, T., Komatsubara, T., Galster, W., Lee, S.M., Mikumo, T., Tomita, Y., Ikezoe, H., Sugiyama, Y. and Hanashima, S.
Characteristics and Classification of Light Heavy Ion Reactions.
Spring Meeting of the Physical Society of Japan in Tokyo (Mar. 29 - Apr. 1, 1986).
T

37. Yoshikawa, H., Hatsukawa, Y., Ohtsuki, T., Endo, K., Nakahara, H., Usuda, S., Shinohara, N., Okashita, H. and Fujiwara, I.
Rapid Chemical Separation of Transplutonium Elements by Ion Exchange (I).
The 29th Symposium on Radiochemistry in Funabashi (Oct. 1-3, 1985).
T

Ⅷ PERSONNEL AND COMMITTEES

8.1 Personnel

Department of Physics			
	Naomoto	Shikazono	Director
	Yoichi	Suto	Administrative Manager
Accelerators Division			
Scientific Staff	Michio	Maruyama*	
	Shiro	Kikuchi	
	Suehiro	Takeuchi	
	Eisuke	Minehara	
	Susumu	Hanashima	
Technical Staff (Tandem, V.D.G.)	Chiaki	Kobayashi**	
	Isao	Ohuchi	
	Yutaka	Sato	
	Tadashi	Yoshida	
	Susumu	Kanda	
	Katsuzo	Horie	
	Satoshi	Tajima	
	Yoshihiro	Tsukihashi	
	Shinichi	Abe	
	Shuhei	Kanazawa	
Technical Staff (Linac)	Katuo	Mashiko**	
	Nobuyoshi	Akiyama	
	Yukio	Nobusaka	
	Tokio	Shoji	
	Nobuhiro	Ishizaki	
Nuclear Physics Laboratory			
Scientific Staff	Mitsuhiko	Ishii***	

* Head, Accelerators Division

** Leader, Technical Staff

*** Head of Nuclear Physics Laboratory

Nuclear Physics Laboratory (continued)

Scientific Staff	Yoshiaki	Tomita
	Yasuharu	Sugiyama
	Akira	Iwamoto
	Kazumi	Ideno
	Hiroshi	Ikezoe
	Masumi	Ohshima
	Takaharu	Ohtsuka
	Tetsuro	Ishii

Linac Laboratory

Scientific Staff	Yuuki	Kawarasaki*
	Yutaka	Furuta
	Makio	Ohkubo
	Yutaka	Nakajima
	Motoharu	Mizumoto
	Yoshimaro	Yamanouchi
	Masayoshi	Sugimoto
	Satoshi	Chiba

Solid State Physics Laboratory I

Scientific Staff	Kazuo	Gesi**
	Yukio	Kazumata
	Hiroshi	Naramoto
	Hiroshi	Tomimitsu

Solid State Physics Laboratory II

Scientific Staff	Tadao	Iwata***
	Saburo	Takamura
	Hiroshi	Maeda
	Shigemi	Sasaki
	Akihiro	Iwase
	Terufumi	Yokota

* Head, Linac Laboratory

** Head, Solid State Physics Laboratory I

*** Head, Solid State Physics Laboratory II

Solid State Physics Laboratory III

Scientific Staff	Masanobu	Sakamoto	

Atomic and Molecular Physics Laboratory

Scientific Staff	Kunio	Ozawa*	(- September, 1985)
	Yohta	Nakai*	(October, 1985 -)
	Kiyoshi	Kawatsura	
	Masao	Sataka	

Department of Chemistry

Nuclear Chemistry Laboratory

Scientific Staff	Hiroshi	Okashita**	
	Toshio	Suzuki	
	Shigekazu	Usuda	
	Nobuaki	Kono	
	Shin-ichi	Ichikawa	
	Nobuo	Shinohara	
	Masaaki	Magara	
Scholarship Fellow	Hideki	Yoshikawa	(Tokyo Metropolitan University) (- September, 1985)

Analytical Chemistry Laboratory

Scientific Staff	Yuji	Baba	

Physical Chemistry Laboratory

Scientific Staff	Mutsuhide	Komaki	

Solid State Chemistry Laboratory

Scientific Staff	Kazuhiko	Izui***	
	Shin-ichi	Ohno	
	Teikichi	Sasaki	
	Shigemi	Furuno	
	Hitoshi	Ohtsu	
	Kiichi	Hojou	

* Head, Atomic and Molecular Physics Laboratory

** Head, Nuclear Chemistry Laboratory

*** Head, Solid State Chemistry Laboratory

Department of Radioisotope Production

Production Development Division

Scientific Staff	Sumiko	Baba
	Hiromitsu	Matsuoka
	Kentaro	Hata
	Toshiaki	Sekine
	Yuichiro	Nagame

Department of Fuels and Materials Research

Physical Matallurgy Laboratory

Scientific Staff	Akimichi	Hishinuma*
	Takeo	Aruga
	Shozo	Hamada
	Tomotsugu	Sawai
	Kenji	Suzuki
	Katsumaro	Fukai

Fuel Property Laboratory

Scientific Staff	Hitoshi	Watanabe**
	Kenji	Noda
	Yoshinobu	Ishii

Function Materials Laboratory

Scientific Staff	Hiroji	Katsuta***
	Hideo	Ohno
	Takanori	Nagasaki

Department of Reactor Engineering

Reactor Instrumentation Laboratory

Scientific Staff	Eiji	Sakai

Radioisotope and Nuclear Engineering School

	Kensuke	Shiraishi

* Head, Physical Matellurgy Laboratory

** Head, Fuel Property Laboratory

*** Head, Function Materials Laboratory

Department of Health Physics

Technical Staff	Shoji	Izawa*
	Toshihiro	Miyamoto
	Takeo	Seki

* Chief of Radiation Control Group, Department of Health Physics

8.2 Tandem Steering Committee

(Chairman)	Toyojiro	Fuketa	(Deputy Director General, Tokai Research Establishment)
	Shojiro	Matsuura	(Director, Department of Reactor Engineering)
	Kazumi	Iwamoto	(Director, Department of Fuels and Materials Research)
	Naomoto	Shikazono	(Director, Department of Physics)
	Kaoru	Ueno	(Director, Department of Chemistry)
	Masatoshi	Tanaka	(Director, Department of Thermonuclear Fusion Research)
	Toshihiko	Abe	(Director, Department of Radioisotopes)
(Secretary)	Masashi	Iizumi	(Deputy Director, Department of Physics)
(Secretary)	Michio	Maruyama	(Head, Accelerators Division)
(Secretary)	Yoichi	Suto	(Administrative Manager, Department of Physics)

8.3 Tandem Consultative Committee

(Chairman)	Tetsuo	Aochi	(Executive Director)
(Vice Chairman)	Toyojiro	Fuketa	(Deputy Director General, Tokai Research Establishment)
(Vice Chairman)	Naomoto	Shikazono	(Director, Department of Physics)
	Hiromichi	Kamitsubo	(Principal Scientist, Institute of Physical and Chemical Research)
	Kōji	Nakai	(Professor, National Laboratory for High Energy Physics)
	Hiroyasu	Ejiri	(Professor, Osaka University)
	Shiori	Ishino	(Professor, University of Tokyo)
	Hiroyuki	Tawara	(Associate Professor, Institute of Plasma Physics, Nagoya University)
	Kohzoh	Masuda	(Professor, University of Tsukuba)
	Shiro	Iwata	(Professor, Kyoto University)
	Ichiro	Fujiwara	(Associate Professor, Kyoto University)
	Kenji	Sumita	(Professor, Osaka University)
	Itsuro	Kimura	(Professor, Kyoto University)
(Secretary)	Masashi	Iizumi	(Deputy Director, Department of Physics)
(Secretary)	Michio	Maruyama	(Head, Accelerators Division)
(Secretary)	Yoichi	Suto	(Administrative Manager, Department of Physics)

8.4 Tandem Program Advisory Committee

(Chairman)	Naomoto	Shikazono	(Director, Department of Physics)
	Masashi	Iizumi	(Deputy Director, Department of Physics)
	Hirokazu	Umezawa	(Senior Staff, Office of Planning)
	Shoji	Izawa	(Chief, Radiation Control Group, Department of Health Physics)
	Hitoshi	Watanabe	(Head, Fuel Property Laboratory, Department of Fuels and Materials Research)
	Hiroshi	Okashita	(Head, Nuclear Chemistry Laboratory, Department of Chemistry)
	Kunio (- September, 1985)	Ozawa	(Head, Atomic and Molecular Physics Laboratory, Department of Physics)
	Yohta (October, 1985 -)	Nakai	(Head, Atomic and Molecular Physics Laboratory, Department of Physics)
	Mitsuhiko	Ishii	(Head, Nuclear Physics Laboratory, Department of Physics)
	Yuuki	Kawarasaki	(Head, Linac Laboratory, Department of Physics)
	Michio	Maruyama	(Head, Accelerators Division, Department of Physics)
	Chiaki	Kobayashi	(Leader, Tandem Operation Group, Department of Physics)

Ⅸ CO-OPERATIVE RESEARCHES

	Title	Co-Operating Institution
2.2	Radiative Electron Capture for $Cl^{16+,17+}$ Ions on He Target	College of General Education, The University of Tokyo*
2.3	Beam-Foil Spectra of Chlorine Ions in High Energy Region (III)	College of General Education, The University of Tokyo* Department of Engineering Science, Kyoto University Faculty of Engineering, Ibaraki University*
2.4	Absence of Stage I Recovery Peak in Nickel Irradiated with Heavy Ions in Energy Range 100-120 MeV	Faculty of Engineering, Ibaraki University*
2.5	Radiation Effects of Negative Thermal Expansion in Semiconductors by Heavy Ion Irradiation	Faculty of Engineering, Tamagawa University*
2.6	Damage Profiles in Metals Irradiated with High Energy Ions	Faculty of Engineering, Ibaraki University*
2.8	Ion Beam Analysis on $Nb_{0.8}Mo_{0.2}$ Alloy I. Lattice Location of Dissolved Deuterium	Department of Nuclear Engineering, Tohoku University*
2.10	Lattice Defects in Silicon Carbide	Faculty of Engineering, Ibaraki University
3.3	Microstructure and Mechanical Properties of He Irradiated Stainless Steel	Faculty of Engineering, Nagoya University*
3.5	Conductivity of A Li_2O Single Crystal Irradiated by Oxygen Ions	Faculty of Engineering, Nagoya University*

3.6	Microstructure of Ion-Irradiated Si_3N_4	Faculty of Engineering, Nagoya University*
4.1	Production of Actinides in Reactions of ^{242}Pu with ^{12}C and ^{238}U with ^{16}O	Faculty of Science, Hiroshima University*
4.2	Transfer Reactions in 105-MeV ^{16}O + ^{197}Au	Faculty of Science, Osaka University*
4.4	A Study of Nuclei far from Stability by Using JAERI ISOL	Faculty of Science, Osaka University*
5.1	B(E2) Anomaly in Ground-State Bands of ^{126}Ce and ^{124}Ce	Department of Applied Physics, Tokyo Institute of Technology*
5.6	Transfer Cross Sections for ^{28}Si+^{58,82}Ni Reactions	Institute for Nuclear Study, The University of Tokyo*
5.8	Coincidence Measurement of Damped Reaction Fragments for the Systems of ^{35}Cl + ^{46}Ti and ^{37}Cl + ^{48}Ti	Tandem Accelerator Center, The University of Tsukuba*
6.1	Scattering of 14.9 and 18.0 MeV Neutrons from ^{118}Sn	Faculty of Engineering, Kyushu University* Faculty of Engineering, Tohoku University*
6.2	Preliminary Measurements for Elastic and Inelastic Neutron Scattering in the Energy Region of 30 MeV	Faculty of Engineering, Kyushu University*

* Travel expense is supplied by JAERI.